



TECHNISCHE  
UNIVERSITÄT  
WIEN

Vienna University of Technology

## DISSERTATION

# **PEEM microscopy and DFT calculations of catalytically active platinum surfaces and interfaces**

ausgeführt zum Zwecke der Erlangung des akademischen Grades eines  
Doktors der technischen Wissenschaften unter der Leitung von

**Assoc.Prof. Dipl.-Phys. Dr.rer.nat. Yuri Suchorski**  
**Univ.Prof. Mag.rer.nat. Dr.rer.nat. Günther Rupprechter**  
E165  
**Institut für Materialchemie**

eingereicht an der Technischen Universität Wien  
**Fakultät für Technische Chemie**

von

**DI Christian Spiel**  
Matrikelnummer 9800675  
Waaggasse 4/8  
1040 Wien

Wien, am 20. Jänner 2012

# Kurzfassung

Das Ziel dieser Dissertation war, die Eigenschaften von katalytisch aktiven Oberflächen und Grenzflächen von Platin sowohl mit experimentellen als auch mit theoretischen Methoden zu untersuchen.

Mit Hilfe von experimentellen Methoden wurde die katalytische CO-Oxidation auf einzelnen Körnern einer polykristallinen Platinfolie *in situ* unter Hochvakuum-Bedingungen untersucht.

Eine polykristalline Platinfolie besteht aus einzelnen  $\mu\text{m}$ -großen Kristallkörnern, die vorwiegend [100]-, [110]- und [111]-orientiert sind und sich in ihrer katalytischen Aktivität beträchtlich voneinander unterscheiden. Um die Unterschiede in der Reaktivität der einzelnen Körner experimentell zu untersuchen, wurde in dieser Arbeit eine Kombination von *Photoemissions-Elektronenmikroskopie* (PEEM) und *Quadrupol-Massenspektrometrie* (QMS) verwendet.

Das Messprinzip von PEEM beruht auf dem photoelektrischen Effekt, der die Emission von Photoelektronen durch Bestrahlung einer Probe mit (UV-)Licht bewirkt. Die emittierten Photoelektronen werden zur Abbildung der Probenoberfläche verwendet (die typische Auflösung liegt im Bereich von wenigen Mikrometern). Der Kontrast von PEEM-Bildern rührt von Unterschieden in der lokalen Austrittsarbeit her, die durch unterschiedliche Oberflächenorientierungen und/oder Änderungen der Adsorbatbedeckung hervorgerufen werden können.

Mit einer Kombination von PEEM und QMS war es möglich, die Kinetik der katalytischen CO-Oxidation auf einer polykristallinen Platinfolie gleichzeitig sowohl in globaler als auch in orts aufgelöster Weise zu untersuchen. Verfolgt man die katalytische CO-Oxidation auf Platinoberflächen bei konstanter Temperatur und konstantem Sauerstoffpartialdruck unter zyklischer Veränderung des CO-Partialdruckes, so kann man im bi-stabilen Bereich der Reaktion eine Hysterese der  $\text{CO}_2$ -Produktionsrate beobachten, wel-

che zwei kinetische Phasenübergänge ( $\tau_A$  und  $\tau_B$  genannt) bei unterschiedlichen CO-Partialdrücken aufweist, bei denen die Katalysatoroberfläche zwischen den zwei stabilen Zuständen hoher und niedriger Reaktivität hin- und herwechselt und die Platinoberfläche entsprechend mit Sauerstoff bzw. mit CO bedeckt ist. Im Bistabilitätsbereich zwischen  $\tau_A$  und  $\tau_B$  befindet sich das System (bei denselben externen Parametern  $p_{CO}$ ,  $p_{O_2}$ ,  $T$ ) in einem der beiden stabilen Zustände, abhängig von der Vorgeschichte des Systems.

Die bistabile Reaktionskinetik kann auf globale Weise mit QMS untersucht werden, und die Lage der globalen Übergangspunkte  $\tau_A$  und  $\tau_B$  im Parameterraum kann so bestimmt werden. Mit einer Reihe von Experimenten dieser Art ist es möglich, ein globales kinetisches Phasendiagramm zu erstellen, das ein nützliches Werkzeug zur Charakterisierung des gemittelten Verhaltens einer heterogenen Probe ist. Mit Hilfe von PEEM können wiederum die kinetischen Phasenübergänge auch orts aufgelöst für jede einzelne Oberflächendomäne bestimmt werden, indem man die Veränderungen in der lokalen PEEM-Intensität analysiert.

In der vorliegenden Arbeit wurden Experimente mit QMS und PEEM durchgeführt, mit deren Hilfe sowohl globale als auch orts aufgelöste kinetische Phasendiagramme einer polykristallinen Platinfolie und ihrer [100]-, [110]- und [111]-orientierten Domänen erhalten wurden. Die kinetischen Phasendiagramme wurden sowohl bei konstantem Sauerstoff-Partialdruck unter Veränderung der Temperatur als auch bei konstanter Temperatur unter Veränderung des Sauerstoff-Partialdruckes gemessen. Darüber hinaus wurden auch die kinetischen Übergänge, die die katalytische Zündung und Extinktion der CO-Oxidation auslösen, *in situ* auf derselben Probe untersucht und mit Resultaten aus *Feldionenmikroskopie*-Experimenten verglichen.

Die einzelnen Domänen der polykristallinen Platinfolie stellen ein fast perfektes Modell von räumlich begrenzten, Mikrometer großen Einkristall-Oberflächen dar. Diese Tatsache erlaubt es, die Ausbreitung der lokalen Reaktions-Diffusionsfronten *in situ* mit PEEM zu untersuchen. Eine solche Untersuchung wurde auf den anisotropen, [110]-orientierten Domänen der Folie durchgeführt. Die Ausbreitungsgeschwindigkeiten der elliptisch geformten Fronten wurden in der Richtung der Ellipsen-Hauptachsen analysiert, und die Ergebnisse zeigten eine hervorragende Übereinstimmung mit einer Modellierung, die mit Hilfe der *Luther-Gleichung* auf der Basis von Reaktions- und Diffusionsparametern aus der Literatur durchgeführt wurde.

Der zweite Teil dieser Doktorarbeit besteht aus einer theoretischen Untersuchung von  $CeO_2$ -Monolagen, die auf der Pt(111) Oberfläche adsorbiert sind. Zu diesem Zweck wurde

die Dichtefunktionaltheorie (DFT) in der Implementierung der *WIEN2k*-Software verwendet.

In diesem Teil der Doktorarbeit wurden zwei verschiedene, aus der Literatur bekannte experimentelle Strukturen des  $\text{CeO}_2/\text{Pt}(111)$ -Adsorbatsystems untersucht: eine  $(4 \times 4)$  und eine  $(1.4 \times 1.4)$ -Überstruktur, die einem Verhältnis der Gitterkonstanten von Cerdioxid und Platin von 3 : 4 bzw. 5 : 7 entsprechen. Diese Strukturen wurden durch Konstruktion von drei verschiedenen Geometrien im Falle der “3:4” und einer Geometrie im Falle der “5:7”-Struktur untersucht, die sich durch die jeweilige lokale Adsorptionsgeometrie voneinander unterscheiden. Die Lage der Atome in allen Strukturen wurde unter Beibehaltung der Symmetrie optimiert, was zu einer starken Korrugation der Adsorbatschicht führte. Die energetische Stabilität aller Strukturen wurde durch Berechnung der jeweiligen Gesamtenergie untersucht und miteinander verglichen. Darüber hinaus wurde die Adsorptionsenergie der Ceroxid-Schicht auf dem Platinsubstrat für jede Geometrie berechnet. Es zeigte sich, dass diejenige unter den untersuchten Strukturen am stabilsten war, die eine on-top Koordination von Sauerstoffatomen, welches sich an der Oberfläche der Ceroxid-Schicht befinden, mit dem Platinsubstrat aufweist.

Zusätzlich wurden sowohl die globale Zustandsdichte als auch die partiellen Zustandsdichten einzelner Atome innerhalb der Strukturen berechnet. Dabei zeigte sich, dass kleine Unterschiede in der lokalen Adsorptionsgeometrie zu beträchtlichen Änderungen der Zustandsdichten der betroffenen Atome führen. Dasselbe Resultat brachte auch eine Analyse der Differenz-Elektronendichte. Die Auswertung der Ladungstransfers, die bei der Bildung der Grenzflächenstruktur auftreten, ergab, dass einige Cer-Atome durch Atome des Platinsubstrats reduziert wurden, ein Ergebnis, welches auch aus dem Experiment bekannt ist. Der Bindungscharakter und die Verschiebungen der 1s-Kernniveaus der Sauerstoffatome wurden ebenfalls detailliert analysiert. Alle erhaltenen Resultate weisen auf eine starke Wechselwirkung zwischen Adsorbat- und Substratschicht hin, die der Grund für die promotierende Wirkung von Ceroxid als Additiv zu katalytischen Systemen sein könnte.



# Abstract

The aim of this thesis was to investigate the properties of catalytically active platinum surfaces and interfaces both with experimental and theoretical methods.

Using experimental methods, catalytic CO oxidation on individual grains of a polycrystalline platinum foil was studied *in situ* under high vacuum (HV) conditions.

A polycrystalline platinum foil consists of individual  $\mu\text{m}$ -sized crystal grains that are mainly [100]-, [110]- and [111]-oriented and differ significantly in their catalytic activity. In order to elucidate the differences existing between the reactivity of the individual grains, a combination of *photoemission electron microscopy* (PEEM) and *quadrupole mass spectrometry* (QMS) was used in this work.

The working principle of PEEM is based on the photoelectric effect where illumination of the sample with (UV-)light causes emission of photoelectrons. The emitted photoelectrons are used to visualize the sample surface (with typical resolution in the low micrometer range). The PEEM image contrast originates from differences in the local work function that may arise due to different crystallographic orientations and/or changes in the adsorbate coverage.

With a combination of PEEM and QMS, it was possible to study the kinetics of catalytic CO oxidation on polycrystalline platinum foil both in a global and a laterally-resolved way simultaneously. If catalytic CO oxidation on surfaces of platinum is followed at constant temperature and oxygen partial pressure under cyclic variation of the CO pressure, a hysteresis in the  $\text{CO}_2$  production rate is observed in the bistability region with two noticeable kinetic transitions (called  $\tau_A$  and  $\tau_B$ ) taking place at different CO pressures when the catalyst surface switches back-and-forth between two steady states of high and low reactivity while the Pt-surface is, correspondingly, either oxygen- or CO-covered. In the bistability region between  $\tau_A$  and  $\tau_B$ , the system stays (at the same values of the external parameters  $p_{\text{CO}}$ ,  $p_{\text{O}_2}$ ,  $T$ ) in one of both steady states depending on the system's prehistory.

The bistable reaction kinetics can be studied globally with QMS, and the positions of the global transition points  $\tau_A$  and  $\tau_B$  in parameter space can be obtained this way. Based on a series of experiments, a global kinetic phase diagram can be established that is a useful tool to characterize the average behavior of a heterogeneous sample. In turn, using PEEM the kinetic phase transition points can also be obtained in a laterally-resolved way for each individual surface domain by analyzing local PEEM intensity variations.

In the present work, QMS and PEEM experiments were performed, from which both global and laterally-resolved kinetic phase diagrams of polycrystalline platinum foil and, correspondingly, its [100]-, [110]- and [111]-oriented domains were obtained. The kinetic phase diagrams were measured both for constant oxygen partial pressure and varying temperatures as well as for constant temperature and varying oxygen partial pressure. Besides that, kinetic transitions that trigger catalytic ignition and extinction of the CO oxidation reaction were also studied *in situ* on the same sample and compared to results from experiments using *field ion microscopy* (FIM).

The individual domains of the polycrystalline Pt-foil provide an almost perfect model of spatially confined micrometer-sized single crystal surfaces. This allows studying the propagation of the local reaction-diffusion fronts *in situ* with PEEM. Such a study was performed on the anisotropic [110]-oriented domains of the foil. The front propagation velocities of the elliptically shaped fronts were analyzed in the direction of the main axes of the ellipsis, and the results showed an excellent agreement with a fit to *Luther's equation* using reaction and diffusion parameters from literature.

The second part of this thesis consisted of a theoretical study of CeO<sub>2</sub> monolayers adsorbed on the Pt(111) surface. For this purpose, density functional theory (DFT) was applied in the implementation of the *WIEN2k* software package.

In this part of the thesis, two different experimental structures of the CeO<sub>2</sub>/Pt(111) adsorbate system known from literature were studied: a (4×4) and a (1.4×1.4) superstructure, which correspond to a lattice constant ratio of ceria and platinum of 3 : 4 and 5 : 7, respectively. These structures were investigated by setting up three different geometries in case of the “3:4” and one in case of the “5:7” structure with a different atom-to-atom matching geometry. The atomic coordinates of each structure were optimized within symmetry constraints, which led to a significant corrugation of the adsorbate layer. The energetic stability of all structures was investigated by calculating their respective total energy. Furthermore, the adsorption energy of the ceria adlayer on the platinum substrate was calculated for each structure. It was found that a structure with a preferred on-

top coordination of surface oxygen atoms with regard to the platinum substrate is most stable among those investigated.

In addition, the global density of states (DOS) as well as the partial DOS of single atoms within each structure was calculated. It was revealed that small differences in the local adsorption geometry invoke sizable changes in the partial DOS of the involved atoms. The same result was obtained from the analysis of the difference electron density. An investigation of the charge transfer occurring upon forming the interface indicated a reduction of some of the cerium atoms of the adlayer by the interface platinum atoms, a result that is also well known from experiments. The bond character and the oxygen 1s core level shifts were also analyzed in detail. All results indicated strong interaction between adsorbate and substrate layer that may be the reason for the promoting effects observed when using ceria as an additive to catalytic systems.

*To Karin.*

# Acknowledgements

I would like to thank...

my supervisors **Prof. Yuri Suchorski** and **Prof. Günther Rupprechter** for their guidance and many fruitful discussions during all stages of this thesis.

**Prof. Peter Blaha** and **Prof. Karlheinz Schwarz** for providing their know-how and support on performing DFT calculations with WIEN2k.

**Prof. Josef Redinger** for his willingness to review this work.

**Prof. Robert Schlögl** (Fritz Haber Institute, Berlin) for support at various stages of the project.

**Fonds zur Förderung der wissenschaftlichen Forschung (FWF)**, in particular the **Special Research Program “Functional Oxide Surfaces and Interfaces” (SFB F45 “FOXSI”)**, **Österreichische Forschungsgemeinschaft (ÖFG)** and **Gesellschaft österreichischer Chemiker (GOECH)** for financially supporting my research and the attendance of several scientific conferences.

**Diana Vogel** for the very nice collaboration.

**Johannes Frank** and **Wolfgang Drachsel** for improving and extending the experimental setup.

all other **colleagues** at the **Institute of Materials Chemistry (IMC)** for the pleasant atmosphere and many social events after work.

my **family and friends** for their support.

**Karin** for her love.

# Contents

<b>1</b>	<b>Introduction</b>	<b>1</b>
<b>2</b>	<b>Experimental details</b>	<b>5</b>
2.1	The ultra-high vacuum system . . . . .	5
2.2	Samples . . . . .	9
2.3	Evolution of the experimental setup . . . . .	11
2.3.1	Sample holder . . . . .	11
2.3.2	Sample cooling . . . . .	13
2.3.3	Sample heating . . . . .	13
2.3.4	External temperature measurement . . . . .	13
2.3.5	Transfer system and load-lock . . . . .	14
2.4	Measuring techniques . . . . .	15
2.4.1	Photoemission electron microscopy (PEEM) . . . . .	15
2.4.1.1	Working principle of PEEM . . . . .	15
2.4.1.2	Instrumental details . . . . .	18
2.4.1.3	Contrast in PEEM images . . . . .	19
2.4.2	Quadrupole mass spectrometry . . . . .	21
2.4.2.1	Instrumental details . . . . .	21
2.4.3	X-ray photoelectron spectroscopy (XPS) . . . . .	23
2.4.4	Field ion microscopy (FIM) . . . . .	25
2.4.5	Electron backscatter diffraction (EBSD) . . . . .	28
2.4.5.1	Instrumental details . . . . .	29
<b>3</b>	<b>Catalytic CO oxidation on platinum surfaces</b>	<b>30</b>
3.1	Platinum . . . . .	31

## Contents

3.2	Reconstruction of platinum surfaces . . . . .	32
3.2.1	Reconstruction of Pt(100) . . . . .	33
3.2.2	Reconstruction of Pt(110) . . . . .	34
3.3	Adsorption of CO, oxygen and CO <sub>2</sub> on platinum surfaces . . . . .	34
3.3.1	Principles of adsorption . . . . .	35
3.3.2	Adsorption of CO . . . . .	37
3.3.3	Adsorption of oxygen . . . . .	39
3.3.3.1	Surface oxygen . . . . .	39
3.3.3.2	Subsurface oxygen . . . . .	41
3.3.4	Adsorption of carbon dioxide . . . . .	41
3.4	Diffusion of CO and oxygen on platinum surfaces . . . . .	41
3.4.1	Fundamentals of surface diffusion . . . . .	41
3.4.2	Diffusion of CO . . . . .	44
3.4.3	Diffusion of atomic oxygen . . . . .	44
3.5	Catalytic CO oxidation on platinum metal surfaces . . . . .	44
3.5.1	Langmuir-Hinshelwood mechanism . . . . .	45
3.5.2	Bistability and rate oscillations . . . . .	47
3.5.2.1	Bistability . . . . .	47
3.5.2.2	Kinetic phase diagram . . . . .	51
3.5.2.3	Rate oscillations . . . . .	52
<b>4</b>	<b>Experimental study of catalytic CO oxidation on polycrystalline platinum</b>	<b>54</b>
4.1	Motivation for the experiments . . . . .	54
4.2	Principles of the kinetic study . . . . .	56
4.2.1	Determination of the domain orientation . . . . .	59
4.3	Experimental results . . . . .	62
4.3.1	Introduction . . . . .	62
4.3.2	Global kinetic phase diagram for catalytic CO oxidation . . . . .	63
4.3.2.1	Kinetic phase diagram at constant partial pressure of oxygen	64
4.3.2.2	Isothermal global kinetic phase diagram . . . . .	66
4.3.3	Domain-specific kinetic phase diagrams . . . . .	67
4.3.4	Catalytic ignition and extinction experiments on Pt foil . . . . .	70
4.3.4.1	Comparison to the apex of a Pt nanotip . . . . .	73
4.3.5	Variation of oxygen pressure . . . . .	77
4.3.6	Reconstruction of the global kinetic phase diagram . . . . .	79

## Contents

4.3.7	Reaction-diffusion front propagation on Pt(110) domains . . . . .	80
4.3.7.1	Shape and orientation of the reaction-diffusion fronts . . . . .	80
4.3.7.2	Velocity of front propagation . . . . .	82
4.4	Summary and Conclusions . . . . .	85
<b>5</b>	<b>Density functional theory – a (short) introduction</b>	<b>87</b>
5.1	Schrödinger equation . . . . .	87
5.1.1	Approximations to the quantum many-body problem . . . . .	89
5.2	Density functional theory . . . . .	90
5.2.1	Thomas-Fermi theory . . . . .	91
5.2.2	The theorems of Hohenberg and Kohn . . . . .	91
5.2.3	Kohn-Sham equations . . . . .	92
5.2.4	Exchange-correlation functionals . . . . .	94
5.2.4.1	Local density approximation (LDA) . . . . .	95
5.2.4.2	Generalized gradient approximation (GGA) . . . . .	95
5.2.4.3	Strongly correlated systems – LDA/GGA+U . . . . .	96
5.2.5	Basis sets . . . . .	97
5.2.5.1	The basis set of WIEN2k . . . . .	98
<b>6</b>	<b>DFT calculations on the CeO<sub>2</sub>/Pt(111) interface</b>	<b>102</b>
6.1	The importance of CeO <sub>2</sub> for heterogeneous catalysis . . . . .	102
6.2	The structure of the CeO <sub>2</sub> /Pt(111) interface . . . . .	105
6.2.1	Structure of bulk CeO <sub>2</sub> . . . . .	105
6.2.2	Structures of the CeO <sub>2</sub> (111) surface and the CeO <sub>2</sub> /Pt(111) interface . .	106
6.3	Computational details of the DFT calculations . . . . .	108
6.4	Geometrical details . . . . .	109
6.5	Results of the calculations . . . . .	111
6.5.1	Adsorption geometries of the relaxed structures . . . . .	111
6.5.2	Energetics of adsorption geometry . . . . .	116
6.5.3	Total and partial density of states (DOS) . . . . .	118
6.5.3.1	Total density of states . . . . .	118
6.5.3.2	Partial density of states . . . . .	119
6.5.4	Electron density at the CeO <sub>2</sub> /Pt(111) interface . . . . .	122
6.5.5	Charge transfer between ceria and platinum . . . . .	126
6.5.6	Bond character . . . . .	128
6.5.7	Core level shifts of oxygen . . . . .	129



## *Contents*

6.6 Summary and Conclusions . . . . .	130
<b>7 Summary and Conclusions</b>	<b>132</b>
<b>References</b>	<b>140</b>
<b>Publications</b>	<b>152</b>
<b>Curriculum vitae</b>	<b>156</b>

## Introduction

The field of heterogeneous catalysis has greatly evolved since its early days [1]. Back then, *maximizing the catalytic activity* was the primary goal of catalytic research, which, due to the lack of suitable analytic techniques, was often based on pure trial and error where numerous different compounds and mixtures were tried until the right composition with the desired catalytic performance was found. Nevertheless, this screening approach proved to be successful and led to the development of most industrial catalytic processes that are still in widespread use today.

Catalysis has entered everyday life long ago, e.g., in the form of ammonia synthesis [2] which assured the exponential growth of the world population during the last century in the first place. Besides that, modern cars are equipped with a *three-way catalyst* (TWC) that removes large fractions of pollutants from the exhaust gases. Without pollution control by catalysis, the ever-increasing number of automobiles would have had dramatic effects on the ecosystem long ago: while uncontrolled emissions of toxic CO reached levels of 40–60 g/km by the end of the 1960s, they have nowadays dropped to below 1 g/km, thanks to the TWC and today's strict emission standards (at the time of writing: Euro 5) [3].

However, there are many problems in catalysis that are still unsolved: for example, the low temperature activity (i.e., just after the start of the engine) of a TWC leaves much to be desired and has to be further improved. Industry has shifted its paradigm, too: because a highly active catalyst without sufficient selectivity produces a large amount of by-products with potentially hazardous properties to the environment, in today's era of "green" chemistry, the focus of industrial catalytic research has significantly shifted towards maximizing selectivity, i.e., the specificity of a catalytically active material towards *one* desired product.

## 1 Introduction

In order to be able to improve a catalyst's performance, a proper understanding of the underlying reaction mechanisms and structural dependencies is an obvious prerequisite. The lack of knowledge in this area triggered the development and improvement of modern surface science and model catalysis during the last few decades, which was only possible with substantial improvements both in experimental and theoretical methods [4]. This progress was crowned by the awarding of the Nobel Prize in Chemistry to Prof. Gerhard Ertl "for his studies of chemical processes on solid surfaces" in 2007 [5].

Before being able to gain insight into a catalytic surface reaction, a fundamental problem has to be overcome first: most of the industrial ("real") catalyst materials consist of (oxide-)supported (metallic) nanoparticles with a heterogeneously distributed particle size, size-dependent catalytic activity and often strong and manifold interaction with the support material. Besides that, the nanoparticles exhibit many different surface orientations (provided they are fully crystalline at all!) which are known to significantly differ in their respective catalytic activity. Furthermore, all the mentioned features interplay with each other, enhancing the complexity of such a catalytic system even more. In summary, "real" catalysts are usually so complex and parameter-rich that the resulting data obtained with common surface science techniques are almost certainly a superposition of many opposed trends. Such an experimental approach would most probably raise more questions than it could possibly answer.

To improve upon this situation, the complexity of the system has to be significantly reduced, which can be achieved by choosing a well-defined sample material and removing unwanted residuals from the gas atmosphere as far as possible. This is the so-called *vacuum approach* to surface science, where *single crystals* of catalytically active materials are investigated under *ultra-high vacuum* (UHV) conditions [6]. It has been successfully followed in surface science and model catalysis research for a long time now. The low pressure niveau enables to utilize the whole plethora of surface-sensitive techniques to characterize and analyze a sample both *per se* and *in situ* under high vacuum conditions.

The major problems arising from such surface science studies on single crystals can be summarized in the terms "pressure gap" and "materials gap". Pressure gap describes the difference between reality and experiment with regard to (total and partial) gas pressures, namely ambient or enhanced pressure vs. UHV conditions. There is no guarantee that the details of the reaction mechanism are the same in those two vastly different pressure regimes. For example, effects such as mass transport, gas phase coupling or heat transfer through the gas phase are almost completely ruled out and neglected under UHV conditions.

## 1 Introduction

The term *materials gap* accounts for the much reduced complexity of single-crystalline samples compared to conventional industrial catalysts. Single crystal surfaces, which consist of large and defect-lean terraces of only one surface orientation, can hardly serve as a valid model for heterogeneous nanoparticles.

Although the vacuum approach has been hugely successful to gain insight into surface processes and reaction mechanisms of many different systems, both the pressure and materials gaps have to be bridged in order to extend it to real systems [7, 8]. Increasing the pressure asks for even more sophisticated measurement techniques that are able to largely cancel out the contribution of the then dominant gas phase to retain surface sensitivity and/or compensate the much reduced mean free path of, e.g., photoelectrons under these conditions. Increasing the complexity of sample materials goes hand in hand with a (further) development of spatially-resolving techniques that are capable of resolving differences on the nanoscopic scale while still maintaining the ability to detect global effects.

A complementary approach to tackle surface and interface systems is based on theoretical methods: *density functional theory* (DFT), used in its beginning mainly in the field of solid state physics, evolved into the workhorse of theoretical surface science during the last two decades, thanks to the large advances in modern computational performance and the development of more and more accurate exchange-correlation functionals [9]. Nowadays, even large surface and interface systems with unit cells containing several hundreds of independent atoms can be successfully simulated with DFT.

However, both mentioned limitations of the experimental vacuum approach apply to the theoretical approach as well: the size and complexity of systems simulated with DFT is still mostly limited by the need of *periodic boundary conditions* (i.e., periodicity and symmetry constraints), which make the introduction of features such as defect sites and vacancies to the unit cell rather difficult. This limitation can be seen as the theoretical “materials gap”, whereas the “pressure gap” of DFT corresponds to the total absence of the gas phase in common calculations. In addition, a “temperature gap” exists because conventional DFT calculations do not consider temperature effects. Needless to say, all these “gaps” in theory are major areas of research and have already been partly overcome by the use of larger unit cells that allow to include defects, atomistic thermodynamics and finite-temperature DFT [10].

This thesis provides a combination of *experimental* and *theoretical work* performed in the field of *surface science* and *heterogeneous catalysis*. It makes use of some modern

methods and proposes a new approach to partly “bridge” the complexity gaps described above.

The experimental part focuses on a study of catalytic CO oxidation on polycrystalline platinum foil. Following an introduction to the used experimental setup and measuring techniques in chapter 2, the fundamentals of catalytic CO oxidation are outlined in chapter 3. After that, the experiments performed during this work are detailed in chapter 4. A novel experimental approach is presented that involves a combination of differentially pumped *photoemission electron microscopy* (PEEM) and *quadrupole mass spectrometry* (QMS) to study the local kinetics on individual grains of a polycrystalline platinum foil. After that, the results are discussed in detail in the same chapter.

The theoretical part of this work presents an investigation of the  $\text{CeO}_2/\text{Pt}(111)$  interface system with *density functional theory* (DFT) as implemented in the *WIEN2k software package* [11]. This part opens with a short introduction to DFT itself in chapter 5, and the theoretical study on the ceria-Pt interface is presented in chapter 6. Two different experimental structures of this system were investigated with the focus set on determining the most stable adsorption geometry and analysing its electronic structure. It was revealed that major differences exist in the strength of the substrate-adsorbate interaction depending on the individual matching geometry of the atoms involved.

Finally, chapter 7 summarizes the most important findings of this thesis.

## Experimental details

This chapter describes the experimental setup and its evolution in the course of the scientific work as well as the measurement techniques that were preeminently used for the studies performed in this thesis. The ultra-high vacuum (UHV) system and the investigated samples are introduced in section 2.1 and 2.2, respectively, and section 2.3 outlines the evolution of the experimental layout. Section 2.4 is devoted to the description of the measuring techniques: sections 2.4.1, 2.4.2 and 2.4.3 detail photoemission electron microscopy (PEEM), quadrupole mass spectrometry (QMS) and X-ray photoelectron spectroscopy (XPS), respectively, which is followed by a brief description of field ion microscopy in section 2.4.4. Finally, section 2.4.5 closes this chapter with a short overview over electron backscatter diffraction (EBSD).

### 2.1 The ultra-high vacuum system

In order to achieve sample surface conditions that are quasi-free of contaminants, it was necessary to perform most of the measurements described in this work under strongly reduced pressure conditions. Whereas the base pressure in the chamber was always in the UHV range (i.e., well below  $10^{-7}$  mbar), the reaction experiments were performed at a pressure of the reactants in the high-vacuum (HV) range (that is, below  $10^{-5}$  mbar). Such pressure conditions are a requirement for a successful operation of PEEM because the generated photoelectrons must have a *mean free path* that is at least long enough to cross the electron-optical system.

Two photographic images (from different viewing directions) and a flowchart representation of the original UHV setup are shown in Fig. 2.1: it consists of a *single* large vacuum

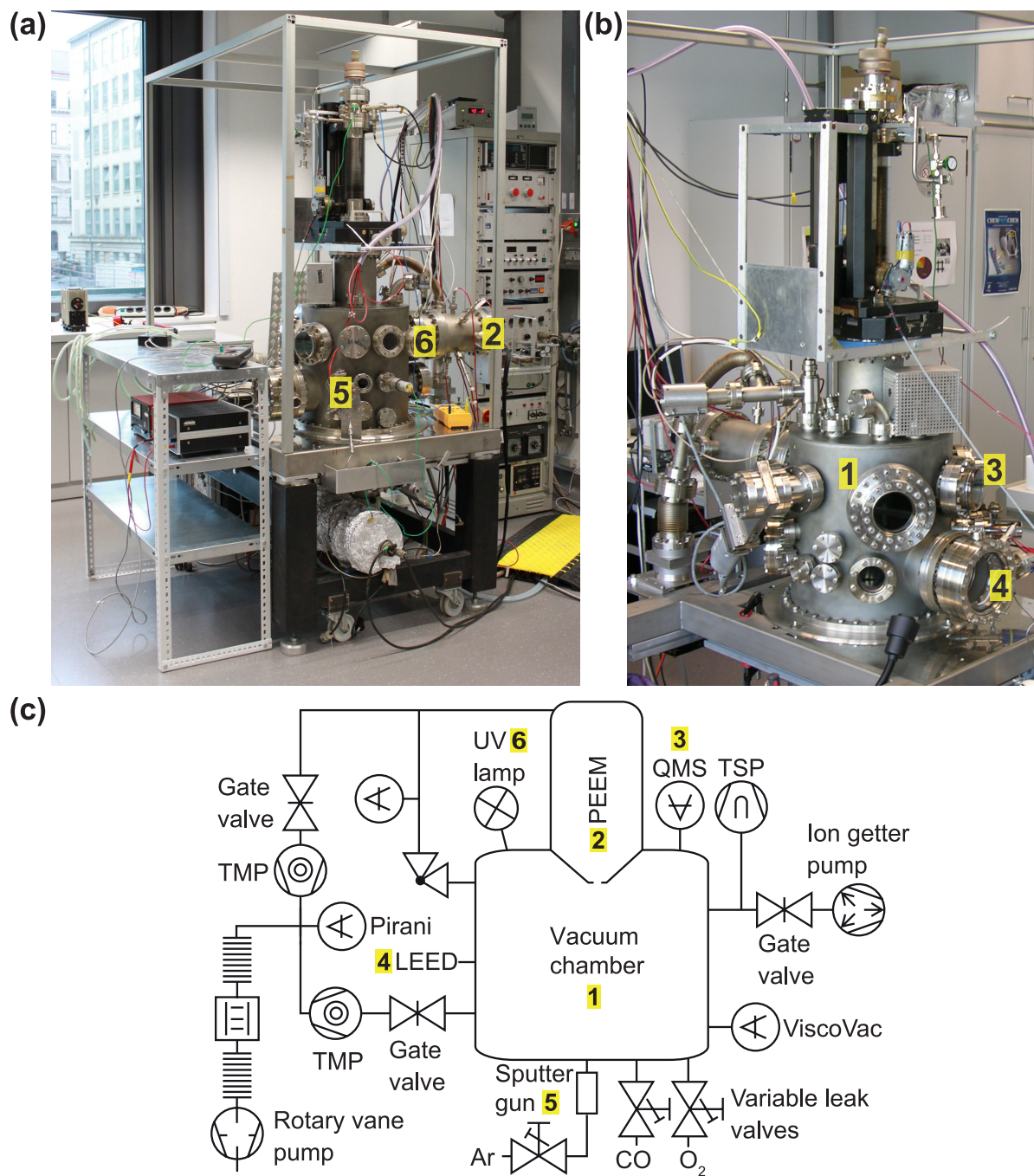


**Figure 2.1:** Original experimental setup consisting of a single vacuum chamber that provides facilities for performing sample preparation, characterization as well as PEEM and QMS experiments under reaction conditions. (a) and (b): Two photographic images of the experimental setup from different viewing directions. (c) Flowchart representation of the experimental setup consisting of (1) UHV chamber, (2) PEEM, (3) QMS, (4) LEED, (5) sputter gun and (6) UV lamp.



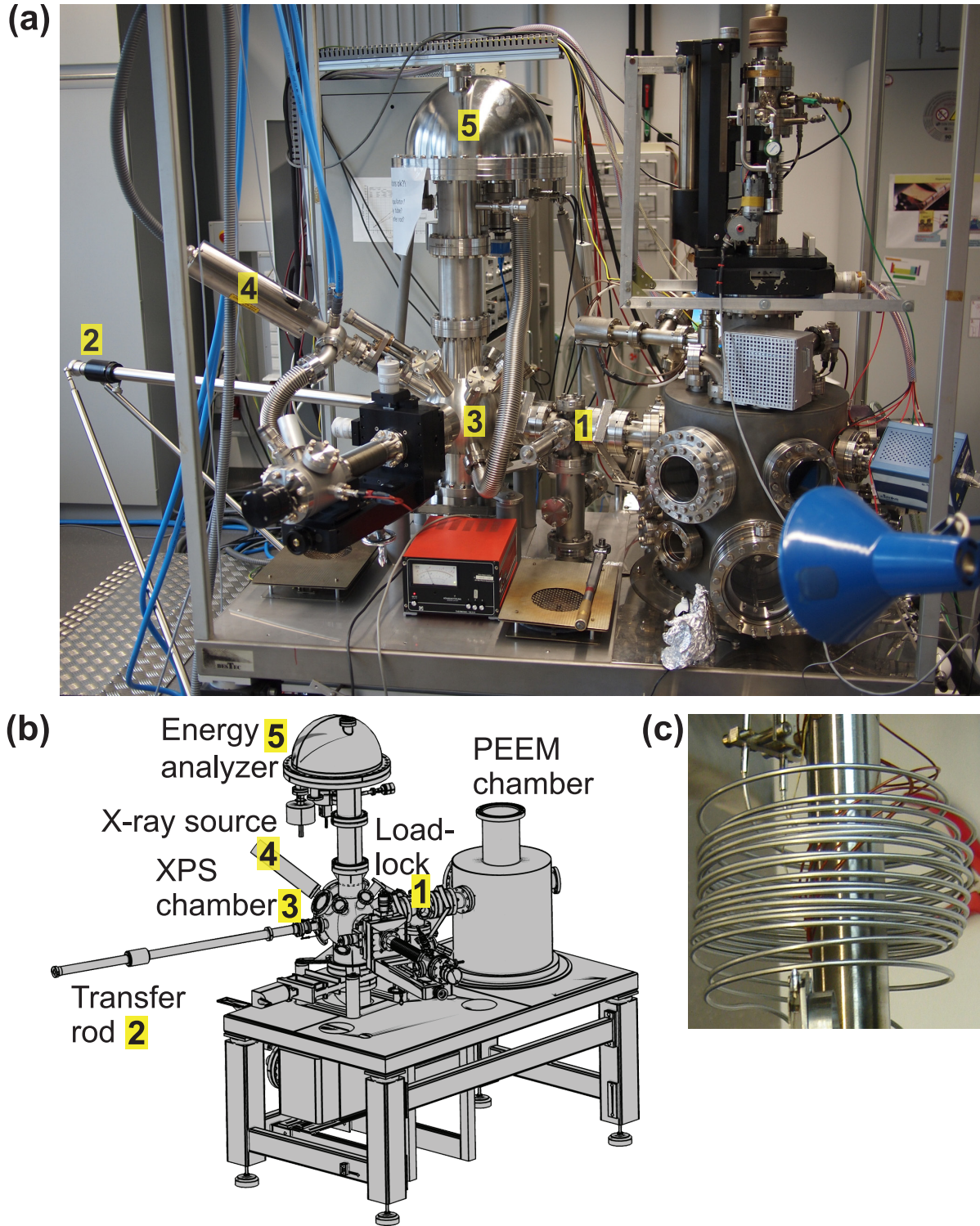


**Figure 2.2:** Final evolution stage of the experimental setup. (a) Photographic image of the apparatus and (b) schematic model of the sample load-lock and the new vacuum chamber for XPS measurements consisting of (1) load-lock, (2) transfer rod, (3) vacuum chamber, (4) X-ray source and (5) energy analyzer. (c) Liquid nitrogen cooling via spiral-shaped tubes.



## 2 Experimental details

chamber (indicated with number 1 in Fig. 2.1), which means that sample preparation, characterization and experiments under reaction conditions are carried out in one and the same system. During the experimental work, this setup was significantly modified with the addition of a second UHV chamber that contains an XPS-system. The new parts are shown in Fig. 2.2 and described in more detail in section 2.3.

The original mu-metal shielded stainless-steel UHV chamber (described in more detail in Ref. [12]) is mounted on a movable table that is equipped with two fan heaters installed in the tabletop, which allow for a bake-out of the UHV chamber to maximum temperatures of 200 °C using a heating tent. The parts of the vacuum chamber that are positioned *below* the tabletop plane are baked out using heating tapes.

The UHV chamber is equipped with a photoemission electron microscope (PEEM 150, STAIB Instruments, Fig. 2.1(2)), a quadrupole mass spectrometer (e-Vision<sup>+</sup>, MKS Instruments, Fig. 2.1(3)), a low-energy electron diffraction (LEED) device (SPECTALEED, Omicron NanoTechnology, Fig. 2.1(4)), gas supply (consisting of CO, O<sub>2</sub> and Ar) and sample preparation facilities, namely an Ar<sup>+</sup> ion sputter gun (IQE 11/35, SPECS, Fig. 2.1(5)). A UV-lamp (Fig. 2.1(6)) necessary for PEEM measurements is attached to the chamber and illuminates the sample through a CF40 window.

The sample is mounted on a 360°-rotatable ( $\phi$ ) manipulator in a 75 mm *off-axis position* that is necessary to minimize the distance between the sample and the first PEEM lens. The manipulator also allows vertical sample movements ( $z$ ) as well as horizontal motion in  $x$  and  $y$  directions. Besides that, the whole sample holder can be tilted in both directions by a few degrees ( $\theta$ ). This is very important for PEEM measurements, since the imaged sample area has to be aligned in a plane *perpendicular* to the optical axis of the PEEM to ensure a homogeneous illumination of the *field of view* (FOV). Because small surface undulations are always present even in case of polished samples, a homogeneous electron emission in the FOV can only be obtained by slight variations of the sample tilting angle.

Gases of high purity (O<sub>2</sub>: 99.999 %, Ar: 99.999 %, Messer; CO: 99.97 %, Linde) were introduced for all experiments from 1 L MINICAN<sup>®</sup> gas bottles attached to the apparatus. The gases were dosed into the vacuum chamber via variable leak valves (Balzers/Varian) that are connected to the gas bottles via 3 mm diameter stainless-steel tubes equipped with Swagelok<sup>®</sup> interconnects.

Once mounted, the sample can be heated up to ~750 K via indirect radiation heating from a thoriated tungsten filament that is positioned behind the back of the sample. Additional electron bombardment allows for maximum a sample temperature of ~1300 K.

## 2 Experimental details

The sample temperature is measured via a type-K (Ni/NiCr) thermocouple spot-welded to the sample surface and connected to a measuring device with electrical feedthroughs. Besides that, another thermocouple is mounted on a linear motion feedthrough (see section 2.3.4 for details). It can be contacted to different areas of the sample surface to check for the presence/absence of significant temperature gradients.

A turbomolecular pump (TMU 260, Balzers) connected to a rotary vane backing pump (TriVac D8B, Leybold) is used to achieve the UHV conditions necessary for the experiments. Another TMP (TMU 071P, Pfeiffer Vacuum), which is attached to the same fore-pump, allows to carry out experiments in the  $10^{-6}$ – $10^{-5}$  mbar range by *differential pumping* the electron optics of the PEEM. In addition, an ion pump (VacIon Plus 500, Varian) that is used to maintain the base pressure of the setup is installed at the bottom of the vacuum chamber. Finally, a titanium sublimation pump (TSP; Varian), which is mainly used to effectively remove hard-to-pump hydrogen ( $H_2$ ) from the residual gas atmosphere (typical conditions:  $\sim 40$  A, 1 minute), is also part of the experimental setup. Except for the TSP, all vacuum pumps can be separated from the main chamber by gate valves (VAT).

Three gauges are used to permanently monitor the total pressure in the vacuum chamber, namely a Bayard-Alpert hot cathode ionization gauge (Varian) for low pressures, a spinning rotor gauge (Viscovac, Leybold) for pressures above  $10^{-6}$  mbar and a thermal conductivity Pirani gauge (ThermoVac, Leybold) for high pressures, e.g., during the initial stages of chamber evacuation. Besides that, an additional glass tubulated Bayard-Alpert pressure gauge (Veeco) is attached to the chamber that was used to calibrate the primary ionization gauge.

## 2.2 Samples

The sample used in the experiments is a high-purity (99.99 %, Goodfellow) polycrystalline platinum foil with a surface area of approximately  $1 \times 1 \text{ cm}^2$  and a thickness of  $\sim 0.25$  mm. Figure 2.3(a) shows a magnified image of the platinum sample surface recorded with an optical microscope (DM 6000M, Leica): the polycrystalline structure of the surface is clearly resolved with pronounced boundaries existing between the individual grains. The optical image was used for calibrating the magnification of PEEM by comparing it to PEEM images of the same sample spot (shown in Fig. 2.3(b)).

The Pt sample was mechanically polished and flame-annealed to ensure proper crystallization in the low Miller-index planes (100), (110) and (111). Prior to mounting in the chamber, it was cleaned in an ultrasonic bath filled with acetone for 10 minutes. After

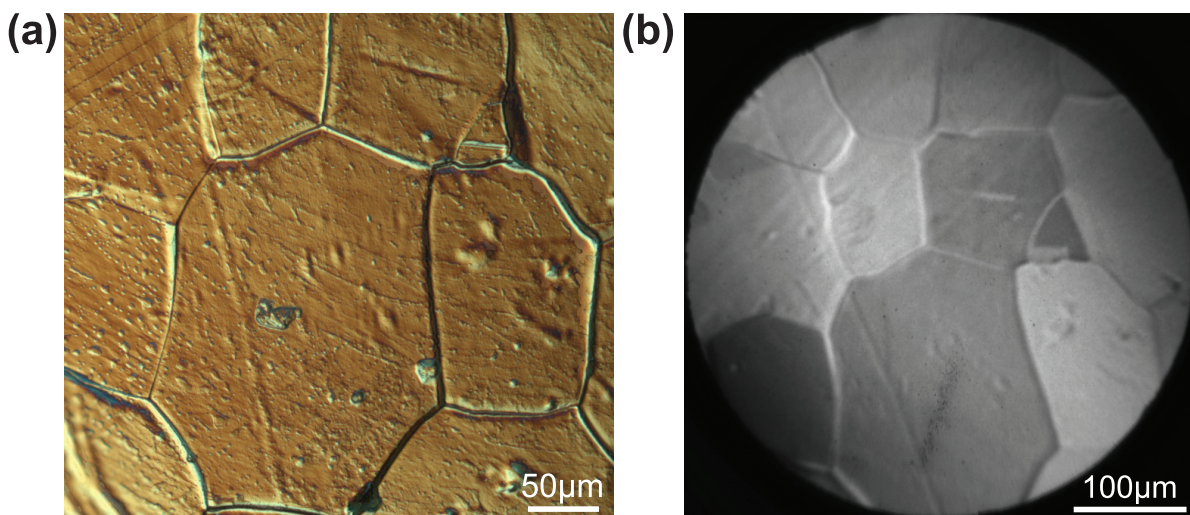


**Figure 2.3:** Platinum sample surface. (a) Optical microscopic image of the area on the polycrystalline platinum sample surface where most of the experiments were performed. (b) PEEM image of the same sample spot.

evacuation and bake-out of the vacuum chamber, repeated cycles of argon ion sputtering ( $p_{Ar} = 1 \times 10^{-5}$  mbar, typical argon ion current: 4–4.5  $\mu$ A) and vacuum annealing at 1000–1100 K were carried out to clean the sample surface from remaining contaminants. Each of those treatments was performed for  $\sim 15$  minutes. Before each kinetic experiment, the sample was cleaned with another cycle of argon sputtering and vacuum annealing, and, in addition to these procedures, the sample was subject to a (mild) oxygen treatment (namely, heating it for 15 minutes in  $5 \times 10^{-7}$  mbar  $O_2$  at 623 K) to oxidatively remove remaining carbonaceous contaminants from the surface. This way, a clean and smooth Pt surface was prepared, and the degree of cleanliness was checked by *X-ray photoelectron spectroscopy* (XPS; see section 2.4.3 for details).

For the kinetic measurements, the sample was positioned  $\sim 5$ –10 mm in front of the cone-shaped transfer lens of the PEEM. Before each experiment, the brightness of the PEEM image was optimized by slight adjustments of the working distance ( $y$ ), the sample rotation ( $\phi$ ,  $\theta$ ) and the voltage settings of the individual PEEM lenses. Quadrupole mass spectrometry was used in parallel to PEEM to collect data on the pressures of the reactant gases. For this purpose, the QMS is positioned in the vicinity of the PEEM in the vacuum chamber. The mass spectra were recorded for mass-to-charge ratios ( $m/z$ ) of 27–45, thus measuring CO ( $m/z = 28$ ), oxygen (32) and  $CO_2$  (44) simultaneously. Each of these range scans took  $\sim 3$ –4 seconds to complete. The pressure data were saved in a computer file and later correlated to the PEEM intensity recorded by a CCD camera.

## 2.3 Evolution of the experimental setup

This section describes several significant changes and improvements to the original setup that were made during the experimental work.

### 2.3.1 Sample holder

The original (manufacturer-provided) sample holder design (shown in Fig. 2.4(a) and described in more detail in Ref. [12]) consisted of a trapezoid-shaped sapphire block with four small holes positioned at the corners of a square, onto which a sample could be mounted with screws and nuts. Another circular hole with a diameter of 8 mm was drilled into the middle of the square, into which a filament could be placed to heat the sample via radiation and/or electron-bombardment. Besides holding the screws, the four small holes also acted as electrical feedthroughs: two screws at the diagonally opposite corners of the square served as resistive heating contacts and the other two as thermocouple contacts. Another two holes were drilled into the top of the sapphire crystal to allow for a sample transfer using a wobble-stick. This way, the sample holder could be inserted *from the top* into a pocket of the copper-made sample stage. The forwarding of sample grounding, temperature signal and direct (resistive) heating current between the sapphire block and the sample stage was achieved via spring-supported ball contacts located in the pocket of the sample stage.

The original layout of the sample holder, as outlined above, had several drawbacks: over time, the ball contacts proved problematic because several *slack joints* occurred during the initial stages of the experiments (a well-grounded sample is necessary for PEEM operation to avoid charging). Besides that, sample transfers would have been nearly impossible without breaking the vacuum because the risk of a sample drop would have been very high using the preinstalled wobble-stick. In addition, the sample holder design would have been totally incompatible with the planned sample transfer system that is detailed in section 2.3.5. Last but not least, sapphire is a very expensive and hard to process choice for a sample holder material, despite its numerous advantageous properties such as excellent thermal conductivity, chemical stability, insulating behavior and a high melting point.

As a first step, the sapphire was therefore replaced with a similarly shaped sample holder made of MACOR<sup>®</sup>, a white machinable glass-ceramic that is a much cheaper and easier to manipulate material (cf. Fig. 2.4(b)). Unfortunately, MACOR<sup>®</sup> is also a much weaker thermal conductor compared to sapphire: this property is detrimental for an ef-

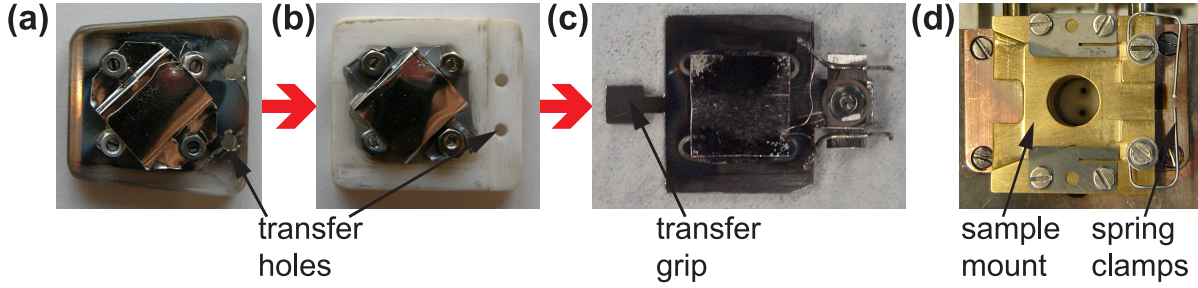


**Figure 2.4:** Evolution of the sample holder design. (a) Original sample holder made from sapphire and (b) revised sample holder made from MACOR<sup>®</sup>. Both designs have holes at the top to allow for a sample transfer using a wobble stick. The temperature signal of the thermocouple and the direct heating current are transported through the nuts and screws at the corners of the sample. (c) New sample holder made from stainless steel. A transfer grip allows for an easy sample transfer with a transfer rod. The temperature signal is forwarded with spring clamps. (d) Gold-coated copper sandwich adapter that is needed to make the new sample holder design compatible with the original layout of the sample stage.

ficient indirect sample cooling because it would have taken a very long time to reach a desired (low) sample temperature with such a sample holder material and the planned cooling system (see section 2.3.2). Therefore, it was decided to completely alter the design of the sample holder.

Based on the experiences described above, the design of the sample holder was significantly altered to a much smaller plate made of stainless steel that is based on an original Omicron/SPECS design (the new sample holder is shown in Fig. 2.4(c)). The plate is equipped with a grip at the end that is suitable for sample transfer with a transfer rod. The sample holder can be mounted onto the manipulator by inserting it *horizontally* into the sample stage, thus allowing the direct usage of a transfer rod without the need of a wobble-stick. In order to retain the original sample stage layout despite this substantial design change, a three-part (gold-coated) copper sandwich adapter (shown in Fig. 2.4(d)) was constructed, whose back part fits into the pocket where the original sapphire sample holder was put. The ball contacts of the old design were discarded in favor of much more reliable connections using spring clamps, thereby also removing the (never-used) resistive sample heating. The thermovoltage signal is transferred from the spring clamps to the manipulator through Kapton<sup>®</sup> insulated wires *around* the sample stage, thereby reducing the possibility of slack joints considerably. In order to measure the Ar<sup>+</sup> ion current during sputtering, the sample must be grounded separately from the chamber. For this purpose, the middle part of the sandwich adapter consists of a thin sapphire plate that effectively insulates the front part (i.e., the sample mount) from the rest of the sample

stage. Another Kapton<sup>®</sup> insulated wire is connected directly to the front-end part of the adapter to ensure a reliable and defined sample grounding.

### 2.3.2 Sample cooling

As shown in Fig. 2.2(c), cooling of the sample with liquid nitrogen (l-N<sub>2</sub>) was realized with two stainless-steel tubes (diameter: 2 mm) bended in a spiral around the axis of the manipulator. This design choice guarantees that the manipulator axis ( $\phi$ ) is still 180°-rotatable both clockwise and counter-clockwise. Both tubes are connected to the copper-made front part of the sample stage, thereby effectively forming a closed circuit through which l-N<sub>2</sub> can be pumped to cool down the sample. The vacuum sealing of the tubes is achieved using VCR<sup>®</sup> copper seals.

### 2.3.3 Sample heating

The filament for indirect radiation heating is installed approximately 6 mm behind the sample in the copper-made sample stage. Originally, it was based on commercially available tungsten lamp filaments that proved to be rather short-living (the average filament lifetime was less than 2 months). Besides that, leak currents to the copper walls of the sample stage occurred frequently during electron bombardment in the beginning because of a poor insulation of the filament-sample distance.

Therefore, the original lamp filaments were replaced by self-made filaments that are manufactured from a coiled thoriated tungsten wire (diameter: 0.12 mm) that is spot-welded to two pins. The lifetime of these filaments turned out to be much higher (i.e., up to a year). In addition, the electrical shielding of the filament was significantly improved by surrounding it with a cylindrically-shaped alumina (Al<sub>2</sub>O<sub>3</sub>) tube. The new filament can be operated in an oxygen pressure of  $\sim 10^{-5}$  mbar at a maximum permanent heating current of 2.2 A.

### 2.3.4 External temperature measurement

As mentioned in the description of the UHV chamber in section 2.1, an additional type-K thermocouple was installed in the chamber to allow for a direct measurement of the temperature in any arbitrarily chosen area of the sample. It consists of Alumel<sup>®</sup> and Chromel<sup>®</sup> wires mounted on a linear motion feedthrough and spot-welded together to form a thermocouple junction that could be gently pressed against the sample surface



to read out the local temperature. Several times, the device was used for controlling the sample temperature at various points on the surface in order to rule out the existence of significant temperature gradients. Since the sample material (Pt) is an excellent thermal conductor, the temperature difference found between different sample spots never exceeded 5 K.

### 2.3.5 Transfer system and load-lock

In the course of the experiments described in this work, the main (PEEM) vacuum chamber was extended with a home-made load-lock, a sample transfer system as well as an additional UHV chamber equipped with XPS (all new components are also shown in Fig. 2.2(a) and (b)).

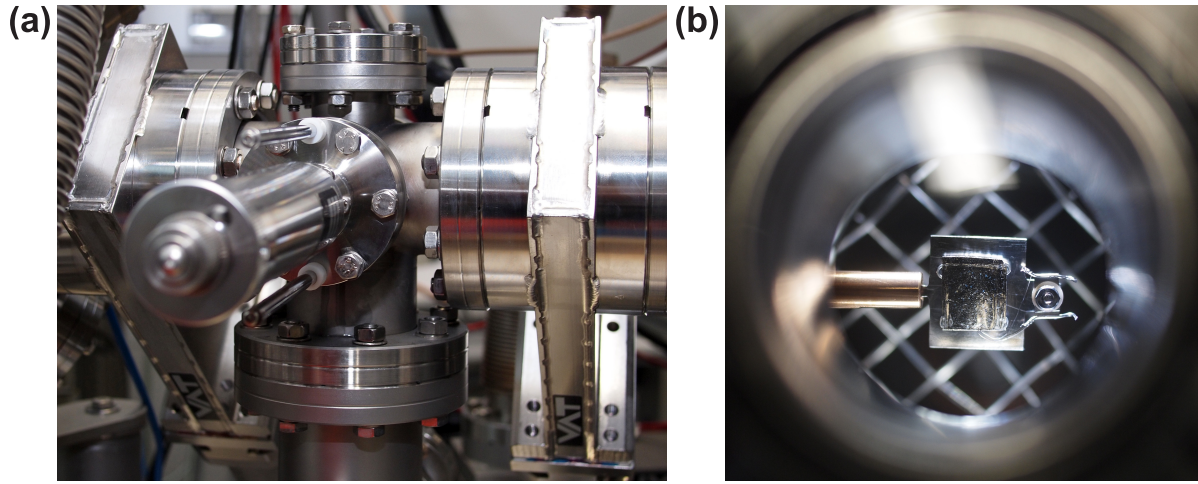


**Figure 2.5:** New sample load-lock. (a) Side view showing the linear motion feedthrough. (b) Top view showing the end of the transfer rod with the platinum sample attached to it.

The sample load-lock (see Fig. 2.5 and number 1 in Fig. 2.2(a), (b)) is positioned *between* the two vacuum chambers and can be separated from them with two gate valves (VAT). It consists of a custom-made CF40/CF63 double cross that is pumped by a turbomolecular pump (HiPace 80, Pfeiffer Vacuum) together with a rotary vane pump (Duo 5, Pfeiffer Vacuum). In order to transfer a sample into one of the UHV chambers, it has to be first mounted on a linear motion feedthrough (MDC Vacuum) that is part of the load-lock. After evacuation of the load-lock, the sample can then be moved by a transfer rod (number 2 in Fig. 2.2(a), (b)) either to the XPS- or to the PEEM-system. This is illustrated in Fig. 2.5(b), which shows a view through a window of the load-lock: the end of the transfer rod is visible with the Pt sample fixed on it.

The new vacuum chamber (number 3 in Fig. 2.2(a), (b)) is equipped with an X-ray source (XR 50, SPECS; number 4 in Fig. 2.2(a), (b)) and a hemispherical electron energy analyzer (Phoibos 100, SPECS; number 5 in Fig. 2.2(a), (b)) that uses a 2D-CCD detector with a micro-channel plate for *spatially-resolved* XPS measurements. The system can be pumped by the TMP of the load-lock and/or by an ion pump (StarCell 300, Varian) that can be separated from the chamber via another CF160 gate valve (VAT).

## 2.4 Measuring techniques

This section gives a short overview over the main measurement techniques used for the experimental work described in chapter 4.

### 2.4.1 Photoemission electron microscopy (PEEM)

Photoemission electron microscopy (PEEM) is a widely used microscopic technique in surface science applications. It utilizes local variations in the photoelectron yield to generate image contrast. Based on the pioneering work by J. Pohl [13] and E. Brüche [14], who constructed the first working photoemission electron microscope already in the 1930s, the development of PEEM into a modern scientific instrument was preeminently done by the groups of Engel [15, 16] and Bauer [17]. PEEM became famous as one of the measuring techniques used prominently by the group of Gerhard Ertl<sup>1</sup> at the Fritz-Haber-Institute (FHI) in Berlin to study oscillating surface reactions with surface science techniques [5, 18].

#### 2.4.1.1 Working principle of PEEM

PEEM uses photoelectrons to generate image contrast. The photoelectrons are created due to the *photoelectric effect*, which was discovered by Hertz and Hallwachs already in the year 1887 [19, 20]. Figure 2.6(a) illustrates the principle of the photoelectric effect, namely the emission of electrons (hence called *photoelectrons*) from a material through absorption of energy from electromagnetic irradiation. The emitted photoelectrons have a kinetic energy spectrum in the range  $0-E_{kin,max}$ , with  $E_{kin,max}$  being defined by Einstein's famous (Nobel Prize) equation [21] as

$$E_{kin,max} = h\nu_{max} - \Phi - E_b, \quad (2.1)$$

---

<sup>1</sup>Nobel Laureate in Chemistry 2007.



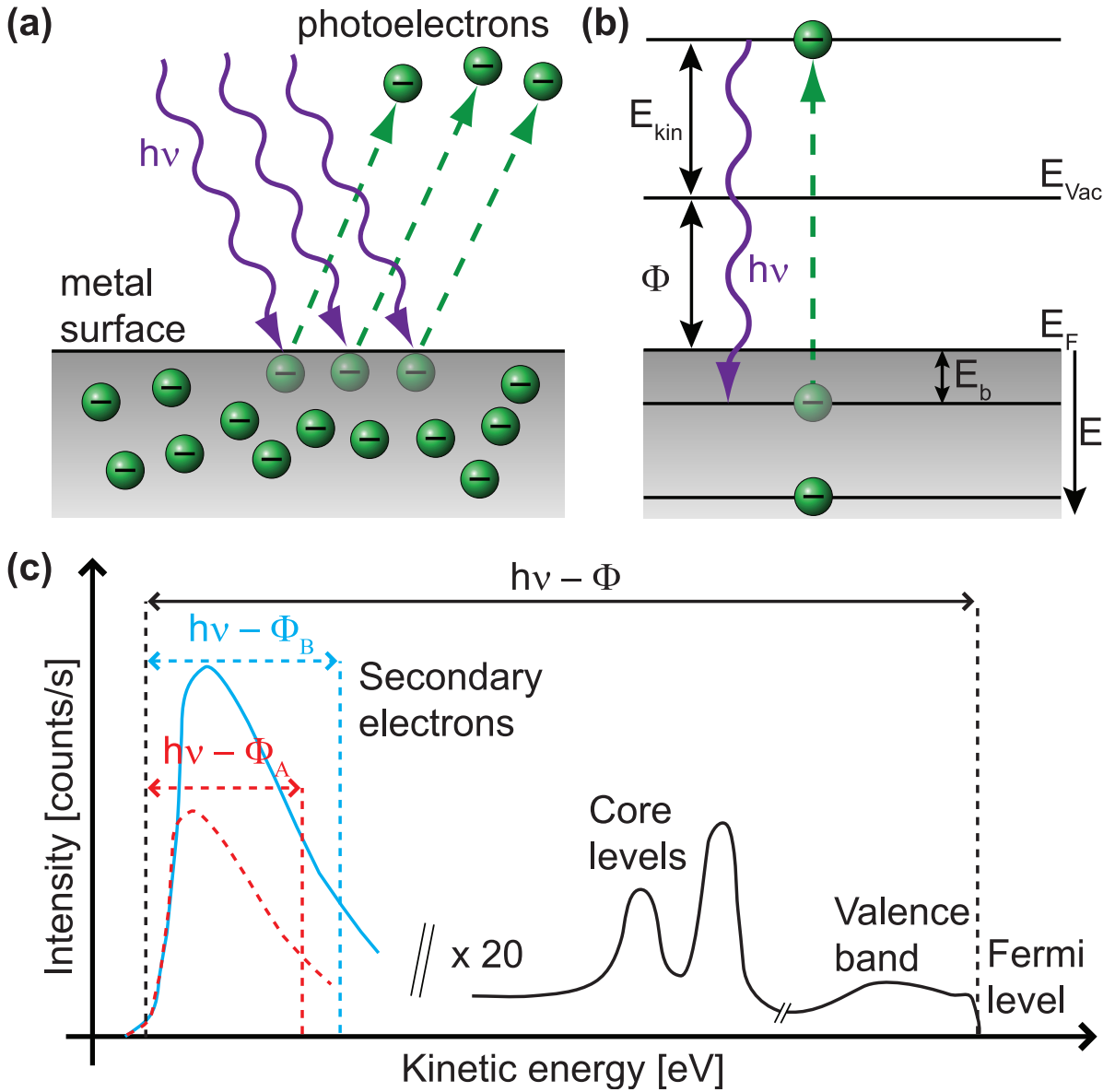


**Figure 2.6:** Photoelectric effect. (a) Schematic illustration: electrons are emitted from a material by illumination with electromagnetic radiation. (b) Energy diagram of the photoelectric effect: the kinetic energy  $E_{kin}$  of the emitted photoelectron is the difference between the energy of the incoming radiation  $h\nu$ , the binding energy  $E_b$  of the electron in the bulk and the work function  $\Phi$  of the material (cf. equation 2.1). (c) Schematic view of a resulting photoemission spectrum: the majority of the emitted photoelectrons are *inelastically scattered* secondary electrons with a low kinetic energy. In consequence, the photoelectron emission intensity relevant for a non-energy-resolving technique like PEEM is mostly dependent on the integral (i.e., peak area) of the secondary electron background as shown in the plot for two different work function values  $\Phi_A$  (red dashed line) and  $\Phi_B$  (blue dashed line) with  $\Phi_A > \Phi_B$ .

## 2 Experimental details

where  $\Phi$  represents the *work function* of the illuminated material, which is defined by

$$\Phi = E_{Vac} - E_F \quad (2.2)$$

as the energy difference between the *vacuum level*  $E_{Vac}$  and the *Fermi level*  $E_F$  of the sample (cf. Fig. 2.6(b)). The term  $E_b$  is the *binding energy* of the emitted photoelectron and  $\nu_{max}$  is the *maximum frequency* in the spectrum of the incident photon beam. In case of PEEM, the incident photons originate normally from either ultraviolet (UV) lamps (e.g., mercury and deuterium lamps with a  $h\nu_{max}$  of 4.9 eV and 6.8 eV, respectively) or synchrotron radiation.

A PEEM without an energy filter is *not* an energy-resolving technique because the local intensity (brightness) of an unfiltered PEEM image does *not* depend on the kinetic energy of the emitted photoelectrons but rather on the sheer *number* of photoelectrons emitted per surface area. This is illustrated in Fig. 2.6(c), which shows a characteristic photoemission spectrum: the vast majority of emitted photoelectrons are *inelastically scattered* on their way to the detector and thus have a much lower kinetic energy than  $E_{kin,max}$ . While being useless (and rather disturbing) for spectroscopic applications, they are very valuable for a microscopic technique like PEEM because a lot of photoelectrons are needed to generate sufficient image brightness. The photoemission yield is strongly dependent on the (local) value of the work function  $\Phi$ , as is shown in Fig. 2.6(c) for two different work function values  $\Phi_A$  and  $\Phi_B$ : even small differences in the value of  $\Phi$  lead to large changes in the area of the inelastic background peak, the photoemission intensity and, consequently, the local PEEM image brightness and contrast.

Since the amount of photoemission mainly depends on the *intensity* (read: number of photons) of the incident light source in the spectral range above the border frequency  $\nu_{Border} = \Phi/h$ , common laboratory light sources produce a rather low intensity of photoemission from most samples. Therefore, the maximum lateral resolution of PEEM is limited and, at best, lies in the range of 10–100 nm. Besides that, also lens aberrations and the spread of the photoelectron emission angle have a negative effect on the PEEM resolution. Consequently, a field of view (FOV) of several micrometers is common for a modern PEEM instrument, which is very large compared to other electron-based microscopic techniques like, e.g., *low energy electron microscopy* (LEEM) [22,23] or *mirror electron microscopy* (MEM) [24]. On the other hand, PEEM is a *parallel imaging technique*, which means that large portions of the sample area can be monitored simultaneously.

## 2 Experimental details

The temporal resolution of PEEM is mainly limited by the latency of the phosphor screen typically used for imaging.

PEEM is a very surface-sensitive technique because the emitted photoelectrons originate only from the few topmost atomic layers of the sample. This is due to the fact that the *inelastic mean free path* (IMFP) of electrons in a bulk material is typically very small (0.5–2 nm) [25].

### 2.4.1.2 Instrumental details

Figure 2.7(a) shows a photographic image of the PEEM instrument that was used for the experiments described in this work. It is mounted on a standard CF160 flange of the vacuum chamber. Both an air-cooled mercury (LOT Oriel, photon energy cut-off at  $\sim 4.9$  eV) and a water-cooled deuterium discharge lamp (D200, Heraeus, Germany) were used as UV light sources. The deuterium lamp has a photon energy cut-off of  $\sim 6.8$  eV, which allows visualizing the surface of high work-function metals like platinum. Two condenser lenses positioned in the optical path focused the UV beam on the sample to a spot with a diameter of a few millimeters.

The following paragraph describes the electrostatic lens system of the PEEM instrument that was used in the experiments (see Fig. 2.7(b) for details). The UV-illuminated sample (also called *cathode*) is electrically grounded to prevent any charging effects. The cone-shaped first transfer electrode (also called *anode*) attracts and accelerates the emitted photoelectrons with a voltage of up to +20 kV. The sample is positioned  $\leq 5$  mm in front of this electrode to ensure that UV illumination is still sufficient for a homogeneous electron emission across the whole sample area. For the measurements described in this work an anode voltage  $U_A$  of +15 kV was typically applied.

The electron-optical system of the PEEM is based on several electrostatic lenses: the *objective* lens (OL, also called *cathode* lens) forms the first real image and can be used for *focusing* (typical voltages of  $U_{OL}$  are +2–4 kV). The voltage of the *intermediate* lens (IL) determines the *magnification* of the image (operating voltages are in the range of 0– $U_A$ ). Finally, the *projective* lens (PL, voltage  $U_{PL}$ : +1.58 kV) and the *deceleration* lens (DL, voltage  $U_{DL}$ : +1.25 kV) are used to reduce the kinetic energy of the photoelectrons to the energy range of the sensitivity maximum (200–2000 eV) of the imaging system. The imaging system consists of a *micro-channel plate* (MCP), which is used for amplification of the emitted photoelectrons, and a phosphor screen (PS) coupled to fiber optics where the microscopic image is finally formed. The MCP and the phosphor screen were usually operated at voltages  $U_{MCP}$  and  $U_{PS}$  of +700 V and +3000 V, respectively.

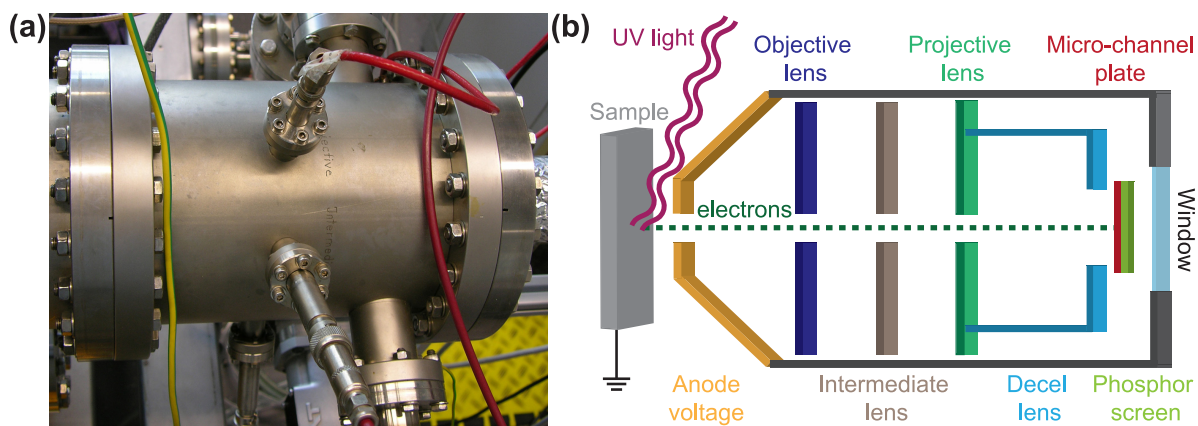


**Figure 2.7:** Image and scheme of a photoemission electron microscope (PEEM). (a) Photographic image of the PEEM instrument (PEEM 150, STAIB Instruments) used in this work. (b) Scheme of a PEEM: the photoelectrons emitted from the sample due to electromagnetic illumination are focused, magnified and amplified using an electron-optical system, which consists of several electrostatic lenses. A microscopic image of the sample surface is formed on a phosphor screen and can be recorded with a high-speed CCD camera.

The PEEM instrument is equipped with two in-line apertures (with diameters of 4.0 mm and 0.3 mm, respectively) along the photoelectron track that ease differential pumping of the electron optics. For this purpose, the PEEM contains a CF40 flange where a TMP can be attached. This enables a maximum pressure in the vacuum chamber of  $\sim 10^{-4}$  mbar and makes *in situ* monitoring of surface reactions possible.

PEEM images were recorded using a high-speed CCD camera (Hamamatsu C9300) that allows for a maximum temporal resolution of less than 50  $\mu$ s (an exposure time of 250 ms per frame was chosen for most of the recorded PEEM sequences). The intensity profiles of the PEEM images were analyzed with the help of both the *HiPic* application suite by Hamamatsu and a self-written software that correlates the PEEM image intensity with the partial pressures of the reactant gases measured simultaneously by quadrupole mass spectrometry.

### 2.4.1.3 Contrast in PEEM images

The contrast of a PEEM image, i.e., the variation of the PEEM image intensity originating from local changes of the photoelectron yield due to work function differences, depends on several surface-specific parameters such as:

- Crystallographic orientation of individual grains
- Local variations in surface topography (rough vs. flat surface areas)

## 2 Experimental details

- Presence or absence of adsorbates on the surface

The *work function*  $\Phi$  of a material is defined as the energy needed to move an electron from the Fermi level  $E_F$  into vacuum (cf. equation 2.2 and Fig. 2.6(b)). The value of  $\Phi$  depends both on the chemical nature of a material – e.g., work function values for different metals range from 2.14 eV (Cs) to  $\sim 6$  eV (Pt) – and on the individual crystallographic orientation of the surface. According to Smoluchowski’s theorem [26], a crystallographic orientation with a higher atomic density also has a higher work function. In a first approximation (given by Fowler’s equation [27]), the photoelectron emission yield (and thus the intensity of a PEEM image) is proportional to  $(h\nu_{max} - \Phi)^2$ . Thus, even small differences in the work function lead to pronounced changes of the PEEM image intensity, as was already discussed in section 2.4.1.1.

Additionally, defect sites, grain boundaries, undulations, texture due to mechanical strain, etc., also influence the local PEEM brightness. Generally speaking, the photoelectron emission intensity depends on the *curvature* of the surface, and, in consequence, rough areas on the surface may show a different PEEM contrast compared to flat regions. Besides that, surface roughness and the accompanying bended electron trajectories lead to a decrease of the PEEM resolution.

The presence of adsorbates on the surface has a pronounced effect on the local work function too, a fact which makes PEEM a particularly useful tool for investigating surface reactions, since changes in adsorbate coverage are usually observed upon variations of external parameters like temperature and pressure. Adsorbates can *increase* (e.g., oxygen on Pt(hkl) [28]) or *decrease* (e.g., hydrogen on Pt(111) [29] or subsurface oxygen on Rh(111) [30]) the work function compared to the clean surface state. In the description of the experimental work in chapter 4, the quantitative effect of individual adsorbates such as CO and oxygen on the work function will be discussed in more detail.

In consequence, the image contrast of PEEM can be used to identify the crystallographic orientation of the individual surface domains via work function differences [28, 31, 32]. Although slight intensity differences between domains of the same orientation may arise due to the variable roughness of the individual surfaces, the change of the image intensity resulting from this contribution is usually much smaller than the difference due to the crystallographic surface orientation. Adsorbates also change the local work function significantly and thus can be used as an additional characteristic to help in the identification of a particular surface orientation (cf. section 4.2.1).

### 2.4.2 Quadrupole mass spectrometry

This section provides a brief introduction to *quadrupole mass spectrometry* (QMS), a technique that was used to monitor the CO<sub>2</sub> production rate and the partial pressures of the reactant gases (O<sub>2</sub> and CO) in the experiments, as well as for routine analysis of the residual gas atmosphere in the vacuum system.

The foundations of QMS were laid by the work of Wolfgang Paul,<sup>2</sup> who invented the so-called *Paul trap*, the first quadrupole-based ion trap, in 1953 [33]. Nowadays, QMS is the most widely applied method to measure partial pressures of gases under reduced pressure conditions.

#### 2.4.2.1 Instrumental details

Figure 2.8 shows a schematic view of the measuring principle of QMS. It is based on the *ionization* and subsequent *separation* and *detection* of atoms and molecules of the residual gas atmosphere according to their individual mass-to-charge ratio  $m/z$ . The gas species are first ionized in a so-called *ion source*. In case of QMS, the method of *electron ionization* is typically applied for this purpose where accelerated electrons with a kinetic energy in the range of ~80–100 eV interact with the atoms or molecules of the gas phase. This way, *single (positively) charged* ions  $M^+$  are preeminently produced from neutral compounds  $M$  according to the following ionization scheme:



Of course, also higher charged ions as well as charged fragments of the original molecules are produced, albeit to a much smaller extent. Nevertheless, these fragments are highly valuable for the interpretation of a mass spectrum because, in most cases, they allow for an unambiguous identification of the original molecules due to the fact that the distribution of these side products is constant and can thus act as a “fingerprint” of a given compound.

After generation, the ions are accelerated towards the detector by applying an electric field. The *quadrupole mass analyzer* is placed in between the ion source and the detector. It separates the ions using a quadrupole electric field that is formed by four parallel cylindrical rods arranged in a cross. Each opposing pair of rods is electrically connected, and two potentials with opposing sign are applied to the two rod pairs, both consisting

---

<sup>2</sup>Nobel Laureate in Physics 1989.

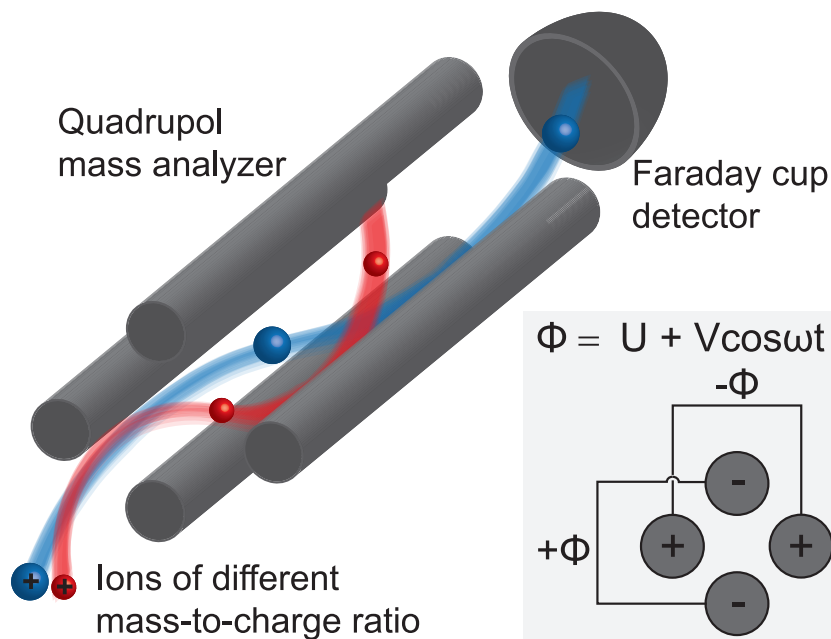


**Figure 2.8:** Scheme of quadrupole mass spectrometry (QMS). Ions are first generated in an ion source and then filtered in a quadrupole mass analyzer according to their different mass-to-charge ratio  $m/z$ . Only ions of a specific  $m/z$  can pass the analyzer and reach the detector. All other ions have unstable trajectories and are neutralized upon hitting the quadrupole rods. The inset on the right shows the polarity of the quadrupole rods.

of a DC ( $U$ ) and an AC ( $V$ ; alternating at radio frequency) voltage contribution (see inset in Fig. 2.8). The quadrupole electric field resulting from the applied voltages strongly influences the trajectories of the generated ions  $M^+$  and thus can be used as a mass filter. By careful adjustment of either the frequency of the AC voltage and/or the value of the DC voltage only ions of a certain mass-to-charge ratio  $m/z$  are able to pass the rods and reach the detector, whereas ions with a different  $m/z$  have unstable trajectories under these conditions and are eventually neutralized by hitting one of the quadrupole rods.

The quantitative detection of the filtered ions is either done via a *Faraday cup* for large ion currents (viz. gas pressures) or via a *secondary electron multiplier* (e.g., a *Channeltron*) for small ion currents.

The Faraday detector is a metal cup that is used to catch the incoming ionic fragments. The number of ions impinging in a given time span is *directly* proportional to the electron current (i.e., number of electrons) needed for neutralization, which can be easily measured. While a Faraday cup is a very robust detector, its drawbacks are a relatively low sensitivity and measurement errors due to the formation of secondary electrons or the

backscattering of the incident ions. The cup shape of the detector is chosen to prevent the escape of charged particles.

For the detection of small ion currents at low partial pressures, the weak original signal has to be first amplified in an *electron multiplier* that uses the effect of *secondary electron emission* for a strong amplification of the primary signal. For this purpose, the walls of the detector are coated with a material that shows strong secondary emission. An incident ion typically causes the emission of 1–3 electrons which can again act as the source of further electron emission upon hitting the walls of the multiplier. The resulting avalanche of secondary electrons is collected at the anode and (similar to the Faraday detector) detected by measuring the electron current. Due to its strong amplification potential, operating this type of detector at too high gas pressures must be avoided in order to prevent signal overloading and damage.

### 2.4.3 X-ray photoelectron spectroscopy (XPS)

XPS is one of the most powerful analysis methods available in surface science today because it combines a very high *surface sensitivity* with the ability to receive both qualitative and quantitative information about the electronic structure (i.e., the chemistry) of the surface of a (conducting) sample. For that reason, the technique is sometimes also called *electron spectroscopy for chemical analysis* (ESCA). The foundations of XPS were laid by the work of Kai Siegbahn,<sup>3</sup> who succeeded in producing the first X-ray photoelectron spectra in the 1960s [34,35].

The working principle of XPS is based on the *photoelectric effect* (cf. section 2.4.1.1), but, unlike PEEM, the emitted photoelectrons are separated according to their individual kinetic energy  $E_{kin}$ . If the photon energy  $h\nu$  of the X-ray source and the work function  $\Phi$  of the analyzer is known, equation 2.1 allows to determine the binding energy  $E_b$  of the photoelectrons in the sample. Due to the high photon energy of the X-ray sources commonly applied for XPS measurements (Mg K $\alpha$ : 1253.6 eV; Al K $\alpha$ : 1486.6 eV), most of the emitted photoelectrons originate from *core levels* of the sample. The energy separation of the photoelectrons is usually done in a *hemispherical analyzer* (HSA). The reason for the pronounced surface-sensitivity of XPS is the reduced inelastic mean free path of the photoelectrons in the bulk, which is only  $\sim 0.5$ – $1.5$  nm for the kinetic energy range typical for XPS (10–1500 eV) [25].

---

<sup>3</sup>Nobel Laureate in Physics 1981.



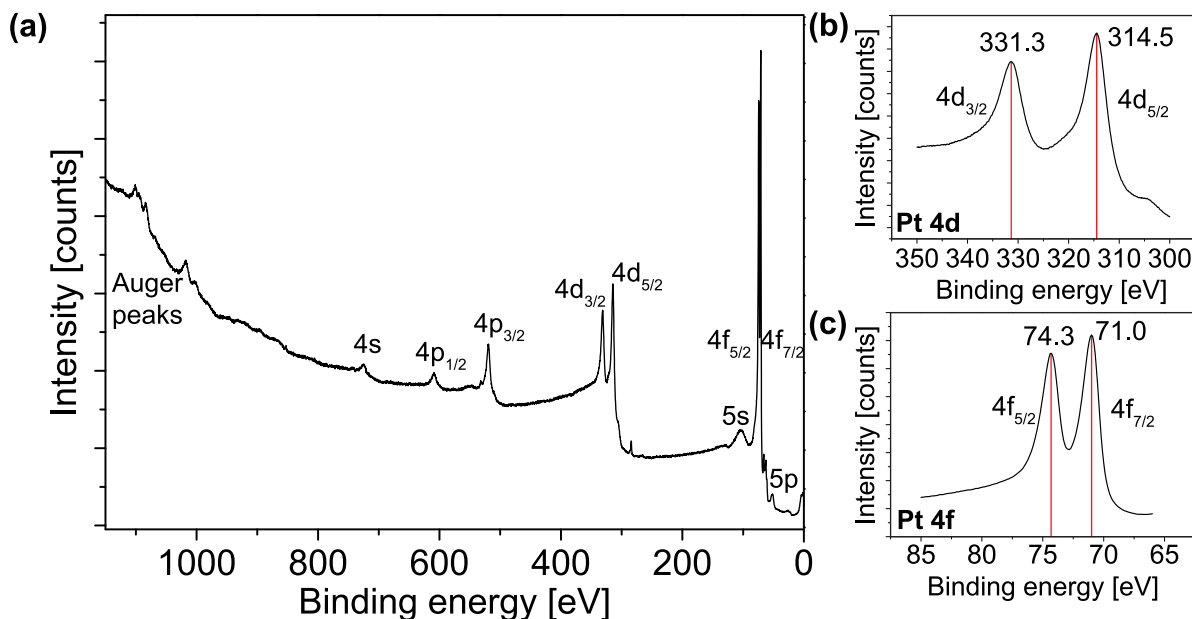


**Figure 2.9:** X-ray photoelectron spectra of the platinum sample using Mg  $K\alpha$  radiation (1253.6 eV) as excitation source. (a) Survey scan and high-resolution scans of the (b) Pt 4d and (c) Pt 4f region.

One of the main advantages of XPS is its high sensitivity towards changes in the electronic structure of an atom, which are most often directly correlated to an altered chemical surrounding. For example, changes in the *oxidation state* are directly accessible with XPS, as they can lead to *shifts* in binding energy of up to 5 eV. Such *chemical shifts* render XPS a very powerful tool for investigating chemical processes and reactions on surfaces [36]. Besides the qualitative information, XPS can also be used to *quantify* surface species directly because, in principle, their concentration is directly proportional to the area of the corresponding XPS peak.

The XPS setup described in section 2.3.5 was used to check the cleanliness of the platinum sample surface. Figure 2.9 shows a typical X-ray photoelectron spectrum of the sample, namely a wide energy-range survey spectrum (Fig. 2.9(a)) as well as two high-resolution scans (Fig. 2.9(b) and (c)) of the Pt 4d and 4f region using Mg  $K\alpha$  radiation as excitation source.

The sample surface is mostly clean, although traces of adsorbed CO with two peaks at  $\sim 285$  eV (C 1s) and  $\sim 531$  eV (O 1s) could still be detected. Elastic peaks corresponding to the 4s, 4p, 4d, 4f, 5s and 5p orbitals of (metallic) platinum are visible in the survey spectrum, with the Pt 4d and Pt 4f peaks having the largest intensities. Therefore, they are taken as “fingerprints” for metallic platinum in the high-resolution spectra shown in Fig. 2.9(b) and (c).

## 2 Experimental details

It is obvious from the shown spectra that electronic states with an angular momentum quantum number  $l$  different from zero (i.e., p, d, f) are split into two peaks in XPS due to *spin-orbit coupling*: the total angular momentum  $j$  is then the sum of  $l$  and the electronic spin momentum quantum number  $s$  ( $\pm\frac{1}{2}$ ). For example, in the case of a p state where  $l = 1$ ,  $j$  assumes values of  $\frac{1}{2}$  ( $1 - \frac{1}{2}$ ) and  $\frac{3}{2}$  ( $1 + \frac{1}{2}$ ). Furthermore, the areas of the two resulting peaks are not equal due to the  $(2j+1)$ -degeneracy of the energy levels that leads to a peak area ratio of 1 : 2 for p, 2 : 3 for d and 3 : 4 for f states. The asymmetric peak-splitting is also visible in the high-resolution scans of the Pt 4d (split into  $4d_{3/2}$  and  $4d_{5/2}$  states) and Pt 4f (split into  $4f_{5/2}$  and  $4f_{7/2}$ ) regions shown in Fig. 2.9(b) and (c), respectively.

Additional peaks are detected in the survey spectrum at higher binding energies of  $\leq 1000$  eV that originate from electrons emitted due to the *Auger process* and therefore do not directly correspond to electronic states. The kinetic energies of the Auger electrons are *independent* of the excitation energy of the X-ray source, which makes it easy to distinguish them from photoelectrons: while photoelectrons have *source-independent* binding energies, the (apparent) “binding energies” of Auger electrons change by switching the anode of the X-ray source.

### 2.4.4 Field ion microscopy (FIM)

In order to compare the catalytic properties of spatially confined platinum domains with the same crystallographic orientation but of different size and different morphology of boundaries, *field ion microscopy* (FIM) was used to visualize the CO oxidation reaction on small facets of a nanosized Pt tip (described in more detail in section 4.3.4.1). The apex of such a tip exhibits a heterogeneous surface formed by differently oriented nanofacets that can serve as a suitable model for a catalytic particle of comparable dimensions. The principle of the technique is explained in Fig. 2.10: the atoms or molecules of an imaging gas (usually He or Ne but also, as in the present case,  $O_2$  can be used) are polarized in a high electric field applied to the tip-shaped sample (10–45 V/nm, depending on the imaging gas) and attracted by polarization forces towards the surface. The imaging gas species are accommodated to the temperature of the sample and *field-ionized* above *protruding* surface atoms because the field strength is highest there due to local field enhancement (Fig. 2.10(a)) [37]. The ionization occurring in high electric field is a tunneling process where valence electrons of the gas species tunnel into unoccupied states just over the Fermi level  $E_F$  of the metal sample (Fig. 2.10(d)).

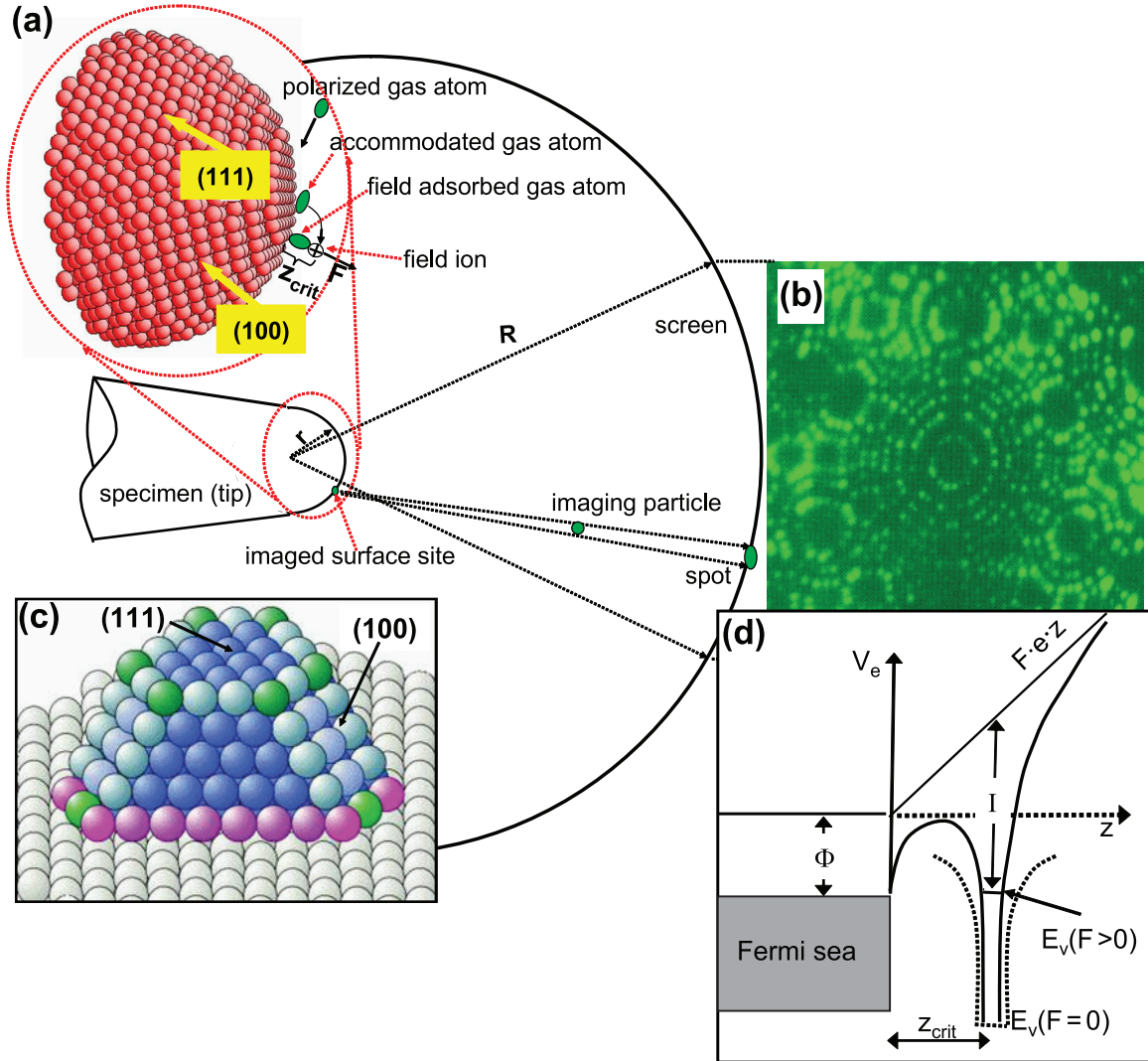


**Figure 2.10:** Principles of field emission based microscopy. (a) Geometry of the point projection. The surface of the specimen apex is projected on a screen by imaging particles with a magnification  $M \approx R/r$ . Imaging particles are either electrons (in FEM), imaging gas ions (in FIM) or  $Li^+$  ions (in Li-FDM). Inset shows a ball model of the apex of a spherical *fcc* tip and illustrates the mechanism of ion formation in FIM. Imaging gas ions are generated above protruding surface atoms covered by field adsorbed gas atoms, and field ionized atoms are replaced by highly mobile accommodated gas atoms (see text). (b)  $Ne^+$  field ion image of a [111]-oriented Rh field emitter tip. (c) Metal aggregate on an oxide substrate. (d) Potential energy diagram for field ionization over a metal surface. Reproduced with permission from Ref. [38].

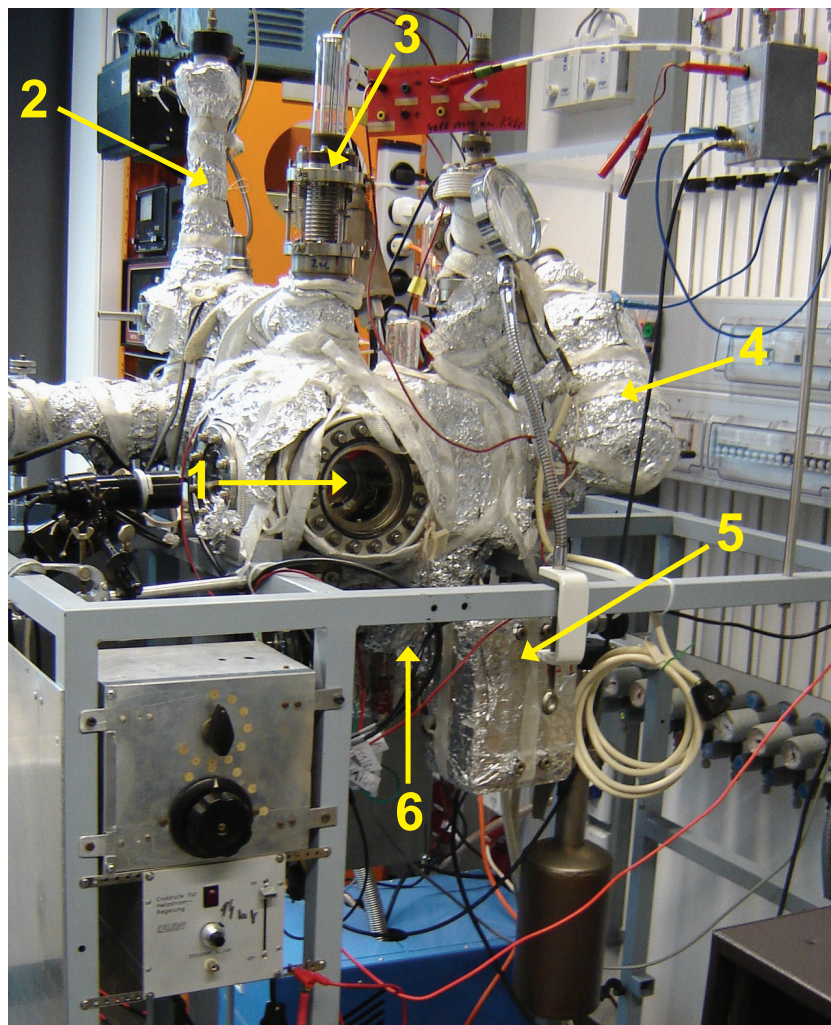


**Figure 2.11:** The FIM UHV system consisting of (1) screen, (2) QMS, (3) cold finger, (4) TSP, (5) ion diode pump and (6) turbomolecular pump.

The ions of the imaging gas (in the present case:  $O_2^+$ ) are repelled in a direction *perpendicular* to the sample surface and move rapidly towards the screen (usually a micro-channel plate (MCP) is used for image amplification) where they create a point projection of the surface as a result (Fig. 2.10(c)). In contrary to conventional microscopes where spatial resolution is limited by the wavelength of the particles used for imaging, the FIM is a *projection-type microscope*. The projection geometry (shown in Fig. 2.10(a)) provides an approximate magnification of a few million times and allows therefore atomic resolution, provided the temperature of the sample is low enough to allow ionization of gas species that are “at rest”. In the present case of CO oxidation, the sample temperature ( $>320$  K) was much higher than the cryogenic temperatures (20–100 K) usually applied in

FIM, therefore atomic resolution was surrendered in favor of the possibility to *in situ* visualize the catalytic CO oxidation reaction.

The FIM setup used in the present work consisted of a UHV chamber (shown in Fig. 2.11) equipped with a tip-assembly (number 3 in Fig. 2.11) that allows heating/cooling of the tip (from 77 K to 900 K), a thermocouple for temperature control mounted directly on the tip, a gas supply system (He, Ne, CO, O<sub>2</sub>) and a pumping system consisting of a rotary vane pump, a turbomolecular pump connected in series (Leybold Heraeus; number 6 in Fig. 2.11), four diode ion pumps (Varian; number 5) as well as a TSP (Varian; number 4). The base pressure of the present UHV system was less than 10<sup>-9</sup> mbar. The compositions of the reactive gas mixtures were controlled by a quadrupole mass-spectrometer (Inficon; number 2 in Fig. 2.11), and the total pressure was monitored by a Bayard-Alpert ionization gauge (Veeco) and a spinning rotor gauge (Viscovac, Leybold). To avoid any hot cathodes in the UHV system during reaction experiments, only the spinning rotor gauge was enabled during the experiments on CO oxidation. Real-time FIM images emerging on the screen (number 1 in Fig. 2.11) during the ongoing CO oxidation reaction were registered with a CCD-camera and a conventional video cassette recorder (with a time resolution of 0.04 s/frame) and later digitized with 8 bit resolution.

### 2.4.5 Electron backscatter diffraction (EBSD)

This section provides a short introduction to *electron backscatter diffraction* (EBSD), a method that can be employed to map the *grain orientation* of a polycrystalline sample [39, 40].<sup>4</sup> In combination with PEEM, it was used to determine the domain orientation on the polycrystalline platinum foil that was used for the experiments (the details are described in section 4.2.1). EBSD is a widely-used technique in materials research and is suited for quantitative grain and texture analysis. It makes use of *dynamical diffraction* that occurs when the *incident electron beam* of a *scanning-electron microscope* (SEM) is multiply diffracted within the sample. The beam is backscattered by the sample into spherical waves, which diffract a few times with the crystal planes into cones before they exit the sample to the detector. The diffraction cones originate from the upper and lower surfaces of opposite lattice planes, e.g., the (001) and (00 $\bar{1}$ ) planes. The cones travel until they intersect the detector plane where they form a pair of *Kikuchi bands* [41, 42], which can be recorded with a CCD camera. The sum of all Kikuchi bands is called the *EBSD pattern* of a given sample spot. By analyzing the Kikuchi bands, the lattice spacing can

---

<sup>4</sup>Because of this, EBSD is sometimes also called *orientation imaging microscopy* (OIM).



be calculated through Bragg's law, and the angles between crystallographic planes can be measured directly from the EBSD pattern.

### 2.4.5.1 Instrumental details

Usually, EBSD is carried out in a SEM that is equipped with an appropriate EBSD detector. A typical layout for EBSD measurements is shown in Fig. 2.12: the sample is mounted in a *tilted* position (usually  $60^{\circ}$ – $70^{\circ}$  away from the horizontal) in the SEM sample stage. When the electron beam is raster scanned across the sample surface, an EBSD pattern is successively recorded for every pixel. In order to perform an orientation analysis, characteristic features in the EBSD pattern are automatically recognized and analyzed by a computer software. The resulting output usually includes an *inverse pole figure* and an *orientation map* of the investigated area where each crystal grain is colored according to its orientation (see Fig. 4.2 in section 4.2.1 for an example of such an orientation map).

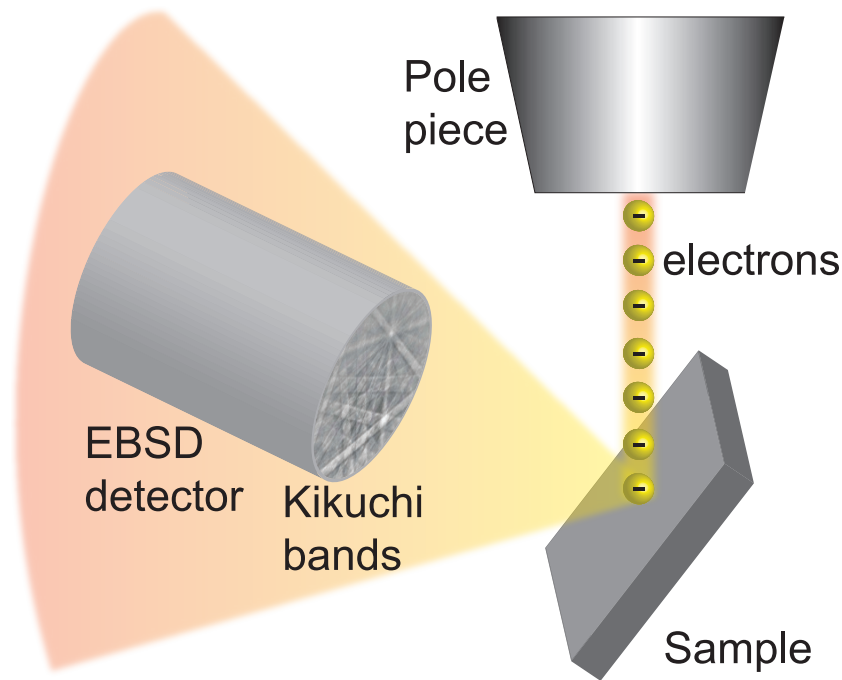


**Figure 2.12:** Scheme of electron backscatter diffraction (EBSD). The electron beam of a SEM is raster scanned across the sample surface, and characteristic Kikuchi bands are obtained for each of the raster points, thus allowing to determine the crystallographic orientation.

## Catalytic CO oxidation on platinum surfaces

This chapter describes the main properties of the catalytic CO oxidation reaction on platinum surfaces, the surface reaction that was preeminently studied in the experiments performed during this thesis.

Catalytic oxidation of carbon monoxide (CO) on surfaces of platinum group metals is one of the most extensively studied reactions in the field of heterogeneous catalysis because the removal of highly toxic CO from exhaust gases is of fundamental importance both in industrial and automotive applications (e.g., to control air pollution [43] or for fuel cell usages [44]). Besides that, this surface reaction follows a (seemingly) simple reaction mechanism that has allowed to study it on model systems both experimentally and theoretically.

The structures of the most important surface planes of platinum are characterized in section 3.1, which is followed by a description of *reconstructions* typical for some surface orientations of platinum under UHV conditions in section 3.2. Sections 3.3 and 3.4 discuss adsorption and diffusion properties of carbon monoxide (CO), carbon dioxide (CO<sub>2</sub>) and oxygen on different platinum surface orientations, respectively. Finally, section 3.5 details the reaction mechanism of the catalytic CO oxidation reaction and outlines its most important features, namely the occurrence of *bistable* and *oscillating* behavior.

### 3.1 Platinum

Elemental platinum (chemical symbol: Pt) is a 5d transition (noble) metal that belongs to group 10 (old IUPAC numbering: group VIII) of the periodic table of the elements. It features a partially filled d shell and has a total electronic configuration of  $[\text{Xe}]4f^{14}5d^96s^1$ . Platinum gives name to the group of *platinum metals*, which also consists of the elements ruthenium (Ru), rhodium (Rh), palladium (Pd), osmium (Os) and iridium (Ir). Although being one of the rarest and therefore most expensive elements on earth, platinum is nevertheless an extensively used metal in the field of heterogeneous catalysis because of its excellent catalytic performance in many industrially important reactions. Due to the high price, major research efforts in industry are devoted to the optimization or even substitution of catalysts based on platinum (or other expensive noble metals) with cheaper alternatives.

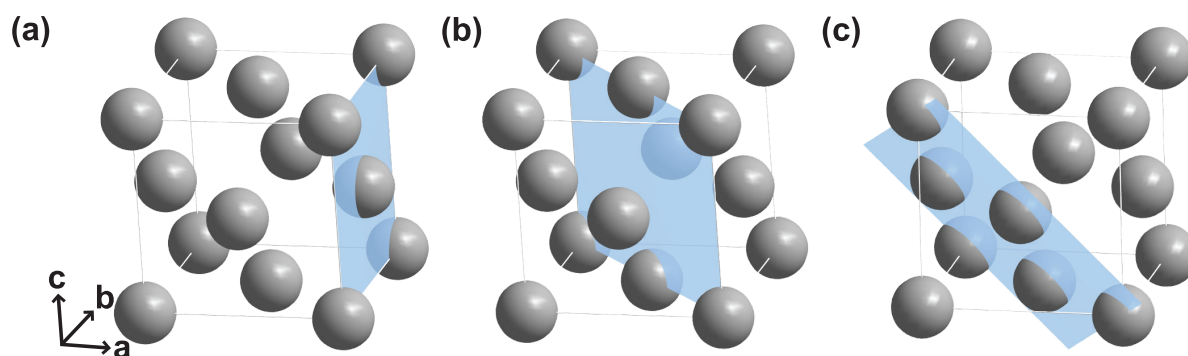


**Figure 3.1:** Crystallographic unit cell and low Miller-index planes of face-centered cubic (*fcc*) platinum. The planes are indicated in light blue color: (a) (100)-plane, (b) (110)-plane and (c) (111)-plane.

Like most other platinum group metals (except ruthenium and osmium, which have a *hexagonal close-packed (hcp)* crystal structure), platinum crystallizes in a *face-centered cubic (fcc)* crystal lattice (shown in Fig. 3.1) with an experimental lattice constant  $a_{Pt}$  of 3.92 Å [45].

In general, heterogeneously catalyzed reactions take place at surfaces or interfaces of catalytically active materials. As the properties of a surface plane strongly depend on its orientation relative to the unit cell lattice, it is necessary to unambiguously identify such a crystallographic surface. For this purpose, *Miller indices* are most commonly applied: the *round bracket* notation ( $hkl$ ) is used for describing planes and the *square bracket* notation  $[uvw]$  for describing directions. Whereas the Miller indices  $h$ ,  $k$  and  $l$  for crystal planes



$(hkl)$  are defined as the *inverse intercepts* along the lattice vectors **a**, **b** and **c**, respectively,<sup>1</sup>  $[uvw]$ -definitions of crystallographic directions use the *direct* lattice basis in the form of a vector  $\mathbf{g}_{uvw} = u\mathbf{a} + v\mathbf{b} + w\mathbf{c}$ .

From a thermodynamic point of view, the most stable surface planes of platinum (that is, the surfaces with the lowest surface energy  $\gamma_{(hkl)}$ ) are known to be the low Miller-index planes, namely cubic Pt(100) (Fig. 3.1(a); lattice constant  $a'_{(100)} = b'_{(100)} = a_{Pt}/\sqrt{2} = 2.77 \text{ \AA}$ ), tetragonal-like Pt(110) (Fig. 3.1(b);  $a'_{(110)} = a_{Pt}/\sqrt{2} = 2.77 \text{ \AA}$ ,  $b'_{(110)} = a_{Pt} = 3.92 \text{ \AA}$ ) and hexagonal-like Pt(111) (Fig. 3.1(c);  $a'_{(111)} = b'_{(111)} = a_{Pt}/\sqrt{2} = 2.77 \text{ \AA}$ ), with the Pt(111) surface having the *highest* atomic density and the *lowest* surface energy  $\gamma_{(hkl)}$  of all [46]. This means that the surface of a well-annealed polycrystalline (platinum) sample should predominantly consist of crystal grains oriented in the low Miller-index directions. This structural picture of a metal surface is, of course, highly idealized because, in general, a surface contains defect sites like *lattice vacancies*, *steps* or *grain boundaries*, even if the sample has been thoroughly prepared beforehand. These defects, together with the presence of mechanical strain that may originate from sample preparation and mounting procedures, play an important role in the initial crystallization of the grains. Hereby, they strongly influence catalytic surface reactions because the adsorption properties (such as sticking coefficients, adsorption energies, etc.) of such sites are known to differ considerably from defect-lean surfaces [47]. For example, this was observed on single crystals of Pt(110) where micro-facetting of the surface during catalytic CO oxidation enhanced the catalytic activity notably [48]. Besides that, such defects often act as a starting point for *reaction-diffusion* fronts on the surface, as has also been observed in the experiments described in chapter 4.

## 3.2 Reconstruction of platinum surfaces

It is well known that both the clean Pt(100) and Pt(110) surfaces are structurally unstable and reconstruct under vacuum conditions whereas Pt(111) does not show any such reconstruction. Figure 3.2 shows ball models of the Pt(100) and Pt(110) surface orientations *with* and *without* reconstruction. The alteration of the surface structures has important consequences because, in both cases, the adsorption and diffusion properties of the two surface states differ strongly from each other.

---

<sup>1</sup>Equivalently, a plane  $(hkl)$  can be defined in terms of the *reciprocal* lattice vectors  $\mathbf{a}^*$ ,  $\mathbf{b}^*$  and  $\mathbf{c}^*$  as being orthogonal to the reciprocal lattice vector  $\mathbf{g}_{hkl} = h\mathbf{a}^* + k\mathbf{b}^* + l\mathbf{c}^*$ .

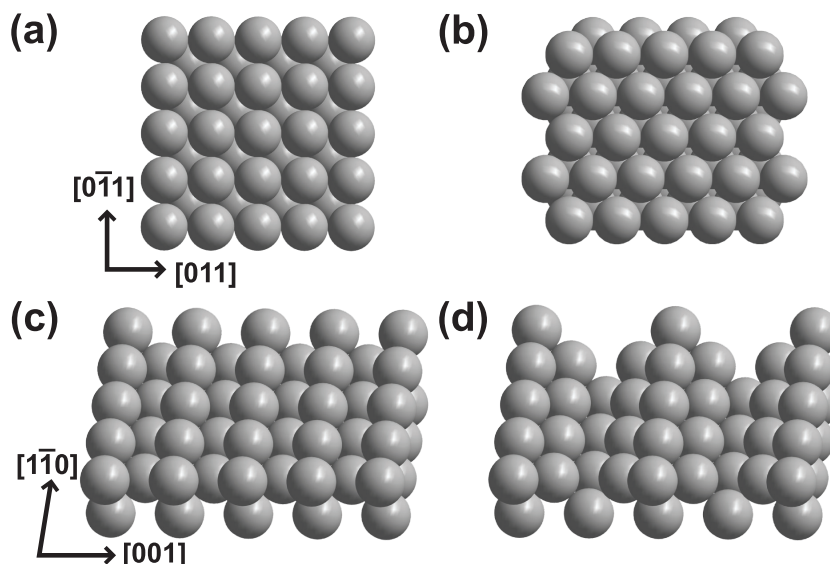


**Figure 3.2:** Surface structures of Pt(110) and Pt(100). (a) Unreconstructed Pt(100)-(1×1) structure. (b) Reconstructed Pt(100)-*hex* structure. (c) Unreconstructed Pt(110)-(1×1) structure. (d) Reconstructed Pt(110)-(1×2) *missing row* structure.

Another important property of surface reconstruction is its reversibility: adsorption of certain gases can lift the reconstruction above a threshold coverage, and the unreconstructed (1×1) structure of Pt(100) or Pt(110) is restored. This plays an important role for the catalytic CO oxidation reaction because, under specific reaction conditions, the repeated adsorbate-induced switching between the two different surface structures can act as a feedback mechanism for *rate oscillations* on both surfaces (see section 3.5.2.3 for more details) [49, 50].

### 3.2.1 Reconstruction of Pt(100)

The clean Pt(100) surface reconstructs in a so-called *hex* phase [51, 52], sometimes also called (5×20) [53, 54] or hex-R0.7° [55] structure in literature. The structure is named after the *quasi-hexagonal* rearrangement of the surface platinum layer (shown schematically in Fig. 3.2(b)). The *hex* surface layer is oriented *nearly parallel* to the  $[0\bar{1}1]$  direction of the original (1×1) lattice and periodically matched with the underlying substrate. The discrepancy between the cubic subsurface and the hexagonal surface symmetry leads to a large (5×20) LEED periodicity. The *hex* surface structure is anisotropic, highly corrugated (a corrugation length of 14 Å and a difference between highest and lowest surface Pt atom of ~1 Å was found in STM experiments [55]) and has a 20–25 % higher atomic density than the unreconstructed (1×1) surface.

However, the *hex* reconstruction is not stable against adsorption, and both adsorbing CO [56] and oxygen [57] are able to trigger its lifting and restore the unreconstructed ( $1 \times 1$ ) surface, which is shown in Fig. 3.2(a). If the so-called *surface phase transition* (SPT) is repeated a number of times, the only partially reversible and anisotropic reconstruction process leads to a *facetting* and *roughening* of the ( $1 \times 1$ ) surface structure [55]: elongated islands (size: 10–15 Å) are formed along the  $[0\bar{1}1]$  direction. The island formation is due to the large difference in atomic density of both surface structures of Pt(100) and the associated significant mass transport of platinum atoms during the SPT. The formation of anisotropic islands significantly influences the surface morphology and diffusion properties of Pt(100) domains, as has been shown, e.g., in PEEM experiments on polycrystalline Pt foil [58].

#### 3.2.2 Reconstruction of Pt(110)

The reconstruction of a clean Pt(110) surface is called the  $(1 \times 2)$ -*missing row* structure [59–61] (see Fig. 3.2(d)) because every *second* atomic row of the topmost layer in  $[1\bar{1}0]$  direction is *missing* compared to an unreconstructed ( $1 \times 1$ ) Pt(110) surface. This leads to an exposure of the *three* topmost atomic layers of the Pt(110) surface. In consequence, the atomic density of the reconstructed surface layer is *halved*, and the lattice constant in  $[001]$  direction (i.e., in the direction perpendicular to the rows) is *doubled* compared to the ( $1 \times 1$ ) structure. As it was the case for *hex* Pt(100), the  $(1 \times 2)$  reconstruction of Pt(110) has serious consequences for the adsorption and diffusion properties.

The  $(1 \times 2)$  structural modification is lifted upon adsorption of CO at a coverage of more than 0.2 monolayers (ML) [51, 60, 62], and thus a Pt(110) surface with a saturation coverage of CO exhibits the ( $1 \times 1$ ) structure (Fig. 3.2(c)). On the other hand (and contrary to Pt(100)), oxygen adsorption is *not* able to remove the  $(1 \times 2)$  reconstruction. Similarly to Pt(100), cyclic repetition of the SPT may eventually lead to facetting (roughening) of the surface that may again result in altered adsorption properties and even enhanced catalytic activity [63].

### 3.3 Adsorption of CO, oxygen and CO<sub>2</sub> on platinum surfaces

Before discussing the characteristics of catalytic CO oxidation on platinum surfaces, it is important to consider the adsorption and desorption properties of the reactant and product gases.

### 3.3.1 Principles of adsorption

In general, *adsorption* is defined as the *adhesion* of different kind of species (be it atoms, molecules or ions) to a surface. The occurrence of adsorption is a direct consequence of the existence of the *surface energy*  $\gamma$ , which reflects the fact that atomic bonds of surface atoms are not fully saturated compared to bulk atoms.

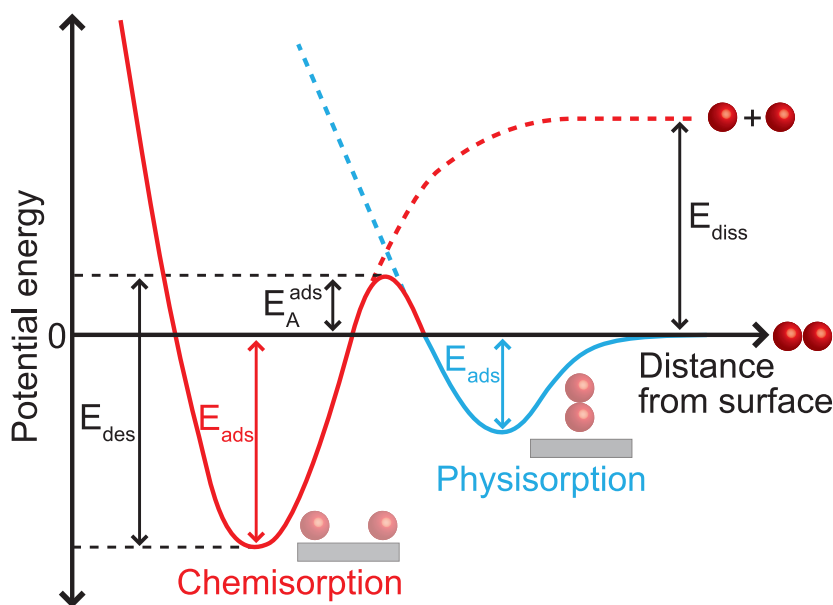


**Figure 3.3:** Potential energy diagram of the adsorption process. See text for details.

The energetic principles of adsorption are shown schematically as a potential energy diagram in Fig. 3.3: a free molecule  $M_2$  can adsorb on a surface in one of two possible ways, namely via *physisorption* or *chemisorption*. Physisorption denotes an adsorbed state where the adsorbate (i.e., the adsorbed species) is only weakly and reversibly bonded to the surface (the substrate) by means of dipole-induced *Van-der-Waals* (VdW) forces. Therefore, small or no changes are observed for bond lengths, vibrational frequencies or electronic structures of both adsorbate and substrate. Physisorption is a very general phenomenon and common to any solid/gas system without chemical specificity. For example, even physisorption of noble gases is observed, albeit at temperatures well below 100 K [64, 65]. It does not have any activation energy and even multilayer adsorption is possible at sufficiently low surface temperatures (i.e., below the condensation temperature of the adsorbate species).

Often, physisorption acts as a precursor step for *chemisorption*. Chemisorption is characterized by a charge transfer and thus the appearance of a chemical bond between ad-

**Table 3.1:** Saturation coverages and adsorption structures of CO and (atomic) oxygen on the individual low Miller-index planes of platinum at room temperature.

Miller-Index	$\Theta_{max}$ (CO)	Structure	$\Theta_{max}$ (Oxygen)	Structure
(100)	0.75	c(4×2)	0.63	complex
(110)	1	(2×1)-p2mg	0.35–0.8	(1×2)
(111)	0.5	c(4×2)	0.25	p(2×2)-O

sorbate and substrate atoms. Therefore, a typical property of chemisorption is a strong interaction between surface and adsorbate, which can even lead to internal bond-breaking in the case of adsorbed molecules (this case is shown in Fig. 3.3). Adsorption involving bond-breaking is also called *dissociative adsorption* and is observed, e.g., for H<sub>2</sub> or O<sub>2</sub> adsorbed on the Pt(111) surface [29]. Sometimes, chemisorption is also *activated*, which means that an additional activation energy barrier  $E_A^{ads}$  has to be overcome to desorb the adsorbate again.

A common measure for the adsorption strength is the *adsorption energy* or *heat of adsorption*  $E_{ads}$ , which is the change in potential energy occurring upon adsorption. If the adsorption is not activated, i.e.,  $E_A^{ads}$  is zero, then  $E_{ads}$  is equal to the activation energy of desorption  $E_{des}$ , that is the energy needed to remove a molecule from the surface. This can be used to directly measure the adsorption energy in experiments using *temperature programmed desorption* (TPD). Because  $E_{ads}$  decreases with increasing adsorbate coverage, usually the initial value  $E_{ads}^0$  (the adsorption energy for the first adsorbing molecule) is given as a measure (and upper bound) of the adsorption strength. For chemisorption  $E_{ads}^0$  is of the order of a few electronvolts (eV) per molecule (several hundreds of kilojoules per mole), whereas it is much smaller (i.e., a few meV per molecule) for physisorption.

Besides the adsorption strength, another important measure is the total number of adsorbates per sample surface area, i.e., the concentration of the adsorbate on the surface. For this purpose, the surface coverage (denoted  $\Theta$ ) is commonly used, which is defined by the following equation:

$$\Theta = \frac{N_{ads}}{N_{max}}, \quad (3.1)$$

where  $N_{ads}$  is the total number of adsorbed molecules on a given surface, and  $N_{max}$  is the maximum number of available adsorption sites on the surface layer of the substrate (i.e., the number of molecules in a completely filled monolayer) [66]. Thus,  $\Theta$  represents the fraction of occupied adsorption sites on a given surface.

In the following subsections, the individual adsorption properties of the main reactant and product gases in catalytic CO oxidation are discussed in more detail. The respective saturation coverages  $\Theta_{max}$  and corresponding structures of CO and oxygen on the individual surface orientations of platinum are listed in table 3.1.

#### 3.3.2 Adsorption of CO

Adsorption of carbon monoxide (CO) on platinum and other metal surfaces has been extensively studied already since the days of Langmuir [67, 68]. CO is known to adsorb *molecularly* (i.e., without dissociation) on platinum surfaces with the carbon atom pointing towards the platinum surface [69]. Adsorbed CO can, in principle, be coordinated in one of three possible ways, which are also shown schematically in Fig. 3.4(a):

- onefold or *on top* coordinated
- twofold or *bridge* coordinated
- threefold (fourfold) coordinated on Pt(111) (Pt(100)), also known as three- or fourfold *hollow* coordination, respectively.

The electronic bonding situation of CO adsorbed on platinum surfaces is successfully described by the so-called *Blyholder model* [70] (schematically shown in Fig. 3.4(b)): the CO-Pt bond is characterized by a transfer of electrons from the energetically highest filled  $5\sigma$  molecular orbital (i.e., the *highest occupied molecular orbital* or HOMO) of CO to the d-band of the surface metal atoms. Due to the non-bonding character of the  $5\sigma$  MO, this has no effect on the strength of the C-O bond. However, to compensate for the large negative charge on the surface metal atoms resulting from this electron transfer, a *back-donation* of electrons from the metal to the energetically lowest empty anti-bonding  $2\pi^*$  orbital (the *lowest unoccupied molecular orbital* or LUMO) of the CO molecule takes place. The transferred electrons originate from filled d- and p-orbitals of the metal. While the back-donation further stabilizes the Pt-CO bond, the addition of electrons to anti-bonding orbitals simultaneously weakens the molecular C-O bond. For instance, this can be observed in IR experiments in a significant red-shift (shift to lower wavenumbers) of the stretching frequency of adsorbed compared to gas phase CO ( $2143\text{ cm}^{-1}$ ). The size of the red-shift depends on the coordination number of CO because the amount of back-donation of electrons from the metal surface to the CO molecule increases with the size of the coordination number, i.e., on top < twofold bridge < (three/four-)fold hollow. For

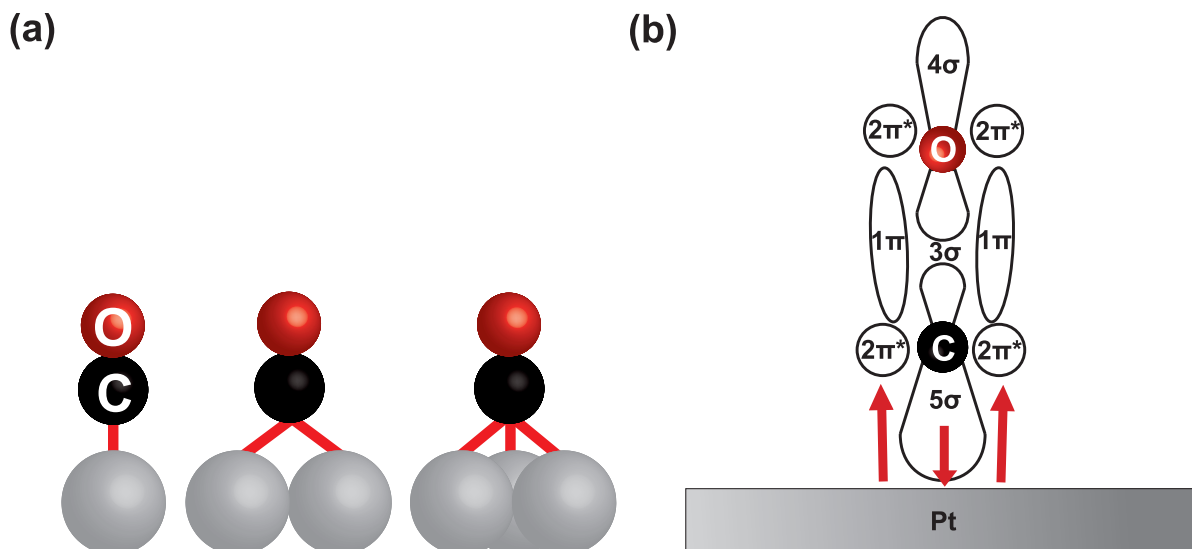


**Figure 3.4:** Geometries and Blyholder model of CO adsorption on platinum surfaces. (a) Adsorption geometries of CO on platinum surfaces. From left to right: on top, bridge, threefold hollow coordination. (b) Blyholder model for CO adsorption on platinum metal surfaces. The molecular orbitals of CO are denoted, and the main electronic interactions with the Pt surface are indicated with arrows.

example, the stretching frequency of bridge-bonded CO on Pt(111) is already shifted by  $\sim 300$  wavenumbers with respect to gas phase CO and assumes values of  $\sim 1850 \text{ cm}^{-1}$  [71, 72].

The saturation coverages and structures of CO at room temperature differ strongly for the different low Miller-index planes (see table 3.1 for details): CO first forms a  $(\sqrt{3} \times \sqrt{3})R30^\circ$  structure at a coverage  $\Theta$  of 0.33 on Pt(111) with CO adsorbed in an on top position. It saturates in a  $c(4 \times 2)$  LEED superstructure at a coverage of 0.5 monolayers with additional bridge bonded CO adsorbed on the surface [69, 73].

CO adsorbs *only* in on top position on Pt(110)-(1  $\times$  1) after the surface reconstruction is lifted [74–76]. Thanks to the relatively low atomic density of this surface, the saturation coverage  $\Theta$  of CO is  $\sim 1$ . The CO molecules are arranged in a (2  $\times$  1)-p2mg periodicity and are positioned in a *tilted* geometry on the Pt rows along the  $[1\bar{1}0]$  direction of the unreconstructed (1  $\times$  1) surface plane (see section 3.2 for details on the surface reconstruction of Pt(110)).

The saturation coverage of CO on Pt(100) was found to be 0.75 at room temperature, and a  $c(4 \times 2)$  periodicity was observed with CO adsorbing both in on top and bridge coordination [51, 77, 78]. As it was the case for Pt(110), this saturation coverage refers the surface after the *hex* reconstruction is lifted.

The *initial sticking coefficient*  $s_0$ , which is defined as the adsorption probability of the first gas phase atom or molecule hitting the clean surface, is very high for CO on all low Miller-index platinum surfaces at room temperature: 0.6–0.8 for Pt(111) [69, 71, 79, 80], 0.8–1 for Pt(110) [74, 75, 80] and 0.6–0.7 in case of Pt(100) [77, 80, 81]. The high value of  $s_0$  is independent of the presence of a surface reconstruction. The sticking coefficient drops rapidly with increasing coverage and, by definition, reaches zero at the saturation coverage of the individual surface.

CO desorption measurements, as, e.g., performed in TPD experiments, yield quite similar results for all three surface orientations: a low-temperature  $\alpha$ -peak at  $\sim 400$ – $420$  K, which evolves only at high CO coverages, and a high-temperature  $\beta$ -peak at  $\sim 500$ – $520$  K [69, 82]. The temperature values indicate that CO desorption already plays an important role in the reaction mechanism of catalytic CO oxidation under typical reaction conditions (see section 3.5.1 for more details on this topic).

Values for initial heat of adsorption  $E_{ads}^0$  are quite similar for all low Miller-index surfaces of platinum, namely 180 kJ/mol for Pt(111) [79], 183 kJ/mol for Pt(110) [75] and 179 kJ/mol for Pt(100)-*hex* [81], whereas  $E_{ads}^0$  is higher (215 kJ/mol) in the case of unreconstructed Pt(100)-(1 $\times$ 1) [81].

#### 3.3.3 Adsorption of oxygen

The details of oxygen adsorption on platinum are more complicated than CO adsorption because oxygen shows both molecular and dissociative adsorption and is able to penetrate the surface layer of platinum to form *subsurface oxygen* species.

##### 3.3.3.1 Surface oxygen

Generally speaking, adsorption of oxygen on platinum surfaces can be divided into two temperature-dependent regimes, as oxygen can adsorb both molecularly and atomically (i.e., via dissociative adsorption). The molecular adsorption state acts as a precursor for the dissociative adsorption of atomic oxygen and can only be stabilized at low temperatures ( $\leq 150$  K; the exact value depends on the surface orientation) [83, 84]. Two different adsorption states can be distinguished for molecular oxygen: a (multilayer) *physisorbed* state, which is stable only at temperatures below 40 K, and a weakly *chemisorbed* (single-layer) state in the temperature region between 40 K and 150 K [85, 86]. The transition to the chemisorbed molecular state can be either precursor-mediated (i.e., via the physisorbed state) or via a direct-sticking mechanism. The bond of the chemisorbed oxygen



molecule is oriented *parallel* to the metal surface, and a  $(3/2 \times 3/2)R15^\circ$  LEED pattern with a saturation coverage of 0.4 ML is observed on Pt(111) [87].

Above 150 K, the molecular oxygen-oxygen bond dissociates upon adsorption on the surface, and single oxygen atoms arrange in a surface-specific way that is summarized in table 3.1. The same result is obtained when a surface pre-covered with oxygen molecules is *heated* to temperatures above 150 K: a fraction of the  $O_2$  molecules desorbs, and the rest dissociates into atomic oxygen [88].

Similar to CO adsorption, the adsorption properties of atomic oxygen vary among the low Miller-index planes: on Pt(111), the saturation coverage  $\Theta$  of atomic oxygen at room temperature is 0.25, and a  $p(2 \times 2)$ -O LEED superstructure is observed [89–91] with oxygen being adsorbed in *fcc* threefold hollow coordination [91, 92]. On reconstructed  $(1 \times 2)$  Pt(110), a saturation coverage of 0.35 was found (still showing a  $(1 \times 2)$  LEED pattern) [93, 94] with oxygen situated at the *fcc* sites of the (111)-microfacet alongside the  $[1\bar{1}0]$ -oriented rows. One has to note at this point that another study found a much higher saturation coverage of 0.8 ML together with a complex LEED pattern for oxygen adsorbing on the  $(1 \times 2)$  reconstruction [95]. The same value of  $\Theta \approx 0.8$  was also estimated for the denser Pt(110)- $(1 \times 1)$  structure [93]. On Pt(100), the saturation coverage for oxygen at room temperature was found to be 0.63 for the  $(1 \times 1)$  structure after lifting the *hex* reconstruction, and a complex LEED pattern was observed [57].

The initial sticking coefficient  $s_0$  of oxygen on platinum surfaces varies strongly between the different surface orientations and depends on the presence/absence of a reconstruction: it is 0.3–0.4 on the reconstructed Pt(110)- $(1 \times 2)$  surface [80, 95–97] and even 50 % higher on Pt(110)- $(1 \times 1)$  [93],  $\sim 0.04$ – $0.05$  on Pt(111) [79, 98] and as low as  $10^{-3}$ – $10^{-4}$  on Pt(100) in the *hex* reconstruction [99, 100]. However, if the *hex* reconstruction is lifted on Pt(100), the value for  $s_0$  on Pt(100) changes drastically to 0.1 [100], which is crucial for the occurrence of non-linear phenomena like rate oscillations on these kinds of surfaces.

Atomic oxygen is much more strongly bonded to platinum surfaces than CO: initial heat of adsorption values are found to be 339 kJ/mol for Pt(111) [79] and 335 kJ/mol for Pt(110) [75].

Desorption of oxygen takes place at much higher temperatures than CO, namely between 600 K and 750 K, depending on the surface orientation and the oxygen coverage [84, 101, 102]. Together with the higher adsorption energy of atomic oxygen, this indicates a much stronger interaction between oxygen and the platinum surface compared to CO. Therefore, the contribution of oxygen desorption to the overall kinetics of catalytic CO oxidation is negligible under the conditions of the experiments performed in this work.

#### 3.3.3.2 Subsurface oxygen

Although platinum surfaces cannot be easily oxidized in UHV [103, 104], oxygen atoms may be able to penetrate the topmost layer of Pt(100) and Pt(110) and form a *subsurface oxygen* species under certain experimental conditions [105–108]. Therefore, apparent values of  $\Theta$  much larger than the respective saturation coverage are observed when subsurface oxygen is formed. Subsurface oxygen is located between the surface and the first subsurface platinum layer in interstitial sites. The formation of this species alters the electronic properties (and thus the work function  $\Phi$ ) of platinum surfaces significantly: the dipole moment changes because the negatively charged oxygen atoms are now covered by the positively charged platinum atoms, and, in consequence, a strong *decrease* in the work function of platinum surfaces containing subsurface oxygen is observed. For example, this has been observed as *bright patches* in PEEM experiments performed on single crystals of Pt(100) [109] and Pt(110) [106, 110, 111].

#### 3.3.4 Adsorption of carbon dioxide

The bond strength between carbon dioxide ( $\text{CO}_2$ ), the reaction product of catalytic CO oxidation, and (unmodified) platinum surfaces is only very weak [112]. Desorption takes place already at temperatures above 80 K [113], and even below that only *physisorbed*  $\text{CO}_2$  is detected [114]. Therefore,  $\text{CO}_2$  does not adsorb on platinum surfaces under the conditions typically applied for catalytic CO oxidation. This is crucial for the excellent catalytic performance of platinum in this reaction because otherwise the active surface area would be covered (read: poisoned) with  $\text{CO}_2$  within a short time.

### 3.4 Diffusion of CO and oxygen on platinum surfaces

This section provides a brief overview over the diffusion properties of CO and oxygen on surfaces of platinum, a topic that plays a fundamental role for a proper understanding of catalytic CO oxidation.

#### 3.4.1 Fundamentals of surface diffusion

*Surface diffusion* describes the motion of adsorbates on solid surfaces between adjacent adsorption sites [115]. Generally speaking, a molecule or atom adsorbed on a metal surface is located in a *local minimum* of the corrugated *potential energy surface* (PES) (shown

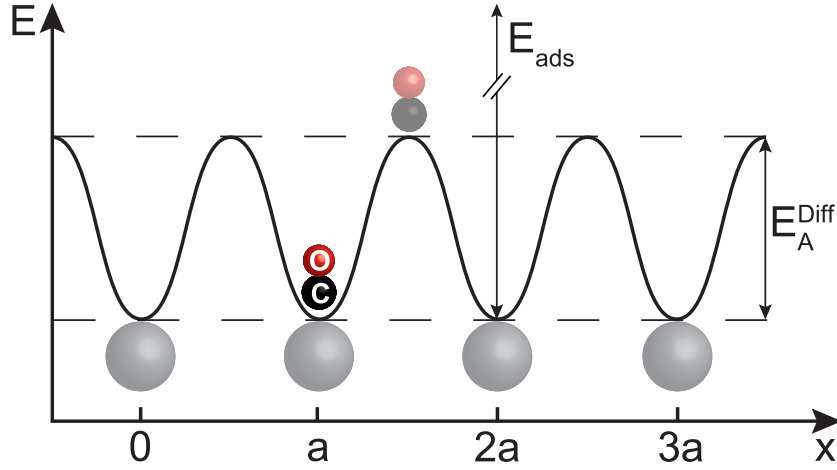


**Figure 3.5:** One-dimensional scheme of surface diffusion of adsorbates. The adsorbates are confined within the potential wells of the corrugated potential energy surface (PES). Exchange of energy with the substrate enables an adsorbate to overcome the activation energy barrier  $E_A^{Diff}$  and move to an adjacent adsorption site, i.e., to the next minimum of the potential energy.

schematically in Fig. 3.5). Surface diffusion is an activated process, which means that an activation energy barrier  $E_A^{Diff}$  has to be overcome before an adsorbate can move from one adsorption site to another. In consequence, the size of  $E_A^{Diff}$  has to be smaller than the desorption energy  $E_{des}$ , otherwise desorption dominates over diffusion. In most cases,  $E_A^{Diff}$  is  $\sim 5\text{--}20\%$  of  $E_{des}$ . The *hopping frequency*  $\Gamma$  of adsorbates between adjacent surface positions is given by the product of a pre-exponential factor  $\nu$  and a *Boltzmann factor* that depends on the temperature  $T$  and  $E_A^{Diff}$ :

$$\Gamma = \nu \exp\left(-\frac{E_A^{Diff}}{kT}\right). \quad (3.2)$$

$\nu$  is also known as the *attempt frequency*, and usually the vibrational frequency of the adsorbate in the potential well of the PES is used for this term. If the overall adsorbate coverage is low and the adsorbed atoms/molecules occupy isolated adsorption sites (i.e., no interactions are happening between them), so-called *tracer diffusion* is taking place. For isotropic surfaces, the *tracer diffusion coefficient*  $D^*$  is defined by:

$$D^* = \frac{\Gamma \langle \lambda \rangle^2}{z}, \quad (3.3)$$

where  $\langle \lambda \rangle$  is the *mean jump length* of the adsorbate and  $z$  is the number of *nearest neighbor atoms* on the given surface (i.e.,  $z$  is 4 in case of square lattices and 6 in case of hexag-

onal lattices). A substitution of  $\Gamma$  in equation 3.3 with equation 3.2 leads to the following equation, which describes the temperature dependence of the tracer diffusion coefficient  $D^*$ :

$$D^* = \frac{\overbrace{v\langle\lambda\rangle^2}^{D_0}}{z} \exp\left(-\frac{E_A^{Diff}}{kT}\right). \quad (3.4)$$

In surface diffusion, *two* major regimes are distinguishable depending on the ratio of  $E_A^{Diff}$  and  $kT$  in equations 3.2 and 3.4 [116]: if the substrate temperature is high enough (i.e.,  $kT \gg E_A^{Diff}$ ), the corrugation of the PES (and therefore also the hopping rate  $\Gamma$ ) can be neglected, and the adsorbates are assumed to *move freely* on the substrate surface in a two-dimensional *Brownian motion*. This state is also called *mobile diffusion*.

In contrast, most of the surface science studies on diffusion are performed under the conditions of the so-called *hopping regime*, i.e., where the condition  $kT < E_A^{Diff}$  holds true. It is assumed that this condition is also fulfilled in most heterogeneously catalyzed processes. In this regime, the adsorbates are mostly confined to their adsorption sites and vibrate with the frequency  $\nu$  until an exchange of energy between substrate and adsorbate enables them to overcome  $E_A^{Diff}$  and randomly jump between adjacent minima in the PES, which is also called the *random walk* motion. If, on the other hand, the sample is cooled to temperatures where  $kT$  becomes much smaller than  $E_A^{Diff}$ , the adsorbates are immobilized at their original adsorption sites, at least for the investigated timescale.

For most processes relevant in heterogeneous catalysis, the adsorbate coverage of the surface is much higher than for the case of tracer diffusion. Under these conditions, *chemical diffusion* takes place that is characterized by the presence of *attractive* or *repulsive* forces between the diffusing adsorbates. This leads to a deformation of the PES ( $E_A^{Diff}$  is decreased (increased) in case of repulsive (attractive) interaction) and thus alters the diffusion properties of the adatoms. In turn, the diffusion coefficient  $D$  for chemical diffusion is *different* from  $D^*$ . It is defined by *Fick's second law*:

$$\frac{\partial}{\partial t}\Theta(\mathbf{r}, t) = D\nabla_r^2\Theta(\mathbf{r}, t). \quad (3.5)$$

If  $D$  is assumed to be independent of  $\Theta$ , it can be obtained by measurements of the evolution of the local adsorbate coverage  $\Theta(\mathbf{r}, t)$  using a variety of techniques like, e.g., the *Boltzmann-Matano* method [115, 117, 118]. The values of the pre-exponential  $D_0$  and  $E_A^{Diff}$  can then be directly determined by plotting  $D$  in an *Arrhenius plot* against reciprocal temperature.

In general, diffusion processes are also highly dependent on the (an-)isotropy of the surface layer. In case of platinum surfaces, this is evident in the orientation dependence of the diffusion coefficient  $D$  on the anisotropic (110) surface in contrast to isotropic Pt(100) and Pt(111) [119–121].

#### 3.4.2 Diffusion of CO

Activation energies  $E_A^{Diff}$  for CO diffusion are in the range of  $\sim 30\text{--}50$  kJ/mol on all low Miller-index surface orientations of platinum [106, 120, 122–124], depending on the measurement method. For example, due to the anisotropy of Pt(110), CO diffusion on unreconstructed Pt(110)-(1 $\times$ 1) is roughly *two times faster* in  $[1\bar{1}0]$  direction than in  $[001]$  direction at a temperature of 443 K [119]. This ratio can be explained, at least to some extent, by the lattice constant ratio of Pt(110)-(1 $\times$ 1):  $a_{[001]}/a_{[1\bar{1}0]} = \sqrt{2}$ .

#### 3.4.3 Diffusion of atomic oxygen

The mobility of atomic oxygen on platinum is much *lower* than that of CO even at temperatures relevant for catalytic processes. One of the reasons for this is the much higher bond strength between the oxygen atom and the metal surface (for details see section 3.3.3). In consequence, also the values of  $E_A^{Diff}$  for oxygen diffusion are much higher than for CO on all low Miller-index planes of platinum, namely in the range of  $\sim 110\text{--}160$  kJ/mol [120, 125].

Based on these findings, oxygen diffusion can be neglected as a major contribution in the reaction mechanism of catalytic CO oxidation, at least in the investigated temperature range and within the timescale of the performed experiments.

### 3.5 Catalytic CO oxidation on platinum metal surfaces

The following section provides an overview on the characteristics of the catalytic CO oxidation reaction on platinum metal surfaces.

### 3 Catalytic CO oxidation on platinum surfaces

Carbon monoxide and oxygen react in a strongly *exothermic* reaction (standard enthalpy of combustion of the gas phase reaction:  $\Delta_c H^0 = -283 \text{ kJ/mol}$ ),<sup>2</sup> according to the following chemical reaction equation:



Despite the pronounced exothermic character of the gas phase combustion reaction, it is hindered by a large activation energy  $E_A$  of  $\sim 200 \text{ kJ/mol}$  [127]. Through adsorption of the reactants on the catalytically active platinum surface, the activation energy  $E_A$  is lowered to a value of less than  $100 \text{ kJ/mol}$  in case of Pt(111) [128, 129], which further decreases to about half of the initial value at higher reactant coverages [130]. Because the lowered value of the activation energy is well below the amount of energy gained during adsorption, the CO oxidation reaction is effectively catalyzed on platinum surfaces. However, since the details of catalytic CO oxidation are far more complex than suggested by equation 3.6, the exact mechanism of the reaction on catalytically active platinum surfaces has to be described in more detail.

#### 3.5.1 Langmuir-Hinshelwood mechanism

It has been revealed in molecular beam experiments [131, 132] that catalytic CO oxidation on platinum surfaces follows the well-established *Langmuir-Hinshelwood* (LH) mechanism [67, 68, 128, 133]. The main feature of this apparently simple mechanistic scheme is the adsorption of *all* reactants on the catalytically active surface prior to reaction. The surface reaction involves only two adsorbed species (CO and oxygen), as shown in Fig. 3.6. It is described by the following reaction equation scheme:



Equation 3.7 and Fig. 3.6(a) describe the molecular adsorption and desorption equilibrium of CO on a free adsorption site on the surface (the free site is denoted with a  $*$  in equation 3.7). The individual concentrations of the reactants strongly depend on the surface temperature because (as outlined in section 3.3.2) desorption of CO plays a signif-

<sup>2</sup>The value of  $\Delta_c H^0$  was calculated by the difference in standard enthalpy of formation  $\Delta_f H^0$  of  $\text{CO}_2$  ( $-393.5 \text{ kJ/mol}$ ) and CO ( $-110.5 \text{ kJ/mol}$ ) [126].

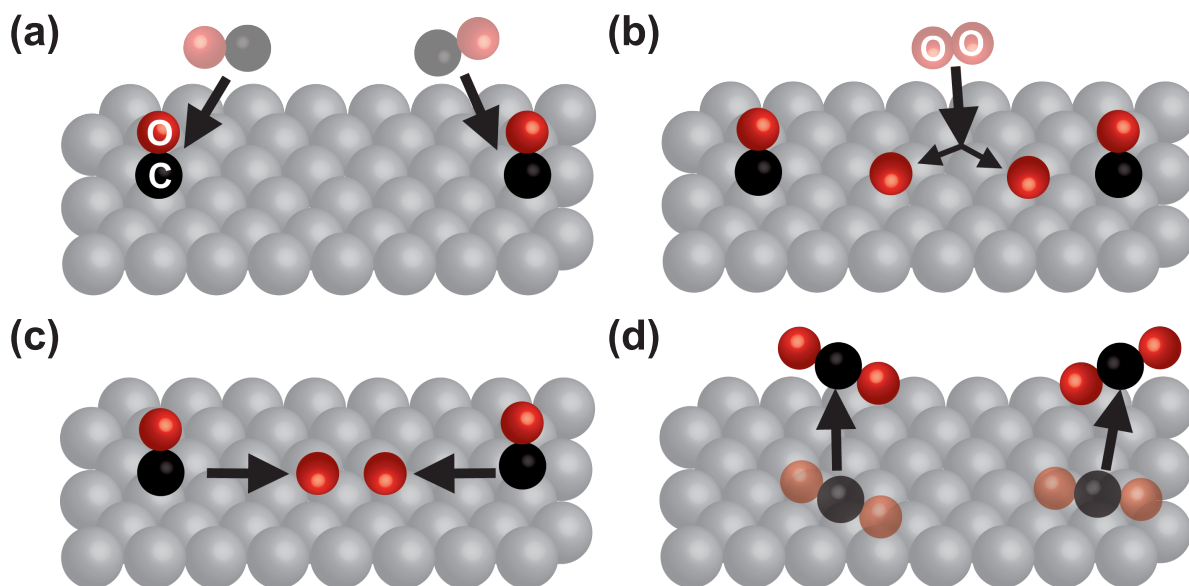


**Figure 3.6:** Scheme of the Langmuir-Hinshelwood mechanism in catalytic CO oxidation on platinum surfaces. (a) Molecular adsorption of CO. (b) Dissociative adsorption of oxygen. (c) Diffusion of CO toward adsorbed oxygen. (d) Formation reaction and desorption of CO<sub>2</sub>.

icant role under typical experimental reaction temperatures (373–520 K) [28, 134]. After adsorption, CO can freely diffuse on the surface (illustrated in Fig. 3.6(c) and described in section 3.3.2). Equation 3.8 and Fig. 3.6(b) describe the atomic (that is: dissociative) adsorption of oxygen on the surface, which, by definition, requires *two adjacent* surface sites. Because desorption of atomic oxygen only takes place at much higher surface temperatures [135] (cf. section 3.3.3), the position of the equilibrium in reaction 3.8 is very much on the right side. The adsorbed oxygen atoms more or less stay at their initial positions because (as already mentioned in section 3.4.3) oxygen diffusion is rather negligible in this temperature range. Thus, CO always diffuses towards oxygen, as illustrated in Fig. 3.6(c). Finally, equation 3.9 and Fig. 3.6(d) describe the surface reaction of both adsorbates to carbon dioxide, which then desorbs immediately under the experimental conditions (cf. section 3.3.4). With this step, all previously blocked adsorption sites are freed, and the surface reaction cycle, as described by the LH-mechanism, is closed.

The exact reaction pathway of catalytic CO oxidation on platinum is shown in Fig. 3.7 for the case of the Pt(111) surface. It is based on DFT calculations and reproduced after [129]. First, CO and atomic oxygen are positioned at their respective stable adsorption site, i.e., CO in on top and oxygen in threefold hollow coordination (Fig. 3.7(a)). CO starts to diffuse toward the oxygen atom via a bridge-bonded intermediate (Fig. 3.7(b), (c)). The pivotal reaction step is the movement of CO to a Pt atom located next to oxygen,

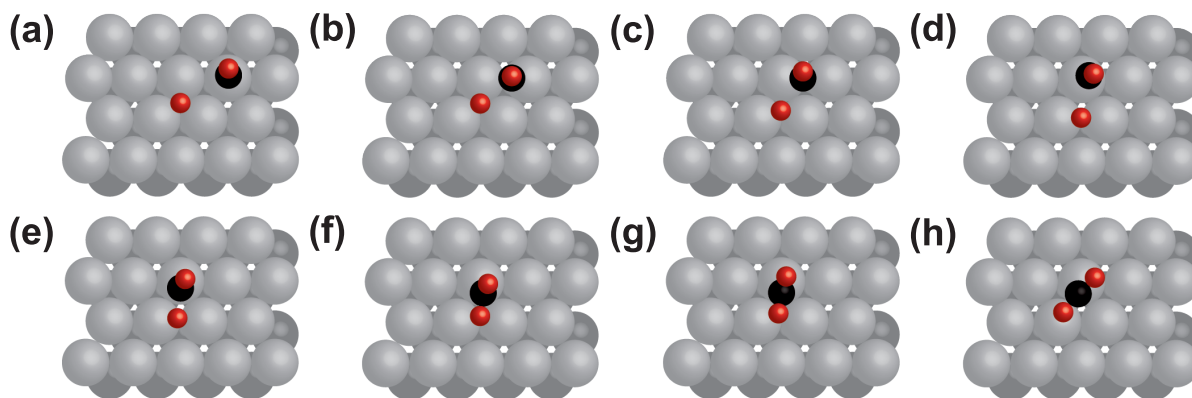


**Figure 3.7:** Reaction pathway of catalytic CO oxidation on Pt(111) as calculated by DFT. The individual reaction steps are described in the text. Reproduced after [129].

which leads to a breaking of the Pt-O bond and a movement of the oxygen atom toward an adjacent bridge site (Fig. 3.7(d), (e)). The last three steps (Fig. 3.7(f)–(h)) describe the further approach of the reactants toward each other and finally the formation of  $\text{CO}_2$ .

Although the LH reaction mechanism of catalytic CO oxidation is seemingly simple and easy to understand, the asymmetric adsorption properties of CO and oxygen render the overall chemical state of the system strongly dependent on external control parameters like temperature and the partial pressures of the reactant gases but also on the prehistory of the system. In particular, the limited number of available adsorption sites on the surface of any catalyst is a feature that is *not* considered in the simple framework of the LH mechanism. If the number of free sites approaches zero, the reaction mechanism as described above cannot happen anymore, and additional phenomena come into play, most notably *bistability* and *rate oscillations*.

### 3.5.2 Bistability and rate oscillations

A prominent feature of catalytic CO oxidation on platinum surfaces is the presence of so-called *non-linear behavior* like *bistability* and *rate oscillations* under certain reaction conditions. In the following sections, a short introduction will be given to these topics, which have large implications on the behavior of the catalyst in certain areas of the parameter space.

#### 3.5.2.1 Bistability

The occurrence of *bistability* is a direct consequence of one of the main attribute of the Langmuir-Hinshelwood mechanism described in section 3.5.1: the necessity for all reac-



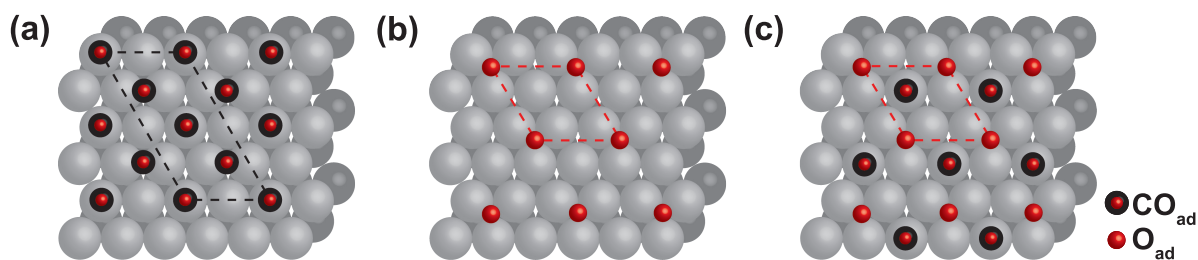


**Figure 3.8:** Asymmetric inhibition in catalytic CO oxidation shown for the case of Pt(111). (a) c(4×2) saturation coverage structure of CO on Pt(111) that effectively blocks any oxygen adsorption. (b) p(2×2) structure of a Pt(111) structure saturated with atomic oxygen. As shown in (c), CO adsorption is still possible on such an open oxygen adlayer.

tants to adsorb on the surface before reacting with each other (cf. equations 3.7 and 3.8). If the adsorption properties of two (or more) reaction partners are not fully independent of each other (a feature called *asymmetric inhibition*), bistable behavior of the catalytic system can be a direct consequence.

Under cyclic variation of the CO partial pressure and isothermal reaction conditions, bistable behavior manifests itself in a *hysteresis* in the CO<sub>2</sub> production rate. The reason for this can be found in the strikingly different adsorption characteristics of oxygen and CO on platinum surfaces (cf. section 3.3), illustrated in Fig. 3.8 for the case of Pt(111): a certain surface coverage of CO (which forms a dense adlayer) can effectively *block* oxygen adsorption due to the fact that oxygen adsorbs dissociatively and thus needs *two adjacent* adsorption sites for each adsorption event (Fig. 3.8(a)). In contrast, adsorption of CO is easily possible even on surfaces saturated with oxygen due to the relatively open structure of the oxygen adlayer (Fig. 3.8(b) and (c)). As mentioned above, this difference leads to an asymmetric inhibition of the surface reaction and results (at least for constant temperature and oxygen partial pressure) in a hysteresis of the CO<sub>2</sub> production rate.

A typical CO<sub>2</sub> production hysteresis is schematically shown in Fig. 3.9(a) for the case of constant oxygen pressure: at low CO partial pressure, the catalytically active surface is essentially covered with oxygen (i.e., oxygen adsorption dominates over CO adsorption). Therefore, the system is in the so-called *active* (or *high-reactivity*) steady state because each adsorbed CO is immediately reacted away by oxygen. Under these conditions, the CO<sub>2</sub> production rate is basically limited by the number of available CO molecules on the surface and thus rises nearly linearly with increasing CO pressure (i.e.,  $R_{\text{CO}_2} \sim p_{\text{CO}}$ ).

However, the reactivity changes drastically at a certain CO to oxygen pressure ratio (indicated by  $p_{\text{CO}}/p_{\text{O}_2} = \tau_A$  in Fig. 3.9(a), (b)) where the coverage of CO on the catalyst surface exceeds a certain value, and, in consequence, the surface is blocked (“poisoned”)

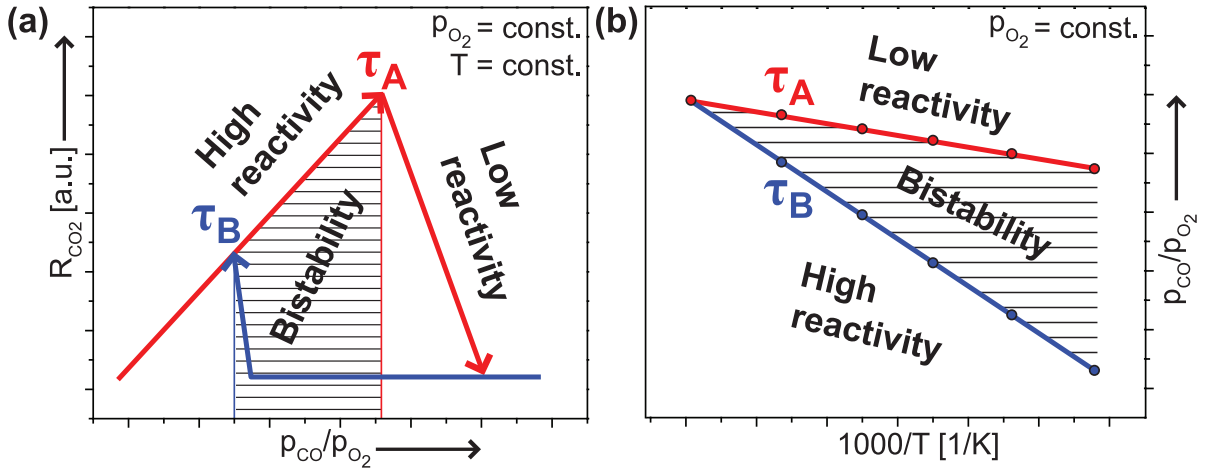


**Figure 3.9:** Schematic hysteresis and kinetic phase diagram. (a) Hysteresis in the CO<sub>2</sub> production rate as a function of CO partial pressure at constant oxygen pressure. (b) Corresponding kinetic phase diagram obtained by plotting the transitions points  $\tau_A$  and  $\tau_B$  as a function of reciprocal temperature at constant oxygen pressure. The region of bistability is indicated with a line pattern in both plots.

for oxygen adsorption. The Langmuir-Hinshelwood mechanism, as described in section 3.5.1, cannot happen without adsorbed oxygen, and the sudden breakdown of the reaction mechanism is visible in a sharp *drop* of the CO<sub>2</sub> production rate to a low level. The catalyst system is now in the so-called *inactive* (or *low reactivity*) steady state, which is characterized by the fact that the CO<sub>2</sub> production rate shows little or no dependence on changes of the CO partial pressure.

Perhaps surprisingly, the catalyst surface remains in the inactive state (and the CO<sub>2</sub> production rate stays low) even if the CO partial pressure is *lowered* to a value of  $p_{\text{CO}} = \tau_A$  again. This can be explained by the asymmetric inhibition of CO and oxygen mentioned above. Only when the CO partial pressure drops to a value of  $p_{\text{CO}} \leq \tau_B < \tau_A$ , oxygen can adsorb again on adjacent adsorption sites. At  $\tau_B$ , the surface gets mostly covered with oxygen again (in other words: it switches back to the *active steady state*), and the rate of CO<sub>2</sub> production returns to the level of the active state under the respective conditions. The parameter space region (temperature, pressure) in between the *transition points*  $\tau_A$  and  $\tau_B$  is called the region of *bistability*, where the system can be in both steady states depending on the prehistory of the system. In contrast, above  $\tau_A$  and below  $\tau_B$  the system is *monostable*, i.e., only one steady state is stable under these conditions.

In order to describe the bistable behavior of catalytic CO oxidation mathematically, a set of coupled differential equations can be used that describe the temporal evolution of

### 3 Catalytic CO oxidation on platinum surfaces

the coverage  $\Theta$  of CO and oxygen as the sum of contributions from *adsorption*, *desorption*, *reaction*, and *diffusion* of CO and oxygen:

$$\frac{\partial}{\partial t}\Theta_{CO} = \overbrace{k_{CO}^{ad}(T)p_{CO}S_{CO}}^{\text{Adsorption}} - \overbrace{k_{CO}^{des}(T)\Theta_{CO}}^{\text{Desorption}} - \overbrace{k^{react}(T)\Theta_{CO}\Theta_O}^{\text{Reaction}} + \overbrace{D_{CO}\nabla^2\Theta_{CO}}^{\text{Diffusion}} \quad (3.10)$$

$$\frac{\partial}{\partial t}\Theta_O = k_O^{ad}(T)p_O S_O - k_O^{des}(T)\Theta_O - k^{react}(T)\Theta_{CO}\Theta_O, \quad (3.11)$$

where

- $\Theta_{CO}$  and  $\Theta_O$  are the *surface coverages* of CO or oxygen;
- $k_{CO}^{ad}$  and  $k_O^{ad}$  are the *adsorption coefficients* of CO or oxygen;
- $k_{CO}^{des}$  and  $k_O^{des}$  are the *desorption coefficients* of CO or oxygen;
- $k^{react}$  is the *reaction rate constant* of catalytic CO oxidation;
- $D_{CO}$  is the *diffusion coefficient* of CO;
- $T$  is the *temperature*;
- $S_{CO}$  and  $S_O$  are the *sticking coefficients* of CO or oxygen.

Many kinetic model studies have been performed over the years on solving equations 3.10 and 3.11 under different assumptions [136, 137]. In general, isothermal solutions under the conditions of the Langmuir-Hinshelwood mechanism (and neglecting the diffusion term in equation 3.10) show the behavior that is depicted in Fig. 3.10: at certain CO partial pressures and coverages (that is, at the so-called *saddle-node bifurcation points*), the *monostable* solutions of equations 3.10 and 3.11 become unstable (indicated by a dashed line in Fig. 3.10). In case of catalytic CO oxidation, these saddle points are equivalent to the kinetic phase transition points  $\tau_A$  and  $\tau_B$ , i.e., the points where a rapid transition between the two steady states is observed in experiments on the  $CO_2$  production hysteresis (indicated with blue arrows in Fig. 3.10). By variation of an external control parameter (in this case, the temperature) between experiments, the positions of the transition points  $\tau_A$  and  $\tau_B$  change.

Since local phenomena on the micro-scale (e.g., *fluctuations*) are not considered when solving differential equations 3.10 and 3.11, using a Monte-Carlo (MC) approach is a valid alternative, which was first demonstrated by the work of Ziff, Gulari and Barshad [138] and further improved later on [139].

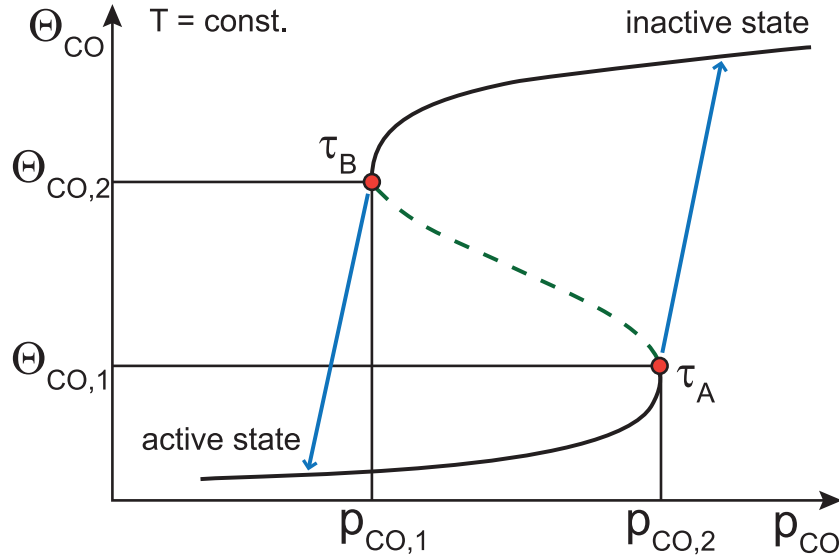


**Figure 3.10:** Schematic plot of the function  $\Theta_{CO}(p_{CO})$  that is obtained as a solution of the coupled differential equations 3.10 and 3.11 at constant temperature. Solid parts of the curve are the stable solutions, dashed regions represent the unstable solutions. At the points  $\tau_A$  and  $\tau_B$ , the transitions (blue arrows) between the monostable and the bistable region take place.

### 3.5.2.2 Kinetic phase diagram

The width of the bistability region varies depending on the value chosen for the external control parameters. Based on the behavior described above, one can effectively characterize a catalytic system showing bistability by the values of  $p_{CO}$  for the two transition points  $\tau_A$  and  $\tau_B$  at constant  $p_{O_2}$  and temperature and illustrate it graphically at constant  $p_{O_2}$  or temperature in a so-called *kinetic phase diagram*, which is shown in Fig. 3.9(b) for the case of constant oxygen pressure. It is commonly plotted either as a function of reciprocal temperature (resulting in an *isobaric* kinetic phase diagram at constant oxygen pressure) or as a function of oxygen partial pressure (resulting in an *isothermal* kinetic phase diagram). The term “phase diagram” for describing kinetic transitions is justified due to its analogy to phase transitions known from (non-)equilibrium thermodynamics [140–142]. Because of their shape, they are also called *cross-shaped diagrams* [143] or *bifurcation diagrams* [144].

A kinetic phase diagram is a useful tool because it can effectively *characterize* the state of a catalytic system. This way, effects that sample modifications (such as evaporation of nanoparticles onto the surface, oxidation of the surface layer, morphological changes through sputtering, etc.) may have on the catalytic performance can be easily made visible and compared to the unaltered state.

Over the years, kinetic phase diagrams have been reported for a number of model systems, including single crystals of Pt(111) [145, 146], Pt(210) [143], Pd(111) [147] or Pt field emitter tips [144]. However, the usage of kinetic phase diagrams on more complex systems is still scarce despite their obvious advantages.

Besides showing bistable behavior, catalytic CO oxidation is also famous for the occurrence of *rate oscillations* on some crystallographic surface orientations of platinum. Although this phenomenon was not a topic in the investigations presented in this work, it will be briefly discussed in the next section due to its importance.

#### 3.5.2.3 Rate oscillations

Although oscillatory behavior in chemical systems had already been known for well over 100 years [148], it only became famous with the discovery of the *Belousov-Zhabotinsky reaction* in the 1950s [149]. Rate oscillations in heterogeneously catalyzed (surface) reactions were first discovered by the group of Wicke in the early 1970s [150], but the theoretical understanding of the underlying mechanistic principles was poor until Gerhard Ertl and coworkers started work on this topic in the early 1980s using platinum single crystals under UHV conditions [151, 152]. For the successful experimental characterization and theoretical modeling of rate oscillations in a variety of systems (as well as for numerous other scientific achievements), Gerhard Ertl was awarded the Nobel Prize in Chemistry in 2007 [5].

Heterogeneously catalyzed reactions are, by definition, reactions *far away* from the thermodynamic equilibrium. However, within the simplified framework of the Langmuir-Hinshelwood mechanism, self-sustained oscillations cannot occur solely due to bistable behavior. In order to obtain solutions for the differential equations of the kinetic model that successfully describe oscillations, an additional mechanistic step (also called a *feedback* mechanism) has to be added to the model that properly considers the periodic activation and deactivation of the surface, i.e., the switching of the system between the high- and the low-reactivity steady states described in the previous section. In case of CO oxidation on the low Miller-index platinum surfaces, several different mechanistic models describing oscillations were proposed over the years based on such diverse assumptions as reversible oxide formation [153], carbon contamination [154, 155] or coverage dependent activation energies [156] among others. Finally, the so-called *surface phase transition* (SPT) model of Ertl and coworkers was accepted as an explanation [152, 157]. It is based on the periodic and reversible reconstruction of the Pt(100) and Pt(110) surfaces (described in section 3.2) during CO oxidation reaction, which in both cases is accom-

panied with a dramatic change in the adsorption properties for the reactant gases (see section 3.3).<sup>3</sup> In the case of Pt(110), this leads to the following oscillatory behavior under certain experimental conditions: an increasing coverage of CO blocks the surface for oxygen adsorption but, at the same time, triggers the lifting of the  $(1\times 2)$  reconstruction of clean Pt(110). As already mentioned, the oxygen sticking coefficient on Pt(110)- $(1\times 1)$  is 50% higher than on  $(1\times 2)$  [93], resulting in increasing oxygen coverage and  $\text{CO}_2$  production. The coverage of adsorbed CO is lowered to a threshold value by reaction with adsorbing oxygen, and the CO-poor  $(1\times 1)$  structure eventually becomes unstable. It reconstructs again to the  $(1\times 2)$  surface structure, and hence the oscillatory cycle is completed. Recently, it has been successfully shown that the feedback mechanism of surface reconstruction, established for macroscopic single crystals, is also valid for heterogeneous nanometer-sized systems [158].

Some noble metal surfaces (e.g., Pd(110)) show oscillations only at intermediate pressures (i.e., at pressures of  $\sim 10^{-3}$ – $10^{-1}$  mbar) that are successfully described by the so-called *surface oxide model* [147, 153]. It models oscillations by a periodic cycle of oxidation and reduction, which means that part of the active metal surface covered with oxygen gets deactivated upon forming a *surface oxide*. Only after reduction by CO, the surface reactivates again.

---

<sup>3</sup>In turn, as Pt(111) does not show any reconstruction (i.e., no abrupt change in the adsorption behavior), no oscillations are observed on this surface orientation, either.

# Experimental study of catalytic CO oxidation on polycrystalline platinum

In this chapter, a systematic investigation of the properties of polycrystalline platinum foil in catalytic CO oxidation is presented. The main experimental tools for this task were quadrupole mass spectrometry (QMS) and photoemission electron microscopy (PEEM; see chapter 2 for more details on these techniques).

A motivation for performing the experiments is given in section 4.1, followed by an introduction to the experimental scheme in section 4.2. After that, section 4.3 details the results of the experiments, which are summarized and concluded in section 4.4.

## 4.1 Motivation for the experiments

One of the main goals of the experimental work performed during this thesis was to transfer the findings from numerous single crystal studies on catalytic CO oxidation to a more complex (read: more “realistic”) polycrystalline material. This effort can be seen as part of the way to bridge the so-called *materials gap* [159], a term that summarizes the difficulties to explain the properties of real catalysts by single crystal studies. The “materials gap problem” is mainly a problem of complexity, since industrial catalysts consist of more than one component and include, besides active particles with different crystallographic orientations, also an oxidic support. The presence of crystallographic defects, a heterogeneous size distribution of the nanoparticles combined with a strong size-dependence of the catalytic properties, interaction of the particles with the oxidic support (also called

*strong metal-support interaction* or SMSI), etc., are only some of the obstacles that point out the enormous complexity of characterizing “real” catalyst materials.

In turn, for a basic understanding of the underlying mechanisms of surface reactions, *single crystals* of noble metals are, due to their well-defined structure, still the most suitable objects in catalytic experiments performed under ultra-high vacuum (UHV) conditions. However, as mentioned above, an easy extrapolation of the results obtained with such model systems to technologically important catalysts is not possible due to the simplification inherent to the UHV approach. To cut things short: in order to improve upon this situation, the differences between model and real systems have to be minimized.

As a first step towards bridging the materials gap, a sample that consists of a polycrystalline material might be used. For example, the crystal grains of the platinum foil used for the present experiments have a mean size of approximately one hundred micrometers, which, on the one hand, is still orders of magnitude larger than the few nanometers of catalytically active nanoparticles. On the other hand, the grains of such a foil exhibit different crystallographic orientations and can thus act as valid models for an ensemble of micrometer-sized single crystal-like entities.

Besides the materials gap, a large discrepancy still exists between real and model-based catalytic research regarding the pressure conditions usually applied. This can be summarized in the technical term *pressure gap*, which describes the difference between observations in “real” catalysis (i.e., catalysis in industrial applications happening at elevated temperatures and pressures well above one atmosphere) and typical surface science experiments under UHV conditions, where the maximum pressure in the chamber is seldom above  $10^{-5}$  mbar. In consequence, major research efforts are devoted to reducing the *pressure gap* as far as possible without losing the sensitivity and variety of modern surface-science techniques [160].

It has been outlined in section 2.4.1 that PEEM is a useful tool to monitor *dynamic processes* on the surface *in situ* during catalytic surface reactions [161, 162]. For instance, PEEM has been used in the past to monitor kinetic phase transitions on the Pt(111) single-crystal surface. However, this was done by averaging the whole image intensity, since the homogeneity of such a surface did not ask for spatially-resolved analysis [145]. Moreover, studies utilizing PEEM for imaging the catalytic CO oxidation reaction on Pt foil (but without analysis of phase transitions) have also been reported [28, 163].

However, there are *two* instrumental properties inherent to PEEM that *limit* the total pressure in the reaction chamber for a successful operation of this technique: first, the mean free path of the emitted photoelectrons has to be big enough so that they are able to



reach the end of the electron-optical system of the PEEM where the micro-channel plate (MCP) and the screen are located. Secondly, the total gas pressure at the MCP should not exceed values of  $\sim 10^{-6}$  mbar in order to avoid damage to its oxidation-sensitive coating. However, such low-pressure conditions are less suited for studies of reaction kinetics because performing experiments at UHV pressures of the reactant gases would result in a bad signal-to-noise ratio of the mass-spectrometric measurements and an again “widened” pressure gap.

Fortunately, the pressure limitation can be (at least partially) circumvented by *differential pumping* of the electron optics of the PEEM. With this method (which is described in more detail in chapter 2), it was possible to increase the reactant gas pressure in the vacuum chamber to a maximum value of  $\sim 10^{-4}$  mbar while maintaining the pressure in the electron optics of the PEEM always well below the critical limit of  $10^{-6}$  mbar.

One has to note that this simple method reduces the *pressure gap* only partially. In turn, the most modern surface science techniques like, e.g., *high-pressure X-ray photoelectron spectroscopy (HP-XPS)* [164], *sum-frequency generation (SFG)* [165] or *polarization-modulation infrared reflection absorption spectroscopy (PM-IRAS)* [166] allow to raise the total reactant gas pressure in the reaction chamber even further to the *low millibar regime* without losing surface sensitivity. However, these techniques are only seldom applied up to date due to their still low availability.

## 4.2 Principles of the kinetic study

The main goal of the present experiments was to characterize the catalytic performance of polycrystalline platinum foil during CO oxidation in the  $(p_{\text{CO}}, p_{\text{O}_2}, T)$ -parameter space, and the focus of this work was set on the *bistability regime* (cf. section 3.5.2.1) of this reaction. It has been outlined in section 3.5.2.2 that it is necessary for such a task to determine the *steady state* regions under variation of temperature and pressure by measuring the *kinetic phase transition points* of bistability  $\tau_A$  and  $\tau_B$  and visualize them in a *kinetic phase diagram*. A novelty of the performed experiments was the acquisition of such phase diagrams both in a *globally* and *laterally-resolved* way during *the same* experiment. Thus, information about the whole sample as well as its individual grains (to be more specific: about those that lie within the *field of view* of the PEEM) are obtained at the same time and under exactly the same conditions. For this purpose, combined simultaneous QMS and PEEM measurements were performed in a way that is schematically illustrated in Fig. 4.1: while QMS monitors the hysteresis of the global  $\text{CO}_2$  production rate upon cyclic vari-

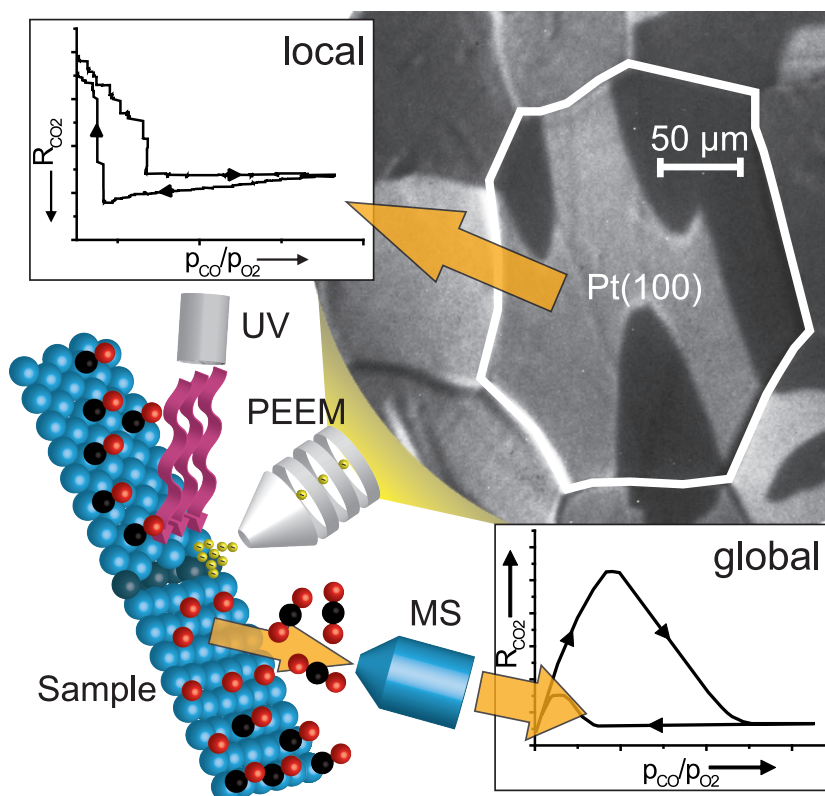


**Figure 4.1:** Scheme of the experiments. A large area ( $\sim 500 \times 500 \mu\text{m}^2$ ) of the sample surface is imaged via PEEM while QMS provides information about the global kinetics during the catalytic reaction by measuring the  $\text{CO}_2$  production rate at the same time (lower inset). A correlation of the changes in local PEEM intensity (upper inset) on a single crystal facet (in this case Pt(100) is shown) during a CO pressure scan with the global  $\text{CO}_2$  production rate allows for the measurement of laterally-resolved kinetics. Based on a similar figure in Ref. [32].

ation of the CO partial pressure, PEEM allows to obtain laterally-resolved kinetic information through a correlation of the photoelectron emission intensity with the CO pressure measured by MS at the same time.

This represents a novel experimental approach because a commonly applied way to study and compare the catalytic properties of different crystallographic orientations of a given material is the use of different single crystals that are cut in the desired surface terminations. At best, experiments on different samples are performed in the same experimental setup *successively*. Numerous studies of this kind have been performed over the years on CO oxidation using platinum single crystals of different orientations, and kinetic phase diagrams for catalytic CO oxidation have been obtained for, e.g., Pt(210) [143] and Pt(111) [145,146]. Nevertheless, to the author's knowledge, no kinetic phase diagrams for the bistability region of Pt(100) and Pt(110) surfaces have been published so far.

However, a drawback of the experimental approach involving a number of single crystals is the *limited comparability* of the results: even if the experiments are performed in the same setup (and by the same team of researchers), it is impossible to provide exactly the same conditions for all the investigated single crystals, simply because the individual measurements are performed *in succession*, and consequently, slight but inevitable differences always exist between the experimental conditions.

A way to overcome this problem is the use of a sample that is still well-defined but exhibits many different crystallographic orientations at the same time. For example, a cylindrically-shaped single crystal of platinum was used for this purpose in the past that exhibits all orientations of the [001] zone [167]. However, curved samples make the use of a microscopic technique like PEEM quite difficult because a homogeneous illumination of such samples is hardly possible this way. In contrast, a planar and well-polished polycrystalline foil is much better suited for microscopic imaging techniques.

Furthermore, quadrupole mass spectrometry (QMS) is applied for an examination of the reaction kinetics of a catalytically active sample under (ultra-)high vacuum conditions in most kinetic studies. This approach suffers from the fact that mass spectrometry is, by definition, an *averaging* technique, which means that the obtained signal is always the *superposition* of the whole sample area *and* other (unwanted) contributions that may not even originate from the sample but from the residual gas atmosphere or the walls of the vacuum chamber. Due to the averaging nature, local deviations from the signal cannot be resolved with common MS techniques. The only way to achieve lateral resolution of a mass-spectrometric signal (that is, in the form of a “scanning-MS”) is to restrict the origin of the gas molecules that can enter the MS to a defined sample area. In general, this can be done by adding some sort of aperture to the experimental setup that effectively blocks off all unwanted molecules. For example, a *capillary leak* can be introduced which scans over the sample surface and only detects atoms/molecules from a sharply defined sample area. Using this approach, a lateral resolution of 0.2 mm has been reported in literature [168].

Unfortunately, the “scanning-MS” method still has several drawbacks: the capillary leak scans only a relatively small sample area, and thus this method inevitably suffers from a low level of intensity and bad signal-to-noise ratio. Besides that, measuring the kinetics of different sample spots *in parallel* is impossible because only a small sample area is considered with each scan, and consequently, large surface scans would take a considerable amount of time, during which important but undetected changes may occur to the state

of the sample. Furthermore, despite the capillary leak, there is always a contribution from gas molecules originating from sample areas in the vicinity of the scanned spot.

A completely different approach to overcome the problem of spatial averaging is the use of laterally-resolved microscopic techniques based on a *parallel imaging principle* (i.e., all regions of a heterogeneous sample are imaged simultaneously), provided the chosen method is capable of imaging the kinetic transitions that happen on the surface *in parallel* to MS measurements. Techniques that match this requirement include, besides PEEM, *low energy electron microscopy* (LEEM) [169] and *metastable impact electron emission microscopy* (MIEEM) [170]. Although these methods were used in the past in numerous catalytic studies performed on single crystals, in most cases spatial averaging over the sample area was applied because the structural homogeneity of single crystal surfaces did not ask for local resolution. PEEM observations of CO oxidation on polycrystalline Pt foil have also been reported before [28, 163]. However, domain-specific kinetic measurements for individual grains have not been performed yet.

In conclusion, the approach presented here improves upon previous methods by utilizing the spatial resolution of PEEM to obtain laterally-resolved kinetics of all grains on a relatively large surface area simultaneously and *in situ* during the catalytic reaction (cf. Fig. 4.1). We have successfully applied the present method in recent experimental studies on platinum [32, 58, 171] and palladium foils [172].

### 4.2.1 Determination of the domain orientation

In order to successfully study locally-resolved kinetics on individual domains of a polycrystalline material, it is necessary to first identify the crystallographic orientation of the individual crystal grains. In general, it is possible to utilize PEEM for such a task because the work function  $\Phi$  is highly dependent on the crystallographic orientation (see sections 2.4.1.1 and 2.4.1.3 for background information).

The work function of metal surfaces is very sensitive to adsorption because the presence of an adsorbate directly affects and modifies the electron density distribution near the metal surface (or, in a very simplified picture, the surface dipole) and consequently, the work function. Both reactants in catalytic CO oxidation, CO and oxygen, change the work function of all low Miller-index platinum surfaces upon adsorption. Table 4.1 lists the respective work function values of the clean, CO- and oxygen-covered Pt(hkl) surfaces. Whereas CO adsorption increases the work function only by  $\sim 0.1$ – $0.3$  eV (curiously, some studies even find a work function *decrease* upon CO adsorption [69]), oxygen adsorption has a much larger effect on the size of  $\Phi$ . Besides that (and more importantly), the work

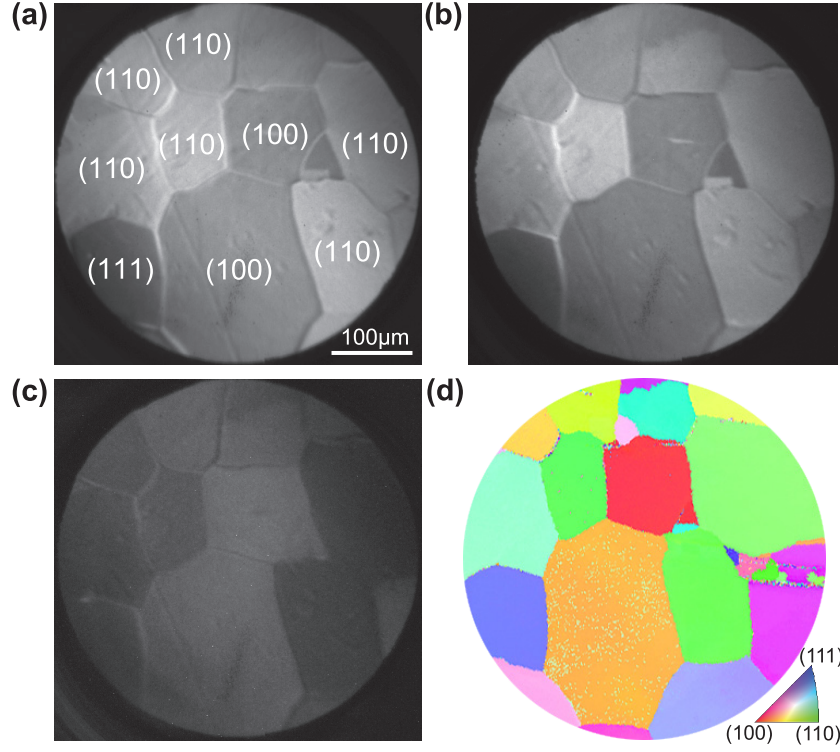


**Figure 4.2:** Domain orientation by PEEM and EBSD. PEEM images of an (a) clean, (b) CO-covered and (c) oxygen-covered platinum surface. The orientations of the individual domains are identified according to their work function and the resulting contrast as described in the text. The field of view (FOV) of the images is  $\sim 500 \mu\text{m}$ , indicated by a scale bar in (a). (d) Corresponding orientation map of the same sample area measured by EBSD. The colors of the individual domains in the map correspond to their crystallographic orientation.

functions of the individual crystallographic orientations change *differently* upon oxygen adsorption, which is a key feature for a successful domain identification [28, 163].

Clean platinum surfaces behave more or less like predicted by *Smoluchowski's theorem* [26], which states that *more densely* packed metal surfaces should, in general, also have a *higher* work function. The work functions of clean surfaces increase in the order of their respective atomic densities, which for the case of face-centered cubic Pt corresponds to:  $\Phi_{\text{Pt}(110)}$  (atomic density:  $9.2 \times 10^{14} \text{ atoms/cm}^2$ )  $< \Phi_{\text{Pt}(100)}$  ( $1.3 \times 10^{15} \text{ atoms/cm}^2$ )  $< \Phi_{\text{Pt}(111)}$  ( $1.5 \times 10^{15} \text{ atoms/cm}^2$ ). This order remains also in the case of CO adsorption, i.e.,  $\Phi_{\text{CO/Pt}(110)} < \Phi_{\text{CO/Pt}(100)} < \Phi_{\text{CO/Pt}(111)}$ .

In contrast, oxygen adsorption *changes* this order by increasing the work function of [110]-oriented facets much stronger (i.e., by  $\sim 1 \text{ eV}$ , cf. table 4.1) than the other two low Miller-index orientations [119, 173]. In consequence, oxygen-covered platinum surfaces have a work function in the order  $\Phi_{\text{O/Pt}(100)} < \Phi_{\text{O/Pt}(111)} < \Phi_{\text{O/Pt}(110)}$ .

**Table 4.1:** Work function values for the clean, CO- and oxygen-covered Pt(hkl) surface orientations. Work function values are given in eV.

Orientation	Clean (eV)	CO-covered (eV)	Oxygen-covered (eV)
(100)	5.84 <sup>a</sup>	6.04 <sup>b</sup>	6.30 <sup>b, c</sup>
(110)	5.49 <sup>d-f</sup>	5.80 <sup>d, e</sup>	6.50 <sup>d, e</sup>
(111)	5.93 <sup>a, b, f</sup>	6.13 <sup>b</sup>	6.38 <sup>b</sup>

<sup>a</sup> Ref. [174]    <sup>b</sup> Ref. [28]    <sup>c</sup> Ref. [100]    <sup>d</sup> Ref. [119]    <sup>e</sup> Ref. [173]    <sup>f</sup> Ref. [175]

The local intensity of a PEEM image is directly related to the local work function, and therefore, this effect can be used to unambiguously identify the facets by comparing their contrast in a clean, CO- and oxygen-covered state.

To illustrate the identification process in more detail, Fig. 4.2 shows three PEEM images of the same area of the sample surface in an (a) clean, (b) CO- and (c) oxygen-covered state. The field of view (FOV) of the images is approximately 500  $\mu\text{m}$ , as indicated by the scale bar in Fig. 4.2(a). The magnification of the images was calibrated by measuring the size of the domains with an optical microscope that has a known magnification (see section 2.2 for details). The individual PEEM images were recorded after cleaning the sample by  $\text{Ar}^+$  ion sputtering (15 minutes, ion current  $\sim 4 \mu\text{A}$ ) and subsequent annealing at 1100 K for another 15 minutes. For the PEEM images of the adsorbate-covered surfaces, the sample was cooled in either CO or oxygen (background pressure of the respective gas:  $1 \times 10^{-6}$  mbar) starting from a temperature of 600 K. All images were taken at a sample temperature of  $\sim 373$  K, which is well below the desorption temperatures of all the reactant gases involved (see section 3.3). The crystallographic orientations of the individual domains that could be deduced from a comparison of the corresponding images are also indicated in Fig. 4.2(a).

In addition to PEEM, electron backscatter diffraction (EBSD) (see section 2.4.5 for experimental details) was utilized at a later stage of the work to prove the domain orientation. The resulting *orientation map* is shown in Fig. 4.2(d) and is in excellent agreement with the PEEM results.

After the orientation of the crystallographic domains of a significant sample area had been determined, their individual behavior during catalytic CO oxidation was examined. An open question in this regard was whether domains with the same crystallographic orientation also behave in the same way in CO oxidation.

## 4.3 Experimental results

In this section, the results of combined PEEM/QMS experiments performed on polycrystalline platinum foil for investigating global and locally-resolved kinetics of the catalytic CO oxidation reaction are presented in detail.

### 4.3.1 Introduction

It has been noted in the introduction to bistability in section 3.5.2.1 that, during CO oxidation, the platinum surface can either be in an inactive/low-reactivity steady state of low CO<sub>2</sub> production (where the surface is mostly CO-covered) or in an active/high-reactivity state of high CO<sub>2</sub> production that is characterized by a high surface coverage of oxygen. The region in between those two states is called the *region of bistability*, where both steady states are possible at the same values of the external parameters ( $p_{CO}$ ,  $p_{O_2}$ ,  $T$ ), and the actual state of the system is depending on the *prehistory*, namely on the steady state from which the bistability region was entered by variation of an external control parameter (e.g.,  $p_{CO}$ ,  $p_{O_2}$ ,  $T$ ). By entering the region of bistability from *high temperatures* and *low* values of  $p_{CO}/p_{O_2}$ , the system will be in the active state, whereas the inactive version of bistability is present when entering the bistability region from *low temperatures* and *high*  $p_{CO}/p_{O_2}$ -ratios.

The kinetic transition from the active to the inactive state (this corresponds to transition point  $\tau_A$ ; see explanation in section 3.5.2.1) can be either triggered by decreasing the temperature or by increasing  $p_{CO}/p_{O_2}$ . Correspondingly, the position of  $\tau_B$  in parameter space can be obtained by inducing a kinetic transition from the inactive to the active state either by increasing the temperature or decreasing  $p_{CO}/p_{O_2}$ .

Both ways of inducing kinetic phase transitions were investigated in the experiments described in the following. Each single experiment was preceded by sample preparation, i.e., Ar<sup>+</sup> ion sputtering (15 minutes, ~1 keV energy, ion current ~4  $\mu$ A) and subsequent annealing to 1100 K for another 15 minutes. After that, the sample was positioned a few millimeters in front of the first PEEM lens for the experiment. In order to improve comparability, the sample spot where the domain-specific kinetics were recorded by PEEM was fixed for all measurements.

### 4.3.2 Global kinetic phase diagram for catalytic CO oxidation

To characterize the global bistable behavior of the platinum foil, a *global* kinetic phase diagram for catalytic CO oxidation was obtained which represents the “averaged” behavior of the whole sample under variation of *one* external parameter while the other two are set to constant values. However, this represents just a two-dimensional *slice* of the system’s behavior in the three-dimensional parameter space. In order to get a more complete picture of the reaction kinetics, it is thus beneficial to perform measurements of the  $\text{CO}_2$  production hysteresis as a function of CO pressure: at (i) varying temperatures and at constant oxygen pressure or (ii) by variation of the oxygen partial pressure  $p_{\text{O}_2}$  and a constant sample temperature for each experiment. In this way, kinetic phase diagrams (see section 3.5.2.2) can be obtained.

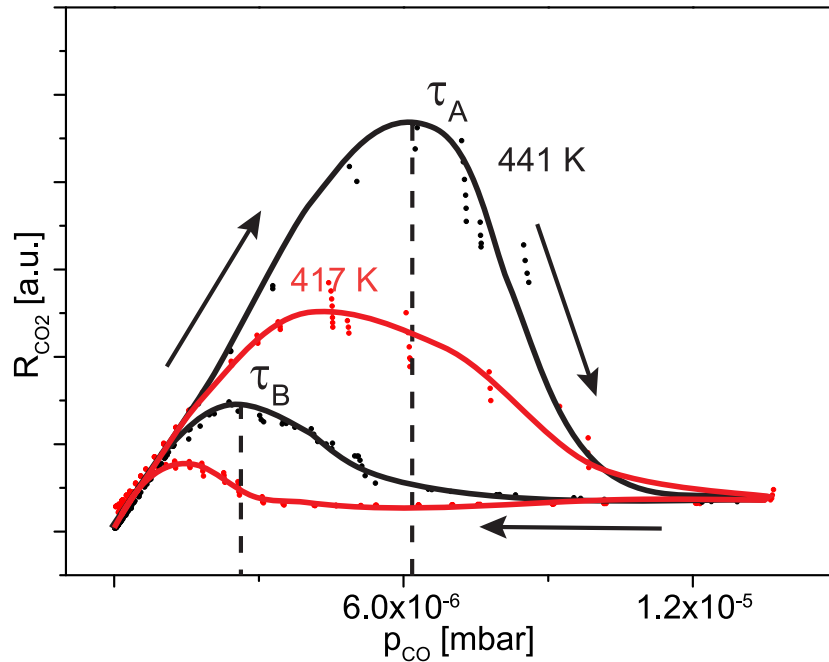


**Figure 4.3:** Hysteresis in the  $\text{CO}_2$  production rate during cyclic variation of the CO partial pressure. Two plots are shown of the  $\text{CO}_2$  production rate during cyclic variation of the CO partial pressure at 417 K (red line) and 441 K (black line) and a constant oxygen partial pressure of  $1.3 \times 10^{-5}$  mbar. Arrows indicate the direction of the pressure cycle. The position of the transition points  $\tau_A$  and  $\tau_B$  for the measurement at 441 K are indicated in the plot by dashed lines [171].

For establishing a global kinetic phase diagram of type (i), i.e., at constant  $\text{O}_2$  partial pressure, cyclic CO pressure scans were performed at different sample temperatures and a constant oxygen partial pressure of  $p_{\text{O}_2} = 1.3 \times 10^{-5}$  mbar. The  $\text{CO}_2$  partial pressure was monitored using QMS, and the sample surface was simultaneously imaged with PEEM



using an exposure time of 250 ms per frame. Figure 4.3 shows two characteristic (global) results of such experiments on polycrystalline Pt foil, namely the mass-spectrometric  $\text{CO}_2$  production rates  $R_{\text{CO}_2}$  as a function of the CO partial pressure at sample temperatures of 417 K and 441 K, respectively. The plots were matched at the level of low  $\text{CO}_2$  production (i.e., post  $\tau_A$ ) to allow for a direct comparison of the  $\text{CO}_2$  production rates at the two different temperatures. In both cases, a prominent *hysteresis* in the  $\text{CO}_2$  production rate is visible, which means that the system is showing bistable behavior at these temperatures. The transition points  $\tau_A$  and  $\tau_B$ , which mark the phase transitions between the two steady states (cf. section 3.5.2.1), are indicated in the plot for the measurement at 441 K.

It is obvious from the shape of the plots that both kinetic phase transitions do *not* occur at a sharply defined CO pressure but rather in a (more or less) narrow pressure range. In consequence, it is necessary to define criteria that allow determining  $\tau_A$  and  $\tau_B$  unambiguously in all experiments. In the present case, the definitions chosen for  $\tau_A$  and  $\tau_B$  are the same as those in Refs. [143, 145]: transition point  $\tau_A$  is defined as the *maximum* of the  $\text{CO}_2$  production rate and  $\tau_B$  as the corresponding *maximum value* in  $\text{CO}_2$  production *after* the reactivation of the platinum surface through oxygen adsorption. In contrast, the *onset* of the  $\text{CO}_2$  production would not be an appropriate choice as a definition for  $\tau_B$  in case of a polycrystalline material because this point would rather correspond to the *first* domains switching (back) to the active state and not to the ones representing the *average* (read: global) kinetics of the foil.

In comparison to the experiment at 441 K, both kinetic transition points are significantly *down-shifted* in CO pressure at 417 K. This highlights the strong temperature dependence of the bistability region. As expected, the maximum level of the  $\text{CO}_2$  production rate  $R_{\text{CO}_2}$  (i.e., at  $\tau_A$ ) is much higher at 441 K than at 417 K.

##### 4.3.2.1 Kinetic phase diagram at constant partial pressure of oxygen

For setting up a kinetic phase diagram at constant oxygen partial pressure, the experiments described in the last section were repeated at a number of temperatures in the range of 393–573 K. This range was chosen because the  $\text{CO}_2$  production rate of the sample arrived at very low levels at temperatures below 393 K, whereas at temperatures around 573 K the system is *definitely not* in the bistable state anymore. The highest temperature, where a hysteresis could still be detected, is 561 K, which is consequently also the highest temperature shown in the kinetic phase diagrams.

The CO pressures of the transition points  $\tau_A$  and  $\tau_B$  were extracted from each corresponding hysteresis plot by applying the criteria defined above and plotted (using a semi-

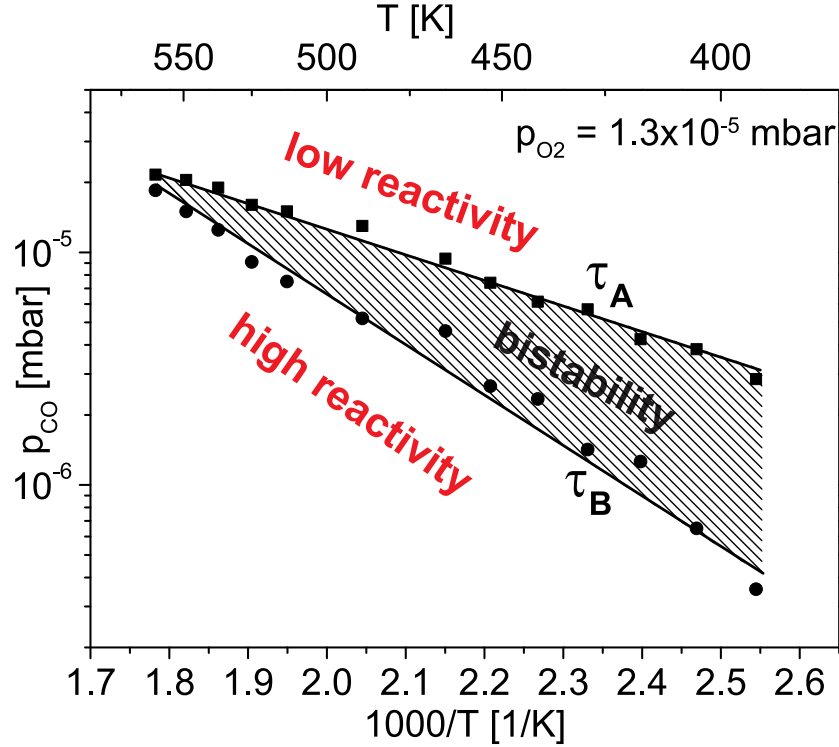


**Figure 4.4:** Global kinetic phase diagram for catalytic CO oxidation on polycrystalline Pt foil recorded at a constant oxygen partial pressure of  $p_{O_2} = 1.3 \times 10^{-5}$  mbar in the temperature range of 393–561 K. The area below  $\tau_B$  marks the region of high reactivity, while above  $\tau_A$  the sample is in the low reactivity steady state with CO effectively blocking oxygen adsorption. The bistability region in between is indicated with a diagonal line pattern.

logarithmic scale) against the *reciprocal temperature*. In the resulting plot shown in Fig. 4.4, the two steady states of high- and low-reactivity are indicated as well as the region of bistability in between them. The bistability region in  $(\lg p_{CO}, 1/T)$ -coordinates is *scissors-shaped*: the pressure gap between  $\tau_A$  and  $\tau_B$  gets smaller with increasing temperatures and, as noted above, vanishes at a temperature close to 561 K. The reason for this can be found in the already dominating *desorption* of CO at these temperatures, which leads to a very short residence time and low coverages of CO on the platinum surface. Thus, CO is not able to block oxygen adsorption anymore, which, in turn, makes bistable behavior impossible. In contrast, at the other end of the temperature range in Fig. 4.4 (i.e., at a temperature of 393 K), the bistability region is very broad and spans nearly one order of magnitude in CO pressure.

#### 4.3.2.2 Isothermal global kinetic phase diagram

A different way to obtain a global kinetic phase diagram for catalytic CO oxidation is to measure the hysteresis in  $\text{CO}_2$  production upon cyclic variation of the CO partial pressure at different oxygen partial pressures and *constant temperature* throughout all experiments. This way, the *pressure dependence* of the bistability region can be elucidated. Again, the individual measurements of the  $\text{CO}_2$  hysteresis and the determination of transition points  $\tau_A$  and  $\tau_B$  were done as described in section 4.3.2. The sample temperature was set to a constant value of 441 K, and several oxygen partial pressures in the range from  $2 \times 10^{-6}$  mbar to  $4 \times 10^{-5}$  mbar were investigated in a number of experiments. Figure 4.5 shows the corresponding *isothermal* kinetic phase diagram. This time, the *abscissa* displays the CO partial pressure and the *ordinate* denotes the oxygen pressure chosen for the experiment.

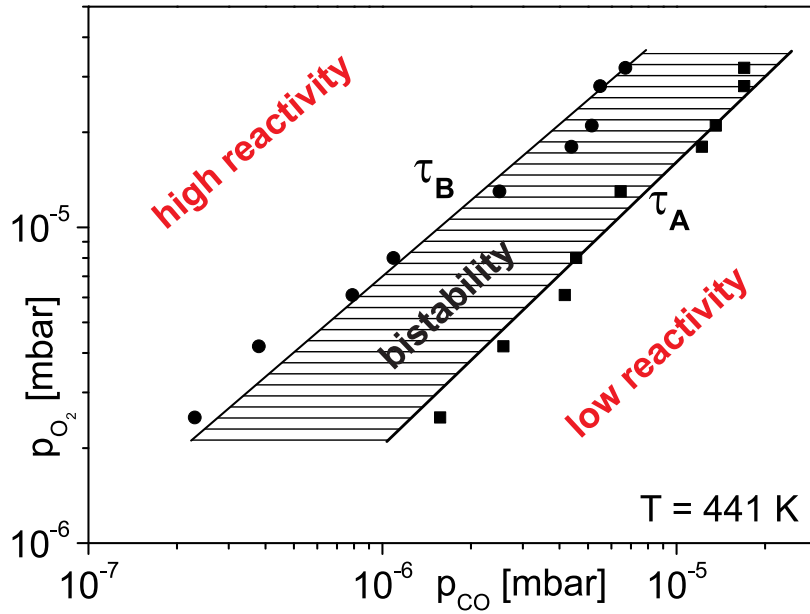


**Figure 4.5:** Global kinetic phase diagram measured at a constant temperature of 441 K under variation of the oxygen partial pressure  $p_{\text{O}_2}$ . The sample is in the high reactivity state for CO pressures of  $p_{\text{CO}} < \tau_B$  and deactivated at  $p_{\text{CO}} > \tau_A$ . The dashed region in between is the region of bistability [171].

Compared to the global kinetic phase diagram at constant oxygen pressure (shown in Fig. 4.4), the isothermal kinetic phase diagram in  $(\lg p_{\text{CO}}, \lg p_{\text{O}_2})$ -coordinates (Fig. 4.5) has a completely different appearance: it is characterized by two (nearly) *parallel* lines representing the position of the transition points  $\tau_A$  and  $\tau_B$  as a function of oxygen pressure.

### 4.3.3 Domain-specific kinetic phase diagrams

As has been outlined in section 4.2, domain-specific kinetic phase diagrams can be obtained *in situ* and simultaneously to the QMS measurements by measuring and analyzing the local PEEM image intensity. A plot of the local PEEM intensity during the ongoing CO oxidation would correspond to a local QMS measurement of the given domains. Such a plot of the local PEEM intensity is shown in Fig. 4.6 for the case of a single Pt(110) domain that is confined by a white border line in the figure. The PEEM intensity plotted in the figure was obtained by averaging over the pixel intensities of a rectangular area (*region of interest* (ROI)) defined within the selected domain. As a higher CO<sub>2</sub> production rate normally corresponds to a lower PEEM intensity on surfaces of platinum, the PEEM intensity is plotted in *reverse direction* in Fig. 4.6 in order to highlight the similarity of the plot's appearance with the CO<sub>2</sub> production rate hysteresis in Fig. 4.3.

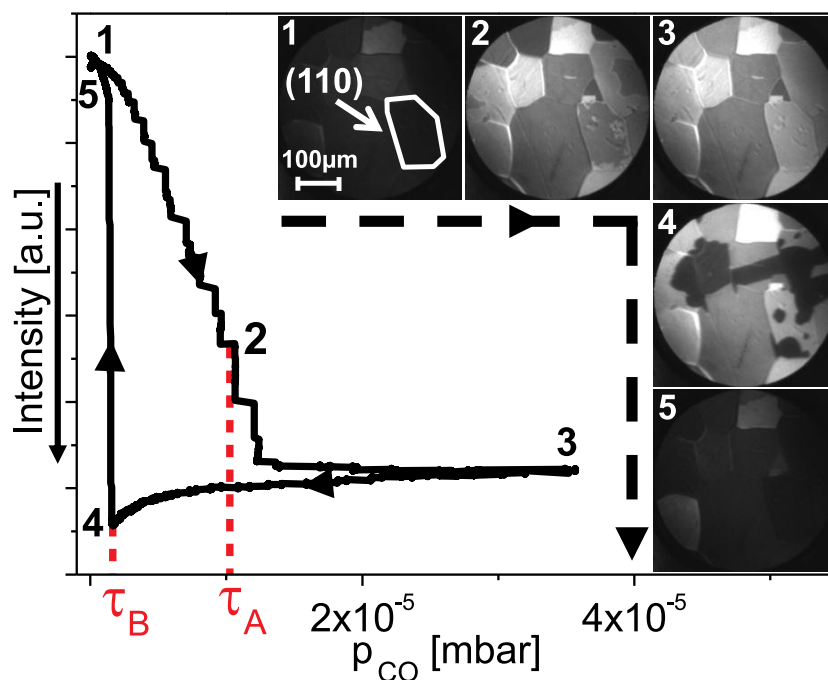


**Figure 4.6:** Plot of the local PEEM intensity for a single Pt(110) facet versus CO partial pressure, as measured *in situ* during catalytic CO oxidation at a temperature of 417 K and  $p_{O_2} = 1.3 \times 10^{-5}$  mbar. The selected [110]-oriented domain is indicated in frame 1 with a white border. The insets show PEEM images at characteristic points during the pressure cycle. Arrows indicate the direction of the pressure cycle, and the numbers along the hysteresis curve correspond to the PEEM frames [171].

In addition, Figure 4.6 provides five PEEM images at distinct points during the CO pressure scan. Frame 1 shows an *oxygen-covered* surface with a corresponding *low* PEEM in-

tensity due to the high work function  $\Phi$  of such surfaces (cf. section 4.2.1). The second frame in Fig. 4.6 characterizes the state of the surface typical for the kinetic transition from the active to the inactive state (i.e., near  $\tau_A$ ): *reaction-diffusion fronts* are visible as *bright patches* on the otherwise still mostly dark domain. The bright patches correspond to those areas of the domain that are already covered with CO and thus have switched to the inactive state. Starting from domain boundaries or defect sites, the fronts are moving across the domains with a velocity that depends on the sample temperature. The third frame (recorded at a high CO partial pressure) documents the inactive steady state due to CO poisoning of the complete surface area. Its high PEEM image intensity (brightness) is due to the fact that the work function of the CO-covered Pt(110) surface is significantly lowered compared to the oxygen-covered state (in fact, the work function is almost equal to that of a clean surface, cf. section 4.2.1). After  $p_{CO}$  is decreased again, frame 4 shows a situation that is characteristic for the kinetic transition from the inactive to the active state (i.e., near  $\tau_B$ ): dark *elliptical patches* (indicating *high oxygen coverage*) are forming on the still CO-covered Pt(110) domains. The pronounced elliptical form of these patches is due to the fact that the *fcc* (110) surface termination has an *anisotropic* surface structure (cf. sections 3.1 and 3.2.2), and therefore the CO diffusion also differs along the two main crystallographic directions  $[1\bar{1}0]$  and  $[001]$  (see section 3.4), leading to anisotropic reaction front propagation. This topic will be covered in more detail in section 4.3.7. Finally, after completion of the cyclic CO pressure scan, the fifth frame corresponds to frame 1 in representing the (oxygen-covered) active steady state of the surface.

The domain-specific transition points  $\tau_A$  and  $\tau_B$  for Pt(110) can be easily extracted from the distinct drops and jumps in the PEEM intensity plot that are visible in Fig. 4.6 and visualized in a domain-specific kinetic phase diagram. Of course, the same procedure can also be applied to the corresponding intensity plots of Pt(100) and Pt(111) domains. Figure 4.7 shows the resulting domain-specific phase diagrams for catalytic CO oxidation on the [100]-, [110]- and [111]-oriented crystal domains. It is obvious from the diagrams that the individual domains on the polycrystalline foil behave very differently during CO oxidation.

The differences in the positions of the domain-specific phase diagrams have the following meaning: imagine a point  $\mathbf{A}(p_{CO}, p_{O_2}, T)$ , placed arbitrarily as is shown in Fig. 4.7. At the parameter values corresponding to  $\mathbf{A}$ , the [111]-oriented domains are already in the inactive state. However, under the same conditions, the [110]- and [100]-oriented facets are still catalytically active (i.e., they still have a predominantly oxygen-covered surface).

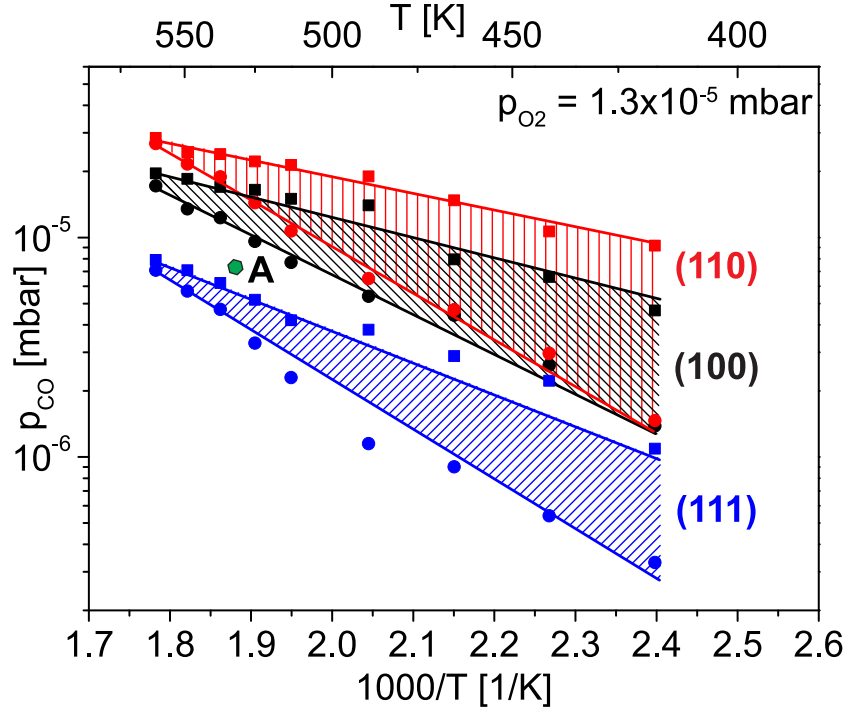


**Figure 4.7:** Local (domain-specific) kinetic phase diagrams for (100), (110) and (111) domains of polycrystalline Pt foil. The diagrams were obtained by an analysis of the PEEM intensity during catalytic CO oxidation at constant oxygen pressure of  $1.3 \times 10^{-5}$  mbar in the temperature range from 417 K to 561 K. The data points refer to the CO pressures at kinetic transition points  $\tau_A$  (squares) and  $\tau_B$  (circles). The straight lines serve solely as guide for the eye, and the bistability regions of all domains are indicated as dashed regions. A description of point A is given in the text.

One has to note at this point that domain-specific results drawn from the PEEM experiments are only reasonable if the chosen conditions and the investigated (polycrystalline) material meet several requirements: the presence of locally-confined kinetics requires that the individual crystal grains of the sample are sufficiently independent of each other. For this purpose, their size has to be much larger than the diffusion length  $2\sqrt{Dt}$  of the involved reactants in the surface reaction under the applied experimental conditions, and the boundaries confining the domains should be difficult to overcome by reactant diffusion. Both conditions ensure that *diffusion coupling* between the individual facets is limited, and the reaction mechanism is still mostly controlled by adsorption and desorption processes on particular domains.

Two other mechanisms have to be ruled out in order to successfully apply the experimental approach, namely the occurrence of *gas phase coupling* which is known to synchronize the kinetics of catalytic systems consisting of different crystallographic orien-

tations at pressures above  $10^{-4}$  mbar [163, 167, 176]. Furthermore, at even higher (i.e., near atmospheric) total pressures, *heat transfer* starts to dominate over spatial coupling [177, 178].

As all the experiments described in this chapter were performed at pressure conditions of  $\sim 10^{-5}$  mbar, which is well below the limit where the mentioned coupling mechanisms are usually observed, none of the above effects should apply. This assertion is corroborated by the PEEM experiments described here, which prove that differently oriented domains really act independently of each other. This result justifies the approach chosen for the experiments because it demonstrates that the averaged  $\text{CO}_2$  signal obtained by QMS measurements is *not sufficient* to describe the kinetics of such a polycrystalline sample, and, in addition, a laterally-resolved technique like PEEM is needed to elucidate the domain-specific details.

The pressure difference of the transition points  $\tau_A$  and  $\tau_B$  for differently oriented domains can be partially explained by the value of the (initial) sticking coefficient of oxygen on the three different low Miller-index facets (cf. section 3.3.3) [28]:  $s_0$  has the highest value on Pt(110)-(1 $\times$ 2) (0.3–0.4), followed by Pt(100)-(1 $\times$ 1) (0.1) and Pt(111) (0.04–0.05). In contrast, all three surface orientations are quite similar concerning the CO adsorption properties (see section 3.3.2), which means that the domain-specific adsorption properties of oxygen seem to be crucial for the relative position of the bistability region.

#### 4.3.4 Catalytic ignition and extinction experiments on Pt foil

Another experimental approach that is often applied for characterizing a catalytically active sample in the ( $p_{\text{CO}}$ ,  $p_{\text{O}_2}$ ,  $T$ )-parameter space is the study of the catalytic *ignition* (also known as “light-off”) and *extinction* temperatures as a function of the reactant gas phase composition. In general, the catalytic ignition point marks the temperature where the rate of exothermic catalytic reactions such as CO oxidation suddenly increases sharply due to *self-acceleration*. It is equivalent to the critical temperature, where a chemical reaction that has been governed solely by reaction kinetics before, becomes determined by mass transport due to the shifted balance between reaction heat generation and energy dissipation in the system [179, 180].

A significant difference exists between catalytic ignition as defined above and kinetic phase transitions accessible to PEEM measurements: in contrast to catalytic ignition, kinetic phase transitions (as observed in the experiments presented here) are pure *kinetic phenomena*, since heat and mass transport do not play a role in the considered pressure regime ( $\sim 10^{-6}$ – $10^{-4}$  mbar) [137, 180]. Nevertheless, in both cases the behavior of the cat-

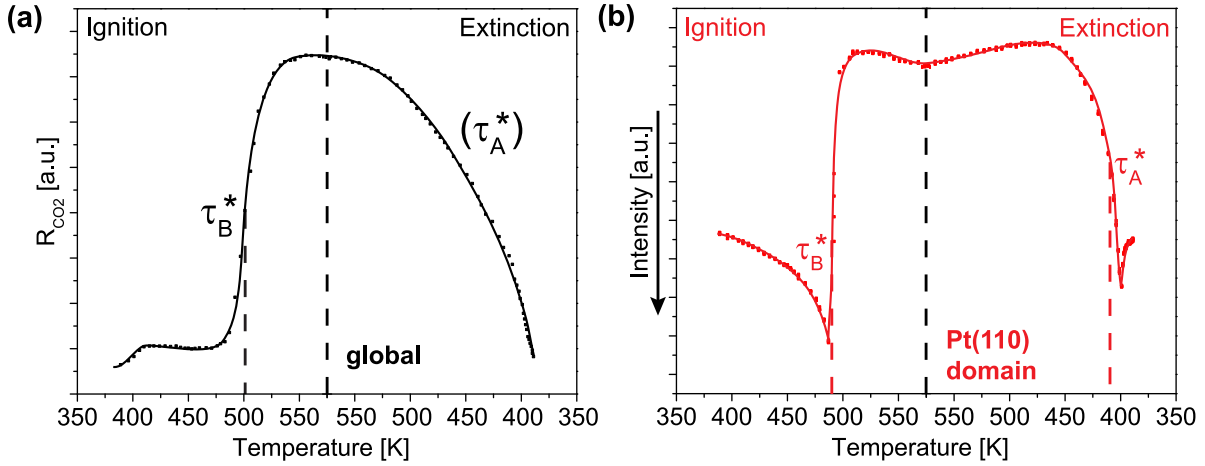


**Figure 4.8:** Global and local results of an ignition/extinction experiment. The experiment was conducted in a constant gas mixture of  $p_{CO} = 6.6 \times 10^{-6}$  mbar and  $p_{O_2} = 1.3 \times 10^{-5}$  mbar by cyclic heating and cooling of the sample with a rate of 0.5 K/s. (a) Global ignition and extinction as measured by QMS. (b) Laterally-resolved ignition and extinction behavior of a single Pt(110) domain as measured by PEEM. The positions of the transition points  $\tau_A^*$  and  $\tau_B^*$  are indicated with dashed lines in both plots (see also text).

alytic system changes qualitatively when a control parameter exceeds a certain (critical) value. There are a lot of studies dedicated both to catalytic ignition in CO oxidation on Pt [181, 182] and to ignition-related kinetic phase transitions from an inactive to an active state at increasing temperature but constant reactant pressures (e.g., for Pd [183]).

Consequently, in case of CO oxidation, catalytic ignition can be (in a first approximation) related to the kinetic transition from the CO-covered inactive to the oxygen-covered active state (i.e.,  $\tau_B$ ). Likewise, extinction then corresponds to the reaction rate drop during poisoning of the catalyst surface with CO (i.e.,  $\tau_A$ ). In order to distinguish these kinetic transition points from those deduced from pressure cycle experiments, they are hence named  $\tau_A^*$  (corresponding to extinction) and  $\tau_B^*$  (ignition), respectively.

In the present study, the kinetic phase transitions related to ignition and extinction were again measured both globally using the  $CO_2$  QMS signal and laterally-resolved by recording the PEEM intensity in one experiment. For this purpose, a *constant* reactant gas ratio  $p_{CO}/p_{O_2}$  was established in the reaction chamber before each experiment, and then the sample was first heated and then cooled again in the constant gas mixture with a rate of  $\sim 0.5$  K/s. A number of such experiments were performed in the temperature range from  $\sim 373$  K to  $\sim 600$  K at varying  $p_{CO}/p_{O_2}$  ratios.

Figure 4.8 shows an exemplary result of such a kinetic transition experiment that was performed at partial pressures of CO and oxygen of  $6.6 \times 10^{-6}$  mbar and  $1.3 \times 10^{-5}$  mbar,



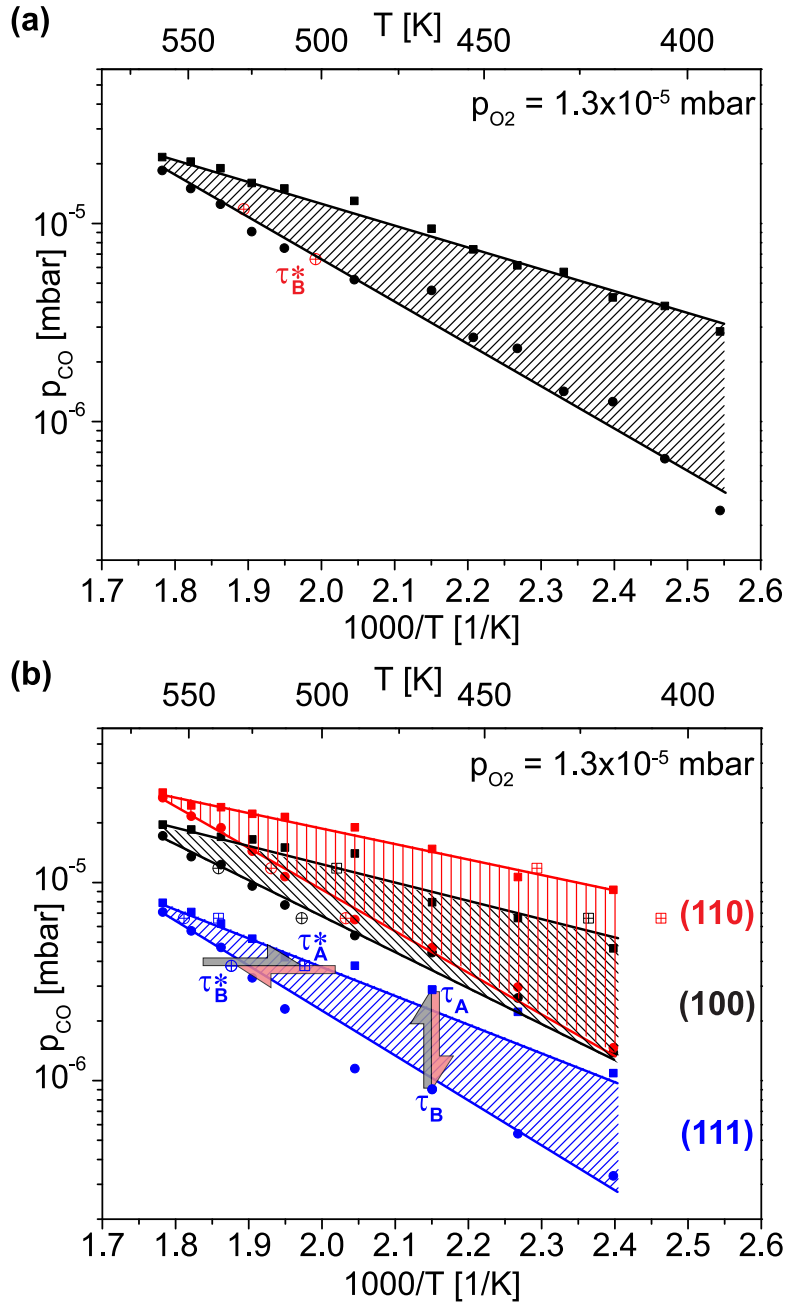


**Figure 4.9:** Global and local kinetic phase diagrams including the kinetic transition points  $\tau_B^*$  (ignition) and  $\tau_A^*$  (extinction) at a constant oxygen partial pressure of  $p_{O_2} = 1.3 \times 10^{-5}$  mbar. (a) Global kinetic phase diagram (as in Fig. 4.4) and (b) domain-specific kinetic phase diagram (as in Fig. 4.7) including the kinetic transition points  $\tau_A^*$  (crossed open squares) and  $\tau_B^*$  (crossed open circles). The transition points  $\tau_A^*$  are omitted in case of the global diagram in (a). Vertical and horizontal arrows indicate the scan direction used for obtaining transition points  $\tau_A/\tau_B$  and  $\tau_A^*/\tau_B^*$ , respectively.

respectively. Figure 4.8(a) illustrates the  $\text{CO}_2$  production rate measured by QMS during the temperature ramp, and Fig. 4.8(b) depicts the local PEEM intensity of a single Pt(110) domain in the same experiment (again plotted in reverse direction). Similar to the pressure cycle experiments described in the previous sections, the kinetic transitions are visible as sudden drops and jumps in the  $\text{CO}_2$  production rate and the PEEM intensity. The positions of the (global and local) transition points  $\tau_A^*$  and  $\tau_B^*$  are defined as the *inflection points* in the corresponding plots. While the local transition points for Pt(110) are rather sharp and well-defined in Fig. 4.8(a) (the same is also true for the case of Pt(100) and Pt(111) domains), the position of the global transition point  $\tau_A^*$  related to extinction is smeared out and difficult to measure.

Using ignition and extinction experiments as described above, one can prove the *correspondence* existing between the kinetic transition points  $\tau_A$  and  $\tau_B$  that were obtained by cyclic pressure experiments as described in section 4.3.2.1 and kinetic transitions  $\tau_A^*$  and  $\tau_B^*$  related to extinction and ignition, which are accessible by experiments under cyclic variation of the temperature at constant  $p_{\text{CO}}/p_{\text{O}_2}$ . This correspondence is illustrated in Fig. 4.9, which again shows both the global (as in Fig. 4.4) and local (as in Fig. 4.7) kinetic phase diagram on polycrystalline Pt foil but, in addition, also the respective global and local transition points of ignition/extinction ( $\tau_A^*$  and  $\tau_B^*$ ). As mentioned above, the global transition points  $\tau_A^*$  related to extinction are too unspecific to be measured reliably and are therefore not depicted in Fig. 4.9.

##### 4.3.4.1 Comparison to the apex of a Pt nanotip

In order to elucidate the possible differences that may exist between micrometer- and nanometer-sized domains of platinum with regard to CO oxidation (i.e., as a partial bridging of the materials gap), the results of the PEEM experiments described above were compared to measurements using *field ion microscopy* (FIM; cf. section 2.4.4). In this case, the sample is the apex of a Pt nanotip. Such an apex exhibits differently oriented nanofacets (size:  $\sim 2\text{--}20\text{ nm}$ ) that are confined by atomic steps (see Fig. 2.10).

Figure 4.10 shows a sequence of six consecutive FIM images of a [100]-oriented Pt field emitter tip recorded during a kinetic transition related to catalytic ignition. The experiment from which these images originate was performed at partial pressures of CO and oxygen of  $5.3 \times 10^{-7}\text{ mbar}$  and  $5.3 \times 10^{-4}\text{ mbar}$ , respectively. A temperature ramp from 325 K to 365 K (at 5 K/s) was applied to the Pt tip.

In frame 1 of Fig. 4.10, the crystallography of the [100]-oriented Pt sample is indicated by the positions of the low Miller-index domains. In the first three frames, the surface of

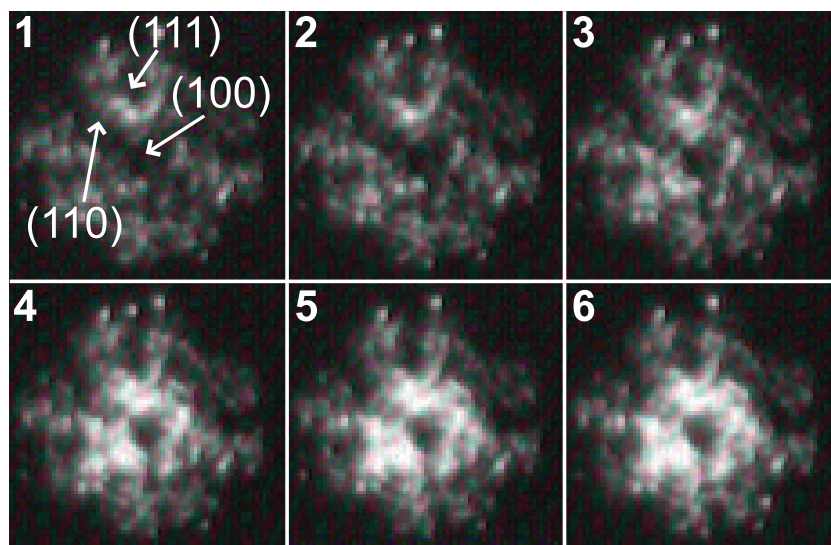


**Figure 4.10:** Sequence of six consecutive FIM images recorded during a kinetic phase transition related to catalytic ignition. The crystallography of the platinum tip (positions of the low Miller-index domains) is shown in the first frame. Whereas in the first three frames the surface of the field emitter tip is still CO-covered and thus inactive, a kinetic transition occurs between frames 3 and 4, and in turn, frames 4–6 show the activated state of the sample after the kinetic phase transition. The frames were recorded at a temperature of  $\sim 331$  K and partial pressures of CO and oxygen of  $5.3 \times 10^{-7}$  mbar and  $5.3 \times 10^{-4}$  mbar, respectively. The frame rate was 25 frames per second (0.04 s/frame).

the field emitter tip is still covered with CO and thus in the inactive state with a correspondingly low FIM image brightness (note that the FIM images have a reversed brightness order compared to PEEM, i.e., areas with low work function appear dark and vice versa). Between frame 3 and 4, the kinetic phase transition starts: the surface gets quickly covered with oxygen, which is visible as a sudden increase in the image brightness (work function) on some areas of the field emitter tip.

After the transition is completed, the intensity and size of the bright area on the sample continues to vary slightly in time. This can be attributed to local reaction-induced *fluctuations*, which accompany any surface reaction when monitored on the nanoscopic scale [184].

For the analysis of the FIM images, both local intensity analysis and *proper orthogonal decomposition* (POD) of a larger area was used. A signal  $w(\mathbf{x}, t)$  that varies in space and time can be decomposed by POD (also called *Karhunen-Loève* (KL) decomposition)

into time-dependent amplitudes  $a_n(t)$  and time-independent modes  $\mathbf{b}_n(\mathbf{x})$  that form an orthogonal basis. The basis functions  $\mathbf{b}_n(\mathbf{x})$  are the eigenvectors of the equation:

$$\hat{\mathbf{S}}\mathbf{b}_n(\mathbf{x}) = \Lambda_n\mathbf{b}_n(\mathbf{x}), \quad (4.1)$$

where  $\Lambda_n$  are the eigenvalues and  $\hat{\mathbf{S}}$  is the correlation matrix. Each eigenvalue  $\Lambda_n$  denotes the weight or energy of the corresponding eigenvector  $\mathbf{b}_n(\mathbf{x})$ , i.e., the variance of the original data set projected along this eigenvector. The eigenvectors are sorted in order of decreasing eigenvalue. The time-dependent amplitudes can be obtained by projecting the original video frames on the KL-basis  $\mathbf{b}_n(\mathbf{x})$ . Because the number of eigenvectors/eigenvalues resulting from a POD analysis is (less than or) equal to the number of time steps  $t$ , and, in general, the first few eigenvectors carry already most of the weight (i.e., they capture the overall dynamics of a system properly), the dimensionality (that is, the number of eigenvectors) of the KL-basis can be chosen much smaller than the original without losing important information. This makes POD a useful method for *complexity reduction* in multidimensional data-sets. However, as in the present case, it can also be used to obtain the main features of a complex data-set like monitoring a large area of an image sequence. The method was successfully utilized for the analysis of reaction-induced fluctuations [185] and oscillatory behavior of complex systems [186].

POD was applied to the FIM image sequence partially shown in Fig. 4.10, and the result of the analysis is presented in Fig. 4.11: Fig. 4.11(a) displays the *region of interest* (ROI) that was chosen for the POD analysis, which includes all three low Miller-index domains (100), (110) and (111). The variances of the resulting POD eigenvectors indicate that the first few eigenvectors dominate the whole decomposition, with the first eigenvector already amounting to 67.7 % of the whole energy. The variances drop rapidly with increasing mode number (e.g., the second eigenvector already contributes only 9.7 % to the total energy), and consequently, the higher modes contribute only little to the overall dynamics of the system. This indicates a high degree of spatial correlation of the whole process. In consequence, the first eigenvector is already sufficient to describe at least the main features of the kinetic phase transition properly. This is highlighted in Fig. 4.11(b) in a comparison of two characteristic frames from the original data with reconstructed frames using the first eigenvector of the KL-decomposition. The frames show the state of the Pt tip apex just *before* and *after* catalytic ignition. As can be seen from the images, both the inactive and the active state are well reproduced by the reconstruction.

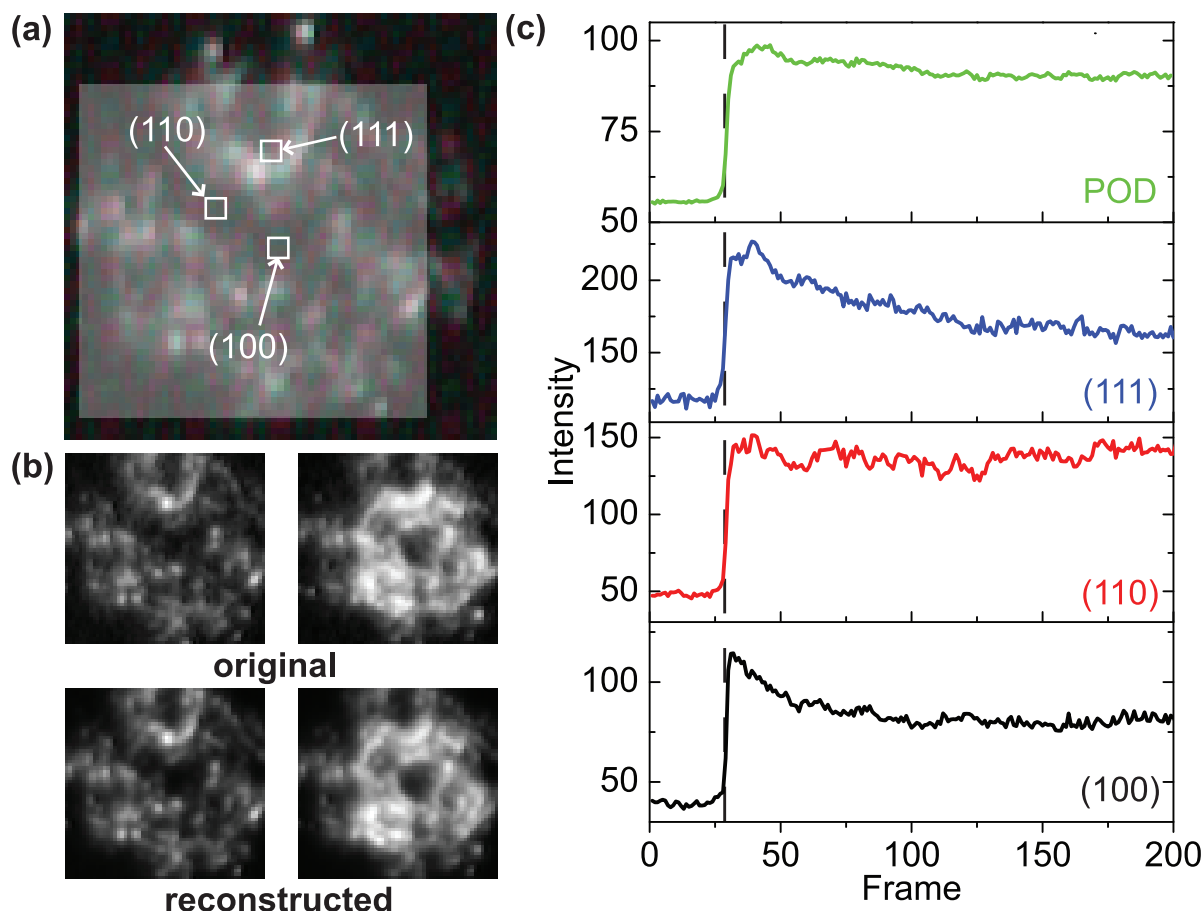


**Figure 4.11:** Comparison of POD and original FIM intensity. (a) FIM image showing the [100]-oriented Pt field emitter tip in the inactive state. The position of the individual domains are indicated with arrows. The region, for which POD was performed, is marked with a semi-transparent square, and the areas where the intensity analysis on the individual facets was performed are indicated with a white border. (b) Original (top row) and reconstructed (bottom row) frames just before (left column) and after (right column) the ignition-related kinetic phase transition. The reconstruction was done with the first eigenvector of the KL-decomposition (67.7%). (c) FIM intensity profiles of the domains as well as the intensity profile of the KL-decomposition using the first eigenvector. The position of the kinetic phase transition in the image sequence is marked with a dashed line.

In addition to KL-decomposition, the intensities of the low Miller-index domains on the tip were also analyzed. For this purpose, the FIM intensity was integrated in three small ROIs in the vicinity of the domains. Figure 4.11(c) shows a comparison of the resulting intensity profiles with the POD data of the large ROI as reproduced by the *first* eigenvector. It is obvious from the plots that all the main features of the intensity plots are sufficiently reproduced by the reconstruction, which is characterized by a sharp jump in intensity at the point of the kinetics phase transition (at about frame 29 of the sequence) and a subsequent drop to a slightly lower level. The image intensity then fluctuates around this level for the rest of the image sequence (which consists of  $\sim 200$  frames). The differently oriented domains are *synchronized* by diffusion, which means that the kinetic phase transition happens at the same time for all different surface orientations. This is highlighted by a dashed line in Fig. 4.11(c) that marks the onset of the kinetic phase transition.

The result obtained for the field emitter tip is in strong contrast to the observations made by PEEM for the micrometer-sized domains on polycrystalline Pt foil where a quasi-independent behavior of the individual domains was observed. The difference in behavior can be attributed to the high degree of spatial coupling existing on nanometer-sized samples, in contrary to the micrometer-sized domains of a Pt foil where neither diffusion coupling (interrupted by boundaries) nor gas phase coupling (low pressure) are sufficient to synchronize the kinetic transitions.

#### 4.3.5 Variation of oxygen pressure

Similar experiments to those described in the previous sections were also conducted at a higher oxygen partial pressure of  $p_{O_2} = 2.7 \times 10^{-5}$  mbar, and the results are shown in Fig. 4.12. Not surprisingly, compared to the experiments at  $p_{O_2} = 1.3 \times 10^{-5}$  mbar, all kinetic phase transition points are shifted toward *higher* CO pressures. On the other hand, the approximate temperature of the cusp point remains constant. The same is true for the width of the bistability region, which also remains nearly unchanged.

Besides that, Fig. 4.12 also shows the global and domain-specific kinetic transition points  $\tau_A^*$  and  $\tau_B^*$  related to catalytic extinction and ignition, which were obtained from several experiments at higher oxygen pressure ( $p_{O_2} = 2.7 \times 10^{-5}$  mbar). Similar to the experiments described in section 4.3.4, the values are in good agreement with the kinetic phase diagrams deduced from pressure-cycle experiments.

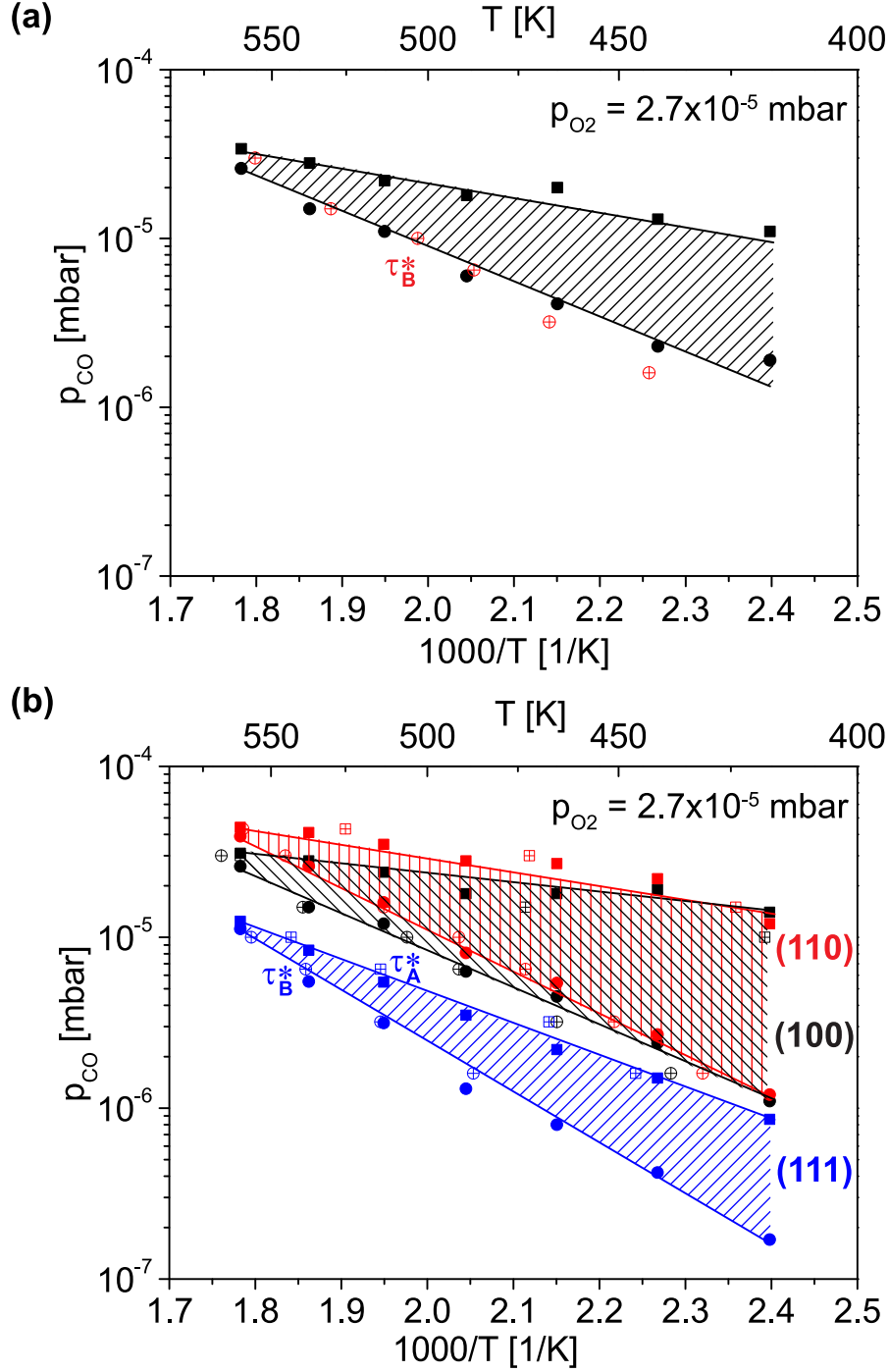


**Figure 4.12:** Global and local kinetic phase diagrams including the transition points  $\tau_B^*$  (ignition) and  $\tau_A^*$  (extinction) measured at a constant oxygen partial pressure of  $p_{O_2} = 2.7 \times 10^{-5}$  mbar. (a) Global kinetic phase diagram and (b) domain-specific kinetic phase diagram including the kinetic transition points  $\tau_A^*$  (crossed open squares) and  $\tau_B^*$  (crossed open circles). The transition points  $\tau_A^*$  are omitted in case of the global diagram in (a).

### 4.3.6 Reconstruction of the global kinetic phase diagram

A comparison of the global phase diagram that represents the overall activity of the polycrystalline foil for CO oxidation with laterally-resolved phase diagrams for the individual low Miller-index domains demonstrated that a single global kinetic phase diagram does not sufficiently describe the catalytic behavior of a polycrystalline sample. Question remains whether the kinetics of catalytic CO oxidation on polycrystalline Pt foil is adequately described by a set of domain-specific phase diagrams of the low Miller-index domains. This question is reasonable because the contributions to the overall kinetics originating from defect sites, grain boundaries, etc., cannot be resolved with the present experimental approach.

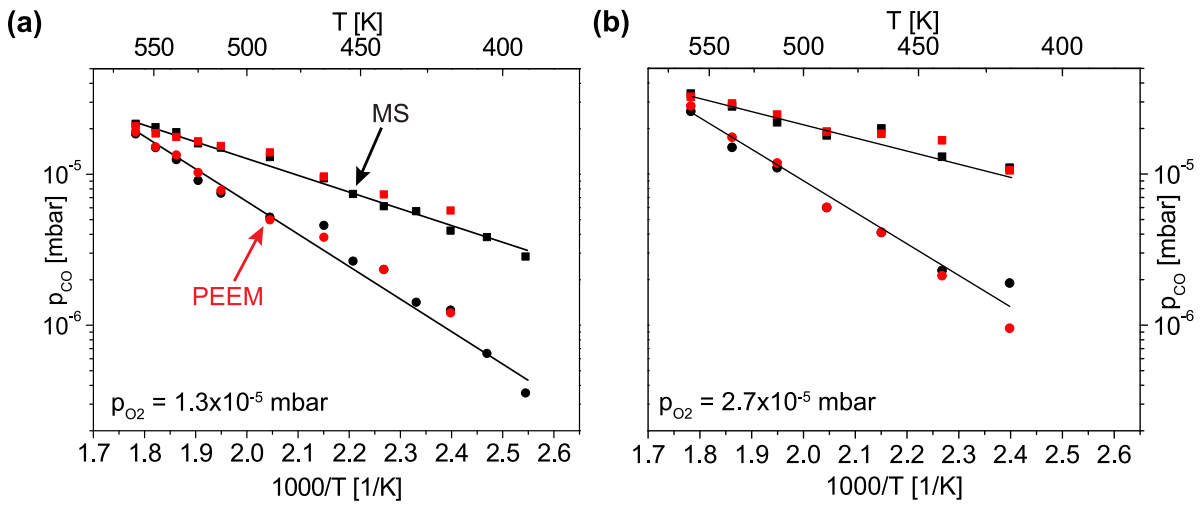


**Figure 4.13:** Global kinetic phase diagrams for catalytic CO oxidation on polycrystalline Pt foil (red squares and circles), reconstructed from the domain-specific diagrams and compared to the corresponding global kinetic phase diagrams obtained from mass spectroscopic measurements of  $CO_2$  production (black squares and circles). Two different oxygen pressures were investigated: (a)  $p_{O_2} = 1.3 \times 10^{-5}$  mbar, (b)  $p_{O_2} = 2.7 \times 10^{-5}$  mbar.

The answer to the question proposed above is quite simple: if it is possible to “reconstruct” the global kinetic phase diagram using the laterally-resolved data, all major contributions to the global kinetics must have been considered.

For this purpose, the distribution of the low Miller-index facets on polycrystalline platinum must be known. In Ref. [28], an average distribution of 40 % (100), 40 % (110) and 20 % (111) is given after evaluating the orientation of many domains on a polycrystalline Pt foil. Using these numbers, *reconstructed* global kinetic phase diagrams were calculated by summing up the weighted contributions of the different domains. Figure 4.13



shows such reconstructed phase diagrams (red squares and circles) for both applied oxygen pressures together with the original global kinetic phase diagrams that were obtained with QMS (black squares and circles). In both cases, the reconstructed phase diagrams are in quantitative agreement with the corresponding global kinetic phase diagram from QMS measurements, indicating that all major contributions to the global kinetics have been considered.

### 4.3.7 Reaction-diffusion front propagation on Pt(110) domains

Because PEEM is a microscopic technique with a parallel imaging principle, it is particularly well suited to investigate the temporal evolution of reaction-diffusion fronts on single crystals [161, 162, 187] as well as on polycrystalline surfaces [28, 163]. In the following section, the reaction-diffusion front propagation on the [110]-oriented domains of polycrystalline Pt foil in catalytic CO oxidation is investigated in more detail.

Although this is a well-studied topic (a lot of experimental studies on reaction-diffusion fronts have already been performed on single crystals of Pt(110) in the past [119, 121, 188], and the diffusion properties of CO and oxygen on Pt(110) have also been determined by PEEM experiments [120]), a polycrystalline Pt foil provides the opportunity to compare the front propagation on different (hkl) domains on the *same* sample [28] as well as the properties of the domains with the same orientation (e.g., (110)) but of different size.

Besides that, open questions still exist in the cited studies regarding the ratio of the front propagation velocities  $v_{[1\bar{1}0]}/v_{[001]}$  along the main crystallographic directions  $[1\bar{1}0]$  and  $[001]$  on the Pt(110) surface. While the experimental studies performed by Jakubith and coworkers (Ref. [188]) as well as Nettesheim and coworkers (Ref. [119]) found a velocity ratio of  $v_{[1\bar{1}0]}/v_{[001]} \approx 2$ , Patchett et al. (Ref. [121]) estimated a much larger number of  $v_{[1\bar{1}0]}/v_{[001]} \approx 10$ . The latter authors attributed this increased anisotropy to a higher step density on the utilized single crystal due to roughening effects. In order to shed light on this discrepancy, the present results for single Pt(110) domains of polycrystalline Pt foil are compared to the earlier single crystal studies in the following sections.

#### 4.3.7.1 Shape and orientation of the reaction-diffusion fronts

In section 4.3.3, reaction-diffusion fronts propagating on the Pt(110) domains during kinetic transitions in CO oxidation were described as being mostly *elliptical* in shape. The reason for this behavior was also mentioned there, namely the different diffusion parameters along the two main crystallographic directions  $[1\bar{1}0]$  and  $[001]$ . This implies that

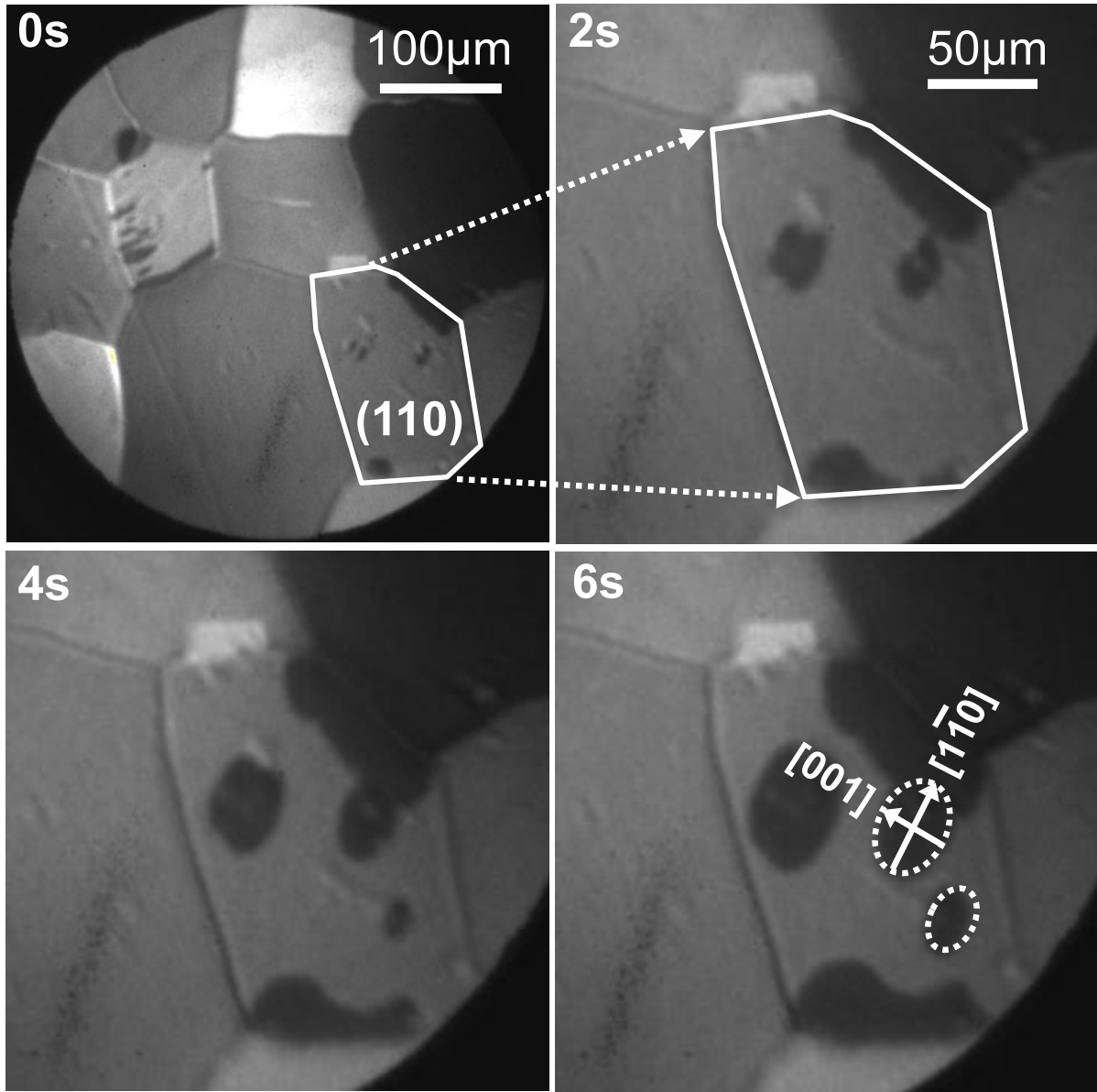


**Figure 4.14:** Propagation of elliptic oxygen reaction-diffusion fronts on an anisotropic Pt(110) domain during catalytic CO oxidation at 441 K,  $p_{O_2} = 1.3 \times 10^{-5}$  mbar and  $p_{CO} = 3.8 \times 10^{-6}$  mbar. The orientations of the elliptic reaction fronts on the domain allow to determine the azimuthal orientation of the main crystallographic axes, as is indicated in the plot by arrows [171].

the two main axes of the ellipses formed by the reaction-diffusion fronts should also be aligned along these two directions, and thus the azimuthal orientation of the crystallographic axes of individual (110) domains on polycrystalline Pt foil can, in principle, be deduced from examining the temporal evolution of reaction-diffusion front propagation.

This was done for the case of the investigated Pt(110) domains and is illustrated in Fig. 4.14, which shows a series of successive PEEM images where *four* independent oxygen reaction-diffusion fronts are propagating on the same Pt(110) domain near kinetic transition point  $\tau_B$ . The frames correspond to snapshots taken during a PEEM experiment at a sample temperature of 441 K and an oxygen partial pressure of  $1.3 \times 10^{-5}$  mbar with an interval of *two* seconds in between them. The corresponding CO partial pressure was  $3.8 \times 10^{-6}$  mbar, which is slightly larger than the value of  $\tau_B$  at this temperature in the domain-specific phase diagram shown in Fig. 4.7.

All the elliptical oxygen reaction-diffusion fronts are aligned in the same way, which confirms that the surface structure determines the shape of the emerging reaction fronts.

#### 4.3.7.2 Velocity of front propagation

In order to determine the propagation velocity of the elliptical reaction-diffusion fronts, PEEM video-sequences from several cyclic CO pressure scans at different temperatures in the temperature range from 417 K to 489 K were analyzed. The lengths of the two main axes of each elliptical reaction-diffusion front were obtained with the help of the *ImageJ* application software,<sup>1</sup> and the resulting front propagation velocities  $v_{[hkl]}$  were calculated using the following equation:

$$v_{[hkl]} = \frac{1}{2} \frac{\Delta x}{\Delta t}, \quad (4.2)$$

where  $\Delta x$  is the change in axis length and  $\Delta t$  is the interval between two successive PEEM frames (here:  $\Delta t = 250$  ms). The factor of  $\frac{1}{2}$  accounts for the fact that the propagation of the reaction-diffusion fronts proceeds in *both* opposing directions simultaneously. The front propagation velocities resulting from this analysis are presented in table 4.2 for different sample temperatures.

In addition, the data given in table 4.2 were fitted to Luther's equation [189, 190], which approximately describes the temperature dependence of the propagation velocity  $v(T)$  of a reaction-diffusion front in homogeneous media:

$$v(T) = a\sqrt{k(T)D(T)}, \quad (4.3)$$

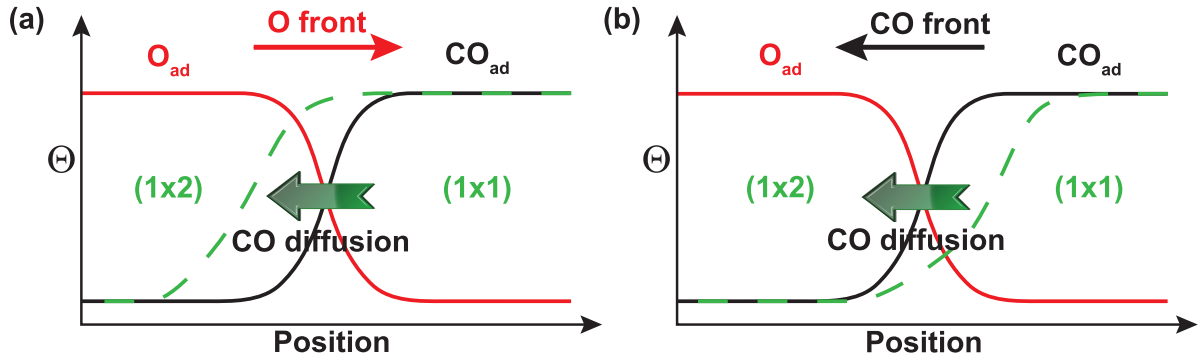
---

<sup>1</sup><http://rsbweb.nih.gov/ij/>

**Table 4.2:** Reaction-diffusion front propagation velocities on Pt(110) domains as a function of sample temperature.

Temperature (K)	$v_{[1\bar{1}0]}$ ( $\mu\text{m/s}$ )	$v_{[001]}$ ( $\mu\text{m/s}$ )
417	1.94	1.44
441	2.40	1.58
465	3.65	2.05
489	5.60	3.07

where  $k(T)$  is the apparent (effective) first-order reaction rate constant of the surface reaction ( $\text{CO}_{\text{ad}} + \text{O}_{\text{ad}} \rightarrow \text{CO}_2$ ) and  $D(T)$  is the diffusion coefficient of the most mobile species (i.e.,  $\text{CO}_{\text{ad}}$ , as the migration of adsorbed oxygen can be neglected under the experimental conditions; cf. section 3.4) at a given temperature  $T$ . Luther's equation can be deduced as a solution of the differential equations that include reaction/diffusion coupling (e.g., Fisher's equation [191]) and fits the experimental data well, as has been shown in the past for CO fronts in the  $[1\bar{1}0]$  direction on a Pt(110) single crystal [119].


**Figure 4.15:** Qualitative scheme of reaction-diffusion front propagation. (a) Oxygen fronts, (b) CO fronts. A detailed description is given in the text. Based on a similar figure in Ref. [192]

The equation was applied to both velocity components  $v_{[1\bar{1}0]}$  and  $v_{[001]}$  of the oxygen reaction-diffusion front on a  $\sim 100 \mu\text{m}$  wide Pt(110) domain (cf. Fig. 4.14). The values given in Refs. [120] (diffusion) and [50, 134] (reaction) were used for the parameters of reaction and CO diffusion that are also listed in table 4.3. Note that the applied diffusion coefficient and activation energy are those of the unreconstructed Pt(110)-(1 $\times$ 1) surface: as shown schematically in Fig. 4.15(a), this assumption is justified only for the case of *oxygen* reaction-diffusion fronts where the CO coverage is always high enough to prevent the formation of the (1 $\times$ 2) surface reconstruction in the reaction-diffusion zone. Thus, the CO molecules always diffuse on the Pt(110)-(1 $\times$ 1) structure. In contrast (and shown

**Table 4.3:** Diffusion and reaction parameters used for the fit to Luther's equation (equation 4.3).

	Parameter	[1 $\bar{1}$ 0]	[001]
Diffusion	$D_0$ (cm <sup>2</sup> /s) <sup>a</sup>	$5 \times 10^{-3}$	$7 \times 10^{-4}$
	$E_A^{Diff}$ (kcal/mol) <sup>a</sup>	10.0	8.9
Reaction	$k_0$ (s <sup>-1</sup> ) <sup>b</sup>	$3 \times 10^6$	
	$E_A$ (kcal/mol) <sup>c</sup>	8	

<sup>a</sup> Ref. [120]    <sup>b</sup> Ref. [134]    <sup>c</sup> Ref. [50]

in Fig. 4.15(b)), CO reaction-diffusion fronts propagate already partly on reconstructed Pt(110)-(1 $\times$ 2) with, of course, modified diffusion parameters [120, 192].

The resulting fit to Luther's equation, which shows a quantitative agreement with the measured data, is depicted in Fig. 4.16 (dashed lines) together with the measured velocities (squares and circles). The inset shows the ratio of the velocities in [1 $\bar{1}$ 0] and [001] direction: it changes from a value of  $\sim 1.4$  at 417 K to  $\sim 1.8$  at 489 K. The range of 1.4 to 1.8 in the temperature range of 417–489 K is in agreement with the results of Jakubith et al. and Nettesheim et al. (Refs. [119, 188]).

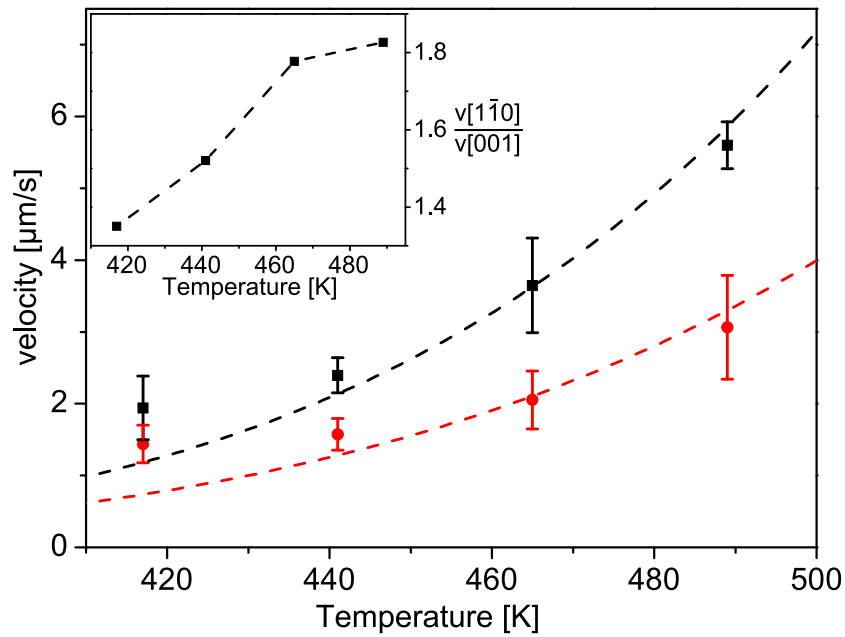


**Figure 4.16:** Front propagation velocities of the elliptical oxygen reaction-diffusion fronts at various temperatures. Velocity in the [1 $\bar{1}$ 0] direction is indicated with black squares, in the [001] direction with red circles. The dashed lines show the fit with Luther's equation (parameters given in table 4.3), and the inset shows the ratio of the velocities as a function of temperature.

## 4.4 Summary and Conclusions

In this chapter, a combined QMS/PEEM investigation of catalytic CO oxidation on polycrystalline platinum foil was presented. Global kinetics was measured *in situ* during the catalytic reaction with QMS, while laterally-resolved kinetics for individual (100), (110) and (111) domains were studied by an intensity analysis of the video-PEEM sequences, which were acquired simultaneously with QMS measurements. The crystallographic orientations of the individual domains were determined with PEEM based on local work function changes upon CO and oxygen adsorption, and the results were later verified with EBSD by analyzing the diffraction patterns of the backscattered electrons. Both global (for the whole polycrystalline Pt foil) and local orientation-specific (for individual domains) kinetic phase diagrams were measured at two different oxygen partial pressures of  $1.3 \times 10^{-5}$  mbar and  $2.7 \times 10^{-5}$  mbar, and the reaction conditions of high activity, low activity and bistability were determined for the three low Miller-index surface terminations Pt(100), Pt(110), Pt(111). The differently oriented domains showed independent reaction behavior, a result that is also corroborated by the observed confinement of the propagating reaction-diffusion fronts within the crystal grains. Thus, the different micrometer-sized domains of a polycrystalline Pt foil represent suitable models for a set of single crystals of different orientations, with the advantage that the processes are studied on all the orientations simultaneously, in one single experiment and under exactly the same conditions.

Based on the PEEM-derived domain-specific kinetic phase diagram, a global phase diagram for catalytic CO oxidation was modeled by summing up the weighted contributions of the (100), (110) and (111) domains. For both applied oxygen pressures, the reconstructed global phase diagrams were in quantitative agreement with the global phase diagram measured experimentally by quadrupole mass spectroscopy, indicating that all relevant catalytic processes of a surface reaction are taken into account by the applied PEEM-video analysis.

Kinetic transitions related to catalytic ignition and extinction during CO oxidation were investigated both in a global (QMS) and a laterally-resolved (PEEM) way. The resulting global and local kinetic phase diagrams correspond one-to-one to those established by the pressure-cycle experiments.

The independent behavior of the differently oriented domains indicates that a synchronization of the surface reaction via adsorbate diffusion or gas phase coupling does not take place under the applied conditions due to the macroscopic size of the domains

#### *4 Experimental study of catalytic CO oxidation on polycrystalline platinum*

(mean size of  $\sim 100\text{ }\mu\text{m}$ ), the presence of grain boundaries and the low total pressure ( $10^{-5}\text{ mbar}$ ).

For Pt(110) domains, elliptic reaction-diffusion fronts were observed that illustrate the anisotropy of the surface diffusion properties. The observed anisotropic propagation of the reaction-diffusion fronts on Pt(110) domains is similar to observations made in earlier studies on Pt(110) single crystal surfaces.

The propagation velocities of the reaction-diffusion fronts along the main crystallographic directions were found to be in quantitative agreement with literature data from single-crystal studies.

## Density functional theory – a (short) introduction

This chapter provides a short introduction to *density functional theory* (DFT), a theoretical framework that has been widely used in solid state physics and materials science to study electronic and structural properties of bulk materials for many years. Nowadays, DFT-based methods are also heavily employed in the field of surface science and catalysis because fast improvements in available computational performance enable to use DFT for calculating extended surface and interface systems with chemical accuracy. WIEN2k,<sup>1</sup> a software package that was used in the present work for the theoretical study on the CeO<sub>2</sub>/Pt(111) interface system (chapter 6), is based on the DFT methodology [11].

The introduction to DFT presented in this chapter is mainly based on introductory texts by Kohanoff [193], Capelle [194] and Cottenier [195].

### 5.1 Schrödinger equation

In order to be able to describe all kinds of matter with quantum-mechanical methods, it is necessary to model them in a very general way, i.e., as a collection of atoms interacting with each other by means of electrostatic forces in the presence or absence of an external field. The *Schrödinger equation*, the equation which successfully describes such quantum-mechanical systems, was named after Erwin Schrödinger,<sup>2</sup> who published it in

---

<sup>1</sup>[www.wien2k.at](http://www.wien2k.at)

<sup>2</sup>Nobel Laureate in Physics 1933.



1926 [196]. In its general form it describes the time-dependency of the *quantum state* of a system and is written as

$$\hat{H}\Psi = i\hbar \frac{\partial \Psi}{\partial t}, \quad (5.1)$$

where  $\hat{H}$  is the *Hamiltonian operator*, i.e., the operator acting on the *wavefunction*  $\Psi$  and corresponding to the *total energy* of the quantum-mechanical system. In principle, the wavefunction  $\Psi$  contains all possible physical information that is available on the investigated quantum-mechanical system because the expectation value  $\langle q \rangle$  of a given physical quantity  $q$  can be calculated from  $\Psi$  by evaluating the following expression:

$$\langle q \rangle = \langle \Psi | \hat{q} | \Psi \rangle = \int \Psi^* \hat{q} \Psi \, d\mathbf{r}, \quad (5.2)$$

where  $\hat{q}$  is the quantum-mechanical operator corresponding to the desired observable  $q$ . In the same way,  $\hat{H}$  corresponds to the expectation value for the total energy of a quantum system.

In order to describe *stationary* (i.e., time-independent) quantum-mechanical systems, the general Schrödinger equation 5.1 can be simplified and assumes the following stationary form:

$$\hat{H}\Psi = E\Psi, \quad (5.3)$$

with  $E$  being the total energy of the system. In mathematical terms, the total energy  $E$  is thus an *eigenvalue* of the *eigenfunction*  $\Psi$ .

Generally speaking, solving a given quantum-mechanical problem consists of: (i) describing the system through the definition of a Hamiltonian operator  $\hat{H}$ , (ii) solving the Schrödinger equation to obtain the system's wavefunction  $\Psi$  and (iii) calculating expectation values of physical observables by applying operators (like, e.g.,  $\hat{H}$ ) to the many-body wavefunction  $\Psi$  (cf. equation 5.2).

For a quantum many-body system consisting of electrons and nuclei, the full definition of the Hamiltonian operator  $\hat{H}$  is composed of the sum of operators for the kinetic  $\hat{T}$  and potential energies  $\hat{V}$  of the nuclei  $N_a$  (with atomic number  $Z_a$ , position  $\mathbf{R}_a$  and mass  $M_a$ ) and the electrons  $e_i$  (with mass  $m_e$  and position  $\mathbf{r}_i$ ).  $\hat{V}$  splits up into terms for inter-

nuclear ( $\hat{V}_{NN}$ ), electron-electron ( $\hat{V}_{ee}$ ) as well as nuclear-electron interaction ( $\hat{V}_{Ne}$ ). The exact definition of  $\hat{H}$  is written out in its entire form in the following equation:

$$\hat{H} = \underbrace{-\frac{\hbar^2}{2} \sum_a \frac{\nabla_{\mathbf{R}_a}^2}{M_a}}_{\hat{T}_N} \underbrace{-\frac{\hbar^2}{2} \sum_i \frac{\nabla_{\mathbf{r}_i}^2}{m_e}}_{\hat{T}_e} \underbrace{-\frac{1}{4\pi\epsilon_0} \sum_{a,i} \frac{e^2 Z_a}{|\mathbf{R}_a - \mathbf{r}_i|}}_{\hat{V}_{Ne}} + \underbrace{\frac{1}{8\pi\epsilon_0} \sum_{i \neq j} \frac{e^2}{|\mathbf{r}_i - \mathbf{r}_j|}}_{\hat{V}_{ee}} + \underbrace{\frac{1}{8\pi\epsilon_0} \sum_{a \neq b} \frac{e^2 Z_a Z_b}{|\mathbf{R}_a - \mathbf{R}_b|}}_{\hat{V}_{NN}}. \quad (5.4)$$

Unfortunately, the general formulation of  $\hat{H}$ , as given by equation 5.4, allows analytic solutions of the Schrödinger equation only for very simple chemical systems like, e.g., the hydrogen atom or the molecular  $\text{H}_2^+$  ion. For more complex systems (actually, systems consisting of more than *one* electron), only *numerical* or *approximate solutions* are obtainable due to the two-body nature of the Coulomb terms in equation 5.4 that makes a separation of the variables of the individual single-particle equations mathematically impossible. This is known as the *quantum many-body problem*, although many-body problems are not only found in quantum mechanics: they have been known in classical mechanics for many centuries, for example, in the description of planetary movement in the gravitational field of stars. Even in this case, analytical solutions for the interaction of more than three celestial bodies cannot be found.

In consequence, several approximations have to be made to the exact definition of the Hamiltonian in equation 5.4 in order to make calculations of larger systems possible.

### 5.1.1 Approximations to the quantum many-body problem

One simplification commonly applied to  $\hat{H}$  is the so-called *Born-Oppenheimer (BO) approximation* [197]: it states that the movements of the nuclei relative to the electrons can be discarded because the mass of any nucleus is many times larger than the electron mass, and thus the electrons instantaneously follow the motion of the nuclei.<sup>3</sup> If the Born-Oppenheimer approximation is applied to  $\hat{H}$ , the individual nuclei are assumed to be at fixed positions, and, consequently, the first term in equation 5.4 (i.e., the kinetic energy operator  $\hat{T}_N$  of the nuclei) can be completely discarded, and the last term (the op-

<sup>3</sup>Even the nuclear mass of the lightest element hydrogen, which consists of a single proton, is already 1836 times higher than the electron mass  $m_e$ .

erator  $\hat{V}_{NN}$  corresponding to the Coulomb interaction between the nuclei) reduces to a constant.

The BO-approximation considerably reduces the mathematical complexity of the quantum many-body problem because now only the movements of the electrons in an *external* potential  $V_{ext}$  of the nuclei have to be considered. The resulting Hamiltonian  $\hat{H}$  simplifies to the sum of the kinetic energy operator of the electrons  $\hat{T}_e$ , the potential energy operator  $\hat{V}_{ee}$  that represents the repulsive electron-electron Coulomb interaction, and the potential energy operator  $\hat{V}_{ext}$  that consists of the attractive interaction of the electrons with the external potential of the nuclei ( $\hat{V}_{Ne}$ ) as well as the now constant contribution of the repulsive inter-nuclear interaction ( $\hat{V}_{NN}$ ):

$$\hat{H} = \hat{T}_e + \hat{V}_{ee} + \overbrace{\hat{V}_{Ne} + \hat{V}_{NN}}^{\hat{V}_{ext}}. \quad (5.5)$$

An important observation has to be made at this point: both  $\hat{T}_e$  and  $\hat{V}_{ee}$  in equation 5.5 contain only universally defined parameters that just depend on the type of the described quantum system (i.e., electronic, protonic, etc.). In turn, this implies that the term of the operator corresponding to the external potential ( $\hat{V}_{ext}$ ) must include the complete chemical information specific to the investigated system.

## 5.2 Density functional theory

Despite the significant progress made with the introduction of the Born-Oppenheimer approximation, the definition of  $\hat{H}$  in equation 5.5 has to be further simplified in order to be applicable to real systems. Various methods on different levels of approximation have been developed over the years to tackle this problem.

The main idea behind all DFT-based methods is to use the *electronic density*  $\rho(\mathbf{r})$  as the fundamental variable of a given quantum system, whose exact knowledge enables to calculate the total energy (and, consequently, all other desired properties) of the system. A big advantage of DFT over approaches with a comparable level of accuracy (like, for instance, approaches based on the Hartree-Fock method [198, 199]) is a significantly lower computational effort, which makes it applicable for large systems like, e.g., surface or interface structures. On the other hand, DFT suffers from the fact that the correct form of the *exchange-correlation functional* is unknown and no universally applicable approximation for it has been found so far, despite intensive research efforts and substantial improvements in this area.

The following sections provide a short introduction to the mathematical approach that is usually applied in modern DFT calculations.

### 5.2.1 Thomas-Fermi theory

The electron density approach fundamental to DFT was first independently proposed by L.H. Thomas [200] and E. Fermi<sup>4</sup> [201] already in the 1920s, leading to the development of so-called *Thomas-Fermi theory*: the authors proposed an approximation where the total energy of an electronic system is defined as a *functional*  $E_{TF}[\rho(\mathbf{r})]$  of its electronic density  $\rho(\mathbf{r})$ , – without giving a proof whether this definition is physically justified at all. For this purpose, well-known approximations of a *homogeneous electron gas* are used for all energy terms of  $E_{TF}[\rho(\mathbf{r})]$ , which is given by

$$E_{TF}[\rho(\mathbf{r})] = C_k \int \rho(\mathbf{r})^{\frac{5}{3}} d\mathbf{r} + \int \rho(\mathbf{r}) v_{ext}(\mathbf{r}) d\mathbf{r} + \frac{e^2}{2} \iint \frac{\rho(\mathbf{r})\rho(\mathbf{r}')}{|\mathbf{r}-\mathbf{r}'|} d\mathbf{r}d\mathbf{r}' - C_x \int \rho(\mathbf{r})^{\frac{4}{3}} d\mathbf{r} + E_c[\rho(\mathbf{r})], \quad (5.6)$$

where the first term on the right side represents the *kinetic energy*, the second term describes the attractive *Coulomb interaction* between electrons and nuclei, the third term characterizes the repulsive electron-electron Coulomb interaction and the last two terms are the contribution of *exchange* and *correlation* to the total energy, respectively.

Although being a rather crude approximation, Thomas-Fermi theory works quite well for simple metals, especially where the electronic conditions of a homogeneous electron gas are reasonable fulfilled. However, it fails miserably in case of atomic or molecular systems, mainly because the term for the kinetic energy in equation 5.6 is inadequate to describe even fundamental things like (covalent) chemical bonds. Nevertheless, the idea of choosing the electronic density  $\rho(\mathbf{r})$  as the fundamental property of a quantum-mechanical many-particle system was intriguing and eventually lead to the development of modern density functional theory.

### 5.2.2 The theorems of Hohenberg and Kohn

A mathematical justification of Thomas-Fermi theory was given by the work of Hohenberg and Kohn,<sup>5</sup> who proved in 1964 that the external potential  $V_{ext}$  (and thus the total

---

<sup>4</sup>Nobel Laureate in Physics 1938.

<sup>5</sup>Nobel Laureate in Chemistry 1998.

energy; see equation 5.5) of a many-particle system is indeed *uniquely defined* by its (non-degenerate) ground-state electronic density  $\rho(\mathbf{r})$  [202]. This famous proof is now known as the *first theorem of Hohenberg and Kohn*. One remarkable thing about this finding is the fact that the correspondence between ground-state density and external potential works in both ways, i.e., there exists a one-to-one mapping between them: a (non-degenerate) ground-state density uniquely defines the external potential and *vice versa*. Furthermore, the ground-state density  $\rho(\mathbf{r})$  of a system can, in principle, be obtained by minimizing its total energy using the *variational principle* of Rayleigh-Ritz, which states that any density different from the ground-state density also implies a higher total energy of the system. The proof of this principle is now known as the *second theorem of Hohenberg and Kohn* and was also given in Ref. [202]. The total energy functional  $E_{HK}[\rho]$  of the ground-state density  $\rho(\mathbf{r})$  is defined in the following way:

$$\begin{aligned} E_{HK}[\rho] &= \overbrace{\langle \Psi | \hat{T} + \hat{V}_{ee} | \Psi \rangle}^{F_{HK}[\rho]} + \langle \Psi | \hat{V}_{ext} | \Psi \rangle \\ &= F_{HK}[\rho] + \int \rho(\mathbf{r}) V_{ext}(\mathbf{r}) d\mathbf{r}. \end{aligned} \quad (5.7)$$

In the same way as  $\hat{T}$  and  $\hat{V}_{ee}$  are universally defined in equation 5.5, the Hohenberg-Kohn density functional  $F_{HK}[\rho]$  of equation 5.7 is also *universal* to any many-electron system, i.e., it does not contain any information specific to a given system. Unfortunately, the mathematical formulation of  $F_{HK}[\rho]$  and, in particular, the kinetic energy functional  $T[\rho]$  are *unknown*. In order to turn the Hohenberg-Kohn theorems into a useful tool for electronic structure calculations, these problems had to be overcome.

### 5.2.3 Kohn-Sham equations

A way to solve the problems outlined above is a calculation scheme introduced by Kohn and Sham [203]: in this approach (shown schematically in Fig. 5.1) a *real* system of *fully-interacting* electrons is replaced by a *fictitious* reference system of *non-interacting* electrons that possesses the *same* charge density  $\rho(\mathbf{r})$ . This mathematical trick makes it possible to use the exactly known kinetic energy operator  $\hat{T}_0$  of a *non-interacting* electron gas,

$$\hat{T}_0 = -\frac{\hbar^2}{2m_e} \nabla^2, \quad (5.8)$$

instead of the unknown operator  $\hat{T}$  in the formulation of the Hohenberg-Kohn density functional  $F_{HK}[\rho]$  in equation 5.7. This step is justified, as the first theorem of Hohenberg

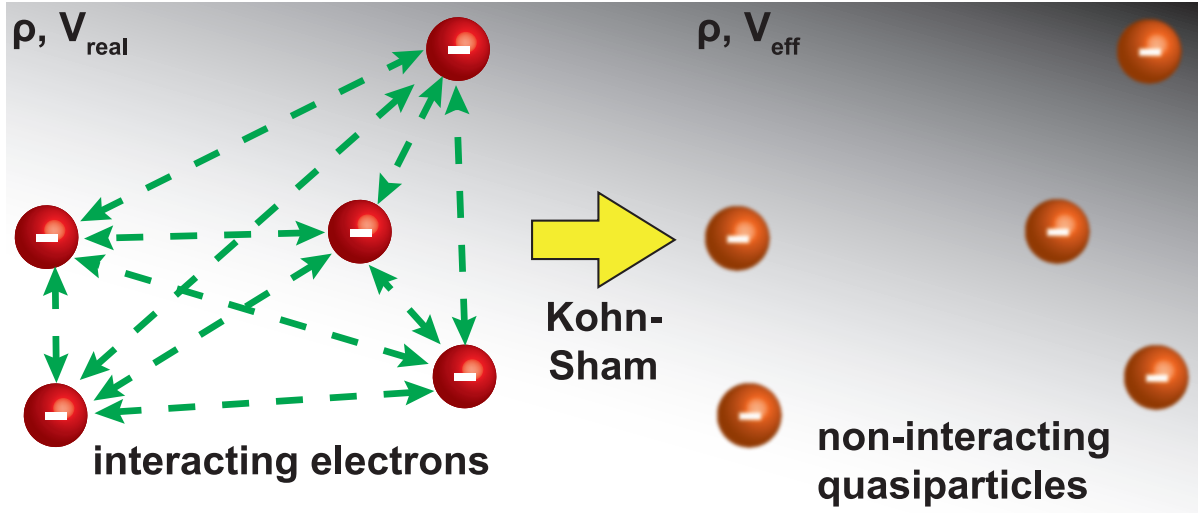


**Figure 5.1:** Scheme of the Kohn-Sham approach to the quantum many-body problem. A real system containing interacting electrons is mapped onto a fictitious system with the same electronic density  $\rho$  that consists of non-interacting quasi-particles moving in an effective potential.

and Kohn guarantees that the resulting external potential  $V_{ext}$  of both systems is the same provided they have the same electronic density.

The total energy functional  $E_{KS}[\rho]$  of the system is thus defined as the sum of the non-interacting kinetic energy functional  $T_0[\rho]$ , the Coulomb interaction of the electrons (the so-called *Hartree term*) as well as the exchange-correlation energy functional  $E_{xc}$ ,<sup>6</sup> which includes *self-interaction correction* and the external potential  $V_{ext}$ :

$$E_{KS}[\rho] = T_0[\rho] + \frac{e^2}{2} \iint \frac{\rho(\mathbf{r})\rho(\mathbf{r}')}{|\mathbf{r} - \mathbf{r}'|} d\mathbf{r} d\mathbf{r}' + E_{xc}[\rho] + \int \rho(\mathbf{r}) V_{ext} d\mathbf{r}. \quad (5.9)$$

Of course, the difference between the kinetic energies of the interacting real system and the non-interacting reference system has to be included as a correction in  $E_{KS}[\rho]$ , which is also done in the functional for the exchange-correlation energy  $E_{xc}[\rho]$ .

The corresponding Kohn-Sham Hamiltonian  $\hat{H}_{KS}$  is defined in the following way:

$$\begin{aligned} \hat{H}_{KS} &= \hat{T}_0 + \hat{V}_H + \hat{V}_{xc} + \hat{V}_{ext} \\ &= -\frac{\hbar^2}{2m_e} \nabla^2 + \underbrace{\frac{e^2}{4\pi\epsilon_0} \int \frac{\rho(\mathbf{r}')}{|\mathbf{r} - \mathbf{r}'|} d\mathbf{r}' + V_{xc} + V_{ext}}_{V_{eff}}. \end{aligned} \quad (5.10)$$

<sup>6</sup>Whereas the exchange contribution can, in principle, be calculated exactly, it is usually approximated together with the correlation energy.

As the particles in the fictitious reference system are by definition *non-interacting*, the many-particle Kohn-Sham wavefunction  $\Psi_{KS}$  can be obtained from a linear-combination of the single-particle wavefunctions  $\psi_i(\mathbf{r})$  that are solutions of the so-called single-particle *Kohn-Sham equations*:

$$\hat{H}_{KS}\psi_i(\mathbf{r}) = \varepsilon_i\psi_i(\mathbf{r}). \quad (5.11)$$

One has to note that the particles described by the Kohn-Sham equations are *not* electrons anymore but *quasi-particles* because of their non-interacting nature. Although the resulting energies  $\varepsilon_i$  are thus physically meaningless, they can be still used as a good estimate for the real energies of the electrons. Finally, the ground-state density  $\rho(\mathbf{r})$  of the system can be obtained by:

$$\rho(\mathbf{r}) = \sum_{i=1}^N \psi_i(\mathbf{r})^* \psi_i(\mathbf{r}). \quad (5.12)$$

This way, the Kohn-Sham equations represent a method to obtain the ground-state density  $\rho(\mathbf{r})$  of a system by solving a set of non-interacting single-particle equations. Unfortunately, as both the Hartree potential  $V_H$  and the exchange-correlation potential  $V_{xc}$  in equation 5.10 depend on the unknown electronic density  $\rho(\mathbf{r})$ , the solution has to be done in a *self-consistent* way, i.e., by performing iterative calculations. For this purpose, one has to provide a starting electron density  $\rho_0(\mathbf{r})$ , from which an initial Kohn-Sham Hamiltonian  $\hat{H}_{KS,0}$  can be set up. After solving the Kohn-Sham equations 5.11 to get  $\psi_{i,0}(\mathbf{r})$ , an improved density  $\rho_1(\mathbf{r})$  can be obtained using equation 5.12. These steps have to be repeated until a self-defined convergence criterion is met.

Furthermore, the Kohn-Sham formalism can also be used to calculate spin-polarized systems by splitting the electronic density into two independent spin densities ( $\rho(\mathbf{r}) = \rho_{\uparrow}(\mathbf{r}) + \rho_{\downarrow}(\mathbf{r})$ ) before solving the Kohn-Sham equations.

### 5.2.4 Exchange-correlation functionals

With the introduction of the Kohn-Sham scheme, the unknown form of  $F_{HK}[\rho]$  was replaced with known or computable quantities, except for one: the correct form of the exchange-correlation functional  $E_{xc}[\rho]$  in equation 5.9 is *not known*. Nevertheless, the Kohn-Sham scheme represents a significant improvement because the contribution (and thus the error!) of exchange and correlation to the total energy is much smaller than that of the kinetic energy, which was the main source of error in Thomas-Fermi theory.

Consequently, major research efforts have been undertaken to find better and better approximations of  $E_{xc}[\rho]$ . In the next sections, a brief overview is given over the two most

widely used types, namely the *local density approximation* (LDA) and the *generalized gradient approximation* (GGA). In addition, there are many more sophisticated types of exchange-correlation functionals available today which, e.g., combine DFT with Hartree-Fock (exact) exchange (so-called *hybrid functionals*) [204–206] or are able to model *non-local effects* such as Van-der-Waals (VdW) interactions properly [207]. However, these functionals are also much more computationally demanding than LDA or GGA and are therefore (still) not applicable to large systems. The WIEN2k software package implements a large number of different exchange-correlation functionals, including LDA, GGA-based and hybrid functionals.

#### 5.2.4.1 Local density approximation (LDA)

The first and most simple approximation of  $E_{xc}[\rho]$  is the so-called *local density approximation* (LDA), where  $E_{xc}[\rho]$  is defined as:

$$E_{xc}^{LDA}[\rho] = \int \rho(\mathbf{r}) \epsilon_{xc}^{hom}(\rho) d\mathbf{r}. \quad (5.13)$$

LDA uses the exchange-correlation energy density  $\epsilon_{xc}^{hom}(\rho)$  of a *homogeneous electron gas* of *equal* local density to describe exchange and correlation. The exchange part of  $\epsilon_{xc}^{hom}(\rho)$  is known exactly, and very accurate numerical approximations exist for the correlation term that were obtained by quantum Monte-Carlo methods [208] and later parameterized [209, 210]. Interestingly, the very first idea of LDA was introduced by Kohn and Sham in the same seminal publication [203] that also introduced the Kohn-Sham equations.

Although LDA seems to be a rather optimistic assumption at first sight, it works surprisingly well and is still widely used for many different systems, especially if the spatial variations of the electron density are small (i.e., if the electron density is similar to a homogeneous electron gas). On the other hand, LDA generally underestimates bond-lengths (a fact that is also called *over-binding*), fails at the description of localized electrons due to their quickly varying density and does not describe hydrogen bonds properly.

#### 5.2.4.2 Generalized gradient approximation (GGA)

In order to correct the inability of LDA to cope with inhomogeneities in the electron density,  $E_{xc}[\rho]$  has to be modified so that it also takes into account the *vicinity* of the density at a given point in space. This can be achieved by adding the *gradient* (or even higher derivatives) of the electron density to the exchange-correlation functional  $E_{xc}[\rho]$ . Exchange-correlation functionals that include a gradient expansion belong to the class of



so-called *generalized gradient approximation* (GGA) functionals and have the following general form:

$$E_{xc}^{GGA}[\rho] = \int \rho(\mathbf{r}) \epsilon_{xc}(\rho(\mathbf{r}), \nabla \rho(\mathbf{r})) d\mathbf{r}. \quad (5.14)$$

In contrast to LDA, where only one definition of the functional exists, there is no uniquely defined form of the gradient dependent term in equation 5.14. In consequence, many different GGA functionals have been proposed in literature over the years [211–214]. All of them have different strengths or weaknesses and some have even been fitted to experimental data, which means that these functionals cannot be considered purely *ab initio* anymore. At the moment, the most frequently used GGA functional is still *PBE*, which was proposed by Perdew, Burke and Ernzerhof in 1996 [215].

#### 5.2.4.3 Strongly correlated systems – LDA/GGA+U

Common LDA or GGA functionals fail to properly reproduce the strongly localized (correlated) d or f electrons of compounds such as transition metal and rare earth oxides (like, e.g.,  $\text{CeO}_2$ , cf. chapter 6). For instance, both LDA and GGA wrongly predict *metallic behavior* for insulators such as  $\text{CoO}$  or  $\text{FeO}$ . In order to correct the result of DFT calculations in such cases, an effective Coulomb potential (usually named *Hubbard U* [216–218]) can be added to the chosen exchange-correlation functional  $E_{xc}[\rho]$  (be it LDA or GGA-based) to describe the strong on-site repulsion of these localized electrons in the following way [219]:

$$E_{xc}^{F+U}[\rho] = E_{xc}^F[\rho] + \overbrace{\frac{U}{2} \sum_{i \neq j} n_i n_j}^{E^{ee}} - \overbrace{\frac{1}{2} U N(N-1)}^{E^{DC}} \quad (\text{with } F = \text{LDA/GGA}), \quad (5.15)$$

where  $n_i$  are the orbital occupancies and  $N = \sum_i n_i$ . This means that  $E_{xc}^{F+U}[\rho]$  consists of the exchange-correlation energy functional of LDA or GGA with the addition of a term representing the Coulomb interaction of the localized (d and f) electrons  $E^{ee}$  in a *mean-field approximation*. As the electron-electron interaction of all (localized and delocalized) electrons has already been taken into account in  $E_{xc}^F[\rho]$ , a double counting correction ( $E^{DC}$ ) has to be subtracted from  $E_{xc}^{F+U}[\rho]$ . If an electron is in such a strongly localized state,  $U$  can be best described as the potential energy cost of placing a second electron into this state.

Applying LDA/GGA+U to a calculation leads to a splitting of the orbital energies  $\epsilon_i$  compared to LDA/GGA:

$$\epsilon_i = \frac{\partial E_{xc}^{F+U}}{\partial n_i} = \epsilon_F + U\left(\frac{1}{2} - n_i\right) \quad (\text{with } F = \text{LDA/GGA}), \quad (5.16)$$

which means that occupied orbitals ( $n_i = 1$ ) are shifted *downwards* in energy by a value of  $-U/2$  and unoccupied orbitals ( $n_i = 0$ ) are shifted *upwards* by  $+U/2$ .

In principle, the size of  $U$  appropriate for a given system, which is usually in the range of a few electronvolts, can be either calculated by variation of the orbital occupation [220, 221] or determined empirically by fitting it to experimental data.

### 5.2.5 Basis sets

In order to solve the actual problem with DFT, that is, finding the wavefunction  $\Psi$  that describes a given quantum system, a mathematical representation has to be chosen for the single-particle wavefunctions  $\psi_i$  of equation 5.11. For this purpose, the wavefunctions are usually expanded in a *basis set*  $b$ , where each  $\psi_i$  is expressed by a linear combination of  $N$  *basis functions*  $\phi_n^b$  as defined by equation 5.17:

$$\psi_i = \sum_{n=1}^N c_n^i \phi_n^b. \quad (5.17)$$

If equation 5.17 is substituted in the Kohn-Sham equation 5.11, an *eigenvalue problem* is obtained, whose solution yields the *expansion coefficients*  $c_n^i$  that constitute the wavefunction  $\psi_i$  for each particle. In order to keep the accuracy of the calculation and the computational demand balanced, a reasonable cut-off value has to be chosen for the total number of basis functions  $N$  that form the basis set  $b$ .

To obtain an efficient basis set, the utilized basis functions should be as similar to the (unknown) wavefunctions  $\psi_i$  as possible, so that only a few of them are needed for an accurate description. On the other hand, the basis functions should still be general enough to describe all possible quantum systems equally well. As these requirements are nearly impossible to meet simultaneously, many different types of basis functions  $\phi_n^b$  have been proposed over the years. Some of the most common are, e.g., Gaussian- [222] or Slater-type [223, 224] orbitals for molecular systems, and plane waves (PW) [225] or projector augmented waves (PAW) [226] for periodic systems. As it was the case for the exchange-correlation functional, no basis set works universally well for all types of compounds. To

overcome the difficulties in describing the wavefunction with only one type of basis function, *mixed basis sets* were introduced that consist of a combination of two (or more) different basis functions. WIEN2k implements such a mixed-basis set, which is described in more detail in the next section.

### 5.2.5.1 The basis set of WIEN2k

The WIEN2k software implements an *all-electron full-potential* DFT scheme (including relativistic effects), which means that no shape approximation is made to the form of the potential and all electrons are simulated in the real potential of the nuclei, in contrast to methods based on *pseudopotentials* and “frozen” core electrons [227, 228]. A more detailed description of the methodology of WIEN2k is given in Ref. [229].

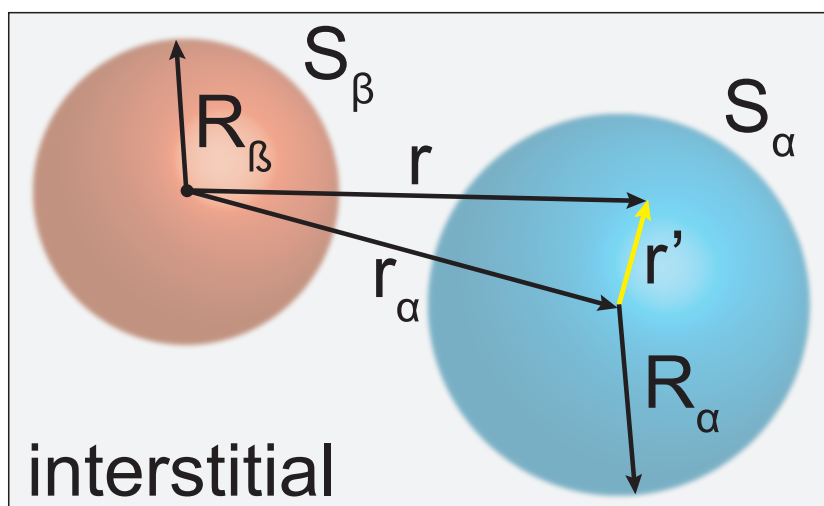


**Figure 5.2:** Scheme of an augmented basis set. The unit cell is divided into (i) spheres  $S_\alpha$  around each atom  $\alpha$  with a corresponding atom-specific radius  $R_\alpha$  and (ii) the interstitial region. The two regions are treated differently in the basis set. The origin of the coordinate system is indicated with a circle in the plot. Based on a similar figure in [195].

The basis set of WIEN2k belongs to the group of *augmented basis sets*, which are among the most accurate types of basis sets available today. Figure 5.2 illustrates the general scheme of such an augmented basis set: the volume of the unit cell is divided into two types of regions, namely (i) *non-overlapping spheres*  $S_\alpha$  around each atom  $\alpha$  defined by an atom-specific cut-off radius  $R_\alpha$  and (ii) a region called *interstitial* in between the atomic spheres. The basis functions are defined differently in the two regions and matched at the border of the spheres to ensure continuity. This approach enables choosing the best-suited basis functions for describing the wavefunction in both regions because, e.g., an

approach based solely on plane waves may be well suited for modeling the smooth wave-function in the interstitial region, but fails at describing the steep variations of the wave-function near the nuclei.

The most prominent members of the group of augmented basis sets are Slater's original *augmented plane wave* (APW) method [230] and the *linear augmented plane wave* (LAPW) method introduced by Andersen [231]. WIEN2k uses a combination of the LAPW and the APW basis sets but adds *local orbitals* in both cases to further improve linearization and convergence [232,233]. In consequence, the full name of the basis set of WIEN2k is LAPW+LO/APW+lo.

### 5.2.5.1.1 LAPW+LO

For an atom  $\alpha$  in an atomic sphere  $S_\alpha$  the LAPW+LO basis functions  $\phi_{\mathbf{K}}^{\mathbf{k}}(\mathbf{r})$  are defined in the following way:

$$\phi_{\mathbf{K}}^{\mathbf{k}}(\mathbf{r}) = \begin{cases} \sum_{l,m} \left[ A_{lm}^{\alpha,\mathbf{k}+\mathbf{K}} u_l^\alpha(\mathbf{r}', \varepsilon_{1,l}^\alpha) + B_{lm}^{\alpha,\mathbf{K}+\mathbf{k}} \dot{u}_l^\alpha(\mathbf{r}', \varepsilon_{1,l}^\alpha) \right] Y_{lm}(\hat{\mathbf{r}}') & \mathbf{r} \in S_\alpha \\ \frac{1}{\sqrt{\Omega}} e^{i(\mathbf{k}+\mathbf{K}) \cdot \mathbf{r}} & \mathbf{r} \in \text{interstitial}, \end{cases} \quad (5.18)$$

where  $\mathbf{K}$  are the reciprocal lattice vectors,  $\mathbf{k}$  is the wave vector inside the first Brillouin zone, and  $\Omega$  is the volume of the unit cell. The vector  $\mathbf{r}'$  is defined as  $\mathbf{r}' = \mathbf{r} - \mathbf{r}_\alpha$ , i.e., the position is given with respect to the center of each atomic sphere  $S_\alpha$ . Within  $S_\alpha$  (top line in equation 5.18) the basis functions are atomic functions (in the case of the LAPW basis set, regular solutions of the radial Schrödinger equation  $u_l^\alpha$  times spherical harmonics  $Y_{lm}$  are used), whereas in the interstitial region (bottom line in equation 5.18)  $\phi_{\mathbf{K}}^{\mathbf{k}}(\mathbf{r})$  is made up of plane waves. In contrast to the original APW method,  $u_l^\alpha$  is not energy-dependent in LAPW anymore, thanks to a Taylor series linearization around a fixed reference energy  $\varepsilon_{1,l}$ . The unknown coefficients  $A_{lm}$  and  $B_{lm}$  in equation 5.18 are determined by matching the basis functions at the border of the atomic spheres in (i) value and (ii) slope. The cut-off value of the basis set is the product  $R_{MT_{min}} K_{max}$ , which is the product of the smallest atomic sphere radius in the unit cell times the magnitude of the largest reciprocal lattice vector. It should be noted that LAPW requires a larger  $R_{MT_{min}} K_{max}$  than APW because of the additional constrain to match value *and* slope.

To improve upon the description of semi-core states with LAPW,<sup>7</sup> local orbitals are added to the original LAPW basis set that include a second reference energy  $\varepsilon_{2,l}$  and are defined as:

$$\phi_{lm}^{\alpha,LO}(\mathbf{r}) = \begin{cases} \left[ A_{lm}^{\alpha,LO} u_l^\alpha(\mathbf{r}', \varepsilon_{1,l}^\alpha) + B_{lm}^{\alpha,LO} \dot{u}_l^\alpha(\mathbf{r}', \varepsilon_{1,l}^\alpha) + C_{lm}^{\alpha,LO} u_l^\alpha(\mathbf{r}', \varepsilon_{2,l}^\alpha) \right] Y_{lm}(\hat{\mathbf{r}}') & \mathbf{r} \in S_\alpha \\ 0 & \mathbf{r} \notin S_\alpha. \end{cases} \quad (5.19)$$

By definition, a local orbital  $\phi_{lm}^{\alpha,LO}(\mathbf{r})$  is *zero* in the interstitial region and in atomic spheres different from  $S_\alpha$ . The coefficients  $A_{lm}$ ,  $B_{lm}$  and  $C_{lm}$  are determined by the conditions of (i) *normalization*, (ii) *zero value* and (iii) *zero slope* of  $\phi_{lm}^{\alpha,LO}(\mathbf{r})$  at the boundary of the atomic sphere  $S_\alpha$ . The addition of local orbitals slightly increases the size of the basis set and therefore the computational effort needed, but also greatly improves the accuracy of the basis set.

#### 5.2.5.1.2 APW+lo

The APW+lo basis set combines the advantages of LAPW and APW: its size is smaller than the LAPW basis set and the energy dependence of  $u_l^\alpha$ , which is the main drawback of Slater's original APW method, is removed by adding local orbitals (here abbreviated *lo* to distinguish them from the *LO* local orbitals of LAPW+LO). The APW+lo basis functions  $\phi_{\mathbf{K}}^{\mathbf{k}}(\mathbf{r})$  are defined by the following expression:

$$\phi_{\mathbf{K}}^{\mathbf{k}}(\mathbf{r}) = \begin{cases} \sum_{l,m} A_{lm}^{\alpha,\mathbf{k}+\mathbf{K}} u_l^\alpha(\mathbf{r}', \varepsilon_{1,l}^\alpha) Y_{lm}(\hat{\mathbf{r}}') & \mathbf{r} \in S_\alpha \\ \frac{1}{\sqrt{\Omega}} e^{i(\mathbf{k}+\mathbf{K}) \cdot \mathbf{r}} & \mathbf{r} \in \text{interstitial.} \end{cases} \quad (5.20)$$

To remove the inaccuracy introduced by using fixed energies  $\varepsilon_{1,l}^\alpha$  in equation 5.20, local orbitals (lo) are added to the basis set that are defined as:

$$\phi_{lm}^{\alpha,lo}(\mathbf{r}) = \begin{cases} \left[ A_{lm}^{\alpha,lo} u_l^\alpha(\mathbf{r}', \varepsilon_{1,l}^\alpha) + B_{lm}^{\alpha,lo} \dot{u}_l^\alpha(\mathbf{r}', \varepsilon_{1,l}^\alpha) \right] Y_{lm}(\hat{\mathbf{r}}') & \mathbf{r} \in S_\alpha \\ 0 & \mathbf{r} \notin S_\alpha. \end{cases} \quad (5.21)$$

Again, the coefficients  $A_{lm}$  and  $B_{lm}$  can be determined by the atomic sphere boundary conditions of (i) *normalization* and (ii) *zero value*.

WIEN2k uses both basis sets described above and chooses the appropriate one depending on the type of the individual atoms in the unit cell: APW+lo is used for hard-

<sup>7</sup>In some cases like, e.g., Ti 3p and 4p, one reference energy  $\varepsilon_{l,1}$  per quantum number  $l$  is not sufficient for the description of two such different energy states.

to-converge transition metal atoms with valence d- and f-states and for atoms with very small atomic spheres, whereas LAPW+LO is applied for all other cases because the size of the LAPW+LO basis set at the same cut-off value  $R_{MT_{min}} K_{max}$  is smaller than for APW+lo [234,235].

## DFT calculations on the $\text{CeO}_2/\text{Pt}(111)$ interface

In this chapter, a theoretical study on the  $\text{CeO}_2/\text{Pt}(111)$  interface using *density functional theory* (DFT) is presented. Ceria ( $\text{CeO}_2$ ) is a very important material in heterogeneous catalysis that is commonly used as an *additive* to catalytically active compounds. The DFT investigation was focused on the case of a *single-layer* of  $\text{CeO}_2$  on the  $\text{Pt}(111)$  surface because this model system has already been extensively characterized in several surface-science studies, but has never been studied theoretically so far. The results of the present calculations have been published in Ref. [236].

First, an introduction to the importance of  $\text{CeO}_2$  in catalysis will be given in section 6.1, and the structure of the model system will be described in section 6.2. The calculation parameters and geometrical details of the DFT study will be given in sections 6.3 and 6.4, respectively. Finally, the results of the calculations are detailed in section 6.5, and a summary to the findings is given in section 6.6.

### 6.1 The importance of $\text{CeO}_2$ for heterogeneous catalysis

Ceria belongs to the class of *reducible oxides*, which are oxidic materials that show easy oxidation-reduction capabilities under reaction conditions. In the case of ceria, the switch between the Ce oxidation state of +III and +IV provides a possibility to *store* and *release* oxygen in a controlled way during reactions. This makes ceria very useful, e.g., as an additive to catalytic converters in automobiles because it allows to compensate transient deviations from the ideal air-to-fuel ratio, which frequently occur during exhaust gas conver-

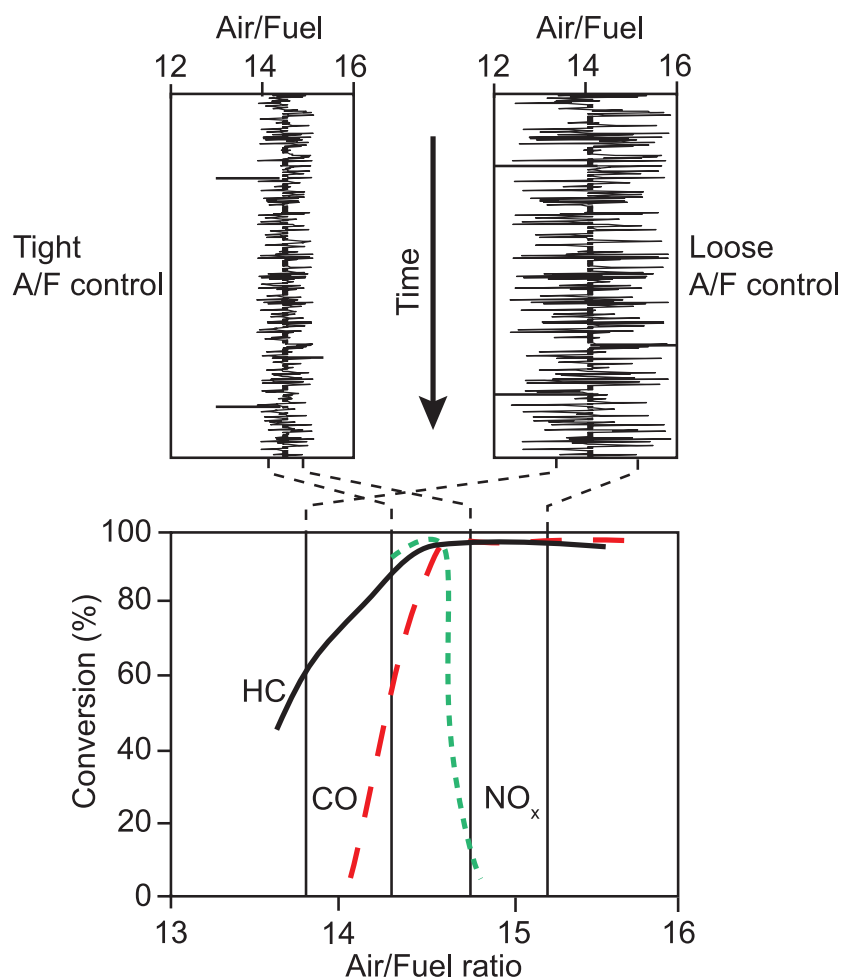


**Figure 6.1:** Relationship between air-to-fuel ratio and three-way catalyst efficiency. Adapted from a similar figure in [3].

sion in *three-way catalysts* (TWC) [237,238]. The problem is illustrated in Fig. 6.1, which is adapted from [3]: because a modern TWC is used to convert CO,  $\text{NO}_x$  and hydrocarbons (HC) into  $\text{CO}_2$ ,  $\text{N}_2$  and  $\text{H}_2\text{O}$  at the same time, optimum performance can only be achieved by controlling the air-to-fuel ratio (A/F) within a tight range. Such a precision of control cannot be solely accomplished with electronic injection systems but only in combination with some sort of additional “chemical control”. Such a control can be achieved via addition of  $\text{CeO}_2$  as a *catalytic promoter* to the TWC. Today, most of the TWCs contain ceria (sometimes in combination with zirconia ( $\text{ZrO}_2$ )).

Besides being widely used in catalytic converters, successful usages of ceria as a catalyst have been reported in literature for the water-gas shift reaction [239]. Furthermore,



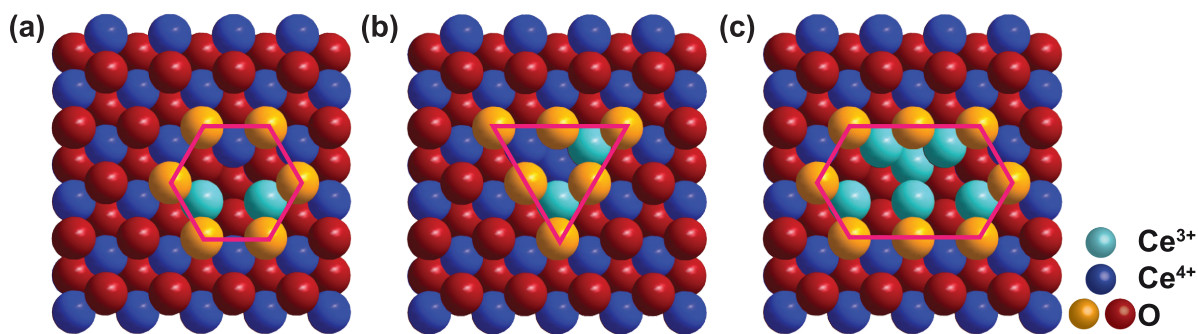


**Figure 6.2:** Oxygen vacancy structures on ceria surfaces shown for the case of  $\text{CeO}_2(111)$ . (a) Single surface vacancy. (b) Single subsurface vacancy. (c) Oxygen vacancy trimer. The oxygen vacancy structure is indicated with a pink line, the oxygen atoms at the rim are colored yellow and the reduced  $\text{Ce}^{3+}$  ions are indicated with a lighter blue color. Based on similar figures in [241].

(doped) ceria shows a very high oxygen ion conductivity, which can, e.g., be utilized in fuel cell electrodes [240].

Although ceria has been known as a promoter in catalytic processes for many years, the underlying mechanism of the promoting effect is much more than just a simple redox phenomenon and is still not fully understood yet. Experimental studies indicate that the highly mobile lattice oxygen of ceria provides both, oxygen supply and promotion of noble metal activity [241]. In turn, these features are dependent on the nucleation and formation of *oxygen vacancies* in the *surface* and *subsurface* layer of ceria and the accompanied formation of  $\text{Ce}^{3+}$  ions. Figure 6.2 shows three ball models of these oxygen vacancy structures on ceria surfaces that were experimentally observed with scanning tunneling microscopy (STM) and published in Ref. [241].

Recently, extensive experimental work has been performed on the performance of the  $\text{CeO}_2/\text{Pt}(111)$  system in catalytic CO oxidation using surface-science techniques under UHV conditions [146, 242]. These studies showed that the presence of ceria shifts the *kinetic phase diagram* (cf. section 3.5.2.2) for CO oxidation on Pt(111) toward *higher* CO partial pressures (in other words: the platinum surface deactivates only at a higher  $p_{\text{CO}}/p_{\text{O}_2}$ -ratio). Thus, ceria is able to *promote* the catalytic activity of platinum in catalytic CO oxidation, a finding that was also observed in experiments on the  $\text{CeO}_x/\text{Cu}(111)$  system [243]: whereas clean Cu(111) is not very active in catalytic CO oxidation, adsorption of ceria nanoparticles on the copper surface drastically increases the *turnover frequency* (TOF) in this reaction to values comparable to those of clean platinum or palladium surfaces. A possible explanation for this behavior was proposed in Ref. [146], which is based on the so-called “active border” concept: it states that the electron density of the surface

metal atoms is altered in the *vicinity* (read: near the border-line) of the nanometer-sized  $\text{CeO}_x$  islands adsorbed on the metal surface. The altered electronic structure leads to a *local* change of the *sticking coefficient* of oxygen at the border of the ceria islands, which then changes the *global* catalytic behavior of the whole system depending on the number of ceria islands. If the catalytic activity is normalized to the still exposed (bare)  $\text{Pt}(111)$  surface area, a significant *increase* in catalytic activity is detected with growing coverage of ceria. This result indicates that the enhanced catalytic activity can be directly correlated to the total perimeter of the ceria islands on the platinum surface and, in combination with the changed electronic structure, this suggests that the enlarged catalytic activity can be attributed to a *spillover* of oxygen from the electronically altered  $\text{CeO}_2$ -Pt border region to the unmodified rest of the exposed platinum surface.

Inspired by these experimental results, a theoretical investigation of the properties of this interface system was undertaken in the present work. To the author's knowledge, no such study has been performed so far: although Alfredsson and Catlow examined *single layers* of Pt and Pd on top of  $\text{CeO}_2(111)$  and  $\text{ZrO}_2(111)$  surfaces [244], the authors used a rather *unrealistic 1 : 1 matching* of the lattice constants of oxide and metal in each individual case. Yang and coworkers investigated systems where a *single Pt atom* is deposited on top of a  $\text{CeO}_2(111)$  surface [245]. This helps to elucidate the changes on the electronic structure during adsorption but does not resemble the adsorption geometry properly. Similar studies were reported by Yang et al. [246] and Wilson and coworkers [247] on  $\text{Pd}/\text{CeO}_2(111)$  and by Lu and Yang on various *noble metal clusters* adsorbed on  $\text{CeO}_2(111)$  [248]. In addition, DFT calculations were performed dealing with the adsorption behavior of CO on ceria-supported Pt clusters [249, 250].

## 6.2 The structure of the $\text{CeO}_2/\text{Pt}(111)$ interface

In the following section, the structures of bulk ceria, the  $\text{CeO}_2(111)$  surface and the resulting  $\text{CeO}_2/\text{Pt}(111)$  interface system after adsorption are described in more detail.

### 6.2.1 Structure of bulk $\text{CeO}_2$

Bulk ceria crystallizes in the cubic *fluorite* structure type (space group:  $\text{Fm}\bar{3}\text{m}$ ) with an experimental lattice constant of 5.41 Å [251]. The unit cell of the crystal structure is shown in Fig. 6.3(a). The fluorite structure type bears its name after the mineral  $\text{CaF}_2$  (trivial

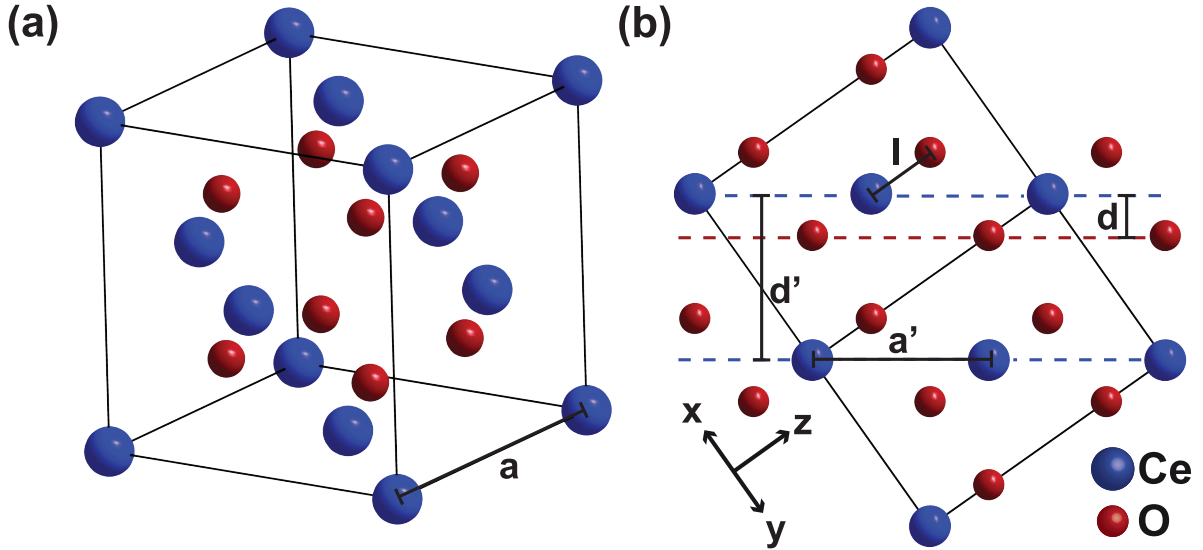


**Figure 6.3:** Structure of bulk ceria. (a) Crystallographic unit cell of bulk  $\text{CeO}_2$ . Cerium atoms are plotted in blue, oxygen atoms in red color. (b) View of the (110)-plane of bulk ceria. The distances  $a'$ ,  $l$ ,  $d$  and  $d'$  indicated in the plot are explained in the text.

name: *fluospar*) and is very commonly found for crystalline materials having an  $\text{AX}_2$ -type stoichiometry.

The structure of ceria is made up of a face-centered cubic (*fcc*) lattice of cerium atoms, whose *tetrahedral sites* are completely occupied by oxygen atoms. Thus, in a *stoichiometric*  $\text{CeO}_2$  crystal, each cerium atom is in the oxidation state of +IV and is *eightfold coordinated* by oxygen atoms in a *cubic* coordination geometry, whereas each oxygen is in the oxidation state of –II and *tetrahedrally* coordinated by *four* cerium atoms. However, one has to note that oxygen vacancies and defect sites are very common in ceria due to its easy oxidation-reduction capabilities, a fact that was already mentioned in section 6.1 [241, 252–254]. Consequently, the tendency to form defects and oxygen vacancies is even more pronounced at surfaces of ceria and can be interpreted as a way to minimize the surface energy  $\gamma_{(hkl)}$ .

### 6.2.2 Structures of the $\text{CeO}_2(111)$ surface and the $\text{CeO}_2/\text{Pt}(111)$ interface

If the bulk  $\text{CeO}_2$  crystal structure described in the previous section is cut along the (111)-plane, the thinnest resulting surface slab that is compatible with both stoichiometry and electrostatics is built up by *three* inequivalent atom types. It consists of *one* layer of cerium atoms and *two* layers of oxygen atoms that together form an O-Ce-O trilayer sand-

wich where one layer of oxygen atoms is positioned *above* and one *below* the plane of cerium atoms. The lattice constant  $a'$  of such a (111)-oriented hexagonal surface slab is given by the formula  $a' = a/\sqrt{2} = 3.83 \text{ \AA}$ , with  $a$  being the lattice constant of bulk CeO<sub>2</sub> (i.e.,  $5.41 \text{ \AA}$ ). The length  $l$  of the Ce-O bonds is given by  $l = a\sqrt{3}/4 = 2.34 \text{ \AA}$ , and the lattice spacing  $d$  between the oxygen and cerium planes is  $d = a\sqrt{3}/12 = 0.78 \text{ \AA}$ . Therefore, the distance  $d'$  between two equivalent (111)-planes of oxygen or cerium atoms amounts to  $d' = 4d = a/\sqrt{3} = 3.12 \text{ \AA}$ , which is also the smallest possible *step height* found in experiments when investigating adlayers of ceria. For a better understanding, the distances described above are also indicated in Fig. 6.3(b), which shows a ball model of the (110)-plane of the ceria unit cell.

It has been shown in several experimental studies that, despite the tendency of ceria surfaces to create defects and vacancies, it is possible to deposit *homogeneous* (ultra-)thin CeO<sub>2</sub> films (i.e., films with a coverage of less than one monolayer) on different noble metal surfaces such as *single crystals* of Au(111) [255], Cu(111) [256, 257], Ni(111) [258], Rh(111) [258, 259], Pd(111) [260] and Pt(111) [146, 242, 261–266]. Although only some of the cited studies succeeded in producing *closed* single-layer films because of the *Volmer-Weber* (island) growth mode [267] commonly found for ceria adlayers [266], in all cases at least large and flat ceria islands (i.e., islands with a mean size of up to several hundred nanometers and a height of a few monolayers of CeO<sub>2</sub>) were found.

The deposited CeO<sub>2</sub> islands are (111)-oriented, which is known to be the most stable surface orientation of ceria [268], and have a height of  $n \times d' = n \times 3.12 \text{ \AA}$  (with  $n$  being the number of atomic layers). Another common feature found in experimental studies is the *oxygen termination* of the islands, although in most cases these oxide layers are very prone to vacancy and defect formation, topics that were not considered in this study.

In conclusion, the experimental findings indicate that the deposited ceria islands consist of one or a few (111)-oriented O-Ce-O trilayer sandwiches deposited on the noble metal surface.

Unfortunately, a relatively large mismatch exists between the lattice constants of [111]-oriented CeO<sub>2</sub> ( $3.83 \text{ \AA}$ ) and Pt(111) ( $2.80 \text{ \AA}$ ), which results in an *incommensurate* lattice constant ratio of  $a_{\text{CeO}_2}/a_{\text{Pt}} = 1.37$ . Therefore, no 1 : 1 matching of the two different structures is observed in experiments: either a  $(4 \times 4)$  [261] or a  $(1.4 \times 1.4)$  [262, 265] *low energy electron diffraction* (LEED) pattern has been found instead, corresponding to a *commensurate* 3 : 4 (lattice constant ratio of 1.33) or 5 : 7 (ratio of 1.40) matching of the ceria and platinum lattices, respectively. In comparison, the smaller lattice mismatch in the

case of the  $\text{CeO}_2/\text{Cu}(111)$  system leads to a  $(1.5 \times 1.5)$  periodicity or a simpler 2 : 3 lattice matching [256, 257].

From this follows that a  $3 \times 3$  ( $5 \times 5$  in case of the  $(1.4 \times 1.4)$  structure) supercell of  $[111]$ -oriented  $\text{CeO}_2$  matches a  $4 \times 4$  ( $7 \times 7$ ) supercell of  $\text{Pt}(111)$  with a small adaption of the ceria lattice constant: the former “4:4” superstructure implies a contraction of the  $\text{CeO}_2(111)$  lattice constant by  $\sim 3\%$  to  $3.73 \text{ \AA}$ , while the ceria lattice gets expanded by  $\sim 2\%$  to  $3.92 \text{ \AA}$  upon forming the latter “5:7” geometry. Thus, in the following sections the  $(4 \times 4)$  and  $(1.4 \times 1.4)$  are referred to as “3:4” and “5:7”, respectively because, in the author’s opinion, this nomenclature describes the lattice matching more clearly.

### 6.3 Computational details of the DFT calculations

All calculations in this study were performed using the WIEN2k software package [11]. As already mentioned, this *ab-initio*<sup>1</sup> software package is based on density functional theory (DFT) and has implemented the *full-potential APW+lo/LAPW+LO method* [232, 233] (see chapter 5 for a short introduction to these topics), one of the most accurate calculation schemes available at the time of this writing. Furthermore, it offers the possibility to use a variety of different *exchange-correlation potentials* [229].

All calculations of the “3:4” structure were performed in  $k$ -point parallel mode on a number of Linux workstation computers, each equipped with a quad-core *central processing unit* (CPU) and 4 gigabytes of *random access memory* (RAM). In contrast, all calculations of the computationally more demanding “5:7” structure were performed on several nodes of the *Vienna Scientific Cluster*<sup>2</sup> (VSC) with fine-grained parallelization using the *message passing interface* (MPI). The following main parameters were chosen and set constant for all calculations: all calculations were performed in *spin-polarized* mode; the plane-wave cut-off  $R_{MT_{min}} K_{max}$  of the APW+lo/LAPW+LO basis set, which is defined by the product of the smallest atomic sphere radius times the magnitude of the largest reciprocal lattice vector, was set to 5.0 and a  $G_{MAX}$  value (i.e., the magnitude of the largest vector in the charge density Fourier expansion) of  $12 \text{ bohr}^{-1}$  was used. A number of 1500 (4685) *local orbitals* (LO/lo; cf. section 5.2.5.1) were added for an accurate description of lower lying s, p and d semi-core states of the “3:4” (“5:7”) structure. The energetic separation between core and valence region was defined so that the Pt 5p, 5d and 6s, the

<sup>1</sup>This term means that no semi-empirical parameters, tailor-made pseudopotentials or other atom-specific assumptions are needed to perform calculations.

<sup>2</sup><http://vsc.ac.at>

Ce 5s, 5p, 5d, 4f, 6s and the O 2s and 2p states were treated as *valence states* in all the calculations. The atomic sphere radii  $R_{MT}$ , which define the region around each atom in the APW+lo/LAPW+LO basis set where the wavefunction is composed of atomic functions (see section 5.2.5.1), were set to 2.15 bohr (1.14 Å) for Pt, 2.35 bohr (1.24 Å) for Ce and 1.60 bohr (0.85 Å) for oxygen. The number of  $k$ -points in the unit cell (that is, the number of points in *reciprocal space* where the eigenvalues are computed) was set to 49 ( $7 \times 7 \times 1$ ) for the “3:4” structure and 9 ( $3 \times 3 \times 1$ ) for the “5:7” structure. After applying symmetry operations, this results in 16 and 4  $k$ -points in the irreducible wedge of the *Brillouin zone* (IBZ, the highest symmetry cell in reciprocal space), respectively. The Brillouin zone integration was done using a temperature broadening of 0.068 eV, in order to ease the convergence of the calculations. The *generalized gradient approximation* (GGA) in the implementation of Perdew, Burke and Ernzerhof (PBE) [215], which is the most commonly used GGA functional (see section 5.2.4 for details), was used to describe electron exchange and correlation. The GGA+U exchange-correlation scheme was employed by adding an effective Hubbard parameter [217, 219]  $U_{eff} = U - J$  of 5 eV (using the standard *double counting correction*) to account for the strong on-site Coulomb interaction of the Ce 4f orbitals. The size of  $U_{eff}$  was chosen in accordance with earlier theoretical work by Nolan and coworkers [269, 270], who found that with  $U_{eff} \geq 5$  eV the electronic structure of  $\text{CeO}_2$  was essentially converged with respect to localization. The geometry optimizations were performed (using either a quasi-Newton or a steepest-descent algorithm) until the size of the forces on all atoms was below 0.05 eV/Å.

With these calculation parameters, a single iteration step lasted for  $\sim 1$  hour, a *self-consistent field* (SCF) calculation took approximately 2 days, and a full geometry optimization needed several weeks and  $\sim 20$ – $30$  geometry steps to complete.

## 6.4 Geometrical details

In order to set up a reasonable model for the surface of an “infinite” bulk metal, an *inversion-symmetric slab* is commonly used that has to have a sufficient number of atomic layers (for most metals 5–7 layers are enough). This guarantees that the atomic layers well below the surface are independent of any interactions happening on the surface and can thus act as a model for bulk-like behavior. In turn, the two topmost atomic layers are a valid representation of a real surface with *surface* and *subsurface* atoms. The presence of inversion symmetry is very important because it effectively *halves* the computational effort needed for performing DFT calculations. In addition, a separating (pseudo-)vacuum

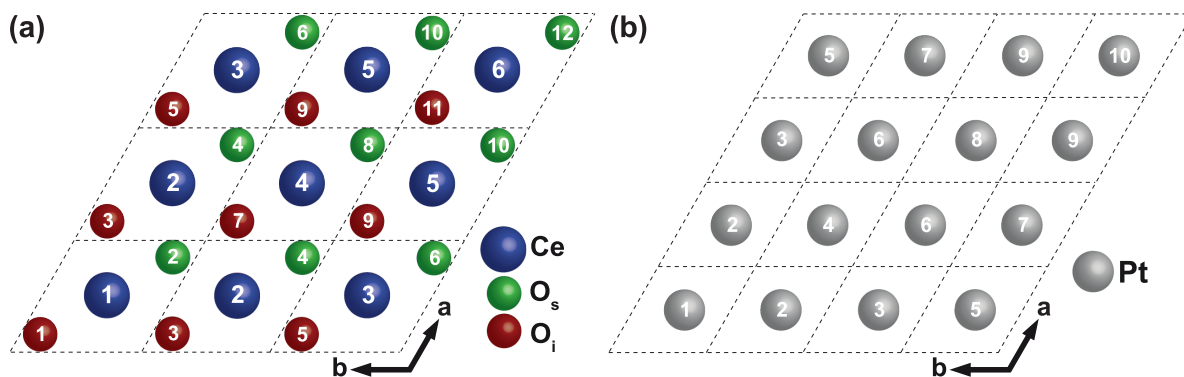


**Figure 6.4:** Schematic top views of the (111) surfaces of adsorbate and substrate layers leading to the periodicity of the “3:4” structure: (a)  $3 \times 3$  supercell of ceria and (b)  $4 \times 4$  supercell of platinum. In the case of ceria, the positions of the two inequivalent oxygen atoms relative to the cerium atoms are indicated by their color (surface  $\text{O}_s$  atoms are colored light green, interfacial  $\text{O}_i$  are colored dark red). The atoms are numbered according to their equivalence in the interface system. The unit cells of the high-symmetry substructures are indicated with dashed lines.

of  $\sim 10\text{--}20 \text{ \AA}$  is usually added at both sides of the slab to suppress any interaction in  $z$  direction between the periodically repeated slabs.

For the  $\text{CeO}_2/\text{Pt}(111)$  system, the model of the platinum surface was set up using an inversion-symmetric slab of  $\text{Pt}(111)$  consisting of *five* atomic layers. A  $4 \times 4$  ( $7 \times 7$ ) supercell of this slab was constructed for the  $(4 \times 4)$  ( $(1.4 \times 1.4)$ ) geometry. The resulting supercells were then matched with a  $3 \times 3$  (“3:4”) and  $5 \times 5$  (“5:7”) supercell of  $\text{CeO}_2(111)$ , respectively, whose geometry had been relaxed beforehand. As described above, a (pseudo-)vacuum of  $17 \text{ \AA}$  was added between the slabs in  $z$  direction. Figure 6.4 shows schematic views of both the platinum and ceria supercells for the case of the “3:4” structure. The relative positions of the oxygen atoms in the ceria layer are indicated by their individual color: *interfacial* oxygen atoms are colored red and *surface* oxygen atoms have a green color. The unit cells of the high-symmetry substructures are indicated with dashed lines to highlight the 3 : 4 matching ratio of adsorbate and substrate layer. The numbers on the individual atoms indicate the lowered symmetry of the combined supercell, leading to a total number of 44 inequivalent atoms, which, in the case of the “3:4” structure, consist of 26 Pt atoms, 6 Ce atoms and 12 oxygen atoms (again split up into 6  $\text{O}_i$  and 6  $\text{O}_s$  atoms). In turn, the unit cell of the “5:7” structure contains a total number of 117 inequivalent atoms.

Since the exact matching geometry of ceria on  $\text{Pt}(111)$  is not (yet) known from experiments, a large variety of initial adsorption geometries is possible depending on the lateral positions between the platinum surface and the ceria adsorbate. This situation is very different from the case of a single atom or molecule adsorption, where only the high-

symmetry adsorption sites (i.e., on top, bridge, hollow) have to be considered as starting geometries. Even if an atom or molecule is not stable at an initially chosen adsorption position, a subsequent optimization of the free internal parameters leads to a rapid movement to the most stable site in most cases. In contrast, the risk of reaching only a *local energy minimum* during geometry optimization is very high in case of an adsorbate layer, as the repulsive interaction between the layer atoms prevents any larger movements of the whole structure. In consequence, it is very crucial to provide a “good” (that is: physically reasonable) starting geometry for calculations of interface systems.

In this work, the efforts of providing such a starting geometry were focused on *three* different matchings for the  $(4\times 4)$  structure type where one atom is essentially above another. A geometry was chosen where (i) Ce6 (in Fig. 6.4(a)) is on top of Pt10 (in Fig. 6.4(b)), which was termed “Ce” type; (ii) a geometry where the *interfacial*  $\text{O}_i$  oxygen atom  $\text{O}_{i1}$  (which is actually the periodic image next to  $\text{O}_s12$ ) is positioned on the same Pt10 atom that was named “ $\text{O}_i$ ” type; and (iii) a geometry where the surface oxygen atom  $\text{O}_s12$  is on top of Pt10. This geometry was accordingly named “ $\text{O}_s$ ” type. For the  $(1.4\times 1.4)$  structure, only *one* geometry was investigated with a Ce atom matching the underlying Pt layer because the sheer size of the supercell already guarantees a large variety of lateral atomic configurations.

## 6.5 Results of the calculations

In the following subsections, the results of the performed DFT calculations are described in more detail. First, the resulting structures are analyzed, which is followed by an analysis of the *density of states* and the *electron density* of the interface systems. The *charge transfer* between substrate and adlayer is examined and the character of the chemical bonds between the different atom types is investigated.

### 6.5.1 Adsorption geometries of the relaxed structures

In general, a theoretical investigation of a given structure starts with the relaxation of its free structural parameters, i.e., the optimization of lattice parameters (volume, lengths, angles; not done in this case because the lattice constant of the Pt slab had already been optimized before) and/or the free internal parameters (i.e., coordinates of the individual atoms with respect of the unit cell). Internal parameters are optimized by slightly moving the individual atoms in order to minimize the forces acting on them. The movements nec-



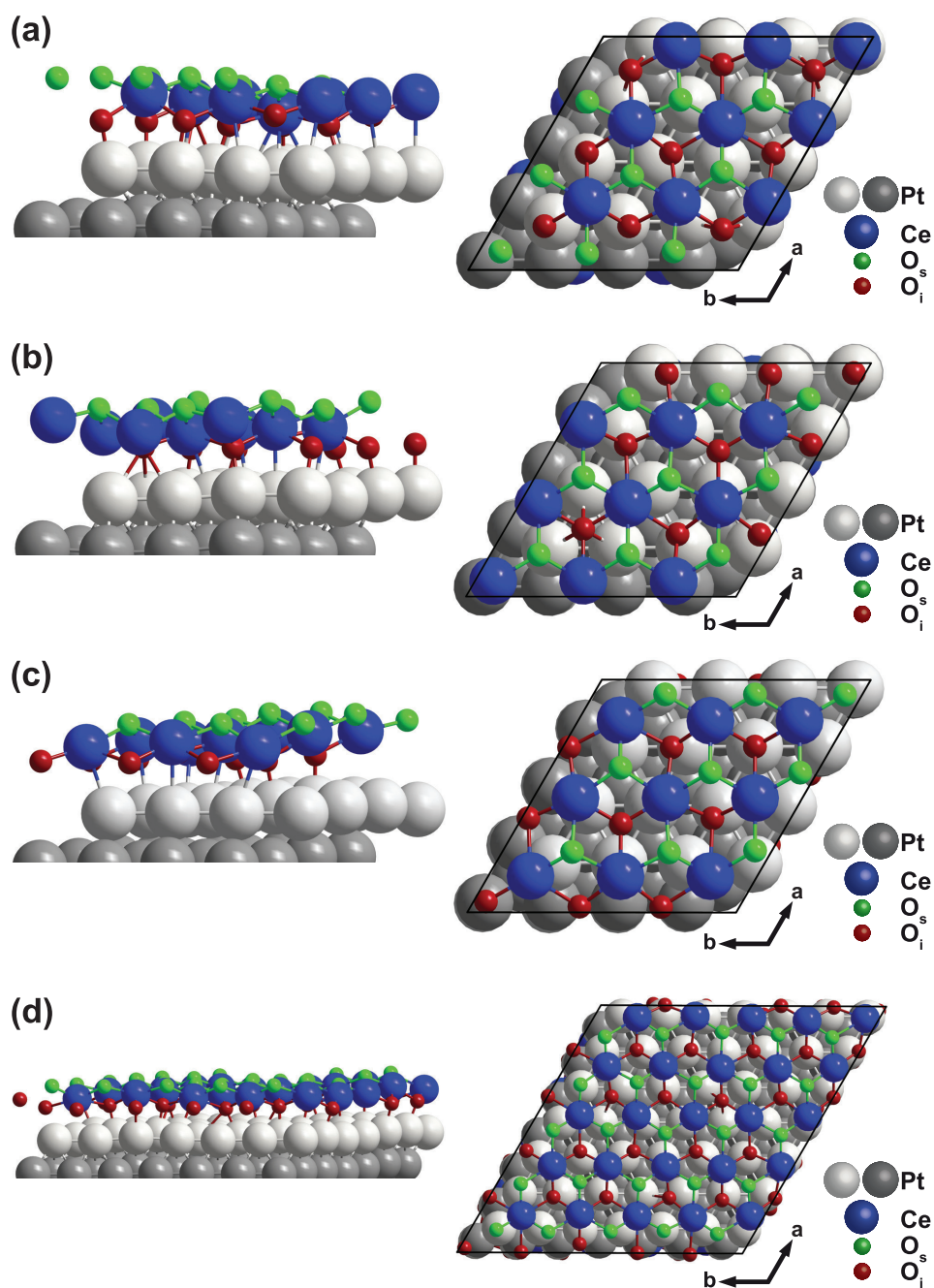


**Figure 6.5:** Ball models of the different “3:4” and “5:7” structure types after geometry optimization: (a) “Ce”-type, (b) “ $\text{O}_i$ ”-type, (c) “ $\text{O}_s$ ”-type and (d) “5:7”-type. Left panels show a side view along the short diagonal of the unit cell, right panels a top view. The original matching was done in all cases by positioning a Ce,  $\text{O}_s$  or  $\text{O}_i$  atom on top of the Pt atom in the upper right corner of the supercell. To improve the visibility of the Pt surface layer, the interface Pt atoms are plotted in light gray color and the subsurface Pt atoms appear in a darker shade.

essary for this task are determined by a chosen optimization-algorithm (steepest-descent, Newton, Simplex, etc.). Generally, a full SCF cycle has to be performed for each geometry step because accurate forces can only be derived from a properly converged electron density. The procedure of moving the atoms and calculating an improved electron density has to be repeated until the forces on all atoms meet a chosen convergence criterion (here: less or equal than  $0.05 \text{ eV/\AA}$ ).

Figure 6.5 shows side and top views of all investigated structures *after* relaxation of the internal parameters. In all investigated cases, the relaxation resulted in a significant *corrugation* of both, the topmost Pt interface layer and the ceria adlayer atoms. The lateral positions of substrate and adlayer atoms relative to each other also changed depending on the starting geometry: for example, oxygen atom  $\text{O}_s12$ , which initially was positioned *on top* of Pt10 in the “ $\text{O}_s$ ”-type geometry, moved away from this position towards Pt8. In contrast, Ce6 in the “Ce”-type and  $\text{O}_i1$  in the “ $\text{O}_i$ ”-type structure retained their original location with respect to the underlying Pt layer.

Table 6.1 lists the displacements (given in  $\text{\AA}$ ) of the individual atoms in z-direction. For a better readability, only the largest movements are listed in case of the “5:7” structure. However, its corrugation follows the same trends as the “3:4” structure, so the following analysis applies to both geometries.

The total corrugation of the surface Pt layer, which is defined as the difference between the highest and lowest surface Pt atom, amounts to a value between  $\sim 0.3 \text{ \AA}$  (in case of the “ $\text{O}_i$ ”-type geometry) and  $\sim 0.5 \text{ \AA}$  (“5:7”). Individual movements of the Pt atoms were measured relative to a free-standing platinum slab without a ceria adlayer. The highest interface Pt atoms were found in all structures to be those with an  $\text{O}_i$ -type oxygen in (or near) an on top position. In case of the “3:4” structures, this is evident in the following examples (cf. table 6.1): (i) in the “Ce” geometry Pt1 and Pt2 are the highest platinum atoms ( $+0.22$  and  $+0.21 \text{ \AA}$  above average) and have  $\text{O}_i1$  and  $\text{O}_i3$  adsorbed on top; (ii) in the “ $\text{O}_i$ ” geometry Pt10 lies high ( $+0.22 \text{ \AA}$ ) with  $\text{O}_i1$  positioned above it; (iii) in the “ $\text{O}_s$ ” geometry Pt8 has  $\text{O}_i11$  on top and thus lies high ( $+0.26 \text{ \AA}$ ), showing the maximum upward movement of all “3:4” structures with respect to a free-standing platinum layer.

The Pt atoms that show the largest downward corrugation (with a movement of up to  $-0.16 \text{ \AA}$  in the direction of the bulk) are always those with an  $\text{O}_s$  atom positioned above them. For example, this applies to Pt6 and Pt8 with  $\text{O}_s4$  and  $\text{O}_s8$  positioned above in case of the “Ce” structure, Pt1 with  $\text{O}_s2$  above for the “ $\text{O}_i$ ” type and again Pt1 with  $\text{O}_s2$  above in case of the “ $\text{O}_s$ ” geometry.

**Table 6.1:** Resulting corrugation of the Pt interface and the ceria adsorbate layer after relaxation in the investigated matching geometries. Movements of the atoms in z-direction are given in Å relative to a relaxed free-standing slab (in case of platinum atoms) or average positions (in case of cerium and oxygen atoms). For the “3:4” geometry, the movements of all atoms in the three types “Ce”, “O<sub>i</sub>” and “O<sub>s</sub>” are listed. For the “5:7” geometry, only the maximum movements of the respective atomic species are included.

Atom	“Ce” (Å)	“O <sub>i</sub> ” (Å)	“O <sub>s</sub> ” (Å)	“5:7” (Å)
Pt1	+0.22	−0.09	−0.10	
Pt2	+0.21	−0.06	−0.06	
Pt3	+0.02	+0.11	−0.06	
Pt4	+0.10	−0.06	−0.02	
Pt5	+0.03	+0.09	−0.08	
Pt6	−0.11	−0.03	+0.15	+0.29/−0.16
Pt7	+0.09	−0.07	+0.13	
Pt8	−0.14	−0.03	+0.26	
Pt9	−0.01	+0.13	+0.15	
Pt10	±0.00	+0.22	−0.07	
Ce1	+0.31	+0.28	−0.26	
Ce2	−0.02	−0.24	−0.05	
Ce3	+0.02	+0.27	−0.25	+0.31/−0.23
Ce4	−0.46	−0.24	−0.02	
Ce5	−0.01	−0.03	+0.28	
Ce6	+0.16	−0.03	+0.29	
O <sub>i</sub> 1	−0.01	+0.07	−0.04	
O <sub>i</sub> 3	−0.03	−0.11	−0.09	
O <sub>i</sub> 5	+0.21	−0.10	−0.09	+0.50/−0.20
O <sub>i</sub> 7	−0.20	−0.07	+0.28	
O <sub>i</sub> 9	−0.20	−0.11	−0.07	
O <sub>i</sub> 11	+0.22	+0.33	+0.11	
O <sub>s</sub> 2	+0.12	−0.09	−0.15	
O <sub>s</sub> 4	−0.23	−0.11	−0.13	
O <sub>s</sub> 6	+0.14	+0.23	−0.10	+0.38/−0.23
O <sub>s</sub> 8	−0.24	−0.14	+0.25	
O <sub>s</sub> 10	+0.09	−0.13	+0.23	
O <sub>s</sub> 12	+0.12	+0.23	−0.10	

The corrugation of the cerium atoms was found to be even bigger: the difference between the highest and lowest Ce atom was  $\sim 0.5 \text{ \AA}$  for both the “ $\text{O}_i$ ” and “5:7” structures,  $\sim 0.6 \text{ \AA}$  in case of the “ $\text{O}_s$ ” structure and even  $0.8 \text{ \AA}$  for the “Ce” geometry. In general, the Ce atoms follow the trend of the Pt atoms: in any case those cerium atoms, which moved away from the interface the most, are always situated above the highest lying Pt atoms: e.g., Ce1 above Pt1/Pt2 for the “Ce” geometry, the Ce1/Ce3 triangle above Pt10 for “ $\text{O}_i$ ” and the Ce5/Ce6 triangle above Pt8 for the “ $\text{O}_s$ ” type, all showing a  $\sim 0.3 \text{ \AA}$  upward movement compared to the average position of all cerium atoms. The same trend can also be observed in the opposite direction: Ce4 (for “Ce”), the Ce2/Ce4 triangle (for “ $\text{O}_i$ ”) and the Ce1/Ce3 triangle (for “ $\text{O}_s$ ”) are the lowest lying Ce atoms, all of which are situated in the vicinity of the lowest Pt atoms.

For the oxygen atoms, the interpretation of the relative movements is not as clear: The highest positioned *interface* oxygen atoms are  $\text{O}_i5/\text{O}_i11$  for “Ce”,  $\text{O}_i11$  for “ $\text{O}_i$ ” and  $\text{O}_i7$  for “ $\text{O}_s$ ”. The highest *surface* oxygen atoms are positioned around the *highest* Pt atoms:  $\text{O}_s2/\text{O}_s6$  around Pt1 and Pt2 for “Ce”,  $\text{O}_s6$  and  $\text{O}_s12$  around Pt10 for “ $\text{O}_i$ ” and  $\text{O}_s8/\text{O}_s10$  around Pt8 for “ $\text{O}_s$ ”. In each case the lowest *interface* oxygen atoms are situated near the lowest Ce atoms: the  $\text{O}_i7$  and  $\text{O}_i9$  triangle around Ce4 for the “Ce”-type,  $\text{O}_i3/\text{O}_i5/\text{O}_i7/\text{O}_i9$  around Ce2/Ce4 for “ $\text{O}_i$ ” and  $\text{O}_i1/\text{O}_i3/\text{O}_i5/\text{O}_i9$  around Ce1/Ce3 for “ $\text{O}_s$ ”. Finally, the lowest lying *surface* oxygen atoms are the  $\text{O}_s4/\text{O}_s8$  triangle for the “Ce” geometry, situated around Ce4, the lowest cerium atom in this particular geometry,  $\text{O}_s2/\text{O}_s4/\text{O}_s8/\text{O}_s10$  around Ce2/Ce4 for “ $\text{O}_i$ ” and  $\text{O}_s2/\text{O}_s4/\text{O}_s6/\text{O}_s12$  around Ce1/Ce3 for “ $\text{O}_s$ ”, thus following (similar to the cerium atoms) the trend of the underlying Pt atoms.

For all calculated geometries, the surface buckling described above resulted in changes with respect to the corresponding Pt-Pt and Ce-O bond lengths. While the Pt-Pt bond lengths on average remained more or less constant (compared to the value of  $2.80 \text{ \AA}$  of bulk platinum), changes of individual bonds were as large as  $\pm 0.05 \text{ \AA}$ , and reduced (enhanced) bond lengths were observed between the lowest (highest) positioned Pt atoms and their respective nearest neighbors. The individual Ce-O bond lengths showed even larger deviations of up to  $\pm 0.15 \text{ \AA}$  from the value of  $2.33 \text{ \AA}$  (“3:4”) or  $2.40 \text{ \AA}$  (“5:7”) of a free-standing  $\text{CeO}_2$  layer relaxed in the corresponding unit cell.

In conclusion of this analysis of the adsorption geometry, one can state that the corrugation of the ceria adsorbate layer follows, in principle, simple trends: *interface* oxygen atoms in (or near) an on top position above an interface Pt atom cause an upward movement of this atom and a reduced Pt-O distance. In turn, *surface* oxygen atoms in an on top position make the interface Pt atoms move toward the bulk. The fact that adlayer and

substrate influence each other so strongly is an indication of the significant interaction strength existing between them.

### 6.5.2 Energetics of adsorption geometry

In order to determine the most stable adsorption geometry among the calculated structures, their total energies as well as the *adsorption energies*  $E_{ads}$  of the ceria adlayers were compared. The resulting values are listed in table 6.2. One has to note that the total energies are given as negative numbers, and thus lower values indicate increased stability. The resulting numbers indicate that the “ $\text{O}_s$ ”-type geometry is the *most stable* among the three “3:4” structures investigated. To explain this result, a simple model can be applied that is based on the results of Yang et al. [245] and Mayernick et al. [271], who compared the various possible adsorption sites of *single* Pt or Pd atoms on the  $\text{CeO}_2(111)$  surface based on their respective adsorption energies, (that is, their stability): the results indicate that the most favorable position for a platinum atom is *on top* of or near an oxygen atom which is in a *subsurface* position, i.e., positioned *away* from the metal/oxide interface. In the case of the investigated *inverse* interface system, this would correspond to a *surface*  $\text{O}_s$ -type oxygen atom. In contrast, the most unfavorable position for a Pt atom was found to be *on top* of a Ce atom. Applying this simple model to the three investigated “3:4”-type geometries (see Fig. 6.5), one recognizes that the relaxed “Ce”-type geometry still contains a Ce atom (namely Ce6) located on top of a platinum atom (Pt10) which leads to a reduced energetic stability of this geometry. This destabilizing feature is absent in both the “ $\text{O}_i$ ” and the “ $\text{O}_s$ ” geometries, which, in addition, have a more favorable match of the  $\text{O}_s$  oxygen atoms with the surface Pt layer and thus increased stability.

As already mentioned, the *adsorption energies*  $E_{ads}$  of the adsorbate layers were calculated for each geometry. In general, the adsorption energy  $E_{ads}$  is equal to the *energy difference* between the total energy of an interface system and the sum of the total energies of the adsorbate-free surface and the free-standing adsorbate. In the present case, it was calculated using the following equation:

$$E_{ads} = \frac{1}{2} (E_{tot} - E_{\text{CeO}_2} - E_{\text{Pt}}), \quad (6.1)$$

where  $E_{tot}$  is the total energy of the individual relaxed adsorption geometry,  $E_{\text{CeO}_2}$  is the total energy of *two* nonadsorbed ceria layers and  $E_{\text{Pt}}$  is the total energy of a free-standing platinum slab without adsorbates. The factor of  $\frac{1}{2}$  in equation 6.1 accounts for the presence of *two* ceria adsorbate layers on both sides of the slab (due to inversion symmetry,

**Table 6.2:** Total energies  $E_{tot}$  and adsorption energies  $E_{ads}$  of the investigated “3:4” and “5:7” geometries. Total energies are given in eV relative to  $-44572770$  eV (“3:4”) and  $-135246955$  eV (“5:7”). Adsorption energies are given in eV per formula unit  $\text{CeO}_2$ .

Geometry	$E_{tot}$ (eV)	$E_{ads}$ (eV/formula unit)
“Ce”-type	−0.8301	−0.50
“O <sub>i</sub> ”-type	−0.8989	−0.50
“O <sub>s</sub> ”-type	−1.1150	−0.52
“5:7”	−0.2501	−0.83

cf. section 6.4). For the determination of  $E_{ads}$ , it is important that all structures have *well-relaxed geometries* to make sure that the ground-state energy is obtained in each case. For this purpose, geometry relaxations of a free-standing Pt slab as well as two free-standing ceria layers were performed (in the same-sized unit cell).

A negative value of the resulting adsorption energy corresponds to a stabilizing interaction between metal surface and adsorbate layer, and thus the lowest obtained number represents the most stable adsorption geometry. For a comparison of the different structure types, it is necessary to divide the resulting energy by the number of  $\text{CeO}_2$  *formula units* (FU; 9 and 25 for the “3:4” and “5:7” geometry, respectively) present in the investigated supercell.

Although the differences between the adsorption energies listed in table 6.2 are rather small, the “O<sub>s</sub>” geometry still shows the highest value of  $E_{ads}$  (−0.52 eV/FU  $\text{CeO}_2$ ) among the “3:4” structures, a result which corroborates the finding from the total energy analysis that this structure is indeed the most stable at least among those investigated. The adsorption energy for the “5:7” structure is even higher with a value of −0.83 eV/FU  $\text{CeO}_2$ , which is also consistent with the fact that the mean distance between the layers of surface Pt and Ce atoms is smaller in this geometry (decrease of  $\sim 0.15$  Å) compared to the “3:4”-type geometries. This may be due to the fact that the  $\text{CeO}_2$  lattice constant had to be *contracted* for setting up the “3:4” structure and *expanded* for the construction of the “5:7” structure (compared to bulk ceria, cf. section 6.2). Therefore, also the Ce-O bond distances differ significantly between the two matching geometries (cf. section 6.5.1).

Based on the findings described above, the most stable “O<sub>s</sub>”-type geometry was chosen for all further analyses performed for the “3:4” geometry.

### 6.5.3 Total and partial density of states (DOS)

It is a well-known fact (and has also been observed in the experiments that are described in section 6.1) that the bonding character between a substrate and an adsorbate directly affects the catalytic behavior of the resulting interface system. Thus, special attention has to be paid to the analysis of the *electronic structure* of the interface system, which can be done by investigating the density of states (DOS). The DOS of a given system is defined as the number of states  $N$  per energy interval  $[E, E + dE]$ . A DOS analysis is a very important “fingerprint” technique to characterize the electronic structure of a system because even slight structural or chemical modifications of the system result in fundamental changes of the DOS. With the WIEN2k software, the DOS can be calculated either for the whole system (resulting in the *total density of states* or TDOS) or for a single atom (giving the *partial density of states* or PDOS). Moreover, a single-atom PDOS can be further decomposed with regard to quantum numbers  $l$  and  $m$ , which allows for a fine-grained analysis of the interactions that are present between the orbitals of the individual atoms.

#### 6.5.3.1 Total density of states

Figure 6.6 shows a combined plot of the total density of states (TDOS) of three different compounds: (i) the  $\text{CeO}_2/\text{Pt}(111)$  interface system (“3:4”, “ $\text{O}_s$ ”-type geometry), (ii) a free-standing ceria layer (note that, for better comparability, its TDOS has been down-shifted in energy by 0.65 eV to match its Ce-4f peak with the Ce-4f peak of the interface system) and (iii) an adsorbate-free Pt slab *after* geometry relaxation. Contrary to the insulating behavior of the free-standing ceria layer, which has a *calculated band gap* between O-2p and Ce-4f states of  $\sim 2.5$  eV,<sup>3</sup> the  $\text{CeO}_2/\text{Pt}(111)$  interface system clearly shows metallic character (i.e., filled states are present in the DOS at the Fermi energy  $E_F$ ). One has to note at this point that the calculated size of the ceria band gap is much smaller than the experimentally reported value ( $\sim 6$  eV) [273]. It is a well-known fact that common DFT methods (including the one that was used in this study) largely *underestimate* the band gap of most compounds, although, recently, modified exchange-correlation functionals have shown very promising improvements in this area [274].

The additional gap states of the interface system that are not present in the free ceria layer originate from 5d states of the Pt slab that fall in the energy gap between the O-2p and Ce-4f bands. The same observation was made in a study on single Pt atoms adsorbed on  $\text{CeO}_2(111)$ : in that case, it was attributed to the occurrence of *metal induced gap states*

<sup>3</sup>Or  $\sim 5$  eV if the strongly localized Ce-4f peak is *not* regarded as conduction state [272].

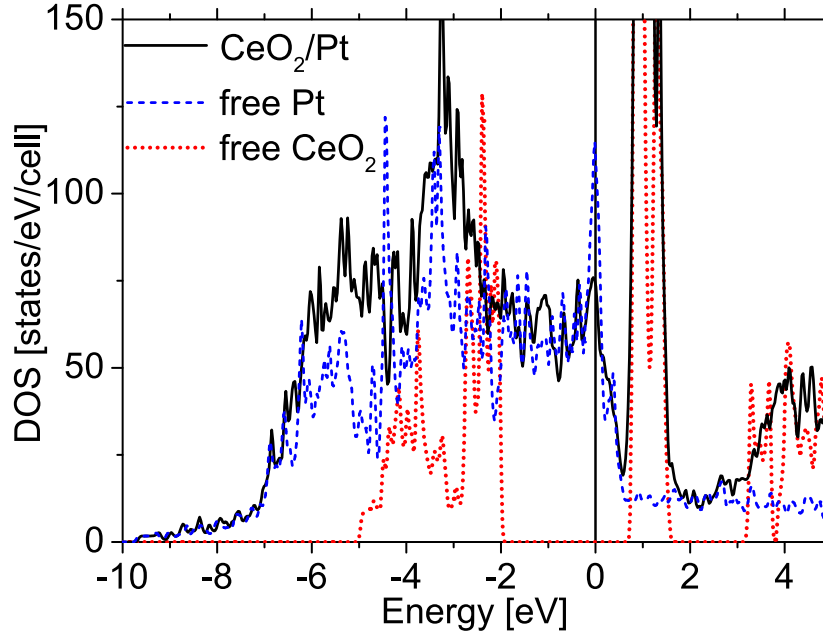


**Figure 6.6:** Total density of states (TDOS) of  $\text{CeO}_2/\text{Pt}$  (solid black line), a free Pt slab (dashed blue line) and nonadsorbed  $\text{CeO}_2$  (dotted red line) for the “3:4” (“ $\text{O}_s$ ”-type) structure. Values are given in states/eV/cell. The Fermi energy  $E_F$  is marked with a line. Energies are given in eV relative to  $E_F$ . The DOS of nonadsorbed  $\text{CeO}_2$  is down-shifted by 0.65 eV to align the Ce-4f peak of this structure with the Ce-4f peak of the interface system.

(MIGS) [245]. Correspondingly, the total DOS of the interface system (i) can, in principle, be seen as a superposition of the two free-standing structures of Pt (ii) and ceria (iii). For example, the contribution from the O-2p states of free ceria (present between  $-2$  eV and  $-5$  eV) is visible between  $-4$  eV and  $-7$  eV in the interface system. The bandwidth of the Pt states is hardly modified upon forming the interface, whereas the O-2p band of  $\text{CeO}_2$  becomes much wider in the interface system and thus the interface DOS (i) is much *larger* than the superposition of (ii) and (iii) in this energy range. This indicates that some O-2p states must have been shifted *downwards*.

### 6.5.3.2 Partial density of states

To further elucidate the electronic structure, the partial densities of states (PDOS) of all atomic species were calculated and are shown in Fig. 6.7 (again for the case of the “3:4” “ $\text{O}_s$ ”-type geometry) for the energy range  $[E_F - 10 \text{ eV}, E_F + 5 \text{ eV}]$ . For this plot, only the Pt atoms of the interface layer have been considered. The total DOS of the interface system, which was already presented in Fig. 6.6, is again shown for easier comparison. Because



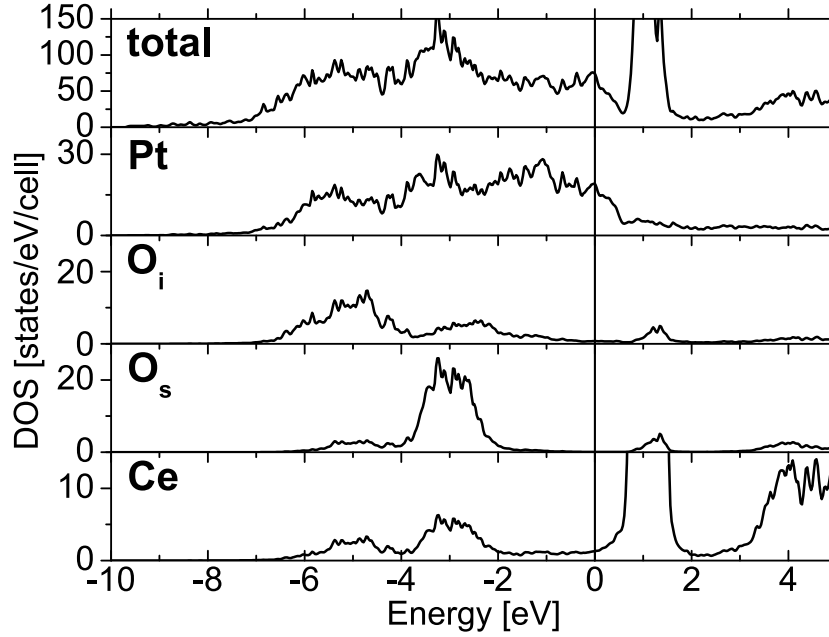


**Figure 6.7:** Total density of states (TDOS) and partial density of states (PDOS) of all atomic species for the “3:4” ( $\text{O}_s$ )-type structure. Values are given in states/eV/cell. Only the platinum atoms of the interface layer were included in the respective PDOS. The Fermi energy  $E_F$  is marked with a line. Energies are given in eV relative to  $E_F$ .

the DOS of the “5:7” geometry is very similar, it is not shown here and the following analysis applies to both interface structure types.

The PDOS of cerium consists of 5s bands, which are low lying in energy at  $\sim -35$  eV, 5p bands at  $\sim -20$  eV (both of which are not shown in Fig. 6.7) and 5d states in the valence band region as minor contributions. It is mostly dominated by the 4f states that are situated both *below* and *above* the Fermi level with a *small bonding* and a *large antibonding* contribution. Additional antibonding contributions from 5d and 6s orbitals at even higher energies are also not included in the plot in Fig. 6.7. The PDOS of the platinum atoms is dominated by broad peaks around the Fermi level  $E_F$  (ranging from  $\sim -7$  eV to  $\sim +1$  eV) that originate from 5d states. As mentioned above, these states are responsible for the metallic character of the interface system. The oxygen PDOS, split into  $\text{O}_i$  and  $\text{O}_s$  oxygen in Fig. 6.7, consists of low lying 2s states at  $\sim -20$  eV (not shown), bonding 2p states just below the Fermi level and antibonding 2p states at  $+1.3$  eV that interact with the Ce-4f and 5d states. One striking feature of the oxygen PDOS is the remarkable difference between  $\text{O}_i$ - and  $\text{O}_s$ -type oxygen: whereas the  $\text{O}_i$  PDOS shows *two peaks* at about  $-5$  and  $-2.5$  eV, the  $\text{O}_s$  PDOS has *only one* at about  $-3$  eV. The *center of gravity* of the  $\text{O}_i$  states is significantly *down-shifted* in energy from  $-3$  eV to  $-5$  eV, and 4f and 5d states

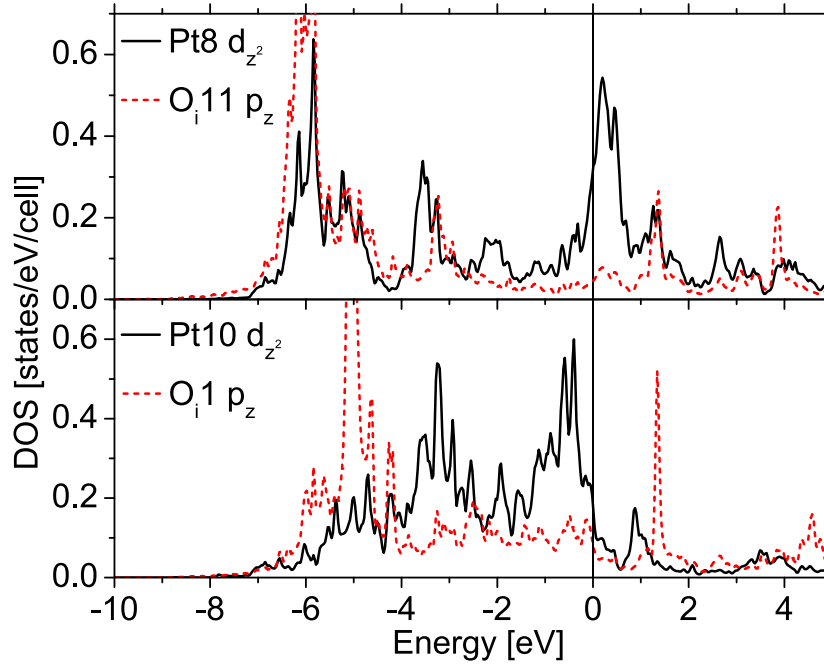


**Figure 6.8:** Two PDOS plots for the “3:4” (“ $\text{O}_s$ ”-type) structure illustrating the differences in interaction between substrate and adsorbate layer. Upper panel: PDOS of Pt8 ( $5d_{z^2}$  orbital, solid black line) and  $\text{O}_i11$  ( $2p_z$  orbital, dashed red line) as an example for a strong interaction between interface oxygen and platinum. Lower panel: PDOS of Pt10 ( $5d_{z^2}$  orbital, solid black line) and  $\text{O}_i1$  ( $2p_z$  orbital, dashed red line), which do not match well geometrically. Values are given in states/eV/cell. The Fermi energy  $E_F$  is marked with a line. Energies are given in eV relative to  $E_F$ .

of Ce as well as Pt-5d states interact with all these ( $\text{O}_i$  and  $\text{O}_s$ ) oxygen peaks below  $E_F$ . Again, the combined results indicate strong interactions existing between the oxide layer and the metal surface.

The interaction strength between the topmost platinum atoms and the ceria layer is, of course, not homogeneously distributed over the whole unit cell. On the contrary, it strongly depends on the individual atom-to-atom matching situation existing between Pt and ceria. This can be highlighted in two contrasting examples of the metal-oxide interaction strength with different local matching geometries, illustrated in Fig. 6.8: the top panel of Fig. 6.8 shows the PDOS of the  $5d_{z^2}$  orbital of Pt8 and the  $2p_z$  orbital of  $\text{O}_i11$ , atoms, which are situated on top of each other (as can be seen in Fig. 6.5(c) when using the labels of Fig. 6.4). The  $5d_{z^2}$  orbital of Pt8 is split in energy with characteristic bonding peaks at  $\sim -6$  eV and  $\sim -3.3$  eV that both show a strong overlap with the  $2p_z$  orbital of  $\text{O}_i11$ . Besides that, a non-bonding contribution at  $E_F$  and an antibonding interaction with  $\text{O}_i11$  at  $\sim +1.3$  eV are also evident in this DOS plot.

In contrast, the bottom panel of Fig. 6.8 gives an example of a rather weak interaction between substrate and adsorbate layer: it shows the PDOS of the  $5d_{z^2}$  orbital of Pt10 and the  $2p_z$  orbital of  $\text{O}_i1$ . Due to the fact that these atoms do not nearly have the same geometric matching as the above example (as can be seen in Fig. 6.5(c),  $\text{O}_i1$  is more in a *threefold hollow* position above Pt5/Pt10), the overlap between the displayed orbitals is rather poor. Only a weak overlap at  $\sim -5$  eV is observed between the  $\text{O}_i1$  2p states and the  $5d_{z^2}$  states of Pt10. Additionally, the sharp antibonding 2p peak at +1.3 eV is not matched with a corresponding Pt state this time.

Concluding the above DOS analysis, the interaction strength between the oxide layer and the metal substrate depends very strongly on the individual atom-to-atom matching of both atomic layers, a finding that was also evident in the sizable dependence of the total energy and adsorption energy on small variations of the matching geometry (see section 6.5.2).

#### 6.5.4 Electron density at the $\text{CeO}_2/\text{Pt}(111)$ interface

As was shown in the previous sections, the interaction strength between adsorbate and substrate is highly dependent on the matching geometry. To analyze the bonding character of the interface in a spatially-resolved way, its *electron density* was investigated. Figure 6.9 shows the *difference electron density* (i.e., crystalline minus superposed atomic densities) in the  $(11\bar{2}0)$  plane (namely, the plane in the *longer diagonal* of the unit cell). Again, only the “3:4” structure in the “ $\text{O}_s$ ”-type geometry is considered here since the “5:7” structure behaves rather similarly. A difference electron density is a very useful tool to elucidate the changes on the electronic density distribution of the atoms upon forming the interface. However, the major contribution to the electron density comes from *core* and *semi-core* states, which are more or less unaffected by chemical interaction and overshadow the small changes happening in the valence band region. In order to remove the dominant contribution of these states to the electron density, it is necessary to include just the valence states in the electron density plot. Thus, the energy range for the calculation of the electron density was chosen between  $-9.5$  eV and  $E_F$  in the present case.

The relaxed  $\text{CeO}_2$  layer (with  $\text{O}_s$ ,  $\text{O}_i$  and Ce atoms) on top of the Pt atoms is clearly visible in the plot in Fig. 6.9. All atomic types in the interface system differ strongly in their electron density compared to the free atomic state. A significant polarization is observed on those Pt atoms that have an oxygen sitting on top due to a strong electrostatic field, e.g., Pt8 and  $\text{O}_i11$  in Fig. 6.4 and 6.9. Such a feature is absent for all the other Pt atoms shown in the plot. The shape of the  $5d_{z^2}$  orbital of Pt11 is visible in the electron density

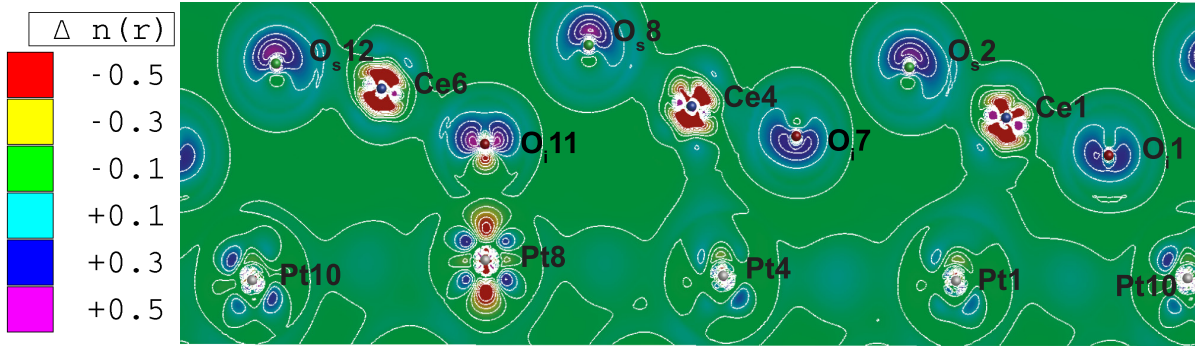


**Figure 6.9:** Difference electron density  $\Delta n(r)$  in the  $(11\bar{2}0)$  plane of the “3:4” (“ $\text{O}_s$ ”-type) structure taken for the valence states that lie in the energy range between  $-0.7$  Ry ( $-9.5$  eV) and  $E_F$ . The positions and labels of the atoms correspond to Fig. 6.4, going from the top right (Pt10) via Pt8 and Pt4 to the bottom left (Pt1). The electron density is given in  $\text{e}/\text{\AA}^3$ . Electron excess is marked with pink, electron deficiency with red color and green color marks areas with electron density differences close to zero. The graph was produced using the XCrysDen software [275].

map, and an electron deficiency is present compared to the atomic density. On the other hand, there is an *increase* of electron density in the  $5d_{xz}$  and  $5d_{yz}$  orbitals of the same Pt11 atom, a fact which can be interpreted as *backdonation* from  $2p$  states of  $\text{O}_i11$  to the Pt8  $5d$  states. This claim is corroborated by the negative electron density (read: electron loss) visible on  $\text{O}_i11$  in the direction of the Pt-O bond. Such strong interaction between Pt and oxygen was already observed in the DOS plots (see section 6.5.3, Figs. 6.7 and 6.8).

Within the  $\text{CeO}_2$  layer, a significant polarization of the cerium electron densities in the direction of the Ce-O bonds is visible. The  $\text{O}_s$  and  $\text{O}_i$  oxygen atoms differ strongly in their electron density distribution, similar to what was already observed in the PDOS plots in Fig. 6.7: all the  $\text{O}_s$ -type oxygen atoms have a rather similar electron density distribution with the lone electron pair pointing toward (pseudo-)vacuum (correspondingly, only one peak is visible in the PDOS), whereas the electron density of the  $\text{O}_i$ -type atoms strongly depends on the chemical environment (two peaks are present in the PDOS). The splitting of the  $\text{O}_i$ -type atoms becomes also evident in the orientation of the lone electron pair of  $\text{O}_i11$  (pointing toward vacuum) compared to, e.g.,  $\text{O}_i1$  and  $\text{O}_i7$  (pointing toward the interface).

In order to compare the relaxed structures with data from STM experiments, the (constant height) *local density of states* (LDOS) was calculated for both structures in a plane a few  $\text{\AA}$  above the sample surface. It is shown in Figs. 6.10 and 6.11 for the “3:4” and “5:7” geometry, respectively. Filled states in the energy range  $[E_F - 3.2 \text{ eV}, E_F]$  were considered for the LDOS plots, in agreement with typical sample bias voltages used in STM experiments on the  $\text{CeO}_2/\text{Pt}(111)$  system [264, 265].

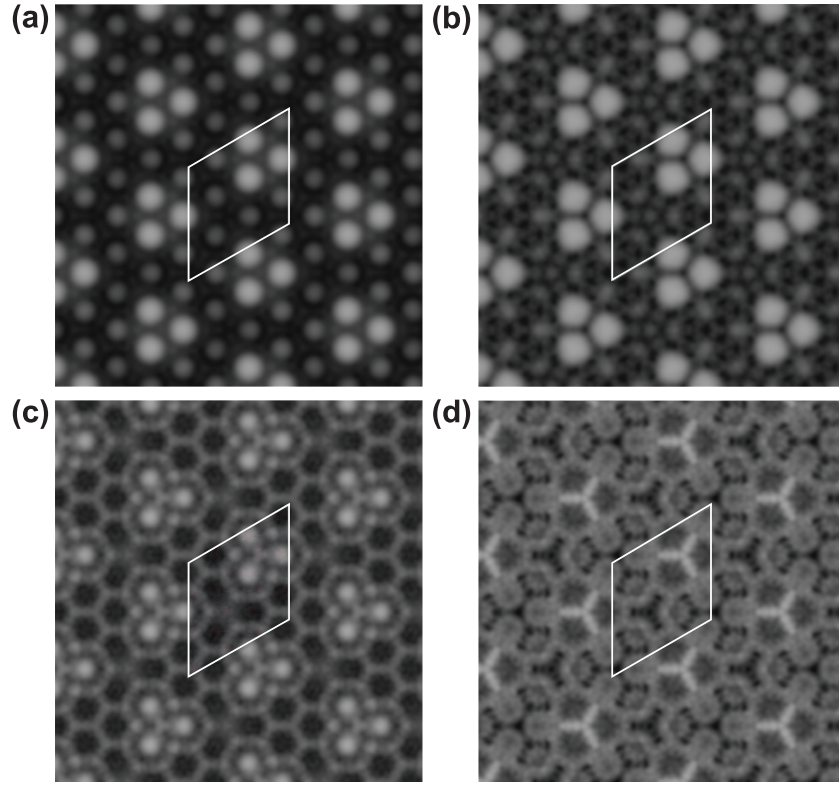


**Figure 6.10:** Constant height local density of states (LDOS) plots of the “3:4” ( $\text{O}_s$ -type) structure for different distances to the sample surface. Distances are (a) 2.2 Å, (b) 3.2 Å, (c) 3.6 Å and (d) 3.9 Å with respect to the average height of the  $\text{O}_s$  layer. The plots show filled states in the energy range  $[E_F - 3.2 \text{ eV}, E_F]$  in a plane above the topmost  $\text{O}_s$  oxygen atom. The unit cell of the “3:4” structure is indicated with solid lines (cf. Fig. 6.5(c)).

The distance between the plane chosen for the LDOS and the topmost  $\text{O}_s$  atom of the surface was found to be very crucial for the appearance of the resulting plots. This dependence is highlighted in Fig. 6.10, where four different LDOS plots of the “3:4” structure are given in the order of increasing distance of the LDOS plane to the sample surface. Figs. 6.10 (a) and (b) are very similar to each other and mainly highlight the positions of the  $\text{O}_s$  atoms through the dominant contribution of the O 2p orbitals. Besides that, the pronounced corrugation of the ceria layer (discussed in section 6.5.1) is visible in the different brightnesses of the oxygen atoms. In contrast, Figs. 6.10 (c) and (d) are much more feature-rich: in these LDOS plots both the positions of the Ce atoms and even the (subsurface)  $\text{O}_i$  atoms (!) are visible in a honeycomb-like pattern.

However, if the distance to the surface is chosen too large, e.g.,  $\geq 5.7 \text{ Å}$ , an almost featureless electron density is obtained that does not provide any information about the positions of the surface atoms anymore. This observation is, in principle, comparable to the

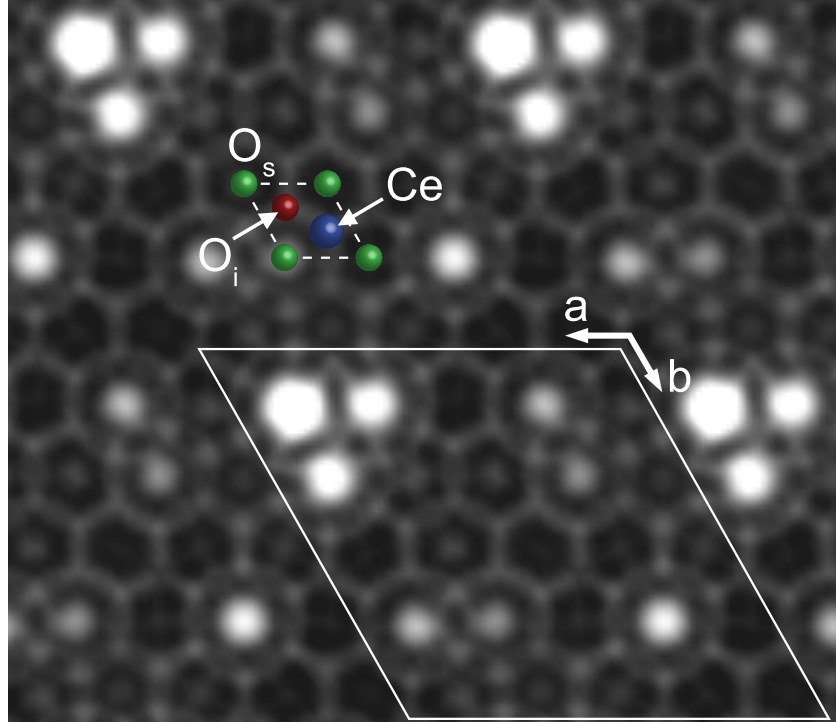


**Figure 6.11:** Constant height local density of states (LDOS) plot of a  $2 \times 2$  supercell of the “5:7” structure. The plot shows filled states in the energy range  $[E_F - 3.2 \text{ eV}, E_F]$  in a plane  $3.6 \text{ \AA}$  above the topmost  $\text{O}_s$  oxygen atom. The unit cell of the “5:7” structure (solid lines; see Fig. 6.5(d) for details) and a high-symmetry  $\text{CeO}_2$  unit cell (dashed lines) are indicated in the plot. The positions of the individual atoms are denoted by colored spheres.

experimental difficulties in obtaining an STM image of ceria surfaces with atomic resolution because typical working distances between the STM tip and the sample surface are in the range of  $5\text{--}10 \text{ \AA}$ .

Based on these observations, an *intermediate* distance of  $3.6 \text{ \AA}$  was chosen for the LDOS plot of the “5:7” structure shown in Fig. 6.11. Filled states from the surface  $\text{O}_s$  atoms but also contributions from Ce and  $\text{O}_i$  atoms are visible in the plot. Again, the varying intensity of the  $\text{O}_s$  oxygen atoms reflects the corrugation of the ceria adlayer, as discussed in section 6.5.1. Besides that, the Ce and  $\text{O}_i$  atoms also form a honeycomb-like pattern around the  $\text{O}_s$  oxygen atoms.

Unfortunately, the comparability of the presented LDOS plots to experimental results from STM measurements is rather limited due to the fact that experimentally observed ceria films are usually defect-rich with features such as oxygen vacancies, adsorbed water, hydroxyl groups, etc. [265]. As already mentioned in the description of the experimental

structure in section 6.2.2, all these properties were not considered in this study and are topics of future work.

### 6.5.5 Charge transfer between ceria and platinum

As mentioned in the previous section, a *charge transfer* between the substrate and the adsorbate was detected in the electron density. In order to obtain a deeper understanding of these changes in the electronic distribution occurring upon adsorption, the charges on the interface atoms were analyzed using the *atoms in molecules* [276] (AIM) method. This scheme analyzes the *topology* of the charge density. For this purpose, it divides the space of the unit cell into atomic volumes (called *basins*) that contain exactly *one nucleus*. The volume of the basins is determined by the definition of an *interatomic surface* that satisfies the zero-flux boundary condition

$$\nabla\rho(\mathbf{r}_s)\mathbf{n}(\mathbf{r}_s) = 0, \quad (6.2)$$

where  $\mathbf{n}(\mathbf{r}_s)$  is the unit vector normal to the surface and  $\nabla\rho(\mathbf{r}_s)$  is the gradient of the electron density at position  $\mathbf{r}_s$ . This decomposition of the unit cell volume is *uniquely defined* and thus considerably improves comparability of charge transfer between different calculation methods since it is independent of the chosen basis set.<sup>4</sup>

The AIM charges of the atoms *before* and *after* adsorption of the ceria adlayer were compared for both structure types. Subtraction of the resulting values allows estimating the charge transfer due to adsorption. The results of this analysis are listed in table 6.3 for the “3:4” (“O<sub>s</sub>”-type) structure. Note that only the Pt atoms of the topmost, i.e., surface layer of the slab were considered for this analysis because the charge transfer happening on the subsurface Pt atoms is already negligible.

All cerium atoms gain electrons during adsorption and show a decrease of positive charge between 0.03 and 0.15 e for the “3:4” and between 0.03 and 0.17 e for the “5:7” structure. The gain of electrons is dependent on the relative position of the Ce atoms: it is higher on those cerium atoms that have moved closer to the interface during relaxation (see section 6.5.1 for details), e.g., Ce1 and Ce3 in the “O<sub>s</sub>”-type structure.

The charge of the oxygen atoms in the surface O<sub>s</sub> position (even numbers in Fig. 6.4(a) and table 6.3) is almost unperturbed by adsorption – at most, a very small transfer of electrons of  $\pm 0.01$  e is observed for the “3:4” structure and  $\pm 0.02$  e for the “5:7” structure. In

<sup>4</sup>In augmented basis sets like LAPW+LO/APW+lo used in this study, the charge “belonging” to an atom  $\alpha$  depends on the sphere radius  $R_\alpha$  chosen for that atom (cf. section 5.2.5.1).

**Table 6.3:** Atomic charges and resulting charge transfer compared to the free substructures of Pt and  $\text{CeO}_2$  obtained with AIM for the “3:4” (“ $\text{O}_s$ ”-type)  $\text{CeO}_2/\text{Pt}(111)$  structure.

Atom	$\text{CeO}_2/\text{Pt}(111)$	free substructure	Charge transfer
Pt1	-0.178	-0.047	-0.131
Pt2	-0.168	-0.047	-0.121
Pt3	-0.176	-0.047	-0.129
Pt4	-0.158	-0.047	-0.110
Pt5	-0.109	-0.047	-0.061
Pt6	+0.192	-0.047	+0.239
Pt7	+0.191	-0.047	+0.238
Pt8	+0.207	-0.047	+0.255
Pt9	+0.197	-0.047	+0.244
Pt10	-0.106	-0.047	-0.058
Ce1	+2.402	+2.545	-0.142
Ce2	+2.468	+2.544	-0.076
Ce3	+2.390	+2.544	-0.154
Ce4	+2.466	+2.544	-0.078
Ce5	+2.515	+2.545	-0.030
Ce6	+2.517	+2.544	-0.027
$\text{O}_i1$	-1.182	-1.271	+0.089
$\text{O}_i3$	-1.215	-1.272	+0.056
$\text{O}_i5$	-1.212	-1.272	+0.060
$\text{O}_i7$	-1.213	-1.272	+0.059
$\text{O}_i9$	-1.215	-1.271	+0.055
$\text{O}_i11$	-1.220	-1.272	+0.052
$\text{O}_s2$	-1.264	-1.271	+0.007
$\text{O}_s4$	-1.261	-1.272	+0.011
$\text{O}_s6$	-1.271	-1.271	$\pm 0.000$
$\text{O}_s8$	-1.285	-1.272	-0.013
$\text{O}_s10$	-1.285	-1.271	-0.014
$\text{O}_s12$	-1.271	-1.271	$\pm 0.000$



contrast, all interface  $\text{O}_i$  atoms (odd numbers in Fig. 6.4(a) and table 6.3) *lose* a small fraction of electrons in both structure types, namely between 0.05 and 0.09 e (“3:4”) and 0.04–0.12 e (“5:7”). This loss can be attributed to the aforementioned backdonation of electrons from  $\text{O}_i$ -type oxygen to some of the Pt atoms, which was also visible for  $\text{O}_{i11}/\text{Pt8}$  in the electron density map in Fig. 6.9.

All Pt atoms of the “3:4” geometry that have moved toward the ceria adlayer during relaxation (see section 6.5.1 for details), namely Pt6 to Pt9, lose a significant fraction of electrons (0.24–0.26 e), whereas the ones that moved farther away from the interface (Pt1 to Pt5 and Pt10) show a slightly increased number of electrons (0.06–0.13 e). The same is true for the “5:7” structure with an electron increase of 0.05–0.18 e for the Pt atoms corrugated toward the bulk and an electron decrease of 0.09–0.25 e for the Pt atoms corrugated toward the ceria layer.

The loss of electrons on the Pt atoms positioned close to the interface and the overall gain of electrons on the Ce atoms is in qualitative agreement with results from literature on a  $\text{NM}/\text{CeO}_2(111)$  system (with NM being Pt and Pd), for which an overall electron transfer from the noble metal atoms to the  $\text{Ce}^{4+}$  surface ions was observed [247,248]. The electron transfer causes a reduction of some of the  $\text{Ce}^{4+}$  ions and an increase of  $\text{Ce}^{3+}$  ions on the catalyst surface and, in this way, significantly alters the *catalytic properties* of the whole system.

### 6.5.6 Bond character

A useful tool to interpret the character (i.e., covalent, metallic, ionic) of the individual chemical bonds is the analysis of the metallicity/ionicity at the *bond critical points* (BCPs) that were also obtained with the help of the AIM method. For this purpose, three common measures of bond metallicity that were proposed in Refs. [277,278], namely the values of  $\xi_j$  and  $\xi_m$ , as well as Bohm’s quantum potential  $W_{\text{GEA}}$ , were calculated for all atoms of the “3:4” (“ $\text{O}_s$ ”-type) geometry. These quantities are defined by the following equations:

$$\xi_j(\mathbf{r}_{bcp}) = \frac{\rho(\mathbf{r}_{bcp})}{\nabla^2 \rho(\mathbf{r}_{bcp})} \quad \text{for } \nabla^2 \rho(\mathbf{r}_{bcp}) > 0, \quad (6.3)$$

$$\xi_m(\mathbf{r}_{bcp}) = \frac{36(3\pi^2)^{\frac{2}{3}} (\rho(\mathbf{r}_{bcp}))^{\frac{5}{3}}}{5 \nabla^2 \rho(\mathbf{r}_{bcp})} \quad \text{for } \nabla^2 \rho(\mathbf{r}_{bcp}) > 0, \quad (6.4)$$

$$W_{\text{GEA}}(\mathbf{r}_{bcp}) = \frac{5}{36} (\xi_j(\mathbf{r}_{bcp}))^{-1} - \frac{1}{5} (3\pi^2 \rho(\mathbf{r}_{bcp}))^{\frac{2}{3}}. \quad (6.5)$$

In the above equations  $\rho(\mathbf{r}_{bcp})$  and  $\nabla^2\rho(\mathbf{r}_{bcp})$  are the *electron density* and the *Laplacian* at the bond critical point  $\mathbf{r}_{bcp}$ , respectively. According to the studies cited above, values of  $\xi_j(\mathbf{r}_{bcp}) > 1$ ,  $\xi_m(\mathbf{r}_{bcp}) > 10$  and  $W_{GEA}(\mathbf{r}_{bcp}) < 0$  indicate metallic interaction (at least in the case of compounds).

As expected, the bonds between the surface Pt atoms have *metallic* character with an average value for  $\xi_j(\mathbf{r}_{bcp}) \approx 1.2$ ,  $\xi_m(\mathbf{r}_{bcp}) \approx 13$  and  $W_{GEA}(\mathbf{r}_{bcp}) \approx -0.17$ . The metallicity of these surface Pt-Pt bonds is slightly increased compared to the bonds between the sub-surface Pt atoms, which have values of  $\xi_j(\mathbf{r}_{bcp}) \approx 1$ ,  $\xi_m(\mathbf{r}_{bcp}) \approx 10$  and  $W_{GEA}(\mathbf{r}_{bcp}) \approx -0.15$ . This is comparable to the average bond metallicity of a free-standing Pt layer without ceria adsorbates.

In agreement with the analysis of the electron density in section 6.5.4, the Pt-O bonds are mainly of *ionic* character. They have an average  $\xi_j(\mathbf{r}_{bcp}) \approx 0.3$ ,  $\xi_m(\mathbf{r}_{bcp}) \approx 3$  and a  $W_{GEA}(\mathbf{r}_{bcp}) \approx 0.1$ . The values for the Ce-O bonds are somewhere in between these two extremes with an average  $\xi_j(\mathbf{r}_{bcp}) \approx 0.5$ ,  $\xi_m(\mathbf{r}_{bcp}) \approx 6$  and  $W_{GEA}(\mathbf{r}_{bcp}) \approx 0$ . Perhaps surprisingly, there is no significant difference between O<sub>i</sub>- and O<sub>s</sub>-type oxygen with regard to these parameters.

The obtained numbers indicate that the Ce-O bonds show some signs of *covalency*, an observation that was also made in STM measurements on CeO<sub>2</sub>/Pt(111) [264].

### 6.5.7 Core level shifts of oxygen

Another area where significant differences exist between surface and interface oxygen atoms is the position of the O 1s core level. A histogram plot of the distribution of the 1s levels relative to  $E_F$  is shown in Fig. 6.12 for all oxygen atoms of the “5:7” structure. The 1s binding energies of the O<sub>s</sub> type oxygen atoms are centered around  $-506.0$  eV (“3:4”) and  $-505.6$  eV (“5:7”), respectively, whereas the levels of the O<sub>i</sub>-type oxygen atoms are *down-shifted* in energy to  $-506.8$  eV (“3:4”) and  $-506.6$  eV (“5:7”), respectively, in agreement with a general loss of electrons observed on these atoms in the AIM analysis discussed in section 6.5.5. Furthermore, the binding energies of the O<sub>s</sub>-type oxygen atoms show a narrow distribution, whereas the differences in binding energy among the O<sub>i</sub> species are much more pronounced: e.g., O<sub>i</sub>1 in the “3:4” structure shows the largest electron loss in the AIM analysis upon adsorption (0.089 e; cf. table 6.3), but also has a smaller 1s binding energy ( $-506.7$  eV) than the average.

The distance from the surface Pt layer seems to play an even more important role: the O<sub>i</sub>-type oxygen atoms that have moved farthest away during relaxation (see section 6.5.1), have also by far the smallest 1s binding energy of  $-505.8$  eV, which is already very close

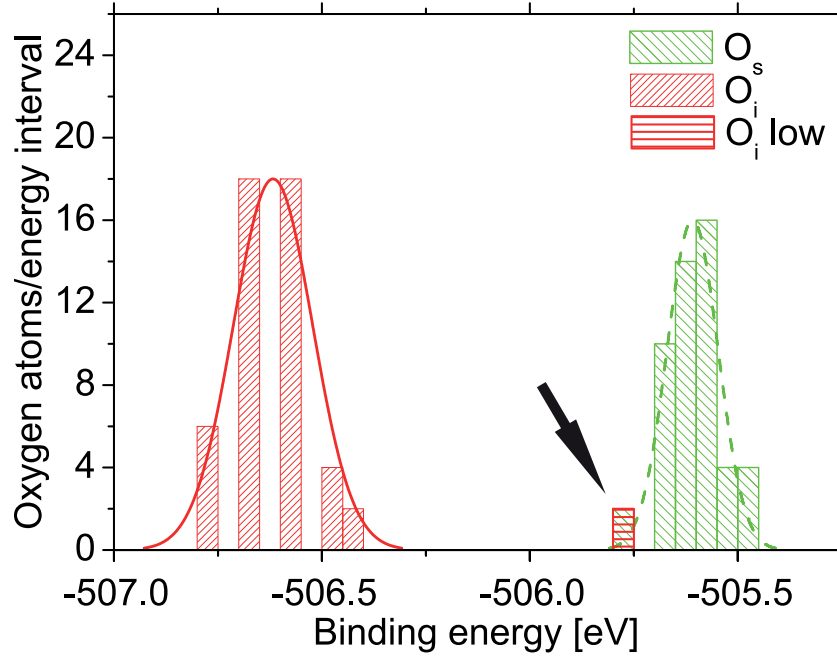


**Figure 6.12:** Histogram plot (bin size 0.05 eV) and distribution of the O 1s core levels of  $\text{O}_i$  (solid red line and bars) and  $\text{O}_s$  (dashed green line and bars) type oxygen atoms in the “5:7” structure. The arrow indicates the special  $\text{O}_i$  type oxygen atom named “ $\text{O}_i$  low” (red horizontal pattern) that has moved far away from the platinum surface and thus has a considerably lower O 1s binding energy.

to the value of the  $\text{O}_s$  type oxygen atoms. This indicates a much *reduced* interaction (and charge transfer) of these  $\text{O}_i$  oxygen atoms with the interface Pt atoms.<sup>5</sup> This special  $\text{O}_i$  1s core level is indicated with an arrow and a horizontal pattern in Fig. 6.12 to improve visibility.

## 6.6 Summary and Conclusions

In this chapter, a detailed DFT-based study on the experimentally reported structures of the  $\text{CeO}_2/\text{Pt}(111)$  interface system was presented. The experimental structures were analyzed by relaxing three different starting geometries in case of the “3:4” structure and one in case of the “5:7” structure. The relaxation resulted in significant corrugation of the Pt surface and the ceria adlayers. The total energies of the structures were compared and the corresponding adsorption energy of the ceria adsorbate was calculated for each geometry. The corrugation of the topmost Pt layer in all considered structures followed a systematic

<sup>5</sup>In the case of the “3:4” “ $\text{O}_s$ ” structure, the corresponding atom is  $\text{O}_i7$  with a binding energy of  $-506.3$  eV.

pattern where the highest Pt atom always had an interface oxygen atom adsorbed on top. It was found that a simple model based on the stability of different adsorption sites qualitatively explains the energy differences found in the resulting geometries of the whole interface system. Furthermore, it was revealed that a direct matching of Ce and Pt is particularly unfavorable for the overall energetic stability of the interface.

An insight into the electronic properties and the bonding character was achieved by analysis of the density of states and the electron density. Strong interactions were detected that are mainly based on electrostatic interactions between the topmost Pt layer and the oxygen atoms at the interface, but some small contributions from hybridization have been found as well. These results were corroborated by the analysis of the bond character at the bond critical points (BCPs). A significant charge transfer occurs between the surface Pt atoms and the cerium and oxygen atoms of the ceria adlayer upon adsorption, depending on the distance between the individual atoms. This was also seen experimentally (see, e.g., Ref. [279]) and is related to *strong metal support interaction* (SMSI) often observed in metal/oxide catalytic systems [280–283]. The reduction of some of the  $\text{Ce}^{4+}$  ions seems crucial for the catalytic properties of the system. The position of the O 1s core levels is a good measure for the binding situation and depends on the local bond lengths and the charge transfer.

Despite of restricting the structure models to an idealized situation which ignores topics such as non-stoichiometry, vacancies, stepped surfaces, formation of islands, etc., the present calculations have shown a rich variety of bonding situations with varying bond lengths and charges depending on the local geometry. This provides a new insight into the structure-property relations which are relevant for ceria based catalysis.

## Summary and Conclusions

In this thesis, both experimental and theoretical methods were used to study the properties of catalytically active platinum surfaces and interfaces.

The experimental part of the work consisted of a comprehensive study of *catalytic CO oxidation on individual grains* of a *polycrystalline platinum foil* under high-vacuum conditions ( $\sim 10^{-5}$  mbar pressure range). The measurements were performed in a UHV apparatus consisting of a photoemission electron microscope (PEEM), a quadrupole mass spectrometer (QMS), sample preparation facilities, gas supply and, at a later stage of the experimental work, of an X-ray photoelectron spectroscopy (XPS) system. The experiments were based on a novel approach that comprised a combination of PEEM and QMS to study both global and spatially-resolved kinetics *in situ* under fully *identical conditions* for individual differently oriented crystal grains of a polycrystalline platinum sample.

This experimental approach was used to shed light on the specifics of differently oriented domains of a polycrystalline platinum foil in catalytic CO oxidation, with the focus being put on the *bistability region* of this reaction. First, the global (average) behavior of the polycrystalline sample was characterized with QMS by setting up *kinetic phase diagrams* both at (i) *constant oxygen pressure* under variation of temperature and (ii) at *constant temperature* for different oxygen pressures in the  $10^{-7}$ – $10^{-5}$  mbar range. These diagrams characterize the temperature and pressure dependence of the bistability region, respectively.

For setting up the phase diagrams, repeated experiments were performed where the *hysteresis* in the  $\text{CO}_2$  production rate under cyclic variation of the CO pressure was monitored at different temperatures. The positions of the kinetic phase transition points  $\tau_A$  and  $\tau_B$  were extracted from the individual hysteresis plots and either plotted against reciprocal temperature (giving the phase diagram at constant oxygen partial pressure) or

against the oxygen partial pressure chosen in the experiments (leading to the isothermal phase diagram). The kinetic phase diagram at constant oxygen partial pressure is *scissors-shaped* in  $(\lg p_{\text{CO}}, 1/T)$ -coordinates, i.e., the region of bistability becomes narrower with increasing temperature and eventually *vanishes* at higher temperatures. In turn, the isothermal kinetic phase diagram in  $(\lg p_{\text{O}_2}, \lg p_{\text{CO}})$ -coordinates consists of two nearly *parallel* lines that indicate the position of  $\tau_A$  and  $\tau_B$ .

The laterally resolving PEEM technique was used to study the catalytic properties of individual crystallographically differently oriented grains of the same sample. In a first step, PEEM was utilized to identify the orientation of different domains by comparing the domain-specific *work functions* of the clean and the adsorbate-covered surface. The resulting domain-orientation map was later validated by independent measurements using *electron backscatter diffraction (EBSD)*.

In the next step, digital video-PEEM sequences of the ongoing CO oxidation reaction were recorded simultaneously with QMS measurements. The sequences were then analyzed, and local kinetic transitions for individual (100), (110) and (111) domains were determined. These data were summarized in *local kinetic phase diagrams* for individual low Miller-index orientations.

The results of the PEEM measurements have shown that significant differences exist in the catalytic activity of the individual differently oriented domains according to their respective *crystallographic orientation*. For example, it was found that the crystal grains always deactivate catalytically in the order  $\tau_{A,Pt(111)} < \tau_{A,Pt(100)} < \tau_{A,Pt(110)}$  at increasing CO pressure and reactivate in the opposite order. The present locally-resolved PEEM studies indicated a *quasi-independent behavior* of the individual domains with respect to CO oxidation. This can be rationalized by considering potential mechanisms of reactive coupling (synchronization) between the facets, namely *diffusion coupling* that is responsible for synchronization of local transitions at small (i.e., nanometer) length scales and *gas phase coupling* at pressures higher than  $10^{-4}$  mbar. Apparently, the domain boundaries effectively block diffusion coupling, and the applied pressure conditions ( $\sim 10^{-5}$  mbar) seem insufficient for synchronization via gas phase coupling.

Furthermore, the experiments showed that a simple averaging technique like QMS does not characterize a polycrystalline sample sufficiently, since conditions are possible where the overall catalytic activity may be still at a relatively high level although some of the domains are already deactivated due to CO poisoning. The same may take place during the reactivation of the sample, i.e., some of the domains may already be activated (oxygen-

covered) again while the global  $\text{CO}_2$  production rate is still at a low overall level, since the majority of the domains is still inactive (CO-covered).

On the basis of the domain-dependent PEEM data, it was possible to “reconstruct” the global kinetic phase diagram from the local kinetic phase diagrams by a superposition based on the distribution of the individual crystallographic domains on the polycrystalline sample surface. The resulting reconstruction was in quantitative agreement with the original phase diagram obtained by QMS measurements, indicating that all major contributions to the global kinetics have been considered by the PEEM experiments.

Kinetic transitions that are related to *catalytic ignition* and *extinction* were also studied in this work by performing simultaneous PEEM and QMS experiments at constant  $p_{\text{CO}}/p_{\text{O}_2}$ -ratio under variation of the sample temperature at a constant heating/cooling rate. The transition points  $\tau_A^*$  and  $\tau_B^*$  resulting from these experiments on ignition and extinction could also be used for setting up kinetic phase diagrams. Comparing the results from variation of  $p_{\text{CO}}$  with those obtained by temperature variation (ignition/extinction) showed a quantitative agreement, thereby proving the correspondence of the two different experimental approaches.

The PEEM results on catalytic ignition/extinction were compared to experiments using *field ion microscopy (FIM)* that were performed on the nanometer-sized apex of a Pt field emitter tip in the similar pressure range. The method of *proper orthogonal decomposition (POD)* was used for the analysis of the corresponding FIM-video sequences, which allows to calculate the spatial correlations and thus helps to reveal the spatial coupling occurring during the catalytic ignition. In contrast to the quasi-independent behavior of the macroscopic domains of polycrystalline Pt foil observed with PEEM, the nanometer-sized domains on the tip (which are separated by atomic steps) act in a coherent way due to synchronization by diffusion coupling, i.e., the kinetic transitions take place on the different (hkl)-domains simultaneously.

*Elliptic reaction-diffusion fronts* were studied in PEEM experiments for [110]-oriented domains of different sizes present on the surface of the polycrystalline Pt foil. Analyzing the temporal evolution of the axes lengths of elliptical fronts from corresponding PEEM video sequences allowed to obtain the propagation velocities of the reaction-diffusion fronts along the main crystallographic directions. The resulting velocities are in quantitative agreement with literature data from single-crystal studies on Pt(110). In addition, the elliptic shape of the reaction-diffusion fronts allows determining the azimuthal orientation of different Pt(110) domains on the polycrystalline Pt foil, since the main axes of the ellipses are aligned along the main crystallographic directions  $[1\bar{1}0]$  and  $[001]$ .

## 7 Summary and Conclusions

Summarizing the experimental part, it was shown in the present work that both the spatially-resolved (domain dependent) and global kinetics of a polycrystalline sample can be monitored in one experiment under fully identical conditions for all differently oriented domains. This can, e.g., be used to identify pace-making specifics of a catalytic surface reaction on heterogeneous samples and thereby may pave the way for subsequent optimization of the catalyst material.

The theoretical part of this work consisted of a comprehensive investigation of the  $\text{CeO}_2/\text{Pt}(111)$  interface by means of *first-principles density functional theory calculations*. The ceria-platinum system is very important for catalysis because ceria is known both for its excellent *oxygen-storage capacity (OSC)* and for its *promoting effect* in catalytic CO oxidation. Two different experimentally known surface structures of this system, namely a  $(1.4 \times 1.4)$  (equal to a 5 : 7 matching of  $\text{CeO}_2$  and Pt) and a smaller  $(4 \times 4)$  structure (3 : 4 matching), were considered in this study that made use of the WIEN2k software.

In case of the investigated interface structure, many different adsorption geometries are possible depending on the exact matching of adsorbate and substrate layer. Three such geometries were investigated in case of the  $(4 \times 4)$  structure, whereas the large size of the unit cell of the  $(1.4 \times 1.4)$  structure already includes a large variety of local matching geometries, and therefore only one of them was considered here.

Geometry relaxation of the structures leads to the corrugation of the adsorbate and substrate layer in all investigated cases. In order to figure out the most stable structure, the total energies and adsorption energies of all the different matching geometries for the  $(4 \times 4)$  structure type were compared. It was revealed that a geometry with a preferential on-top matching between *surface oxygen* and platinum is the most stable one among those investigated.

The electronic properties and the bonding character were studied by analyzing the total and partial *density of states (DOS)* as well as the *difference electron density*. The DOS analysis indicated that even slight differences in the individual atom-to-atom matching geometry between  $\text{CeO}_2$  and Pt have a profound effect on the partial densities of states of the involved atoms, a result that was also affirmed by evaluating the electron density. The *local density of states (LDOS)* was calculated at different distances to the sample surface, and the corresponding plots were compared to experimental STM measurements. The plots showed a strong dependence on the distance of the LDOS plane to the surface and reproduced the main features of the experiments.

The “atoms in molecules” (AIM) method was used to estimate the charge transfer occurring during  $\text{CeO}_2$  adsorption, which indicated a reduction of some of the  $\text{Ce}^{4+}$  ions



## 7 Summary and Conclusions

in the adsorbate layer to  $\text{Ce}^{3+}$  due to the interaction with the interface platinum atoms. Besides that, also the bond character and the O 1s core level shifts were analyzed in this work.

Summarizing the theoretical part, strong interactions were found to exist between ceria and the Pt(111) surface depending on the individual atom-to-atom matching geometry. Although the present study did not take into account defects in the surface structure (e.g., oxygen vacancies, which are very common for ceria), the observed partial reduction of  $\text{Ce}^{4+}$  to  $\text{Ce}^{3+}$  ions by the platinum substrate is crucial for the unique properties of ceria-containing catalysts.

# List of Figures

2.1	Original experimental setup. . . . .	6
2.2	Final evolution stage of the experimental setup. . . . .	7
2.3	Platinum sample surface. . . . .	10
2.4	Evolution of the sample holder design. . . . .	12
2.5	New sample load-lock. . . . .	14
2.6	Photoelectric effect. . . . .	16
2.7	Image and scheme of a photoemission electron microscope (PEEM). . . . .	19
2.8	Scheme of quadrupole mass spectrometry (QMS). . . . .	22
2.9	X-ray photoelectron spectra of the platinum sample. . . . .	24
2.10	Principles of field emission based microscopy. . . . .	26
2.11	The FIM UHV system. . . . .	27
2.12	Scheme of electron backscatter diffraction (EBSD). . . . .	29
3.1	Crystallographic unit cell and low Miller-index planes of face-centered cubic ( <i>fcc</i> ) platinum. . . . .	31
3.2	Surface structures of Pt(110) and Pt(100). . . . .	33
3.3	Potential energy diagram of the adsorption process. . . . .	35
3.4	Geometries and Blyholder model of CO adsorption on platinum surfaces. . . . .	38
3.5	One-dimensional scheme of surface diffusion of adsorbates. . . . .	42
3.6	Scheme of the Langmuir-Hinshelwood mechanism in catalytic CO oxidation on Pt surfaces. . . . .	46
3.7	Reaction pathway of catalytic CO oxidation. . . . .	47
3.8	Asymmetric inhibition in catalytic CO oxidation. . . . .	48
3.9	Schematic hysteresis and kinetic phase diagram. . . . .	49
3.10	Schematic plot of the function $\Theta_{CO}(p_{CO})$ . . . . .	51
4.1	Scheme of the experiments. . . . .	57
4.2	Domain orientation by PEEM and EBSD. . . . .	60
4.3	Hysteresis in the CO <sub>2</sub> production rate during cyclic variation of the CO partial pressure. . . . .	63
4.4	Global kinetic phase diagram for catalytic CO oxidation at constant oxygen pressure. . . . .	65
4.5	Global kinetic phase diagram at constant temperature. . . . .	66
4.6	Plot of the local PEEM intensity for a single Pt(110) facet. . . . .	67

## List of Figures

4.7	Local (domain-specific) kinetic phase diagrams for (100), (110) and (111) domains. . . . .	69
4.8	Global and local results of an ignition/extinction experiment. . . . .	71
4.9	Global and local kinetic phase diagrams with transition points related to ignition/extinction. .	72
4.10	Sequence of FIM images recorded during a kinetic phase transition related to catalytic ignition.	74
4.11	Comparison of POD and original FIM intensity. . . . .	76
4.12	Global and local kinetic phase diagrams with ignition/extinction points at higher oxygen pres- sure. . . . .	78
4.13	Global kinetic phase diagrams obtained by superposition of domain-specific diagrams. . . . .	79
4.14	Propagation of elliptic oxygen reaction fronts on an anisotropic Pt(110) domain during cat- alytic CO oxidation. . . . .	81
4.15	Qualitative scheme of reaction-diffusion front propagation. . . . .	83
4.16	Front propagation velocities of the elliptical reaction-diffusion fronts at various temperatures.	84
5.1	Scheme of the Kohn-Sham approach to the quantum many-body problem. . . . .	93
5.2	Scheme of an augmented basis set. . . . .	98
6.1	Relationship between air-to-fuel ratio and three-way catalyst efficiency. . . . .	103
6.2	Oxygen vacancy structures on ceria surfaces. . . . .	104
6.3	Structure of bulk ceria. . . . .	106
6.4	Schematic top views of the (111) surfaces of adsorbate and substrate layers leading to the pe- riodicity of the “3:4” structure. . . . .	110
6.5	Ball models of the different “3:4” and “5:7” structure types after geometry optimization. . . . .	112
6.6	Total density of states (TDOS) of CeO <sub>2</sub> /Pt, a free Pt slab and nonadsorbed CeO <sub>2</sub> for the “3:4” (“O <sub>s</sub> ”-type) structure. . . . .	119
6.7	Total density of states (TDOS) and partial density of states (PDOS) of all atomic species for the “3:4” (“O <sub>s</sub> ”-type) structure. . . . .	120
6.8	Two PDOS plots for the “3:4” (“O <sub>s</sub> ”-type) structure illustrating the differences in interaction between substrate and adsorbate layer. . . . .	121
6.9	Difference electron density $\Delta n(r)$ in the (11 $\bar{2}$ 0) plane of the “3:4” (“O <sub>s</sub> ”-type) structure. . . . .	123
6.10	Constant height local density of states (LDOS) plots of the “3:4” structure for different dis- tances to the sample surface. . . . .	124
6.11	Constant height local density of states (LDOS) plot of a 2 × 2 supercell of the “5:7” structure. .	125
6.12	Histogram plot and distribution of the O 1s core levels of O <sub>i</sub> and O <sub>s</sub> type oxygen atoms in the “5:7” structure. . . . .	130

# List of Tables

3.1	Saturation coverages and adsorption structures of CO and (atomic) oxygen on the individual low Miller-index planes of platinum at room temperature. . . . .	36
4.1	Work function values for the clean, CO- and oxygen-covered Pt(hkl) surface orientations. . . .	61
4.2	Reaction-diffusion front propagation velocities on Pt(110) domains as a function of sample temperature. . . . .	83
4.3	Diffusion and reaction parameters used for the fit to Luther's equation. . . . .	84
6.1	Resulting corrugation of the Pt interface and the ceria adsorbate layer after relaxation in the investigated matching geometries. . . . .	114
6.2	Total energies $E_{tot}$ and adsorption energies $E_{ads}$ of the "3:4" and "5:7" geometries. . . . .	117
6.3	Atomic charges and resulting charge transfer compared to the free substructures of Pt and CeO <sub>2</sub> obtained with AIM for the "3:4" ("O <sub>s</sub> "-type) CeO <sub>2</sub> /Pt(111) structure. . . . .	127

# References

- [1] W. OSTWALD, *Z. Phys. Chem.* **15**, 705 (1894). 1
- [2] F. HABER, *Z. Elektrochem.* **16**, 244 (1910). 1
- [3] R. DI MONTE and J. KAŠPAR, *Top. Catal.* **28**, 47 (2004). 1, 103
- [4] G. A. SOMORJAI, *Chem. Rev.* **96**, 1223 (1996). 2
- [5] G. ERTL, *Angew. Chem. Int. Ed.* **47**, 3524 (2008). 2, 15, 52
- [6] G. A. SOMORJAI and Y. LI, *Introduction to Surface Chemistry and Catalysis*, John Wiley & Sons Inc, 2010. 2
- [7] F. ZAERA, *Surf. Sci.* **500**, 947 (2002). 3
- [8] G. RUPPRECHTER, *Adv. Catal.* **51**, 133 (2007). 3
- [9] B. HAMMER and J. NØRSKOV, *Adv. Catal.* **45**, 71 (2000). 3
- [10] K. REUTER and M. SCHEFFLER, *Phys. Rev. Lett.* **90**, 46103 (2003). 3
- [11] P. BLAHA, K. SCHWARZ, G. K. H. MADSEN, D. KVASNICKA, and J. LUITZ:, *WIEN2k: An Augmented Plane Wave + Local Orbitals Program for Calculating Crystal Properties*, Vienna University of Technology, Techn. Universität Wien Getreidemarkt 9/156 A-1060 Wien/Austria, 2001. 4, 87, 108
- [12] W. WEISS, M. RITTER, D. ZSCHERPEL, M. SWOBODA, and R. SCHLÖGL, *J. Vac. Sci. Technol., A* **16**, 21 (1998). 8, 11
- [13] J. POHL, *Z. Tech. Phys.* **15**, 579 (1934). 15
- [14] E. BRÜCHE, *Z. Phys. A: Hadrons Nucl.* **86**, 448 (1933). 15
- [15] W. ENGEL, M. E. KORDESCH, H. H. ROTERMUND, S. KUBALA, and A. VON OERTZEN, *Ultramicroscopy* **36**, 148 (1991). 15
- [16] M. E. KORDESCH, W. ENGEL, G. J. LAPEYRE, E. ZEITLER, and A. M. BRADSHAW, *Appl. Phys. A* **49**, 399 (1989). 15
- [17] E. BAUER, M. MUNDSCHAU, W. SWIECH, and W. TELIEPS, *Ultramicroscopy* **31**, 49 (1989). 15

## References

- [18] H. H. ROTERMUND, W. ENGEL, S. JAKUBITH, A. VON OERTZEN, and G. ERTL, *Ultramicroscopy* **36**, 164 (1991). 15
- [19] H. HERTZ, *Ann. Phys.* **267**, 983 (1887). 15
- [20] W. HALLWACHS, *Ann. Phys.* **269**, 301 (1888). 15
- [21] A. EINSTEIN, *Ann. Phys.* **322**, 132 (1905). 15
- [22] E. BAUER, *Rep. Prog. Phys.* **57**, 895 (1994). 17
- [23] E. BAUER, *Surf. Rev. Lett.* **5**, 1275 (1998). 17
- [24] R. M. OMAN, *Adv. Electron El. Phys.* **26**, 217 (1969). 17
- [25] M. P. SEAH and W. A. DENCH, *Surf. Interface Anal.* **1**, 2 (1979). 18, 23
- [26] R. SMOLUCHOWSKI, *Phys. Rev.* **60**, 661 (1941). 20, 60
- [27] R. H. FOWLER, *Phys. Rev.* **38**, 45 (1931). 20
- [28] J. LAUTERBACH, G. HAAS, H. H. ROTERMUND, and G. ERTL, *Surf. Sci.* **294**, 116 (1993). 20, 46, 55, 59, 60, 61, 70, 79, 80
- [29] K. CHRISTMANN, G. ERTL, and T. PIGNET, *Surf. Sci.* **54**, 365 (1976). 20, 36
- [30] A. SCHAAK and R. IMBIHL, *J. Chem. Phys.* **116**, 9021 (2002). 20
- [31] O. RENAULT, R. BROCHIER, A. ROULE, P.-H. HAUMESSER, B. KRÖMKER, and D. FUNNEMANN, *Surf. Interface Anal.* **38**, 375 (2006). 20
- [32] Y. SUCHORSKI, C. SPIEL, D. VOGEL, W. DRACHSEL, R. SCHLÖGL, and G. RUPPRECHTER, *ChemPhysChem* **11**, 3231 (2010). 20, 57, 59
- [33] W. PAUL and H. STEINWEDEL, *Z. Naturforsch., A: Phys. Sci.* **8**, 448 (1953). 21
- [34] S. HAGSTRÖM, C. NORDLING, and K. SIEGBAHN, *Phys. Lett.* **9**, 235 (1964). 23
- [35] A. FAHLMAN, K. HAMRIN, J. HEDMAN, R. NORDBERG, C. NORDLING, and K. SIEGBAHN, *Nature* **210**, 4 (1966). 23
- [36] U. GELIUS, *Phys. Scr.* **9**, 133 (1974). 24
- [37] Y. SUCHORSKI, W. A. SCHMIDT, N. ERNST, J. H. BLOCK, and H. J. KREUZER, *Prog. Surf. Sci.* **48**, 121 (1995). 25
- [38] G. FRIEDBACHER and H. BUBERT, editors, *Surface and Thin-Film Analysis*, Wiley-VCH, 2011. 26
- [39] F. J. HUMPHREYS, *J. Mat. Sci.* **36**, 3833 (2001). 28
- [40] A. J. SCHWARTZ and M. KUMAR, *Electron backscatter diffraction in materials science*, Springer Verlag, 2009. 28
- [41] S. NISHIKAWA and S. KIKUCHI, *Nature* **121**, 1019 (1928). 28
- [42] Y. KAINUMA, *Acta Crystallogr.* **8**, 247 (1955). 28
- [43] J. T. KUMMER, *J. Phys. Chem.* **90**, 4747 (1986). 30

## References

- [44] J. N. ARMOR, *Appl. Catal., A* **176**, 159 (1999). 30
- [45] B. EISENMANN and H. SCHÄFER, 6.1 Elements, in *Landolt-Börnstein - Group III Condensed Matter*, edited by K.-H. HELLWEGE and A. M. HELLWEGE, volume 14a. 31
- [46] M. MCLEAN and H. MYKURA, *Surf. Sci.* **5**, 466 (1966). 32
- [47] J. T. YATES, *J. Vac. Sci. Technol., A* **13**, 1359 (1995). 32
- [48] S. LADAS, R. IMBIHL, and G. ERTL, *Surf. Sci.* **197**, 153 (1988). 32
- [49] M. P. COX, G. ERTL, and R. IMBIHL, *Phys. Rev. Lett.* **54**, 1725 (1985). 33
- [50] M. EISWIRTH and G. ERTL, *Surf. Sci.* **177**, 90 (1986). 33, 83, 84
- [51] R. J. BEHM, P. A. THIEL, P. R. NORTON, and G. ERTL, *J. Chem. Phys.* **78**, 7437 (1983). 33, 34, 38
- [52] A. BARALDI, E. VESSELLI, L. BIANCHETTIN, G. COMELLI, S. LIZZIT, L. PETACCIA, S. DE GIRONCOLI, A. LOCATELLI, T. O. MENTES, L. ABALLE, et al., *J. Chem. Phys.* **127**, 164702 (2007). 33
- [53] H. P. BONZEL, C. R. HELMS, and S. KELEMEN, *Phys. Rev. Lett.* **35**, 1237 (1975). 33
- [54] P. R. NORTON, J. A. DA VIES, D. K. CREBER, C. W. SITTER, and T. E. JACKMAN, *Surf. Sci.* **108**, 205 (1981). 33
- [55] A. BORG, A. M. HILMEN, and E. BERGENE, *Surf. Sci.* **306**, 10 (1994). 33, 34
- [56] P. A. THIEL, R. J. BEHM, P. R. NORTON, and G. ERTL, *Surf. Sci. Lett.* **121**, L553 (1982). 34
- [57] K. GRIFFITHS, T. E. JACKMAN, J. A. DAVIES, and P. R. NORTON, *Surf. Sci.* **138**, 113 (1984). 34, 40
- [58] D. VOGEL, C. SPIEL, Y. SUCHORSKI, A. URICH, R. SCHLÖGL, and G. RUPPRECHTER, *Surf. Sci.* **605**, 1999 (2011). 34, 59
- [59] P. FERY, W. MORITZ, and D. WOLF, *Phys. Rev. B* **38**, 7275 (1988). 34
- [60] T. GRITSCH, D. COULMAN, R. J. BEHM, and G. ERTL, *Phys. Rev. Lett.* **63**, 1086 (1989). 34
- [61] K. SWAMY, E. BERTEL, and I. VILFAN, *Surf. Sci.* **425**, L369 (1999). 34
- [62] P. THOSTRUP, E. K. VESTERGAARD, T. AN, E. LÆGSGAARD, and F. BESENBACHER, *J. Chem. Phys.* **118**, 3724 (2003). 34
- [63] R. IMBIHL, A. E. REYNOLDS, and D. KALETTA, *Phys. Rev. Lett.* **67**, 275 (1991). 34
- [64] T. NIEDERMAYER, H. SCHLICHTING, D. MENZEL, S. H. PAYNE, and H. J. KREUZER, *Phys. Rev. Lett.* **89**, 126101 (2002). 35
- [65] K. WANDELT and J. E. HULSE, *J. Chem. Phys.* **80**, 1340 (1984). 35
- [66] A. MCNAUGHT and A. WILKINSON, *IUPAC compendium of chemical terminology*, volume 2, Blackwell Scientific Publications, 1997. 36
- [67] I. LANGMUIR, *Trans. Faraday Soc.* **17**, 607 (1922). 37, 45
- [68] I. LANGMUIR, *Trans. Faraday Soc.* **17**, 621 (1922). 37, 45
- [69] G. ERTL, M. NEUMANN, and K. M. STREIT, *Surf. Sci.* **64**, 393 (1977). 37, 38, 39, 59

## References

- [70] G. BLYHOLDER, *J. Phys. Chem.* **68**, 2772 (1964). 37
- [71] H. STEININGER, S. LEHWALD, and H. IBACH, *Surf. Sci.* **123**, 264 (1982). 38, 39
- [72] B. E. HAYDEN and A. M. BRADSHAW, *Surf. Sci.* **125**, 787 (1983). 38
- [73] D. F. OGLETREE, M. A. VAN HOVE, and G. A. SOMORJAI, *Surf. Sci.* **173**, 351 (1986). 38
- [74] R. W. MCCABE and L. D. SCHMIDT, *Surf. Sci.* **60**, 85 (1976). 38, 39
- [75] C. E. WARTNABY, A. STUCK, Y. Y. YEO, and D. A. KING, *J. Phys. Chem.* **100**, 12483 (1996). 38, 39, 40
- [76] M. NOWICKI, A. EMUNDTS, G. PIRUG, and H. P. BONZEL, *Surf. Sci.* **478**, 180 (2001). 38
- [77] G. BRODÉN, G. PIRUG, and H. P. BONZEL, *Surf. Sci.* **72**, 45 (1978). 38, 39
- [78] R. MARTIN, P. GARDNER, and A. M. BRADSHAW, *Surf. Sci.* **342**, 69 (1995). 38
- [79] Y. Y. YEO, L. VATTUONE, and D. A. KING, *J. Chem. Phys.* **106**, 392 (1997). 39, 40
- [80] W. A. BROWN, R. KOSE, and D. A. KING, *Chem. Rev.* **98**, 797 (1998). 39, 40
- [81] Y. Y. YEO, L. VATTUONE, and D. A. KING, *J. Chem. Phys.* **104**, 3810 (1996). 39
- [82] J. FAIR and R. J. MADIX, *J. Chem. Phys.* **73**, 3480 (1980). 39
- [83] J. L. GLAND, B. A. SEXTON, and G. B. FISHER, *Surf. Sci.* **95**, 587 (1980). 39
- [84] Y. OHNO and T. MATSUSHIMA, *Surf. Sci.* **241**, 47 (1991). 39, 40
- [85] A. C. LUNTZ, J. GRIMBLot, and D. E. FOWLER, *Phys. Rev. B* **39**, 12903 (1989). 39
- [86] A. N. ARTSYUKHOVICH, V. A. UKRAINTSEV, and I. HARRISON, *Surf. Sci.* **347**, 303 (1996). 39
- [87] H. STEININGER, S. LEHWALD, and H. IBACH, *Surf. Sci.* **123**, 1 (1982). 40
- [88] A. C. LUNTZ, M. D. WILLIAMS, and D. S. BETHUNE, *J. Chem. Phys.* **89**, 4381 (1988). 40
- [89] D. R. MONROE and R. P. MERRILL, *J. Catal.* **65**, 461 (1980). 40
- [90] C. T. CAMPBELL, G. ERTL, H. KUIPERS, and J. SEGNER, *Surf. Sci.* **107**, 220 (1981). 40
- [91] C. PUGLIA, A. NILSSON, B. HERNNÄS, O. KARIS, P. BENNICHI, and N. MÄRTENSSON, *Surf. Sci.* **342**, 119 (1995). 40
- [92] Z. GU and P. B. BALBUENA, *J. Phys. Chem. C* **111**, 9877 (2007). 40
- [93] N. FREYER, M. KISKINOVA, G. PIRUG, and H. P. BONZEL, *Surf. Sci.* **166**, 206 (1986). 40, 53
- [94] J. SCHMIDT, C. STUHLMANN, and H. IBACH, *Surf. Sci.* **284**, 121 (1993). 40
- [95] A. V. WALKER, B. KLÖTZER, and D. A. KING, *J. Chem. Phys.* **109**, 6879 (1998). 40
- [96] R. DUCROS and R. P. MERRILL, *Surf. Sci.* **55**, 227 (1976). 40
- [97] E. JANIN, H. VON SCHENCK, M. GÖTHELID, U. KARLSSON, and M. SVENSSON, *Phys. Rev. B* **61**, 13144 (2000). 40
- [98] G. N. DERRY and P. N. ROSS, *J. Chem. Phys.* **82**, 2772 (1985). 40



## References

- [99] G. KNERINGER and F. P. NETZER, *Surf. Sci.* **49**, 125 (1975). 40
- [100] P. R. NORTON, K. GRIFFITHS, and P. E. BINDNER, *Surf. Sci.* **138**, 125 (1984). 40, 61
- [101] J. F. WEAVER, J. J. CHEN, and A. L. GERRARD, *Surf. Sci.* **592**, 83 (2005). 40
- [102] R. SHUMBERA, H. H. KAN, and J. F. WEAVER, *Surf. Sci.* **601**, 4809 (2007). 40
- [103] N. A. SALIBA, Y. L. TSAI, C. PANJA, and B. E. KOEL, *Surf. Sci.* **419**, 79 (1999). 41
- [104] W. LI, L. ÖSTERLUND, E. K. VESTERGAARD, R. T. VANG, J. MATTHIESEN, T. M. PEDERSEN, E. LÆGS-  
GAARD, B. HAMMER, and F. BESENBACHER, *Phys. Rev. Lett.* **93**, 146104 (2004). 41
- [105] R. IMBIHL and G. ERTL, *Chem. Rev.* **95**, 697 (1995). 41
- [106] A. VON OERTZEN, A. MIKHAILOV, H. H. ROTERMUND, and G. ERTL, *Surf. Sci.* **350**, 259 (1996). 41, 44
- [107] A. V. WALKER, B. KLÖTZER, and D. A. KING, *J. Chem. Phys.* **112**, 8631 (2000). 41
- [108] N. McMILLAN, T. LELE, C. SNIVELY, and J. LAUTERBACH, *Catal. Today* **105**, 244 (2005). 41
- [109] J. LAUTERBACH, K. ASAKURA, and H. H. ROTERMUND, *Surf. Sci.* **313**, 52 (1994). 41
- [110] A. VON OERTZEN, A. S. MIKHAILOV, H. H. ROTERMUND, and G. ERTL, *J. Phys. Chem. B* **102**, 4966  
(1998). 41
- [111] H. H. ROTERMUND, M. POLLMANN, and I. G. KEVREKIDIS, *Chaos* **12**, 157 (2002). 41
- [112] P. R. NORTON and P. J. RICHARDS, *Surf. Sci.* **49**, 567 (1975). 41
- [113] Z. M. LIU, Y. ZHOU, F. SOLYMOSI, and J. M. WHITE, *J. Phys. Chem.* **93**, 4383 (1989). 41
- [114] H.-J. FREUND and M. W. ROBERTS, *Surf. Sci. Rep.* **25**, 225 (1996). 41
- [115] R. GOMER, *Rep. Prog. Phys.* **53**, 917 (1990). 41, 43
- [116] J. V. BARTH, *Surf. Sci. Rep.* **40**, 75 (2000). 43
- [117] L. BOLTZMANN, *Ann. Phys.* **289**, 959 (1894). 43
- [118] C. MATANO, *Jpn. J. Phys.* **8**, 109 (1933). 43
- [119] S. NETTESHEIM, A. VON OERTZEN, H. H. ROTERMUND, and G. ERTL, *J. Chem. Phys.* **98**, 9977 (1993).  
44, 60, 61, 80, 83, 84
- [120] A. VON OERTZEN, H. H. ROTERMUND, and S. NETTESHEIM, *Surf. Sci.* **311**, 322 (1994). 44, 80, 83, 84
- [121] A. J. PATCHETT, F. MEISSEN, W. ENGEL, A. M. BRADSHAW, and R. IMBIHL, *Surf. Sci.* **454-456**, 341  
(2000). 44, 80
- [122] B. POELSEMA, L. K. VERHEIJ, and G. COMSA, *Phys. Rev. Lett.* **49**, 1731 (1982). 44
- [123] R. IMBIHL, M. P. COX, G. ERTL, H. MULLER, and W. BRENIG, *J. Chem. Phys.* **83**, 1578 (1985). 44
- [124] V. J. KWASNIEWSKI and L. D. SCHMIDT, *Surf. Sci.* **274**, 329 (1992). 44
- [125] A. BOGICEVIC, J. STRÖMQUIST, and B. I. LUNDQVIST, *Phys. Rev. B* **57**, 4289 (1998). 44
- [126] M. W. CHASE JR, *J. Phys. Chem. Ref. Data* **9**, 1 (1998). 45

## References

- [127] W. TSANG and R. F. HAMPSON, *J. Phys. Chem. Ref. Data* **15**, 1087 (1986). 45
- [128] G. ERTL, *Surf. Sci.* **299**, 742 (1994). 45
- [129] A. ALAVI, P. HU, T. DEUTSCH, P. L. SILVESTRELLI, and J. HUTTER, *Phys. Rev. Lett.* **80**, 3650 (1998). 45, 46, 47
- [130] J. WINTTERLIN, S. VÖLKENING, T. V. W. JANSSENS, T. ZAMBELLI, and G. ERTL, *Science* **278**, 1931 (1997). 45
- [131] R. L. PALMER and J. N. SMITH JR, *J. Chem. Phys.* **60**, 1453 (1974). 45
- [132] C. T. CAMPBELL, G. ERTL, H. KUIPERS, and J. SEGNER, *J. Chem. Phys.* **73**, 5862 (1980). 45
- [133] T. ENGEL and G. ERTL, *Adv. Catal.* **28**, 1 (1979). 45
- [134] K. KRISCHER, M. EISWIRTH, and G. ERTL, *J. Chem. Phys.* **96**, 9161 (1992). 46, 83, 84
- [135] D. M. COLLINS and W. E. SPICER, *Surf. Sci.* **69**, 85 (1977). 46
- [136] M. BÄR, C. ZÜLICHE, M. EISWIRTH, and G. ERTL, *J. Chem. Phys.* **96**, 8595 (1992). 50
- [137] V. P. ZHDANOV and B. KASEMO, *Surf. Sci. Rep.* **20**, 113 (1994). 50, 70
- [138] R. M. ZIFF, E. GULARI, and Y. BARSHAD, *Phys. Rev. Lett.* **56**, 2553 (1986). 50
- [139] S. VÖLKENING and J. WINTTERLIN, *J. Chem. Phys.* **114**, 6382 (2001). 50
- [140] F. SCHLÖGL, *Z. Phys. A: Hadrons Nucl.* **248**, 446 (1971). 51
- [141] F. SCHLÖGL, *Z. Phys. A: Hadrons Nucl.* **253**, 147 (1972). 51
- [142] F. SCHLÖGL, *Ber. Bunsen Ges. Phys. Chem.* **84**, 351 (1980). 51
- [143] M. BERDAU, A. KARPOWICZ, G. G. YELENIN, K. CHRISTMANN, and J. H. BLOCK, *J. Chem. Phys.* **106**, 4291 (1997). 51, 52, 57, 64
- [144] Y. SUCHORSKI, R. IMBIHL, and V. K. MEDVEDEV, *Surf. Sci.* **401**, 392 (1998). 51, 52
- [145] M. BERDAU, G. G. YELENIN, A. KARPOWICZ, M. EHSASI, K. CHRISTMANN, and J. H. BLOCK, *J. Chem. Phys.* **110**, 11551 (1999). 52, 55, 57, 64
- [146] Y. SUCHORSKI, R. WROBEL, S. BECKER, and H. WEISS, *J. Phys. Chem. C* **112**, 20012 (2008). 52, 57, 104, 107
- [147] M. EHSASI, M. BERDAU, T. REBITZKI, K. P. CHARLÉ, K. CHRISTMANN, and J. H. BLOCK, *J. Chem. Phys.* **98**, 9177 (1993). 52, 53
- [148] M. G. T. FECHNER, *Schweiggers J. f. Chem. u. Phys.* **53**, 129 (1828). 52
- [149] R. J. FIELD and M. BURGER, *Oscillations and traveling waves in chemical systems*, Wiley New York etc., 1985. 52
- [150] H. BEUSCH, P. FIEGUTH, and E. WICKE, *Chem. Ing. Tech.* **44**, 445 (1972). 52
- [151] G. ERTL, P. R. NORTON, and J. RÜSTIG, *Phys. Rev. Lett.* **49**, 177 (1982). 52
- [152] G. ERTL, *Adv. Catal.* **37**, 213 (1990). 52

## References

- [153] B. C. SALES, J. E. TURNER, and M. B. MAPLE, *Surf. Sci.* **114**, 381 (1982). 52, 53
- [154] V. BURROWS, S. SUNDARESAN, Y. CHABAL, and S. CHRISTMAN, *Surf. Sci.* **180**, 110 (1987). 52
- [155] N. A. COLLINS, S. SUNDARESAN, and Y. J. CHABAL, *Surf. Sci.* **180**, 136 (1987). 52
- [156] C. A. PIKIOS and D. LUSS, *Chem. Eng. Sci.* **32**, 191 (1977). 52
- [157] R. IMBIHL, *Surf. Sci.* **603**, 1671 (2009). 52
- [158] Y. SUCHORSKI, W. DRACHSEL, V. V. GORODETSKII, V. K. MEDVEDEV, and H. WEISS, *Surf. Sci.* **600**, 1579 (2006). 53
- [159] H.-J. FREUND, H. KUHLENBECK, J. LIBUDA, G. RUPPRECHTER, M. BÄUMER, and H. HAMANN, *Top. Catal.* **15**, 201 (2001). 54
- [160] D. GOODMAN, *J. Phys. Chem.* **100**, 13090 (1996). 55
- [161] H. H. ROTERMUND, *Surf. Sci.* **283**, 87 (1993). 55, 80
- [162] G. ERTL, *Appl. Surf. Sci.* **121-122**, 20 (1997). 55, 80
- [163] J. LAUTERBACH and H. H. ROTERMUND, *Catal. Lett.* **27**, 27 (1994). 55, 59, 60, 70, 80
- [164] H. GABASCH, W. UNTERBERGER, K. HAYEK, B. KLÖTZER, E. KLEIMENOV, D. TESCHNER, S. ZAFEIRATOS, M. HAVECKER, A. KNOP-GERICKE, R. SCHLÖGL, et al., *Surf. Sci.* **600**, 2980 (2006). 56
- [165] M. MORKEL, V. V. KAICHEV, G. RUPPRECHTER, H.-J. FREUND, I. P. PROSVIRIN, and V. I. BUKHTIYAROV, *J. Phys. Chem. B* **108**, 12955 (2004). 56
- [166] G. RUPPRECHTER, *Catal. Today* **126**, 3 (2007). 56
- [167] M. SANDER, R. IMBIHL, and G. ERTL, *J. Chem. Phys.* **97**, 5193 (1992). 58, 70
- [168] M. JOHANSSON, J. H. JØRGENSEN, and I. CHORKENDORFF, *Rev. Sci. Instrum.* **75**, 2082 (2004). 58
- [169] B. RAUSENBERGER, W. SWIECH, C. S. RASTOMJEE, M. MUNDSCHAU, W. ENGEL, E. ZEITLER, and A. M. BRADSHAW, *Chem. Phys. Lett.* **215**, 109 (1993). 59
- [170] G. LILIENKAMP and Y. SUCHORSKI, *Surf. Interface Anal.* **38**, 378 (2006). 59
- [171] C. SPIEL, D. VOGEL, Y. SUCHORSKI, W. DRACHSEL, R. SCHLÖGL, and G. RUPPRECHTER, *Catal. Lett.* **141**, 625 (2011). 59, 63, 66, 67, 81
- [172] D. VOGEL, C. SPIEL, Y. SUCHORSKI, and G. RUPPRECHTER, CO oxidation on a mesoscopic scale: from individual  $\mu\text{m}$ -sized Pd grains to oxides, Talk: 13th Palladium Day, Obergurgl, Austria; 04.10.2011 - 05.10.2011. 59
- [173] A. VON OERTZEN, H. H. ROTERMUND, S. JAKUBITH, and G. ERTL, *Ultramicroscopy* **36**, 107 (1991). 60, 61
- [174] B. E. NIEUWENHUYS and W. M. H. SACHTLER, *Surf. Sci.* **34**, 317 (1973). 61
- [175] J. MARIEN, *Bull. Soc. R. Liege* **45**, 103 (1976). 61
- [176] M. EHSASI, O. FRANK, J. H. BLOCK, and K. CHRISTMANN, *Chem. Phys. Lett.* **165**, 115 (1990). 70

## References

- [177] S. Y. YAMAMOTO, C. M. SURKO, and M. B. MAPLE, *J. Chem. Phys.* **103**, 8209 (1995). 70
- [178] M. M. SLINKO, A. A. UKHARSKII, and N. I. JAEGER, *Phys. Chem. Chem. Phys.* **3**, 1015 (2001). 70
- [179] D. A. FRANK-KAMENETSKII and N. THON, *Diffusion and heat exchange in chemical kinetics*, Princeton University Press Princeton, 1955. 70
- [180] M. RINNEMO, D. KULGINOV, S. JOHANSSON, K. L. WONG, V. P. ZHDANOV, and B. KASEMO, *Surf. Sci.* **376**, 297 (1997). 70
- [181] D. J. KAUL, R. SANT, and E. E. WOLF, *Chem. Eng. Sci.* **42**, 1399 (1987). 71
- [182] M. E. GARSKE and M. P. HAROLD, *Chem. Eng. Sci.* **47**, 623 (1992). 71
- [183] M. BOWKER, I. Z. JONES, R. A. BENNETT, F. ESCH, A. BARALDI, S. LIZZIT, and G. COMELLI, *Catal. Lett.* **51**, 187 (1998). 71
- [184] Y. SUCHORSKI, J. BEBEN, R. IMBIHL, E. W. JAMES, D.-J. LIU, and J. W. EVANS, *Phys. Rev. B* **63**, 165417 (2001). 74
- [185] Y. SUCHORSKI, J. BEBEN, and R. IMBIHL, *Surf. Sci.* **454**, 331 (2000). 75
- [186] S. BAGYAN, T. MAIR, Y. SUCHORSKI, M. J. B. HAUSER, and R. STRAUBE, *J. Phys. Chem. B* **112**, 14334 (2008). 75
- [187] H. H. ROTERMUND, *J. Electron. Spectrosc. Relat. Phenom.* **98**, 41 (1999). 80
- [188] S. JAKUBITH, H. H. ROTERMUND, W. ENGEL, A. VON OERTZEN, and G. ERTL, *Phys. Rev. Lett.* **65**, 3013 (1990). 80, 84
- [189] R. LUTHER, *Z. Elektrochem.* **12**, 596 (1906). 82
- [190] J. J. TYSON and J. P. KEENER, *Physica D* **32**, 327 (1988). 82
- [191] R. A. FISHER, *Ann. Human Genetics* **7**, 355 (1937). 83
- [192] F. MEISSEN, *Untersuchung der Musterbildung bei der katalytischen CO-Oxidation auf Pt {110} mittels Niederenergie-Elektronenmikroskopie*, PhD thesis, TU Berlin, 2001. 83, 84
- [193] J. KOHANOFF, *Electronic Structure Calculations for Solids and Molecules: Theory and Computational Methods*, Cambridge University Press, 2006. 87
- [194] K. CAPELLE, *Braz. J. Phys.* **36**, 1318 (2006). 87
- [195] S. COTTENIER, *Density Functional Theory and the family of (L)APW-methods: a step-by-step introduction*, Instituut voor Kern- en Stralingsfysica, K.U.Leuven, Belgium, 2002. 87, 98
- [196] E. SCHRÖDINGER, *Ann. Phys.* **79**, 361 (1926). 88
- [197] M. BORN and R. OPPENHEIMER, *Ann. Phys.* **84**, 457 (1927). 89
- [198] D. R. HARTREE, *Proc. Cambridge Phil. Soc.* **24**, 89 (1928). 90
- [199] V. FOCK, *Z. Phys. A: Hadrons Nucl.* **61**, 126 (1930). 90
- [200] L. H. THOMAS, *Proc. Cambridge Phil. Soc.* **23**, 542 (1927). 91

## References

- [201] E. FERMI, *Z. Phys. A: Hadrons Nucl.* **48**, 73 (1928). 91
- [202] P. HOHENBERG and W. KOHN, *Phys. Rev.* **136**, B864 (1964). 92
- [203] W. KOHN and L. J. SHAM, *Phys. Rev.* **140**, A1133 (1965). 92, 95
- [204] A. D. BECKE, *J. Chem. Phys.* **98**, 5648 (1993). 95
- [205] J. HEYD, G. E. SCUSERIA, and M. ERNZERHOF, *J. Chem. Phys.* **118**, 8207 (2003). 95
- [206] J. HEYD, G. E. SCUSERIA, and M. ERNZERHOF, *J. Chem. Phys.* **124**, 219906 (2006). 95
- [207] M. DION, H. RYDBERG, E. SCHRÖDER, D. C. LANGRETH, and B. I. LUNDQVIST, *Phys. Rev. Lett.* **92**, 246401 (2004). 95
- [208] D. M. CEPERLEY and B. J. ALDER, *Phys. Rev. Lett.* **45**, 566 (1980). 95
- [209] J. P. PERDEW and A. ZUNGER, *Phys. Rev. B* **23**, 5048 (1981). 95
- [210] J. P. PERDEW and Y. WANG, *Phys. Rev. B* **45**, 13244 (1992). 95
- [211] D. C. LANGRETH and M. J. MEHL, *Phys. Rev. Lett.* **47**, 446 (1981). 96
- [212] A. D. BECKE, *Phys. Rev. A* **38**, 3098 (1988). 96
- [213] C. LEE, W. YANG, and R. G. PARR, *Phys. Rev. B* **37**, 785 (1988). 96
- [214] Z. WU and R. E. COHEN, *Phys. Rev. B* **73**, 235116 (2006). 96
- [215] J. P. PERDEW, K. BURKE, and M. ERNZERHOF, *Phys. Rev. Lett.* **77**, 3865 (1996). 96, 109
- [216] J. HUBBARD, *Proc. R. Soc. London, Ser. A* **276**, 238 (1963). 96
- [217] J. HUBBARD, *Proc. R. Soc. London, Ser. A* **277**, 237 (1964). 96, 109
- [218] J. HUBBARD, *Proc. R. Soc. London, Ser. A* **281**, 401 (1964). 96
- [219] V. I. ANISIMOV, J. ZAAENEN, and O. K. ANDERSEN, *Phys. Rev. B* **44**, 943 (1991). 96, 109
- [220] G. K. H. MADSEN and P. NOVÁK, *Europhys. Lett.* **69**, 777 (2005). 97
- [221] C. SPIEL, P. BLAHA, and K. SCHWARZ, *Phys. Rev. B* **79**, 115123 (2009). 97
- [222] S. F. BOYS, *Proc. R. Soc. London, Ser. A* **200**, 542 (1950). 97
- [223] J. C. SLATER, *Phys. Rev.* **36**, 57 (1930). 97
- [224] J. C. SLATER, *Phys. Rev.* **42**, 33 (1932). 97
- [225] F. BLOCH, *Z. Phys. A: Hadrons Nucl.* **52**, 555 (1929). 97
- [226] P. E. BLÖCHL, *Phys. Rev. B* **50**, 17953 (1994). 97
- [227] H. HELLMANN, *J. Chem. Phys.* **3**, 61 (1935). 98
- [228] J. C. PHILLIPS and L. KLEINMAN, *Phys. Rev.* **116**, 287 (1959). 98
- [229] K. SCHWARZ and P. BLAHA, *Comp. Mater. Sci.* **28**, 259 (2003). 98, 108
- [230] J. C. SLATER, *Phys. Rev.* **51**, 846 (1937). 99

## References

- [231] O. K. ANDERSEN, *Phys. Rev. B* **12**, 3060 (1975). 99
- [232] D. SINGH, *Phys. Rev. B* **43**, 6388 (1991). 99, 108
- [233] E. SJÖSTEDT, L. NORDSTRÖM, and D. J. SINGH, *Solid State Commun.* **114**, 15 (2000). 99, 108
- [234] G. K. H. MADSEN, P. BLAHA, K. SCHWARZ, E. SJÖSTEDT, and L. NORDSTRÖM, *Phys. Rev. B* **64**, 195134 (2001). 101
- [235] K. SCHWARZ, P. BLAHA, and G. K. H. MADSEN, *Comput. Phys. Commun.* **147**, 71 (2002). 101
- [236] C. SPIEL, P. BLAHA, Y. SUCHORSKI, K. SCHWARZ, and G. RUPPRECHTER, *Phys. Rev. B* **84**, 045412 (2011). 102
- [237] A. TROVARELLI, *Catal. Rev. Sci. Eng.* **38**, 439 (1996). 103
- [238] A. TROVARELLI, C. DE LEITENBURG, M. BOARO, and G. DOLCETTI, *Catal. Today* **50**, 353 (1999). 103
- [239] G. A. DELUGA, J. R. SALGE, L. D. SCHMIDT, and X. E. VERYKIOS, *Science* **303**, 993 (2004). 103
- [240] H. INABA and H. TAGAWA, *Solid State Ionics* **83**, 1 (1996). 104
- [241] F. ESCH, S. FABRIS, L. ZHOU, T. MONTINI, C. AFRICH, P. FORNASIERO, G. COMELLI, and R. ROSEI, *Science* **309**, 752 (2005). 104, 106
- [242] Y. SUCHORSKI, R. WROBEL, S. BECKER, B. STRZELCZYK, W. DRACHSEL, and H. WEISS, *Surf. Sci.* **601**, 4843 (2007). 104, 107
- [243] F. YANG, J. GRACIANI, J. EVANS, P. LIU, J. HRBEK, J. F. SANZ, and J. A. RODRIGUEZ, *J. Am. Chem. Soc.* **133**, 3444 (2011). 104
- [244] M. ALFREDSSON and C. R. A. CATLOW, *Phys. Chem. Chem. Phys.* **4**, 6100 (2002). 105
- [245] Z. YANG, Z. LU, and G. LUO, *Phys. Rev. B* **76**, 075421 (2007). 105, 116, 119
- [246] Z. YANG, Z. LU, G. LUO, and K. HERMANSSON, *Phys. Lett. A* **369**, 132 (2007). 105
- [247] E. L. WILSON, R. GRAU-CRESPO, C. L. PANG, G. CABAILH, Q. CHEN, J. A. PURTON, C. R. A. CATLOW, W. A. BROWN, N. H. DE LEEUW, and G. THORNTON, *J. Phys. Chem. C* **112**, 10918 (2008). 105, 128
- [248] Z. LU and Z. YANG, *J. Phys.: Condens. Matter* **22**, 475003 (2010). 105, 128
- [249] C. JUNG, H. TSUBOI, M. KOYAMA, M. KUBO, E. BROCLAWIK, and A. MIYAMOTO, *Catal. Today* **111**, 322 (2006). 105
- [250] Y. ITO, C. JUNG, Y. LUO, M. KOYAMA, A. ENDOU, M. KUBO, A. IMAMURA, and A. MIYAMOTO, *Appl. Surf. Sci.* **252**, 2598 (2006). 105
- [251] E. A. KÜMMERLE and G. HEGER, *J. Solid State Chem.* **147**, 485 (1999). 105
- [252] H. NÖRENBERG and G. A. D. BRIGGS, *Phys. Rev. Lett.* **79**, 4222 (1997). 106
- [253] H. NÖRENBERG and G. A. D. BRIGGS, *Surf. Sci.* **402-404**, 734 (1998). 106
- [254] Z. YANG, T. K. WOO, M. BAUDIN, and K. HERMANSSON, *J. Chem. Phys.* **120**, 7741 (2004). 106
- [255] S. MA, J. RODRIGUEZ, and J. HRBEK, *Surf. Sci.* **602**, 3272 (2008). 107

## References

- [256] F. ŠUTARA, M. CABALA, L. SEDLÁČEK, T. SKÁLA, M. ŠKODA, V. MATOLÍN, K. PRINCE, and V. CHÁB, *Thin Solid Films* **516**, 6120 (2008). 107, 108
- [257] T. STAUDT, Y. LYKHACH, L. HAMMER, M. A. SCHNEIDER, V. MATOLÍN, and J. LIBUDA, *Surf. Sci.* **603**, 3382 (2009). 107, 108
- [258] D. R. MULLINS, P. V. RADULOVIC, and S. H. OVERBURY, *Surf. Sci.* **429**, 186 (1999). 107
- [259] S. ECK, C. CASTELLARIN-CUDIA, S. SURNEV, M. G. RAMSEY, and F. P. NETZER, *Surf. Sci.* **520**, 173 (2002). 107
- [260] M. ALEXANDROU and R. M. NIX, *Surf. Sci.* **321**, 47 (1994). 107
- [261] C. HARDACRE, G. M. ROE, and R. M. LAMBERT, *Surf. Sci.* **326**, 1 (1995). 107
- [262] K.-D. SCHIERBAUM, *Surf. Sci.* **399**, 29 (1998). 107
- [263] U. BERNER and K.-D. SCHIERBAUM, *Thin Solid Films* **400**, 46 (2001). 107
- [264] U. BERNER and K.-D. SCHIERBAUM, *Phys. Rev. B* **65**, 235404 (2002). 107, 123, 129
- [265] D. C. GRINTER, R. ITHNIN, C. L. PANG, and G. THORNTON, *J. Phys. Chem. C* **114**, 17036 (2010). 107, 123, 125
- [266] C. BREINLICH, J. M. ESSEN, E. BARLETTA, and K. WANDELT, *Thin Solid Films* **519**, 3752 (2011). 107
- [267] M. VOLMER and A. WEBER, *Z. Phys. Chem.* **119**, 277 (1926). 107
- [268] J. C. CONESA, *Surf. Sci.* **339**, 337 (1995). 107
- [269] M. NOLAN, S. GRIGOLEIT, D. C. SAYLE, S. C. PARKER, and G. W. WATSON, *Surf. Sci.* **576**, 217 (2005). 109
- [270] M. NOLAN, S. C. PARKER, and G. W. WATSON, *Surf. Sci.* **595**, 223 (2005). 109
- [271] A. D. MAYERNICK and M. J. JANIK, *J. Chem. Phys.* **131**, 084701 (2009). 116
- [272] S. FABRIS, S. DE GIRONCOLI, S. BARONI, G. VICARIO, and G. BALDUCCI, *Phys. Rev. B* **71**, 041102 (2005). 118
- [273] E. WUILLOUD, B. DELLEY, W. D. SCHNEIDER, and Y. BAER, *Phys. Rev. B* **53**, 202 (1984). 118
- [274] F. TRAN and P. BLAHA, *Phys. Rev. Lett.* **102**, 226401 (2009). 118
- [275] A. KOKALJ, *J. Mol. Graph. Model.* **17**, 176 (1999). 123
- [276] R. F. W. BADER, *Atoms in Molecules - A Quantum Theory*, Oxford University Press, 1990. 126
- [277] S. JENKINS, *J. Phys.: Condens. Matter* **14**, 10251 (2002). 128
- [278] S. JENKINS, P. W. AYERS, S. R. KIRK, P. MORI-SÁNCHEZ, and A. M. PENDÁS, *Chem. Phys. Lett.* **471**, 174 (2009). 128
- [279] S. IMAMURA, T. HIGASHIHARA, Y. SAITO, H. ARITANI, H. KANAI, Y. MATSUMURA, and N. TSUDA, *Catal. Today* **50**, 369 (1999). 131
- [280] K. HAYEK, M. FUCHS, B. KLÖTZER, W. REICHL, and G. RUPPRECHTER, *Top. Catal.* **13**, 55 (2000). 131

## References

- [281] S. PENNER, D. WANG, D. S. SU, G. RUPPRECHTER, R. PODLOUCKY, R. SCHLÖGL, and K. HAYEK, *Surf. Sci.* **532**, 276 (2003). 131
- [282] S. PENNER, G. RUPPRECHTER, H. SAUER, D. S. SU, R. TESSADRI, R. PODLOUCKY, R. SCHLÖGL, and K. HAYEK, *Vacuum* **71**, 71 (2003). 131
- [283] M. FUCHS, B. JENEWEIN, S. PENNER, K. HAYEK, G. RUPPRECHTER, D. WANG, R. SCHLÖGL, J. J. CALVINO, and S. BERNAL, *Appl. Catal., A* **294**, 279 (2005). 131



# Publications

## Journal Articles

1. D. Vogel, C. Spiel, Y. Suchorski, A. Urich, R. Schlögl, G. Rupprechter:  
*"Mapping the local reaction kinetics by PEEM: CO oxidation on individual (100)-type grains of Pt foil"*  
*Surf. Sci.* **605**, 1999 (2011).
2. C. Weilach, C. Spiel, K. Föttinger, G. Rupprechter:  
*"Carbonate formation on  $Al_2O_3$  thin film model catalyst supports"*  
*Surf. Sci.* **605**, 1503 (2011).
3. C. Spiel, P. Blaha, Y. Suchorski, K. Schwarz, G. Rupprechter:  
*" $CeO_2/Pt(111)$  interface studied using first-principles density functional theory calculations"*  
*Phys. Rev. B* **84**, 045412 (2011).
4. C. Spiel, D. Vogel, Y. Suchorski, W. Drachsel, R. Schlögl, G. Rupprechter:  
*"Catalytic CO Oxidation on Individual (110) Domains of a Polycrystalline Pt Foil: Local Reaction Kinetics by PEEM"*  
*Catal. Lett.* **141**, 625 (2011).
5. C. Spiel, D. Vogel, Y. Suchorski, W. Drachsel, R. Schlögl, G. Rupprechter:  
*"Catalytic CO oxidation on individual (110) domains of a polycrystalline Pt foil: bistability and reaction front propagation"*  
*Proceedings of the 10th International Symposium on Catalysis* **1**, 13 (2010).
6. Y. Suchorski, C. Spiel, D. Vogel, W. Drachsel, R. Schlögl, G. Rupprechter:  
*"Local Reaction Kinetics by Imaging: CO Oxidation on Polycrystalline Platinum"*  
*ChemPhysChem* **11**, 3231 (2010).
7. C. Spiel, P. Blaha, K. Schwarz:  
*"Density functional calculations on the charge-ordered and valence-mixed modification of  $YBaFe_2O_5$ "*  
*Phys. Rev. B* **79**, 115123 (2009).
8. S. Ryu, S. Das, T. Butz, W. Schmitz, C. Spiel, P. Blaha, K. Schwarz:  
*"Nuclear quadrupole interaction at  $^{44}Sc$  in the anatase and rutile modifications of  $TiO_2$ : Time-differential perturbed-angular-correlation measurements and ab initio calculations"*  
*Phys. Rev. B* **77**, 094124 (2008).

## Oral Presentations and Posters

1. D. Vogel, C. Spiel, Y. Suchorski, R. Schlögl, G. Rupprechter:  
*"CO oxidation on a mesoscopic scale: from individual  $\mu\text{m}$ -sized Pd grains to oxides"*  
Presentation: 13th Palladium Day, Obergurgl, Austria; 04.10.–05.10.2011
2. C. Spiel, P. Blaha, Y. Suchorski, K. Schwarz, G. Rupprechter:  
*"An insight into the  $\text{CeO}_2/\text{Pt}(111)$  interface via first-principles DFT calculations"*  
Poster: 14th Austrian Chemistry Days 2011, Linz, Austria; 26.09.–29.09.2011
3. C. Spiel, D. Vogel, Y. Suchorski, A. Ulrich, R. Schlögl, G. Rupprechter:  
*"Reaction-diffusion fronts in catalytic CO oxidation on  $\mu\text{m}$ -sized Pt(110) and Pt(100) domains: a comparative PEEM study"*  
Poster: 5th International Workshop on Surface Physics, Ladek Zdroj, Poland; 02.09.–05.09.2011
4. Y. Suchorski:  
*"Laterally-resolved kinetics of catalytic CO oxidation: from mesoscopic to nano-scale"*  
Presentation: 5th International Workshop on Surface Physics, Ladek Zdroj, Poland; 02.09.–05.09.2011
5. Y. Suchorski, C. Spiel, D. Vogel, R. Schlögl, G. Rupprechter:  
*"Laterally-resolved reaction kinetics by PEEM"*  
Presentation: 28th European Conference on Surface Science ECOS28, Wrocław, Poland; 28.08.–02.09.2011
6. C. Spiel, P. Blaha Y. Suchorski, K. Schwarz, G. Rupprechter:  
*"An insight into the  $\text{CeO}_2/\text{Pt}(111)$  interface via first-principles DFT calculations"*  
Poster: 28th European Conference on Surface Science ECOS28, Wrocław, Poland; 28.08.–02.09.2011
7. D. Vogel, C. Spiel, Y. Suchorski, R. Schlögl, G. Rupprechter:  
*"From single crystal surfaces via defects to surface oxides: Catalytic CO oxidation on an individual  $\mu\text{m}$ -sized Pd(110) domain"*  
Poster: 28th European Conference on Surface Science ECOS28, Wrocław, Poland; 28.08.–02.09.2011
8. D. Vogel, C. Spiel, Y. Suchorski, R. Schlögl, G. Rupprechter:  
*"Locally resolved reaction kinetics: CO oxidation on individual grains of a polycrystalline platinum foil"*  
Poster: 7th Brazilian/German Workshop on Applied Surface Science, Buzios, Brazil; 03.04.–08.04.2011
9. D. Vogel, C. Spiel, Y. Suchorski, R. Schlögl, G. Rupprechter:  
*"Locally Resolved Study of CO Oxidation on Polycrystalline Pd: Reaction Kinetics and Surface Morphology"*  
Presentation: 12th Palladium Day, Berlin, Germany; 21.03.–22.03.2011
10. Y. Suchorski, C. Spiel, D. Vogel, W. Drachsel, R. Schlögl, G. Rupprechter:  
*"Reaction Kinetics via PEEM Imaging: Laterally-Resolved Studies of Catalytic CO Oxidation on Single Grains of Polycrystalline Pd"*  
Presentation: 60th Annual Meeting of Austrian Physical Society, Salzburg, Austria; 06.09.–10.09.2010

## Publications

11. C. Spiel, D. Vogel, Y. Suchorski, W. Drachsel, R. Schlögl, G. Rupprechter:  
*"Catalytic CO oxidation on individual (110) domains of a polycrystalline Pt foil: bistability and reaction front propagation"*  
 Presentation: 10th Pannonian International Symposium on Catalysis, Krakow, Poland; 29.08.–02.09.2010
  
12. C. Spiel, D. Vogel, Y. Suchorski, W. Drachsel, R. Schlögl, G. Rupprechter:  
*"Catalytic CO Oxidation on Polycrystalline Palladium: Local Reaction Kinetics by PEEM"*  
 Poster: International Symposia on Advancing the Chemical Sciences (ISACS), Budapest, Hungary; 13.07.–16.07.2010
  
13. Y. Suchorski, C. Spiel, D. Vogel, W. Drachsel, R. Schlögl, G. Rupprechter:  
*"Laterally-resolved reaction kinetics: PEEM microscopy of catalytic CO oxidation on polycrystalline Pt"*  
 Presentation: International Workshop - In situ characterization of near-surface processes, Eisenerz, Austria; 30.05.–03.06.2010
  
14. D. Vogel, C. Spiel, Y. Suchorski, W. Drachsel, R. Schlögl, G. Rupprechter:  
*"CO oxidation on individual grains of polycrystalline Pt and Pd: Locally resolved reaction kinetics"*  
 Presentation: 10th Palladium Day, Berlin, Germany; 18.05.–19.05.2010
  
15. D. Vogel, C. Spiel, Y. Suchorski, W. Drachsel, R. Schlögl, G. Rupprechter:  
*"Locally resolved kinetics of catalytic CO oxidation on polycrystalline platinum"*  
 Poster: Junior Scientist Conference 2010, Vienna, Austria; 07.04.–09.04.2010
  
16. D. Vogel, C. Spiel, Y. Suchorski, W. Drachsel, R. Schlögl, G. Rupprechter:  
*"Locally resolved kinetics of catalytic CO oxidation on polycrystalline platinum"*  
 Poster: DPG-Frühjahrstagung der Sektion Kondensierte Materie, Regensburg, Germany; 22.03.–26.03.2010
  
17. Y. Suchorski, C. Spiel, D. Vogel, W. Drachsel, R. Schlögl, G. Rupprechter:  
*"Visualizing local reaction kinetics: PEEM studies of catalytic CO oxidation on polycrystalline Pt"*  
 Presentation: Workgroup Meeting of COST D41 "Inorganic oxides: Surfaces and Interfaces", Munich, Germany; 18.03.–19.03.2010
  
18. Y. Suchorski, C. Spiel, D. Vogel, W. Drachsel, R. Schlögl, G. Rupprechter:  
*"Laterally-resolved reaction kinetics: PEEM microscopy of catalytic CO oxidation on polycrystalline Pt"*  
 Presentation: 3S'10, 23. Symposium on Surface Science 2010, St. Christoph/Arlberg, Austria; 07.03.–13.03.2010
  
19. D. Vogel, C. Spiel, Y. Suchorski, W. Drachsel, R. Schlögl, G. Rupprechter:  
*"PEEM microscopy of catalytic CO oxidation on polycrystalline Pt"*  
 Presentation: 9th Palladium Day, Vienna, Austria; 19.10.–20.10.2009
  
20. Y. Suchorski, W. Drachsel, C. Spiel, D. Vogel, R. Schlögl, G. Rupprechter:  
*"Along the complexity axis in catalytic CO oxidation on Pt: single crystal, polycrystalline foil, model of a catalytic particle"*  
 Poster: ÖPG, SPS, ÖGA Joint annual Meeting, Innsbruck, Austria; 02.09.–04.09.2009

## Publications

21. C. Spiel, D. Vogel, Y. Suchorski, W. Drachsel, R. Schlögl, G. Rupprechter:  
*"From single crystals to domain systems: catalytic CO oxidation on Pt"*  
Presentation: 13th Austrian Chemistry Days 2009, Joint Meeting of the Czech, Slovak & Austrian Chemical Societies, Vienna, Austria; 24.08.–27.08.2009
22. C. Weilach, C. Spiel, G. Rupprechter:  
*"The interaction of CO with a Zn/Pd(111) surface alloy"*  
Poster: Bunsentagung 2009, 108. Hauptversammlung der Deutschen Bunsen-Gesellschaft für Physikalische Chemie e.V., Cologne, Germany; 21.05.–23.05.2009
23. C. Weilach, C. Spiel, G. Rupprechter:  
*"Carbonate type species on alumina model catalysts"*  
Poster: COST Action D41 Winter School 2009 "Methods to characterize oxide surfaces", Berlin, Germany; 23.02.–27.02.2009
24. G. Rupprechter, C. Weilach, C. Spiel:  
*"Model studies on PdZn alloys"*  
Presentation: 7th Palladium Day, Bad Dreikirchen, Italy; 28.09.–30.09.2008
25. C. Spiel, S. Abermann, E. Bertagnolli, G. Rupprechter:  
*"New model catalysts prepared by atomic layer deposition (ALD)"*  
Presentation: 9th Pannonian International Symposium on Catalysis, Strbske Pleso, Slovakia; 08.09.–12.09.2008
26. C. Weilach, C. Spiel, G. Rupprechter:  
*"Carbonate formation on alumina model catalysts"*  
Presentation: 9th Pannonian International Symposium on Catalysis, Strbske Pleso, Slovakia; 08.09.–12.09.2008
27. C. Weilach, C. Spiel, G. Rupprechter:  
*"Carbonate formation at defects of Al<sub>2</sub>O<sub>3</sub>/NiAl(110) thin films"*  
Poster: 25th European Conference on Surface Science ECOS25, Liverpool, United Kingdom; 27.07.–01.08.2008
28. K. Föttinger, K. Zorn, C. Weilach, C. Spiel, G. Rupprechter:  
*"Pd nanoparticles on high surface area alumina: surface reactions and catalytic applications"*  
Presentation: CERC3 Young Chemists workshop, Vienna, Austria; 15.05.–16.05.2008
29. C. Weilach, C. Spiel, G. Rupprechter:  
*"PM-IRAS and XPS studies of carbonate formation on model catalysts"*  
Presentation: COST Action D41 Workgroup 3 Meeting, Marseille, France; 24.04.–25.04.2008

# Curriculum vitae

## Personal details

Full name: Christian Johannes Spiel  
Address: Waaggasse 4/8,  
1040 Vienna, Austria  
Email: christian.spiel@imc.tuwien.ac.at  
Birthday: 26. April 1980  
Place of birth: Vienna

## Education

3/2000–4/2007 Studies of Technical Chemistry, Vienna University of Technology,  
Austria  
4/2007 Dipl.-Ing. (M.Sc.), Vienna University of Technology, Austria;  
Thesis: “Gemischtvalente Verbindungen. Berechnungen mit WIEN2k”;  
Thesis supervisor: Prof. K. Schwarz  
8/2007–1/2012 Ph.D. studies in Technical Chemistry, Vienna University of Technology,  
Austria;  
Supervisors: Prof. G. Rupprechter and Prof. Y. Suchorski

January 20, 2012